LOCAL SUSTAINED DELIVERY OF ANTIBODY THERAPEUTICS FROM INJECTABLE HYDROGELS FOR THE TREATMENT OF GLIOBLASTOMA

LOCAL SUSTAINED DELIVERY OF ANTIBODY THERAPEUTICS FROM INJECTABLE HYDROGELS FOR THE TREATMENT OF GLIOBLASTOMA

By VINCENT HUYNH, B.Sc.

A Thesis Submitted to the School of Graduate Studies in Partial Fulfilment of the Requirements for the Degree Doctor of Philosophy

DESCRIPTIVE NOTE

McMaster university DOCTOR OF PHILOSPHY (2021) Hamilton, Ontario (Chemical Biology)

TITLE: Local sustained delivery of antibody therapeutics from injectable hydrogels for the treatment of glioblastoma

AUTHOR: Vincent Huynh, B.Sc. (McMaster University)

SUPERVISOR: Professor Ryan Wylie

NUMBER OF PAGES: XIX, 274

LAY ABSTRACT

Drugs that enable the immune system to recognize cancer have the potential to produce numerous anti-cancer treatments, revolutionizing the field cancer research. However, many of these drugs are clinically ineffective because of toxic side effects from high doses required to achieve therapeutic concentrations. Additionally, physiological transport barriers in cancers, especially brain cancer, impede drug distribution, and make it more difficult to reach therapeutic levels.

Delivering drugs to the correct location and for an optimal amount of time will improve drug efficacy. Drug loaded implants mostly composed of water, known as hydrogels, can be injected at the disease site for the slow infusion of drug into the area. This would simultaneously decrease the need for frequent drug administrations and decrease toxic side effects.

Here, we present the development and testing of a medical implant that delivers drugs that redirect the immune system to recognize and kill brain tumors. The chemical properties of the implant were optimized for safe injection into the brain and for long term drug infusion. By extending the time of drug exposure using the implant, drug effectiveness was increased in mice bearing human brain cancer. Additionally, we showed the development of an in vitro model for brain cancer where anti-cancer effects of the drug loaded implant can be easily observed for applications in drug screening. This thesis, therefore, demonstrates how implantable materials can increase the effectiveness of anti-cancer drugs through efficient drug delivery.

ABSTRACT

Modern production techniques and new therapeutic targets have resulted in the development of different antibody-based treatment modalities, increasing the repertoire of viable drug candidates. The clinical success of immune checkpoint inhibitors (ICIs) has generated great interest in antibody-based drugs as cancer immunotherapeutics.

The lack of treatment options for glioblastoma, the most malignant glioma, has expedited the investigation of antibody immunotherapeutics for glioblastoma. However, glioblastoma's low tumor mutational burden (TMB) and immunosuppressive tumor immune microenvironment (TIME) render ICI monotherapies ineffective. Furthermore, physiological barriers (blood-brain barrier) impede drug localization, requiring high systemic doses that result in severe immunological side effects. To address these limitations, we demonstrate the benefit of: (1) local sustained release of antibody immunotherapeutics to increase the duration and magnitude of anti-cancer response and, (2) combination therapies to further promote immune cell mediated killing of glioblastoma.

With the goal of creating an implant for the local infusion of immunotherapeutics (LIIT), herein, I describe the development of an injectable hydrogel that incorporates an affinity based drug delivery system (DDS). Using well known affinity interactions, a three component DDS referred to as competitive affinity release (CAR) released a bioactive antibody for >100d. CAR was then modified to a new system called displacement affinity release (DAR), for the delivery of minimally modified antibody. An in situ gelling, injectable, low-fouling poly(carboxybetaine) hydrogel was fabricated for the localization of the DDS.

The DDS hydrogel combination was used to deliver a dual antigen T cell engager (DATE) targeting CD133 positive glioblastoma cells in 3D embedded spheroid cultures and a patient derived xenograft model. Controlled release of CD133 targeting DATE increased survival benefit within the xenograft model. Within the 3D embedded spheroid model, the combination therapy of DATE with an αPD-1 ICI increased and sustained cytotoxic effects.

Here I developed a platform technology for the local infusion of immunotherapeutics (LIIT), amenable to any antibody cancer immunotherapeutics. This project demonstrates how local infusion with immunostimulatory drugs can increase the magnitude and duration of anti-cancer immunotherapy in glioblastoma where physiological barriers impede drug accumulation.

ACKNOWLEDGEMENTS

There are many people I would like to thank in this section. I honestly believe this thesis is more so a productive of their investment and time in me than anything I produced. This thesis is more a culmination of everyone's success than my own. To everyone below, thank you for helping me through this time in my life.

Firstly, to my supervisor, Dr. Ryan Wylie, I don't think I would have ever finished or even started grad school without you. Thank you for being a friend and mentor. For being patient with failures and granting me creative freedoms that I never thought I would have as a student. You spurred my creativity, pushed me to strive for better and taught me how to be a skeptic. You taught me what the meaning of perseverance and your work ethic is something I am still trying to emulate. This thesis is more of a testament of your success as a supervisor and a mentor than it is of me as a scientist or student. To my committee members Dr. Todd Hoare and Dr. Alex Adronov, thank you for providing useful feedback and for pushing me in areas where I am weak. You have made me a better scientist.

To the past and current members of the Wylie lab, thank you for your help and aid especially when starting the lab. Thank you all for providing scientific camaraderie. Thank you, Alex for being a good lab partner all these years. To all the undergrads that I have trained, Catherine, Muneeb, Ting, Elise, Jath, Matt, Logan, Marc, Tim, Jaimy, Alex, Mark, Spencer Anthony, Natalie and Kevin. You have all played a part in my experience during these years, although training all of you was hard and sometimes unfruitful, it was undoubtedly my pleasure.

To the friends in the lab who enriched my experience so much more than I ever thought. To Shrav, Rashik, Stu, Jaimy, Jonas and Alex, thank you all for helping me when I felt down and out and lending an ear when I needed it. To Giselle and Ken, thank you for spurring my growth and checking up on me when I needed it.

To my friends on the various dragonboat teams the morning gym bros. Thank you for providing me some respite and escape from grad school, at least for a couple of years. Despite overall adding to my mental stress, those years taught me resilience and perseverance in light of adversity.

And to my family, this work is dedicated to you. Thank you for putting up with me. To Anthony, who is always amusing with his niche habits and helping me whenever I did need it. To mom and dad, I don't believe any of this, my education or my work ethic, is possible without you. Thank you for helping me and supporting me when I most needed it. For your love and care. This thesis is

more yours than it ever will be mine. To my grandparents, I hope you guys are proud. To Pópó, thank you for everything, I hope you are proud of me.

TABLE OF CONTENTS

LIST OF FIGURES

LIST OF SUPPLEMENTARY FIGURES

LIST OF TABLES

LIST OF SUPPLEMENTARY TABLES

LIST OF ABBREVIATIONS

Abbreviation	Definition
3D	Three dimensional
A500	Absorbance at 500nm
Abs	Antibodies
ADCC	Antibody dependent cell mediated cytotoxicity
ADCP	Antibody dependent cell mediated phagocytosis
AgD	Agarose-desthiobiotin
AImT	Antibody immunotherapeutics
APMA	N-(3-aminopropyl)methacrylamide
BBB	Blood brain barrier
B-Bv	Biotinylated bevacizumab
BiTE	Bispecific T cell engager
BLI	Biolayer interferometry
BSA	Bovine serum albumin
BTIC	Brain tumor initiating cells
CAF	Cancer associated fibroblasts
CAR	Chimeric antigen receptor
CB	Carboxybetaine
CBS	Calf bovine serum
CNS	Central nervous system
CR	Checkpoint receptors
CRA	Cytokine release assay
CRS	Cytokine release syndrome
CS	Carbon Spacer
CTL	Cytotoxic T cells
D-Abs	Desthiobiotinylated antibodies
DAR	Displacement affinity release
DARA	Displacement affinity release of antibodies
DATE	Dual antigen T cell engager
DBCO	Dibenzocyclooctyne
D-Bv	Desthiobiotinylated bevacizumab
DCM	Dichloromethane
D-DATE	Desthiobiotinylated DATE
DDS	Drug delivery system
DLS	Dynamic light scattering
DMF	Dimethylformamide

DMSO	Dimethylsulfoxide
EC_{50}	Half maximal effective concentration
EDC	N-(3-dimethylaminopropyl)-N'-ethylcarbodiimide
ELISA	Enzyme linked immunosorbent assay
FBR	Foreign body reaction
FBS	Fetal bovine serum
GBM	Glioblastoma
GPC	Gel permeation chromatography
HA	Hyaluronan
HABA	2-(4-hydroxyphenylazo)benzoic acid
HEPES	4-(2-hydroxyethyl)-1-piperazineethanesulfonic acid
HUVEC	Human umbilical vein endothelial cell
ICI	Immune checkpoint inhibitor
IDO	Indeoleamine 2,3-dioxygenase
IEDDA	Inverse electron demand Diels-Alder
IFNγ	Interferon γ
IL-6	Interleukin 6
IV	Intravenous
IVIS	In vivo imaging system
K_D	Dissociation constant
k_{eff}	Effective first order constant
LCST	Lower critical solution temperature
LIIT	Local infusion of immunotherapeutics
LSPR	Local surface plasmon resonance
MALDI	Matrix assisted laser desorption ionization
MEC	Minimal effective concentration
MHC	Major histocompatibility complex
miRNA	Micro-interfering RNA
MMP	Matrix metalloproteinase
MW	Molecular weight
MWCO	Molecular weight cut-off
NHS	N-hydroxysuccinimide
NIR	Near Infrared
NK	Natural killer
NMR	Nuclear magnetic resonance
NSG	Nonobese diabetic/severe combined immunodeficiency gamma
NT	Neutravidin
OD550	Optical density 550

PBS	Phosphate buffered saline
pCB	Poly(carboxybetaine)
PDMS	Polydimethylsiloxane
PDX	Patient derived xenograft
PEG	Polyethylene glycol
PEGMA	Poly(ethylene glycol) methyl ether methacrylate
PEO	Poly(ethylene oxide)
PHEMA	Poly(hydroxyethyl methacrylate)
PLGA	Poly(lactic-co-glycolic acid)
pNIPAM	poly(N-isopropylacrylamide)
pSB	Poly(sulfobetaine)
PVME	Poly(vinyl methyl ester)
RAFT	Reversible addition fragmentation transfer
RI	Refractive index
ROS	Reactive oxygen species
SA	Streptavidin
SA-DBCO	Streptavidin-dibenzocyclooctyne
scFv	Single chain variable fragment
SDS-PAGE	Sodium dodecyl sulfate polyacrylamide gel electrophoresis
SEC	Size exclusion chromatography
SPAAC	Strain promoted azide alkyne cycloaddition
TAA	Tumor associated antigen
TAM	Tumor associated macrophage
TCP	Tissue culture plate
TCR	T cell receptor
TDLN	Tumor draining lymph nodes
TEA	Triethylamine
TEC	Tumor endothelial cells
T_{Em}	T cell effector memory
T_{Ex}	Exhausted T cell
TFA	Trifluoroacetic acid
THF	Tetrahydrofuran
TIL	Tumor infiltrating lymphocyte
TIME	Tumor immune microenvironment
TLR	Toll like receptor
TMB	Tumor mutational burden
TME	Tumor microenvironment
TNBS	2,4,6-trinitrobenzensulfonic acid

TNFα	Tumor necrosis factor α
TOF	Time of flight
T_{reg}	Regulatory T cells
TriKE	Trispecific killer engagers
TSA	Tumor specific antigen
UCST	Upper critical solution temperature
UV	Ultraviolet
VEGF	Vascular endothelial growth factor

CHAPTER 1. INTRODUCTION

Author's Preface:

Portions of the following chapter was published in *ChemBioChem* under the citation:

Huynh V, Jesmer AH, Shoaib MM, D'Angelo A, Rullo AF and Wylie RG. Improved efficacy of antibody cancer immunotherapeutics through local and sustained delivery

I was responsible for the preparation of the manuscript, a majority of the literature review.

This article has been reprinted with the permission from Wiley.

1.1 Abstract

Biologics made from antibodies are a growing class of cancer immunotherapeutics that facilitate immune cell mediated tumor killing. However, their efficacies against solid tumors are limited by transport barriers, poor tumor uptake, rapid clearance, and low maximum tolerable concentrations (MTCs), which may lead to potentially fatal systemic side effects before reaching the minimum effective concentration (MEC) in cancerous tissue. To increase antibody immunotherapeutic concentrations in tumors while decreasing systemic concentrations, local delivery vehicles for sustained antibody release are being developed. Controlled release mechanisms are incorporated into drug delivery vehicles to maintain the MEC within tumors. Depending on the nature and site of the disease, different vehicles with varying material composition, porosity, stiffness, and method of implantation are being investigated.

The local sustained delivery of immunotherapeutics is particularly difficult for glioblastoma (GBM) due to the blood brain barrier (BBB) and rapid clearance of antibody therapeutics from brain tissue. Here we review current immune modulating materials, with a focus on vehicles for antibody delivery, that elicit T cell anti-cancer responses suitable for GBM treatments.

1.2 Antibody immunotherapeutics for cancer

Antibody immunotherapeutics (AImTs) have emerged as a leading alternative to or combination therapy with traditional cancer treatments such as chemotherapy and radiation; AImTs activate or direct immune effector cells (e.g., macrophages, natural killer (NK) cells and T cells) to recognize and/or kill cancer cells.[1,2] Several AImT scaffolds have been developed to enhance tumor killing through different mechanisms: preventing immune checkpoint blockade, bridging T/NK cells to cancer cells, and antibody dependent cell-mediated phagocytosis/cytotoxicity (ADCP/ADCC; **Figure 1.1**). Agonist antibodies that target co-stimulatory receptors to enhance anti-cancer immune cell functions are also being developed.[2,3] The lower incidence rate of serious side effects from AImTs compared to adoptive cell therapies and cancer vaccines has led to 16 FDA approved AImTs for cancer treatments.[4]

1.2.1 Monoclonal antibodies as immune checkpoint inhibitors and immune stimulators

Many cancer cells contain immune checkpoint surface receptors that inhibit cytotoxic T cell (CTLs) responses (**Figure 1.1**). Immune checkpoint inhibitors (ICIs) competitively bind the checkpoint receptors (CRs) such as PD-1 and CTLA-4 on CTLs and PD-L1 on cancer cells to prevent CR mediated inactivation of CTLs.[1] The success of the αPD-1 and αCTLA-4 inhibitors have sparked intense research resulting in the discovery of numerous checkpoints. ICI efficacy is

partially determined by cancer cell CR expression levels, and are therefore effective against cancers with high CR levels (e.g. melanoma and non small cell lung carcinoma) and not cancers with low CR levels (e.g. glioblastoma) when administered as standalone therapies.[5–7] Recently, NK cell inactivation by the PD-1/PD-L1 blockade was discovered, representing a new therapeutic target for PD-1/PD-L1 ICIs.[8] The PD-1 checkpoint blockade have also been implicated to be effective for the reactivation of tumor associated macrophages (TAMs), polarizing TAMs to an inflammatory phenotype, creating a immunostimulatory tumor immune microenvironment (TIME).[9]

Despite the spectacular clinical success of ICI's, they remain mostly ineffective in tumors with low TMB cancers such as glioblastoma (GBM) due to the lack of an adaptive immune response.[10,11] Therefore, other therapeutics are being developed to promote immune cell recognition of cancer cells.

New therapeutic immune checkpoints targets are still being discovered which also provide therapeutic benefit. Furthermore, immunostimulatory agonist antibodies are also being investigated to stimulate immunes cells in the TIME ultimately leading to CTL activation and recruitment resulting in an anti-cancer effect (**Table 1.1**).[2,3]

Table 1.1 Monoclonal antibodies used as ICI and immunostimulators that enhance anti-cancer responses and reduce tumor burden.

	Target	Target Cell type
ICI monoclonal antibodies	CTLA-4[1,12]	T cells
	PD-1[1,8,13,14]	T cells, Macrophage
	PDL-1[1,13]	Cancer
	LAG-3[15]	T cells
	TIM-3[16]	T cells
	VISTA[17]	T cells
	SIGLEC-10/CD24[18]	Macrophage
	SIGLEC-7/CD43[19]	Cancer/T cells
	CD47[20]	Macrophage
	B7-H3[21]	Cancer
	CD73[22]	NK
	TIGIT[23,24]	T cells, NK cells
Immunostimulatory monoclonal antibodies	OX40[25,26]	T cells
	ICOS[3,27]	T cells
	CD28[3,28]	T cells
	CD137/4-1BB[3,29]	T cells
	CD40[30]	T cells
	GITR[31]	T cells
	CD27[32]	T cells

1.2.2 Bispecific antibodies for cancer cell recognition

To target tumors with low TMB, bispecific and trispecific antibodies were developed to enhance immune cell recognition of cancer cells without the need

for an adaptive immune response (**Figure 1.1**).[33–35] For T cell mediated tumor killing, bi-specific T cell engagers (BiTEs) were constructed to simultaneously bind tumor associated antigens (TAAs) on cancer cells and the CD3 receptor on T cells, which initiates T cell mediated tumor killing.[34] Similar to BiTEs, bispecific killer cell engagers (BiKEs) and trispecific killer cell engagers (TriKEs) bridge cancer cells to the CD16 receptor on NK cells; TriKEs also promote NK cell survival and proliferation through the incorporation of an IL-15 fusion protein as a crosslinker between the two antibody Fab fragments.[33,34,36] Other AImTs induce ADCC upon binding cancer antigens and recruiting NK cells through Fc binding; receptor clustering on NK triggers formation of lytic synapses for cancer cell killing.[30,37]

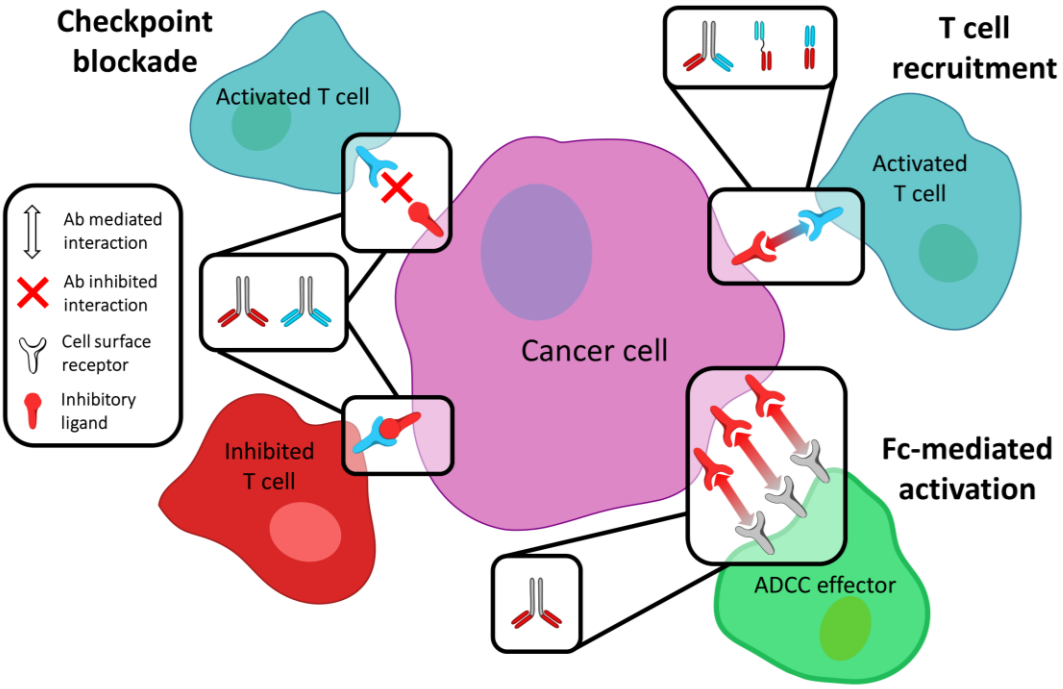

Figure 1.1 Major classes and mechanisms of AImTs to enhance or initiate cancer cell killing by immune cells. ICIs prevents the checkpoint blockade of T cells and inactivation of CTLs by cancer cells. Bispecific AImTs recruit T cells to cancer cells by binding TAAs and T cell receptors. AImTs for Fc mediated activation recruit immune effector cells to cancer cell surfaces through Fc receptor binding and clustering.

1.2.3 Transport barriers and the need for sustained local delivery

Although effective against blood cancers, AImTs suffer from low efficacy against solid tumors; the dense cellular-matrix composition, impaired blood flow and transvascular pressure gradients of solid tumors hinders therapeutic

penetration and accumulation.[22,38,39] To reach therapeutic concentrations, large intravenous (IV) doses of ICIs (up to 10 mg/kg per injection for avelumab, a PD-1 ICI) are required, which leads to side effects such as nausea, fatigue and hyperthyroidism.[14]

Due to the lack of an Fc domain, tumor accumulation of BiTEs is hindered by short plasma half-lives. To overcome half-life limitations, blinatumomab, a BiTE for acute lymphoblastic leukemia targeting CD19, is IV infused at 5-15 $\mu g/m^2$/day (average body surface area of 1.79 m^2)[40] continuously for 4 weeks; higher doses (>30 $\mu g/m^2$/day) produced adverse neurological events as a result of CRS.[41–44] Therefore, slow infusions are also required to avoid potentially fatal side effects (e.g. cytokine release syndrome (CRS)). For solid tumors, intravenous infusions of BiTEs may not achieve the MEC within tumors without potentially fatal side effects.

To minimize side effects and increase efficacy, local sustained AImT release from intratumoral implants can decrease systemic concentrations while maintaining concentrations above the MEC within the TIME for extended periods of time (**Figure 1.2**).[45] Delivery devices should sustain AImT release to maximize the duration and magnitude of immune cell mediated tumor killing. Beyond improved efficacy, local delivery may also decrease treatment cost by lowering dosage and administration frequency. Section 2 defines the material properties

and protein delivery technologies required to achieve AImT local sustained delivery.

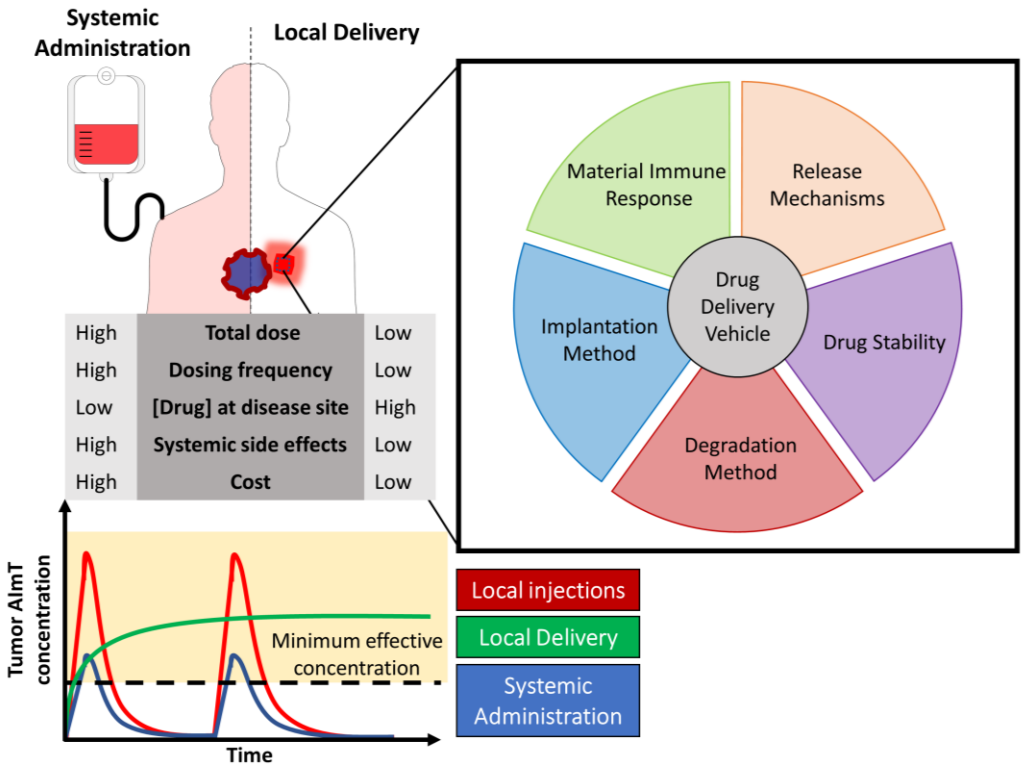

Figure 1.2 Local sustained delivery vs systemic and local injections. Local sustained delivery extends the period of effective AImT concentrations in the tumor compared to systemic or local injections. Vehicles for local sustained release are tailored by release mechanisms, implantation, degradation, AImT stabilization (drug stability) and immune material response.

1.3 Properties for local delivery vehicles for sustained AImTs release

Implantable local delivery vehicles must control AImT release rates while stabilizing encapsulated AImTs. Furthermore, vehicle components and degradation products should promote or not hinder the anti-cancer immune response. Hydrogels, water swollen polymer networks, have been used extensively as drug depots for localized protein delivery due to their high levels of hydration increasing protein stability.[46–48] By controlling hydrogel properties such as porosity, water content and chemical properties, hydrogels can be designed with varying drug release profiles, degradation rates, biological activity, and implantation procedures (**Figure 1.2**).[45,48]

1.3.1 Minimizing deleterious immune responses to implanted materials

Typically, vehicles should have a minimal foreign body response (FBR). FBR is characterized by the recruitment of monocytes upon implant recognition that first differentiate towards M1 like macrophages, then towards M2 like macrophages and the establishment of foreign body giant cells, ultimately leading to the recruitment of fibroblasts that excrete collagen and encapsulates the implant in a fibrous capsule, impeding drug release.[49–51] Currently, there is conflicting data regarding the specific macrophage polarization which induces this response. What can be surmised from current studies is that both M1 like and M2 like macrophages work constitutively to produce the fibrous capsule.[49,52]

Implant composition,[53,54] size,[55] shape,[55] roughness,[51] porosity,[56,57] fouling properties,[53,58] and chemical modifications influence the FBR.[50,54] For example, spherical alginate microgels modified with specific chemical moieties in specific sizes,[54,55,59] low-fouling zwitterionic hydrogels,[53] and hydrogels with uniform porosity[56,57] have been shown to minimize or prevent the FBR. Targeting immune cell bioactivity can also minimize the FBR. For example, immobilization of certain proteins (e.g. CD200),[60] peptides (e.g. CD47 binding peptides)[61] or polysaccharides (e.g. fucoidan)[62] recognized by immune cells on materials attenuates immune and inflammatory responses. Direct modulation of macrophage either through systemic administration of a CSFR-1 inhibitor or local release of a CSFR-1 inhibitor have also been able to inhibit FBR when a polydimethylsiloxane (PDMS) implant was implanted into non-human primates.[63,64] It should be noted that a partial FBR can be advantageous for some applications; for example, the controlled vascularization of a partial FBR capsule around an implant allows immune evasion of allogeneic transplantation of β cells for intravenous infusion of therapeutic biomolecules such as insulin.[65]

Immunogenic or immunosuppressive materials and degradation products that hinder immune and anti-cancer responses should also be avoided. For example, due to the ubiquitous use of polyethylene glycol (PEG) a large portion of the population now produces IgG and IgM anti-PEG antibodies (~42% of blood donors have PEG antibodies) which may limit local delivery by decreasing

implant lifetime.[66,67] Although inherently non-toxic, adverse immune reactions to PEG have been reported further implicating the need for PEG alternatives. Upon intracellular degradation, poly(lactic-co-glycolic acid) (PLGA) has been suggested to be immunosuppressive and decreases T cell proliferation and expression of inflammatory factors.[68] Degradation of poly(glycerol sebacate) results in acidic by-products that may contribute towards mild inflammation and fibrosis.[69] Therefore, vehicle components must be carefully selected to avoid unwanted immune responses.

1.3.2 Vehicles for maintaining AImT bioactivity

Proteins, such as AImTs, may become inactive upon aggregation or enzymatic degradation after implantation, which is particularly important for BiTEs due to their susceptibility to non-specific catabolism.[42] Hydrogels stabilize proteins by hindering protease mediated degradation, preventing aggregation and reducing protein induced immune responses. For example, encapsulation of uricase in polycarboxybetaine (pCB) hydrogels increased protein stability increasing stability at 65°C for over 2 h and reduce immunogenicity, evading immune cell recognition, with no production of inflammatory cytokines.[70] Encapsulation of immunogenic drugs from polyzwitterionic hydrogels have also shown to provide a very similar benefit, evading immune related mechanisms. Conjugation of polymers such as PEG, poly(oligoethylene glycol) methacrylate (PEGMA) or poly-zwitterions to proteins also increases their stability while

reducing immunogenicity.[67] Hydrophilic polymers and hydrogels help stabilize the protein and reduce adverse immune response, making them ideal for AImT delivery.

1.3.3 Implantation methods

Administration of drug loaded vehicles occurs by surgical implantation, injection, or surface application. Surgical implantation of prefabricated vehicles is usually performed immediately after tumor resection. Injectable vehicles are best suitable for injection into tumor resection cavities, surgically inaccessible tumors, and treatments requiring multiple administrations.[45] Microneedle patches are ideal for surface accessible tumors such as melanoma.[71] Due to their minimally invasive nature, injectables and microneedle patches have lower complication rates than surgically implanted vehicles.

Injectable hydrogels that crosslink through biorthogonal reactions or physical transitions (e.g. temperature) are routinely used as local delivery vehicles to achieve in situ crosslinking gels that can occupy void cavities after tumor resection.[47,72,73] Biorthogonal crosslinking chemistries include: aldehyde-hydrazide,[74] Michael addition,[75] strain promoted azide-alkyne cycloaddition (SPAAC),[76] inverse electron demand Diels-Alder (IEDDA),[77] furan-maleimide Diels-Alder cycloaddition,[78] Schiff base,[79] thiol-ene/yne Michael addition[80] or Staudinger ligation.[81] Physical crosslinking chemistries include guest-host interactions (ex. cyclodextrin,[82] cucurbiturils,[83] nucleoside base pairing[84]),

temperature sensitive hydrophobic interactions, peptide self-assembly and ionic interactions. Hydrogels crosslinked via physical crosslinks or reversible covalent bonds can be broken through shear stress and re-assemble, often resulting in self-healing or shear-thinning hydrogels, making them useful as injectables.[82,85,86]

1.3.4 Controlled implant degradation

When designing the hydrogel, the degradation rate and products will partially determine the success of the treatment. Tunable degradation rates are required for many release applications and degradation should primarily occur upon complete release of the drug cargo unless the rate of degradation is related to the release mechanism. In addition, the bioactivity, metabolism and clearance rate of the degradation products should be considered.

1.3.5 Mechanisms of degradation

Implanted materials crosslinked through irreversible bonds can degrade through hydrolytic,[87,88] stimuli induced promoted (light,[89] heat,[90] magnetism, upconversion nanoparticles[91]), and enzymatic bond cleavage of the crosslinks or polymer backbone (**Table 1.2**). Materials with reversible crosslinks may degrade upon clearance of molecules upon disassociation. Materials may also degrade through surface erosion or bulk degradation. Due to their hydrated nature, hydrogels typically experience bulk degradation. For release applications, tuning the rate of hydrogel degradation is necessary to optimize drug concentrations at the disease site. Premature degradation can result in a burst release of toxic drug

concentrations. Although not always desirable, permanent implants may be used, however, fibrosis and other chronic immunological consequences are possible, which may result in patient discomfort.

Table 1.2 Common hydrogel degradation mechanisms.

Degradation Mechanism/ Methods	Bond, Interaction, Material or Recognition sequence	Tuning Method
Hydrolytic degradation/pH response	Carbamate,[87] ester[92]	Crosslink density, polymer concentration
Diffusion based degradation from reversible crosslinks	Schiff base,[79] Furan-maleimide diels-alder,[78] supramolecular complexes,[82,83,90] hydrophobic phase transitions,[93,94] electrostatically driven phase transitions[95]	Crosslink density, polymer concentration, bond/interaction strength
External trigger	Light induced (photocage, heat[89,90]), Upconversion nanoparticles[91]	Triggered response
Enzymatic degradation	MMP peptide,[96] hyaluronan degradation,[97] collagen degradation[98]	Crosslink density, polymer concentration

Crosslink density. To prolong the duration of degradation, the polymer concentration or degree of crosslinking can be increased. However, such strategies can negatively impact the rate of release through changes in porosity and result in a negative immunological response due to increased stiffness of the hydrogel.[48,99] Degradation can impact the rate of release through the relaxation of polymer chains resulting in changes in porosity, strategies to account for this

physical phenomena and tune the time frame of the degradation would have to be considered.

External trigger. Stimuli induced degradation can be advantageous as exogenous signals can induce degradation at specific timepoints to best match requires for drug delivery. For example, light induced photocleavage of nitrobenzyl based crosslinkers degradation can be tuned through the different adjacent labile bonds.[100] By changing the adjacent cleavable bond, the rate of stimuli induced degradation can be tuned.

Hydrolysis and bond half-life. Bonds with well defined half-lives are also advantageous as materials can be tuned to degrade after delivery of the drug cargo. For example, carbamate bonds with well highly tunable hydrolysis half-lives can yield hydrogels for short and long term drug release.[88] This tunability has lead to the fabrication of hydrogels with a wide range of degradation rates from 2 days to >100 days.[87]

Reversible crosslinks and diffusion. Crosslinks formed through reversible covalent bonds can yield hydrogels that degrade through slow diffusion of the polymer chains, crosslinks can include furan maleimide Diels alder adducts,[78] Schiff base crosslinking,[79] supramolecular complexes (cyclodextrins with PEG/adamantane,[82,86,90] cucurbiturils[83]), hydrophobic associations[93] or zwitterionic coacervation.[95] The equilibrium of the interaction, degree of

crosslinking, and polymer molecular weight will directly correlate to the time of degradation.

Enzymatic. Enzymatic degradation occurs if the hydrogel contains a corresponding cleavage site within the crosslinks or polymer backbone. Enzymatic degradation of hydrogels is routinely achieved by incorporated hyaluronan,[97] collagen[98] or matrix metalloproteinase (MMP) cleavable peptides.[96,101]

1.3.6 Degradation products and clearance

Clearance and biological activity of degraded products from implants play important roles in therapeutic efficacy. Degradation products of the hydrogel can enhance drug efficacy by working synergistically with the released drug. For example, a ROS responsive degradable hydrogel modified with D-1MT on the polymer backbone released an αPD-1 antibody. The D-1MT hydrogel degradation aided in the the ICI response against B16F10 melanoma.[102] However, degradation products can also result in immunosuppression, such as PLGA which can supress DC activation needed for vaccines or other immunostimulatory agents.[68] The cytotoxicity of degradation products can also be explored for therapeutic benefit. For example, polyurethane degrades into cytotoxic aromatic isocyanates, which can create localized cytotoxic environments to enhance cancer therapies.[103]

The clearance mechanism of degraded products will depend on their chemical and physical properties. As clearance is a necessary parameter to

optimize for ensuring the degraded products do not interfere with drug efficacy or cause systemic side effects. Furthermore, the mode of clearance is important to avoid potential accumulation of the degraded side products at specific areas which can be toxic. For example, particles < 5.5 nm[104] or PEG < 50 kDa[105] are cleared by the renal system, larger degradation products mainly undergo hepatic clearance. However, some polymers would be resorbable.

1.4 Sustained release mechanisms

Controlling the release rate of therapeutic proteins from hydrogels is crucial to rapidly achieve and maintain MECs at the disease site by optimizing the initial burst release and infusion rate (sustained release rate).[45] If tuned correctly, the burst release will immediately achieve the MEC in the local environment while the infusion rate will maintain the MEC at the disease site in the presence of clearance mechanisms.[48] Without an appropriate burst release and a corresponding infusion rate (release rate), reaching efficacious local concentrations would not be possible. Each release mechanism has a corresponding burst release, therefore choosing the correct release mechanism for the specific disease is important for effective treatment regimes (**Figure 1.3**). The groupings of each release mechanism with respect to their burst release and half life in **Figure 1.3** are approximations from the literature, exceptions exist that do not align with the allocations in the figure.

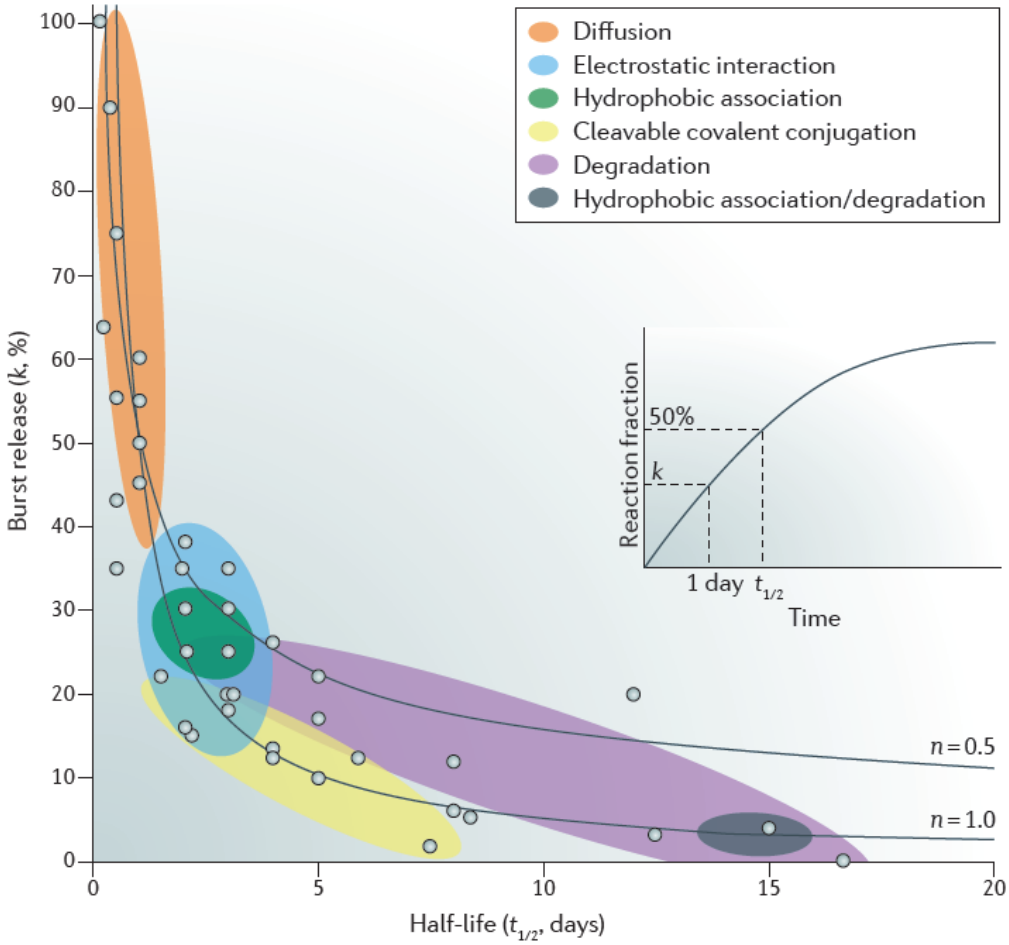

Figure 1.3 Literature values for reported burst release of hydrogel drug delivery systems as a function of half-life and release mechanism. Half-life is defined as the time required to release half of the initial drug loading. Interactions systems with higher affinities result in longer half-life of release and a smaller corresponding burst release. Although these represent common literature trends,

there are exceptions that exist outside of the groupings highlighted here. Figure adapted from Li and Mooney from Nat. Rev. Mater. (2016).[48]

1.4.1 Controlled diffusion.

Release rates from hydrogels are controlled by altering porosity to decrease protein diffusivity inside the gel.[47] For example, controlling polymer branching and crosslink density using defined dendronized networks in hydrogels extended the release of antibodies from ~5 to 100 days.[106] Self-assembling peptide hydrogels with well defined porous networks have been used to study release and diffusion kinetics of different proteins such as lysozyme, BSA and IgG antibodies for over 40 days in vitro, where release rates are predominantly governed by protein hydrodynamic radius.[4] Peptide based hydrogels can also protect physically entrap proteins and sustain the release of brain derived neurotrophic factor (BDNF) for 28 days in vivo and basic fibroblast growth factor (bFGF) for up to 3 weeks.[107,108] Protein release can also be controlled by vehicle degradation, commonly involving hydrolysis.

1.4.2 Affinity Release

Affinity release systems decrease the apparent diffusion of proteins in hydrogels by incorporating protein binding sites within the polymer network; increasing the affinity of the physical interaction will decrease protein release rates (**Figure 1.4**).[48,109] The cumulative interaction or affinity between the two

binding partners is a sum of the electrostatic and hydrophobic interactions of the two molecules. Although powerful, affinity release systems are susceptible to environmental changes as well as hydrophobic and electrostatic variations of hydrogels. Careful selection of the hydrogel components and thorough knowledge of the disease site will provide a means to choose the correct interaction for the specific application.

Affinity systems requires the hydrogel and protein to contain corresponding binding partners and therefore chemical modifications may be required.[110] Careful modification of the protein to maintain its bioactivity and therapeutic benefit is mandatory. Binding partners with facile tuning of binding kinetics can be used to rapidly achieve and screen several protein release profiles to aid in the identification of therapeutic release profiles for drugs (**Table 1.3**).

The first described affinity system released heparin binding proteins (e.g. vascular endothelial growth factor (VEGF), platelet-derived growth factor (PDGF)) from hydrogels containing heparin sulfate.[111] PEG hydrogels with heparin mimicking peptides sustained the release of basic fibroblast growth factor (bFGF) for 30 days.[112] Hydrogels modified with aptamers or cyclodextrins can also control the release of proteins.[85,113] Reversible covalent bonds, such as furan-maleimide Diels-Alder adducts, can mimic a non-covalent interaction and sustain the release of peptides from PEG hydrogels.[114]

Affinity controlled release of therapeutics have also been developed using supramolecular binding. The binding of a cholesterol modified miRNA (microRNA) to an injectable β cyclodextrin modified hyaluronan hydrogel resulted in sustained release of the therapeutic over 20 days, promoting cardiomyocyte proliferation and regeneration after myocardial infarction in a mouse model.[85] Functional recovery was observed and tissue regeneration was also shown through sustained local delivery of the miRNA.

Guanidinium interactions between a negatively charged self assembling peptide hydrogel with a cationic repeating peptide, have been used to prolong the release of different growth factors from a hydrogel.[115] Tunability was achieved through the number of repeating units of the binding peptide which was covalently attached to the growth factor. Similarly, an electrostatically driven affinity system was developed using PLGA nanoparticles imbedded within a hydrogel.[116] Sustained release of growth factors was achieved without encapsulation of the proteins in PLGA but was predominantly governed by electrostatic interactions with the PLGA particle.

Table 1.3 Summary of affinity interactions for sustained release from of biologics from hydrogels

Affinity Interaction	Drug Delivered	Duration of Release (days)
Heparin/VEGF	VEGF[117]	4-40

Heparin/bFGF	bFGF[111]	4-30
SH3/SH3 binding peptide	Chondroitinase ABC[118,119], rFGF2[120], SDF-1α[119]	7-10
Aptamer/growth factor	VEGF, PDGF-BB, bFGF[108]	5-14
Heparin/β-NGF	β-NGF[121]	15
Alginate-sulfate/growth factors	VEGF, PDGF-BB, TGF-β1[122]	1-7
Guanidinium/peptide interaction domain	EGFP, IFNα[115]	14-36
Cyclodextrin/cholesterol	miRNA[85]	20
Furan Maleimide Diels Alder	RGD[114]	1-2

1.4.3 Triggered release

Protein release triggered by external stimuli such as ultrasound, light and magnetism, or endogenous triggers such as controlled tunable hydrolysis creates pulsatile or accelerated release profiles to maintain the MEC (**Figure 1.4**); the trigger frequency is optimized to maintain the therapeutic drug concentrations. Common triggers include:

- *Ultrasound.* Ultrasound can disrupt polymer networks of self-healing gels to release proteins with spatiotemporal control. For example, ionically crosslinked alginate gels released stromal cell-derived factor 1α (SDF-1α) and VEGF upon ultrasound exposure.[123]
- *Light*. UV-visible and NIR light has been used to control the release proteins by cleaving photolabile bonds or producing heat (induces

hydrogel phase transition increasing porosity), respectively. For example, sequential delivery of two therapeutic proteins was achieved from a dual light responsive PEG hydrogel, where each protein was released upon wavelength specific photo-triggered degradation of covalent bonds.[124] NIR triggered local release of bevacizumab conjugated to gold nanorods embedded in a hydrogel patch was effective in a combination therapy against a colon cancer mouse model.[125] Release of the nanorods was achieved through heat generated by the nanorods light absorption, degrading the encapsulating thermosensitive dextran hydrogel.

- *Magnetism*. Magnetic responsive nanoparticles embedded in thermoresponsive hydrogels, such as poly N-isopropylacrylamide,[126] can control the release of encapsulated drug. Application of an external magnetic field produces heat that promotes a phase transition of the hydrogel, shrinking the hydrogel for enhanced drug release rates. Heat dissipation reverts the hydrogel to its swollen state, decreasing drug release rates. The heat generated is required to be below the melting temperature (T_M) of the protein being released.
- *Endogenous triggers*. Proteins conjugated to hydrogels through hydrolytic covalent bonds can achieve controlled releases upon hydrolysis. For example, carbamate bonds with tunable hydrolysis rates controlled the release of peptides from a PEG hydrogel.[127] The hydrolysis of the carbamate bonds was tuned by the addition of electron withdrawing

groups. Matrix metalloproteinase (MMP) degradable gels have also been developed to release drugs upon MMP mediated degradation.[128]

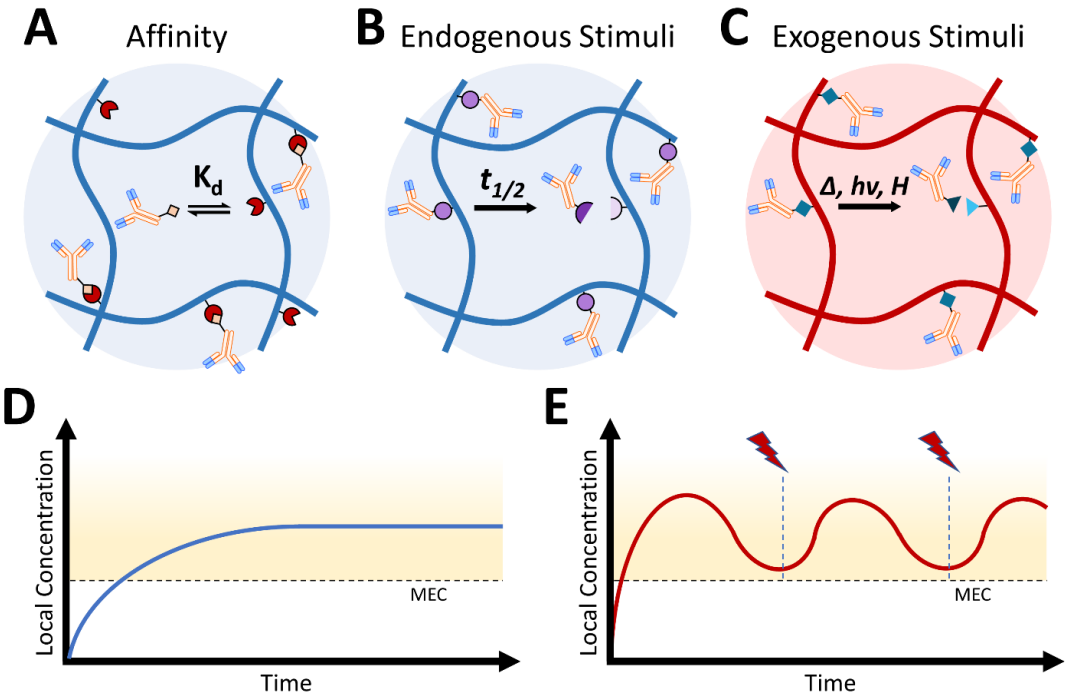

Figure 1.4 Hydrogel controlled release strategies relevant for AImT delivery from hydrogels. A) Affinity release is the sum of non-covalent interactions between the antibody and the hydrogel. Release is primarily governed by interaction strength, which can be expressed as the dissociation constant. B) Endogenous stimuli mostly refer to enzymatically cleavable peptides or hydrolytic degradation. C) Triggered release either through light, heat, or magnetism are considered exogenous triggers for release. D) Affinity and endogenous stimuli aim to provide a steady release of the drug resulting in a sustained local

concentration above the MEC. E) Stimuli responsive release uses external stimuli to achieve local drug concentrations above MEC, often exhibiting pulsatile local concentrations.

1.5 Local sustained delivery of AImTs to enhance cancer immunotherapies

Local and/or sustained delivery of ICIs, bispecific molecules and antibodies enhance cancer immunotherapies alone or in combination with chemotherapy[129] and radiation therapy[130] in pre-clinical models. For example, chemotherapy is believed to enhance immunotherapies by increasing antigen presentation for activation of endogenous T cells.[131] Immunostimulatory molecules with BiTEs have also been shown to enhance the anti-cancer immune response and lead to greater tumor killing and survival,[34,35] likely due to greater recruit or stimulation of CTLs.

1.5.1 Local administration

Local administrations of monoclonal antibodies to enhance anti-cancer immunotherapies have been shown to be beneficial.[26,132] Locoregional administrations of ICI reduces the number of clearance pathways for the antibody. As antibodies are predominantly cleared through a tumor draining lymph node (TLDN), effective concentrations of the antibody can be maintained at the disease site by overloading TLDN with locoregional administrations of the antibody, increasing half-life and thereby efficacy.[132] Improvements in drug efficacy from

TLDN overloading has been demonstrated with intratumoral administrations with ICI's, and immunostimulatory antibodies. For example, a combination of an OX40 antibody and adjuvant TLR9 agonist resulted in the eradication of spontaneous malignancy.[26] Furthermore, intratumoral administration of immunostimulatory CD137 antibodies with αPD-1 ICI have also been shown to provide substantial benefit.[133] The success of local administrations therapeutic antibodies and drugs provides the premise and rationale for seeking methods in creating local sustained release systems which would invariably enhance drug pharmacokinetic parameters by maximising both the localization, duration, and magnitude of the elicited anti-cancer response.

1.5.2 Local delivery of ICIs

The local delivery of ICIs has drawn considerable attention due to the enhanced therapeutic benefit from local drug delivery systems. Systemic administrations of combination therapies often result in off target systemic side effects,[134] therefore local delivery of ICIs using hydrogels in combination with other therapies is an effective method of treating various cancers.[135] ICI local delivery has been demonstrated across different material modalities, such as hydrogels and polymeric microneedles, with both methods enhancing the therapeutic benefit of ICI's.[71,102,136,137]

Local implantation of αPD-1 or CTLA-4 ICI antibody loaded hydrogels are shown to provide both local and systemic anti-cancer effects, while incurring

little systemic toxicity.[71,72,136,137] Local administrations of ICI with combination therapies such as TLR agonists,[138] chemotherapeutics[129] and other immunostimulatory compounds[28] have resulted in enhanced anticancer activity, reducing tumor size and improving murine survival. These compounds enhance tumor recognition by T cells, increasing the number of tumor infiltrating lymphocytes (TILs) and population of activated T cells. These methods of delivery is not limited to T cell modulating antibodies, the delivery of a CD47 ICI antibody targeting macrophages from an in situ forming hydrogel have also shown enhanced therapeutic benefit.[73] Furthermore, by targeting macrophages, growth of distant tumors was also inhibited, which is due innate immune system activation through enhanced macrophage recognition of the cancer and resulting cancer antigen presentation by the macrophages, incurring antibody production and immune cellular reprogramming.

Microneedle patches are small polymeric needles that are easily implanted at the disease site near a surface, the needles would typically degrade over time releasing its drug cargo.[139] The ease of administration and minimally invasive application makes it an attractive material for delivering drug cargo to visible tumors. Microneedle patches have been designed to locally sustain the release of immunotherapeutic antibodies.[72] Efficacy has been demonstrated in a B16F10 melanoma mouse model, where the degradation of hyaluronic acid composed needles results in the sustained release of a αPD-1 ICI.[137]

1.5.3 Local delivery of the immunostimulatory antibodies

Local sustained delivery of immunostimulatory antibodies is an effective strategy to curtail immune related side effects that occur upon systemic administration. Local activation of the immune system results in the conversion of an immunologically cold or immunosuppressive TIME; to a hot or immunostimulatory TIME. For example, trastuzumab and bevacizumab are shown to display increased therapeutic benefit upon sustained release from a hydrogel.[106,140,141] CD40 agonistic antibody increased efficacy upon local sustained release from a nanofluidic device, activating T cells and providing enhanced therapeutic benefit.[142,143] This strategy can easily be translated towards the growing number of immunostimulatory antibodies, widening the repertoire of safe and effective drugs through enhancing pharmacokinetic properties.

1.5.4 Delivery vehicles for BiTE immunotherapies

To overcome their short half-life and poor tumor penetration, BiTEs have recently emerged as a candidate for novel delivery vehicles. Examples of BiTE delivery using hydrogels and secreting cells have been reported.

Hydrogels. Although local delivery of BiTEs using hydrogels has not been reported, subcutaneous injections of BiTE loaded hydrogels that act as implantable infusion pumps have been employed to overcome the BiTE's short plasma half life. In situ gelling triblock PEG-PLA hydrogels encapsulating BiTEs that target prostate-specific membrane antigen (PSMA) were injected

subcutaneously in a LNCaP xenograft prostate cancer mouse model.[144] The hydrogel improved BiTE plasma half-life, T cell tumor infiltration, and survival to >50% at 55 days, whereas no mice survived past 50 days upon IV or subcutaneous injections without the hydrogel.

BiTE secreting cells. Local delivery of BiTEs has been demonstrated using cells that secrete BiTEs. One example encapsulated BiTE expressing mesenchymal stem cells within a PEG-heparin cryogel allowing for continuous secretion of a CD33 targeting BiTE.[145] The treatment saw effective anti-tumour response in acute myeloid leukemia mouse model.

A dual targeting therapy executed by BiTE secreting CAR T cells results in local release of BiTEs within the TIME.[146] CAR T cells targeting EGFRvIII were engineered to secrete an EGFR targeting BiTE. After intraventricular administration, the dual therapy improved efficacy over CD19 BiTE secreting CAR T cells in preclinical models. Despite the presence of EGFR on non-cancer cells, the combination therapy showed limited systemic toxicity. These results imply that release of BiTE within the tumor was necessary for T cell anti-cancer responses without incurring systemic toxicity.

1.6 Immunotherapy for Glioblastoma

Glioblastoma is a recurrent glioma that remains incurable with a median survival time of 14 months from the time of diagnosis,[147] making GBM one of the most deadly cancers.[10] Immunotherapy is a promising treatment for GBM but has

had limited success due to transport barriers, the immunosuppressive TIME, and low tumor mutational burden (lack of adaptive immune response).[148] ICIs with and without chemotherapy have shown limited success in clinical trials, most likely due to the lack of an adaptive immune response.[11,149] Therefore, ICI immunotherapies will require combination therapies.

Neo-antigen personalized vaccines have been shown to recruit TILs and overcome the low TMB of GBM. Neoantigens refer to the tumor specific antigens (TSA) which arise upon non-synonymous mutations.[150,151] In a phase 1b clinical trial, there was an increase in survival for patients treated with neo antigen vaccines in combination with αPDL-1 antibodies as well as bevacizumab supplementation, with a mean progression free survival of 7.6 months and a median overall survival of 16.8 months. This indicates that the use of cancer vaccines targeting neoantigens provides survival benefit despite the low TMB and "cold" TIME. However, many of the patients receiving the vaccine required high doses of immunosuppressants to decrease systemic adverse side effects.

Drugs that target TAA's rather than TSA's, such as CD133 and EGFR, may be a less costly alternative that is more readily available to a broader number of patients as they are not personalized for the specific patient. TAA's however typically result in off target toxicities for this reason. Recently, a study performed by Vora et al, showed the efficacy of BiTEs and CAR T cells targeting $CD133^+$ cells in GBM. CD133 targeting BiTEs were administered intracranially, however,

their short half-life ($t_{1/2}$ ~15.6 h) in brain tissue hindered efficacy in vivo.[152] Despite this, CD133 targeting CAR T cells, when injected intracranially, resulted in eradication of the tumor. The data suggested that CD133 is a viable antigen target, and the lack of BiTE efficacy was due its poor half-life in tumor tissue.

GBM T cell immunotherapies will most likely require combination therapies to direct T cells to TAAs and improve T cell cytolytic activity within the TIME. By targeting resident T cells, tumor associated macrophages (TAMs), the tumor vasculature (tumor endothelial cells (TECs)), and cancer associated fibroblasts (CAFs), CTL infiltration and activity can be improved by altering cytokine and chemokine expression levels.[10,11,148] Therefore, we will require immunotherapeutics to direct T cells to TAAs and alter the TIME for enhanced T cell recruitment and activity.

1.7 Conclusion and Outlook

Transport barriers, protein elimination pathways, and low tumor uptake contribute to the low efficacy of AImTs after systemic administration. Furthermore, the high IV doses of AImTs required to reach the MEC increase treatment costs and incidence rates of serious side effects such as CRS. Locoregional administrations of the therapeutic have been shown to be efficacious in producing pronounced therapeutic benefit in comparison to systemic administrations by decreasing the number of elimination methods, due to regional elimination.

With fewer injections, local sustained delivery from implantable materials can increase the concentration of AImTs within the tumor while lowering systemic concentrations to decrease the rate of adverse events. There is increasing evidence that local delivery systems can maximize the duration and magnitude of AImT anti-cancer responses for increased tumor killing and decreased recurrence. Material properties such as size, shape, porosity, and chemical components influence AImT delivery and should be optimized to increase the efficacy of the local delivery system. Materials can also stimulate the immune system directly through immobilized immunostimulant biomolecules (CD137 and IL-2, anti-CD3 and anti-CD28) to enhance in vivo CTL activation and proliferation,[3,29] enhancing the therapeutic response of AImTs.

GBM, is a cancer where immunotherapy is currently being explored as a treatment option despite current setbacks and failures. With the advent of numerous new treatment modalities, in the form of oncolytic viruses, vaccines, neoantigen technology, CAR T cells, and antibody therapies, immunotherapy remains a viable method to treat the disease. Local delivery of AImTs would bypass physiological barriers while retaining an efficacious concentration (above MEC), localize the treatment, and eliminate the need for systemic administrations.

Therefore, the primary objective of this thesis to combine material design and fabrication, drug delivery, pharmacokinetics, immunology and cancer biology towards developing an effective treatment for GBM.

1.8 Thesis Objectives

The primary objective of this thesis is to design and fabricate an injectable hydrogel drug delivery system to locally deliver an antibody therapeutic for the treatment of GBM. I hypothesize that the sustained localized release from an injectable hydrogel can improve DATE efficacy against GBM. Specific objectives are broken down as follows:

- **Chapter 2 (published): Development of a long-term antibody delivery system with easily tunable release rates.** Using agarose as a model hydrogel, tunable release of a model antibody therapeutic, Avastin, was achieved over 100 days. Here, competing affinities between biotin and desthiobiotin to streptavidin were used to tune antibody release rates without further modifications to the antibody or hydrogel. The dissolution of sparingly soluble biotin derivative pellets imbedded within the hydrogel displaced an immobilized antibody-streptavidin conjugate from an agarose-desthiobiotin hydrogel. Release rates can be rapidly tuned by altering the concentration of the sparingly soluble biotin pellets or the solubility of the biotin derivative. The bioactivity of the antibody-streptavidin conjugate was confirmed through cell angiogenesis assays.

- **Chapter 3 (published): Development of an injectable, low-fouling, in situ gelling hydrogel composed of poly(carboxybetaine) (pCB) as a vehicle for controlled antibody release mechanisms.** Poly(carboxybetaine) copolymers were synthesized via reversible addition fragmentation transfer polymerization (RAFT) and crosslinked in situ using strain promoted azide-alkyne cycloaddition (SPAAC). A poly(carboxybetaine) polymer with an upper critical solution temperature (UCST) was also discovered, the first description in the literature. Furthermore, it is shown that the copolymer composition and degree of crosslinking can encourage electrostatic interactions resulting in a phase transition of the hydrogel.
- **Chapter 4 (published): Development of displacement affinity release (DAR) of antibodies from poly(carboxybetaine) hydrogels for the delivery of minimally modified bispecific antibodies.** The tunable release of a desthiobiotin modified Avastin was demonstrated from an in situ gelling carboxybetaine hydrogel. Carboxybetaine hydrogels that incorporated DAR remained low-fouling and Avastin release was tuned by altering the concentration of the competitor binder.
- **Chapter 5: Demonstrate the benefit of sustained release of a CD133 targeting DATE for glioblastoma.** Release of the DATE

results in increased tissue half-life and prolonged effective local concentrations, increasing the duration and magnitude of tumor killing. Combination therapy with anti-PD-1 antibody was also shown to sustain T cell anti-cancer activity, increasing the duration of drug efficacy in vitro. Using 3D in vitro models and patient derived xenograft (PDX) mouse models, this chapter demonstrates the effectiveness of local sustained release on improving DATE mediated tumor killing.

- **Chapter 6: Significance of local AImT delivery and future directions.** Significance of findings would be discussed with respect to recently developed materials, therapies and techniques discussed in this thesis.

1.9 References

1. Weiner, G. J. Building better monoclonal antibody-based therapeutics. *Nat. Rev. Cancer* **15**, 361–370 (2015).

2. Mayes, P. A., Hance, K. W. & Hoos, A. The promise and challenges of immune agonist antibody development in cancer. *Nat. Rev. Drug Discov.* **17**, 509–527 (2018).

3. Sanmamed, M. F. *et al.* Agonists of Co-stimulation in Cancer Immunotherapy Directed Against CD137, OX40, GITR, CD27, CD28, and ICOS. *Semin. Oncol.* **42**, 640–655 (2015).

4. Koutsopoulos, S., Unsworth, L. D., Nagai, Y. & Zhang, S. Controlled release of functional proteins through designer self-assembling peptide nanofiber hydrogel scaffold. *Proc. Natl. Acad. Sci. U. S. A.* **106**, 4623–4628 (2009).

5. Champiat, S., Ferté, C., Lebel-Binay, S., Eggermont, A. & Soria, J. C. Exomics and immunogenics: Bridging mutational load and immune checkpoints efficacy. *Oncoimmunology* **3**, e278171 (2014).

6. Rizvi, N. A. *et al.* Mutational landscape determines sensitivity to PD-1 blockade in non – small cell lung cancer. *Science* **348**, 124–128 (2016).

7. Khalil, D. N., Smith, E. L., Brentjens, R. J. & Wolchok, J. D. The future of cancer treatment: Immunomodulation, CARs and combination immunotherapy. *Nat. Rev. Clin. Oncol.* **13**, 273–290 (2016).

8. Hsu, J., Raulet, D. H. & Ardolino, M. Contribution of NK cells to immunotherapy mediated by PD-1/PD-L1 blockade. *J. Clin. Invest.* (2018) doi:10.1172/JCI99317.

9. Gordon, S. R. *et al.* PD-1 expression by tumour-associated macrophages inhibits phagocytosis and tumour immunity. *Nature* **545**, 495–499 (2017).

10. Medikonda, R., Dunn, G., Rahman, M., Fecci, P. & Lim, M. A review of glioblastoma immunotherapy. *J. Neurooncol.* **151**, 41–53 (2021).

11. Khasraw, M., Reardon, D. A., Weller, M. & Sampson, J. H. PD-1

Inhibitors: Do they have a Future in the Treatment of Glioblastoma? *Clin. Cancer Res.* **26**, 5287–5296 (2020).

12. Du, X. *et al.* A reappraisal of CTLA-4 checkpoint blockade in cancer immunotherapy. *Cell Res.* **28**, 416–432 (2018).

13. Ohaegbulam, K. C., Assal, A., Lazar-Molnar, E., Yao, Y. & Zang, X. Human cancer immunotherapy with antibodies to the PD-1 and PD-L1 pathway. *Trends Mol. Med.* **21**, 24–33 (2015).

14. Topalian, S. L. *et al.* Safety, Activity, and Immune correlates of Anti-PD-1 Antibody in Cancer. *N. Engl. J. Med.* **366**, 2443–2454 (2012).

15. Lui, Y. & Davis, S. J. LAG-3: a very singular immune checkpoint. *Nat. Immunol.* **19**, 1278–1279 (2018).

16. Anderson, A. C. Tim-3: An emerging target in the cancer immunotherapy landscape. *Cancer Immunol. Res.* **2**, 393–398 (2014).

17. Gao, J. *et al.* VISTA is an inhibitory immune checkpoint that is increased after ipilimumab therapy in patients with prostate cancer. *Nat. Med.* **23**, 551–555 (2017).

18. Barkal, A. A. *et al.* CD24 signalling through macrophage Siglec-10 is a target for cancer immunotherapy. *Nature* **572**, 392–396 (2019).

19. Wisnovsky, S. *et al.* Genome-wide CRISPR screens reveal a specific ligand

for the glycan-binding immune checkpoint receptor Siglec-7. *Proc. Natl. Acad. Sci. U. S. A.* **118**, (2021).

20. Liu, X. *et al.* CD47 blockade triggers T cell-mediated destruction of immunogenic tumors. *Nat. Med.* **21**, 1209–1215 (2015).

21. Lee, Y. H. *et al.* Inhibition of the B7-H3 immune checkpoint limits tumor growth by enhancing cytotoxic lymphocyte function. *Cell Res.* **27**, 1034–1045 (2017).

22. Thurber, G. M., Schmidt, M. M. & Wittrup, K. D. Antibody tumor penetration: Transport opposed by systemic and antigen-mediated clearance. *Adv. Drug Deliv. Rev.* **60**, 1421–1434 (2008).

23. Zhang, Q. *et al.* Blockade of the checkpoint receptor TIGIT prevents NK cell exhaustion and elicits potent anti-tumor immunity. *Nat. Immunol.* **19**, 723–732 (2018).

24. Dougall, W. C., Kurtulus, S., Smyth, M. J. & Anderson, A. C. TIGIT and CD96: new checkpoint receptor targets for cancer immunotherapy. *Immunol. Rev.* **276**, 112–120 (2017).

25. Curti, B. D. *et al.* OX40 is a potent immune-stimulating target in late-stage cancer patients. *Cancer Res.* **73**, 7189–7198 (2013).

26. Sagiv-Barfi, I. *et al.* Eradication of spontaneous malignancy by local immunotherapy. *Sci. Transl. Med.* **10**, (2018).

27. Sharma, P. & Allison, J. P. Dissecting the mechanisms of immune checkpoint therapy. *Nat. Rev. Immunol.* **20**, 75–76 (2020).

28. Hui, E. *et al.* T cell costimulatory receptor CD28 is a primary target for PD-1-mediated inhibition. *Science* **355**, 1428–1433 (2017).

29. Kwong, B., Gai, S. A., Elkhader, J., Wittrup, K. D. & Irvine, D. J. Localized immunotherapy via liposome-anchored anti- CD137 + IL-2 prevents lethal toxicity and elicits local and systemic antitumor immunity. *Cancer Res.* **73**, 1547–1558 (2013).

30. Li, F. & Ravetch, J. V. Inhibitory Fcγ receptor engagement drives adjuvant and anti-tumor activities of agonistic CD40 antibodies. *Science* **333**, 1030–1034 (2011).

31. Ko, K. *et al.* Treatment of advanced tumors with agonistic anti-GITR mAb and its effects on tumor-infiltrating Foxp3+CD25+CD4+ regulatory T cells. *J. Exp. Med.* **202**, 885–891 (2005).

32. Van De Ven, K. & Borst, J. Targeting the T-cell co-stimulatory CD27/CD70 pathway in cancer immunotherapy: Rationale and potential. *Immunotherapy* **7**, 655–667 (2015).

33. Vallera, D. A. *et al.* IL15 Trispecific Killer Engagers (TriKE) Make Natural Killer Cells Specific to CD33+ Targets while Also Inducing Persistence, in Vivo Expansion, and Enhanced Function. *Clin. Cancer Res.*

22, 3440–3450 (2016).

34. Goebeler, M. E. & Bargou, R. C. T cell-engaging therapies — BiTEs and beyond. *Nat. Rev. Clin. Oncol.* **17**, 418–434 (2020).

35. Huehls, A. M., Coupet, T. A. & Sentman, C. L. Bispecific T-cell engagers for cancer immunotherapy. *Immunol. Cell Biol.* **93**, 290–296 (2015).

36. Tay, S. S., Carol, H. & Biro, M. TriKEs and BiKEs join CARs on the cancer immunotherapy highway. *Hum. Vaccines Immunother.* **12**, 2790–2796 (2016).

37. Boyerinas, B. *et al.* Antibody-Dependent Cellular Cytotoxicity Activity of a Novel Anti-PD-L1 Antibody Avelumab (MSB0010718C) on Human Tumor Cells. *Cancer Immunol. Res.* **3**, 1148–1157 (2015).

38. Vasalou, C., Helmlinger, G. & Gomes, B. A Mechanistic Tumor Penetration Model to Guide Antibody Drug Conjugate Design. *PLoS One* **10**, e0118977 (2015).

39. Marucci, F., Berenson, R. & Corti, A. Improving drug uptake and penetration into tumors: current and forthcoming opportunities. *Front. Oncol.* **3**, (2013).

40. Sacco, J. J., Botten, J., Macbeth, F., Bagust, A. & Clark, P. The average body surface area of adult cancer patients in the UK: A multicentre retrospective study. *PLoS One* **5**, e8933 (2010).

41. Buie, L. W., Pecoraro, J. J., Horvat, T. Z. & Daley, R. J. Blinatumomab: A First-in-Class Bispecific T-Cell Engager for Precursor B-Cell Acute Lymphoblastic Leukemia. *Ann. Pharmacother.* **49**, 1057–1067 (2015).

42. Topp, M. S. *et al.* Safety and activity of blinatumomab for adult patients with relapsed or refractory B-precursor acute lymphoblastic leukaemia: A multicentre, single-arm, phase 2 study. *Lancet Oncol.* **16**, 57–66 (2015).

43. Von Stackelberg, A. *et al.* Phase I/Phase II study of blinatumomab in pediatric patients with relapsed/refractory acute lymphoblastic leukemia. *J. Clin. Oncol.* **34**, 4381–4389 (2016).

44. Topp, M. S. *et al.* Phase II trial of the anti-CD19 bispecific T cell-engager blinatumomab shows hematologic and molecular remissions in patients with relapsed or refractory B-precursor acute lymphoblastic leukemia. *J. Clin. Oncol.* **32**, 4134–4140 (2014).

45. Fenton, O. S., Olafson, K. N., Pillai, P. S., Mitchell, M. J. & Langer, R. Advances in Biomaterials for Drug Delivery. *Adv. Mater.* **30**, 1–29 (2018).

46. Augst, A. D., Kong, H. J. & Mooney, D. J. Alginate hydrogels as biomaterials. *Macromol. Biosci.* **6**, 623–633 (2006).

47. Hoare, T. R. & Kohane, D. S. Hydrogels in drug delivery: Progress and challenges. *Polymer* vol. 49 1993–2007 (2008).

48. Li, J. & Mooney, D. J. Designing hydrogels for controlled drug delivery.

Nat. Rev. Mater. **1**, 16071 (2016).

49. O'Brien, E. M., Risser, G. E. & Spiller, K. L. Sequential drug delivery to modulate macrophage behavior and enhance implant integration. *Adv. Drug Deliv. Rev.* **149**–**150**, 85–94 (2019).

50. Chen, W., Yung, B. C., Qian, Z. & Chen, X. Improving long-term subcutaneous drug delivery by regulating material-bioenvironment interaction. *Adv. Drug Deliv. Rev.* **127**, 20–34 (2018).

51. Anderson, J. M., Rodriguez, A. & Chang, D. T. Foreign body reaction to biomaterials. *Semin. Immunol.* **20**, 86–100 (2008).

52. Witherel, C. E., Abebayehu, D., Barker, T. H. & Spiller, K. L. Macrophage and Fibroblast Interactions in Biomaterial-Mediated Fibrosis. *Advanced Healthcare Materials* vol. 8 (2019).

53. Zhang, L. *et al.* Zwitterionic hydrogels implanted in mice resist the foreign-body reaction. *Nat. Biotechnol.* **31**, 553–556 (2013).

54. Vegas, A. J. *et al.* Combinatorial hydrogel library enables identification of materials that mitigate the foreign body response in primates. *Nat. Biotechnol.* **34**, 345–352 (2016).

55. Veiseh, O. *et al.* Size- and shape-dependent foreign body immune response to materials implanted in rodents and non-human primates. *Nat. Mater.* **14**, 643–651 (2015).

56. Sussman, E. M., Halpin, M. C., Muster, J., Moon, R. T. & Ratner, B. D. Porous implants modulate healing and induce shifts in local macrophage polarization in the foreign body reaction. *Ann. Biomed. Eng.* **42**, 1508–1516 (2014).

57. Madden, L. R. *et al.* Proangiogenic scaffolds as functional templates for cardiac tissue engineering. *Proc. Natl. Acad. Sci. U. S. A.* **107**, 15211–15216 (2010).

58. Xie, X. *et al.* Reduction of measurement noise in a continuous glucose monitor by coating the sensor with a zwitterionic polymer. *Nat. Biomed. Eng.* **2**, 894–906 (2018).

59. Vegas, A. J. *et al.* Long-term glycemic control using polymer-encapsulated human stem cell-derived beta cells in immune-competent mice. *Nat. Med.* **22**, 306–311 (2016).

60. Kim, Y. K., Que, R., Wang, S. W. & Liu, W. F. Modification of Biomaterials with a Self-Protein Inhibits the Macrophage Response. *Adv. Healthc. Mater.* **3**, 989–994 (2014).

61. Tsai, R. K. & Discher, D. E. Minimal " Self " Peptides That Inhibit Delivery of Nanoparticles. *Science* **339**, 971–975 (2013).

62. Maclean, F. L., Ims, G. M., Horne, M. K., Williams, R. J. & Nisbet, D. R. A Programmed Anti-Inflammatory Nanoscaffold (PAIN) as a 3D Tool to

Understand the Brain Injury Response. *Adv. Mater.* 1805209 (2018) doi:10.1002/adma.201805209.

63. Doloff, J. C. *et al.* Colony stimulating factor-1 receptor is a central component of the foreign body response to biomaterial implants in rodents and non-human primates. *Nat. Mater.* **16**, 671–680 (2017).

64. Farah, S. *et al.* Long-term implant fibrosis prevention in rodents and non-human primates using crystallized drug formulations. *Nat. Mater.* **18**, 892–904 (2019).

65. Pepper, A. R. *et al.* A prevascularized subcutaneous device-less site for islet and cellular transplantation. *Nat. Biotechnol.* **33**, 518–523 (2015).

66. Yang, Q. & Lai, S. K. Anti-PEG immunity: Emergence, characteristics, and unaddressed questions. *Wiley Interdiscip. Rev. Nanomedicine Nanobiotechnology* **7**, 655–677 (2015).

67. Pelegri-Oday, E. M., Lin, E. W. & Maynard, H. D. Therapeutic protein-polymer conjugates: Advancing beyond pegylation. *J. Am. Chem. Soc.* **136**, 14323–14332 (2014).

68. Allen, R. P., Bolandparvaz, A., Ma, J. A., Manickam, V. A. & Lewis, J. S. Latent, Immunosuppressive Nature of Poly(lactic- co -glycolic acid) Microparticles. *ACS Biomater. Sci. Eng.* **4**, 900–918 (2018).

69. Pomerantseva, I. *et al.* Degradation behavior of poly(glycerol sebacate). *J.*

Biomed. Mater. Res. - Part A **91**, 1038–1047 (2009).

70. Zhang, P. *et al.* Zwitterionic gel encapsulation promotes protein stability, enhances pharmacokinetics, and reduces immunogenicity. *Proc. Natl. Acad. Sci. U. S. A.* **112**, 12046–12051 (2015).

71. Wang, C., Ye, Y. & Gu, Z. Local delivery of checkpoints antibodies. *Human Vaccines and Immunotherapeutics* vol. 13 245–248 (2017).

72. Chen, Q., Wang, C., Chen, G., Hu, Q. & Gu, Z. Delivery Strategies for Immune Checkpoint Blockade. *Adv. Healthc. Mater.* **7**, 1800424 (2018).

73. Chen, Q. *et al.* In situ sprayed bioresponsive immunotherapeutic gel for post-surgical cancer treatment. *Nat. Nanotechnol.* **14**, 89–97 (2019).

74. Smeets, N. M. B., Bakaic, E., Patenaude, M. & Hoare, T. Injectable and tunable poly(ethylene glycol) analogue hydrogels based on poly(oligoethylene glycol methacrylate). *Chem. Commun.* **50**, 3306–3309 (2014).

75. Hiemstra, C., Van Der Aa, L. J., Zhong, Z., Dijkstra, P. J. & Feijen, J. Novel in situ forming, degradable dextran hydrogels by michael addition chemistry: Synthesis, rheology, and degradation. *Macromolecules* **40**, 1165–1173 (2007).

76. Hodgson, S. M. *et al.* Reproducible Dendronized PEG Hydrogels via SPAAC Cross-Linking. *Biomacromolecules* **18**, 4054–4059 (2017).

77. Alge, D. L., Azagarsamy, M. A., Donohue, D. F. & Anseth, K. S. Synthetically tractable click hydrogels for three-dimensional cell culture formed using tetrazine-norbornene chemistry. *Biomacromolecules* **14**, 949–953 (2013).

78. Nimmo, C. M., Owen, S. C. & Shoichet, M. S. Diels-alder click cross-linked hyaluronic acid hydrogels for tissue engineering. *Biomacromolecules* **12**, 824–830 (2011).

79. Tan, H., Chu, C. R., Payne, K. A. & Marra, K. G. Injectable in situ forming biodegradable chitosan-hyaluronic acid based hydrogels for cartilage tissue engineering. *Biomaterials* **30**, 2499–2506 (2009).

80. Fairbanks, B. D., Scott, T. F., Kloxin, C. J., Anseth, K. S. & Bowman, C. N. Thiol−Yne Photopolymerizations: Novel Mechanism, Kinetics, and Step-Growth Formation of Highly Cross-Linked Networks. *Macromolecules* **42**, 211–217 (2009).

81. Madl, C. M., Katz, L. M. & Heilshorn, S. C. Bio-Orthogonally Crosslinked, Engineered Protein Hydrogels with Tunable Mechanics and Biochemistry for Cell Encapsulation. *Adv. Funct. Mater.* **26**, 3612–3620 (2016).

82. Rodell, C. B., Kaminski, A. L. & Burdick, J. A. Rational design of network properties in guest-host assembled and shear-thinning hyaluronic acid

hydrogels. *Biomacromolecules* **14**, 4125–4134 (2013).

83. Appel, E. a. *et al.* Supramolecular Cross-Linked Networks via Host- Guest Complexation with Cucurbit [8] uril. *J. Am. Chem. Soc.* **132**, 14251–14260 (2010).

84. Peters, G. M. & Davis, J. T. Supramolecular gels made from nucleobase, nucleoside and nucleotide analogs. *Chem. Soc. Rev.* **45**, 3188–3206 (2016).

85. Wang, L. L. *et al.* Sustained miRNA delivery from an injectable hydrogel promotes cardiomyocyte proliferation and functional regeneration after ischaemic injury. *Nat. Biomed. Eng.* **1**, 983–992 (2017).

86. Yang, J. A., Yeom, J., Hwang, B. W., Hoffman, A. S. & Hahn, S. K. In situ-forming injectable hydrogels for regenerative medicine. *Prog. Polym. Sci.* **39**, 1973–1986 (2014).

87. Ashley, G. W., Henise, J., Reid, R. & Santi, D. V. Hydrogel drug delivery system with predictable and tunable drug release and degradation rates. *Proc. Natl. Acad. Sci. U. S. A.* **110**, 2318–2323 (2013).

88. Santi, D. V., Schneider, E. L., Reid, R., Robinson, L. & Ashley, G. W. Predictable and tunable half-life extension of therapeutic agents by controlled chemical release from macromolecular conjugates. *Proc. Natl. Acad. Sci.* **109**, 6211–6216 (2012).

89. Huynh, C. T. *et al.* Cytocompatible Catalyst-Free Photodegradable

Hydrogels for Light-Mediated RNA Release to Induce hMSC Osteogenesis. *ACS Biomater. Sci. Eng.* **3**, 2011–2023 (2017).

90. Wang, X., Wang, C., Zhang, Q. & Cheng, Y. Near infrared light-responsive and injectable supramolecular hydrogels for on-demand drug delivery. *Chem. Commun.* **52**, 978–981 (2016).

91. Yan, B., Boyer, J. C., Habault, D., Branda, N. R. & Zhao, Y. Near infrared light triggered release of biomacromolecules from hydrogels loaded with upconversion nanoparticles. *J. Am. Chem. Soc.* **134**, 16558–16561 (2012).

92. Zustiak, S. P. & Leach, J. B. Hydrolytically degradable poly(ethylene glycol) hydrogel scaffolds with tunable degradation and mechanical properties. *Biomacromolecules* **11**, 1348–1357 (2010).

93. Cao, M. *et al.* Reversible Thermoresponsive Peptide−PNIPAM Hydrogels for Controlled Drug Delivery. *Biomacromolecules* **20**, 3601–3610 (2019).

94. Jeong, B., Kim, S. W. & Bae, Y. H. Thermosensitive sol-gel reversible hydrogels. *Adv. Drug Deliv. Rev.* **64**, 154–162 (2012).

95. Yang, B. *et al.* A thermoresponsive poly(N-vinylcaprolactam-co-sulfobetaine methacrylate) zwitterionic hydrogel exhibiting switchable anti-biofouling and cytocompatibility. *Polym. Chem.* **6**, 3431–3442 (2015).

96. Sridhar, B. V. *et al.* Development of a cellularly degradable PEG hydrogel to promote articular cartilage extracellular matrix deposition. *Adv. Healthc.*

Mater. **4**, 702–713 (2015).

97. Huynh, V., D'Angelo, A. D. & Wylie, R. G. Tunable degradation of low-fouling carboxybetaine-hyaluronic acid hydrogels for applications in cell encapsulation. *Biomed. Mater.* **14**, (2019).

98. Helling, A. L. *et al.* In Vitro Enzymatic Degradation of Tissue Grafts and Collagen Biomaterials by Matrix Metalloproteinases: Improving the Collagenase Assay. *ACS Biomater. Sci. Eng.* **3**, 1922–1932 (2017).

99. Annabi, N. *et al.* 25th anniversary article: Rational design and applications of hydrogels in regenerative medicine. *Adv. Mater.* **26**, 85–124 (2014).

100. Levalley, P. J. *et al.* Photolabile Linkers: Exploiting Labile Bond Chemistry to Control Mode and Rate of Hydrogel Degradation and Protein Release. *J. Am. Chem. Soc.* **142**, 4671–4679 (2020).

101. Patterson, J. & Hubbell, J. A. Enhanced proteolytic degradation of molecularly engineered PEG hydrogels in response to MMP-1 and MMP-2. *Biomaterials* **31**, 7836–7845 (2010).

102. Ruan, H. *et al.* A Dual-Bioresponsive Drug-Delivery Depot for Combination of Epigenetic Modulation and Immune Checkpoint Blockade. *Adv. Mater.* **31**, 1806957 (2019).

103. Guelcher, S. A. *et al.* Synthesis of biocompatible segmented polyurethanes from aliphatic diisocyanates and diurea diol chain extenders. *Acta*

Biomater. **1**, 471–484 (2005).

104. Soo Choi, H. *et al.* Renal clearance of quantum dots. *Nat. Biotechnol.* **25**, 1165–1170 (2007).

105. Yamaoka, T., Tabata, Y. & Ikada, Y. Distribution and tissue uptake of poly(ethylene glycol) with different molecular weights after intravenous administration to mice. *J. Pharm. Sci.* **83**, 601–606 (1994).

106. Gregoritza, M., Messmann, V., Abstiens, K., Brandl, F. P. & Goepferich, A. M. Controlled Antibody Release from Degradable Thermoresponsive Hydrogels Cross-Linked by Diels-Alder Chemistry. *Biomacromolecules* **18**, 2410–2418 (2017).

107. Nisbet, D. R. *et al.* Shear Containment of BDNF within Molecular Hydrogels Promotes Human Stem Cell Engraftment and Postinfarction Remodeling in Stroke. *Adv. Biosyst.* **2**, 1800113 (2018).

108. Gelain, F., Unsworth, L. D. & Zhang, S. Slow and sustained release of active cytokines from self-assembling peptide scaffolds. *J. Control. Release* **145**, 231–239 (2010).

109. Pakulska, M. M., Miersch, S. & Shoichet, M. S. Designer protein delivery: From natural to engineered affinity-controlled release systems. *Science* **51**, aac4750 (2016).

110. Vulic, K. & Shoichet, M. S. Affinity-based drug delivery systems for tissue

repair and regeneration. *Biomacromolecules* **15**, 3867–3880 (2014).

111. Sakiyama-Elbert, S. E. & Hubbell, J. a. Development of fibrin derivatives for controlled release of heparin-binding growth factors. *J. Control. Release* **65**, 389–402 (2000).

112. Lin, C. C. & Anseth, K. S. Controlling affinity binding with peptide-functionalized poly(ethylene glycol) hydrogels. *Adv. Funct. Mater.* **19**, 2325–2331 (2009).

113. Soontornworajit, B., Zhou, J., Shaw, M. T., Fan, T. H. & Wang, Y. Hydrogel functionalization with DNA aptamers for sustained PDGF-BB release. *Chem. Commun.* **46**, 1857–1859 (2010).

114. Koehler, K. C., Anseth, K. S. & Bowman, C. N. Diels−Alder Mediated Controlled Release from a Poly(ethylene.pdf. *Biomacromolecules* **14**, 538–547 (2013).

115. Miller, S. E. *et al.* Electrostatically Driven Guanidinium Interaction Domains that Control Hydrogel-Mediated Protein Delivery in Vivo. *ACS Cent. Sci.* **5**, 1750–1759 (2019).

116. Pakulska, M. M. *et al.* Encapsulation-free controlled release: Electrostatic adsorption eliminates the need for protein encapsulation in PLGA nanoparticles. *Sci. Adv.* **2**, e1600519–e1600519 (2016).

117. Pike, D. B. *et al.* Heparin-regulated release of growth factors in vitro and

angiogenic response in vivo to implanted hyaluronan hydrogels containing VEGF and bFGF. *Biomaterials* **27**, 5242–5251 (2006).

118. Pakulska, M. M., Vulic, K. & Shoichet, M. S. Affinity-based release of chondroitinase ABC from a modified methylcellulose hydrogel. *J. Control. Release* **171**, 11–16 (2013).

119. Pakulska, M. M., Vulic, K., Tam, R. Y. & Shoichet, M. S. Hybrid Crosslinked Methylcellulose Hydrogel: A Predictable and Tunable Platform for Local Drug Delivery. *Adv. Mater.* **27**, 5002–5008 (2015).

120. Vulic, K. & Shoichet, M. S. Tunable growth factor delivery from injectable hydrogels for tissue engineering. *J. Am. Chem. Soc.* **134**, 882–885 (2012).

121. Sakiyama-Elbert, S. E. & Hubbell, J. A. Controlled release of nerve growth factor from a heparin-containing fibrin-based cell ingrowth matrix. *J. Control. Release* **69**, 149–158 (2000).

122. Freeman, I. & Cohen, S. The influence of the sequential delivery of angiogenic factors from affinity-binding alginate scaffolds on vascularization. *Biomaterials* **30**, 2122–2131 (2009).

123. Huebsch, N. *et al.* Ultrasound-triggered disruption and self-healing of reversibly cross-linked hydrogels for drug delivery and enhanced chemotherapy. *Proc. Natl. Acad. Sci. U. S. A.* **111**, 9762–7 (2014).

124. Azagarsamy, M. A. & Anseth, K. S. Wavelength-controlled photocleavage

for the orthogonal and sequential release of multiple proteins. *Angew. Chemie - Int. Ed.* **52**, 13803–13807 (2013).

125. Conde, J., Oliva, N., Zhang, Y. & Artzi, N. Local triple-combination therapy results in tumour regression and prevents recurrence in a colon cancer model. *Nat. Mater.* **15**, 1128–1138 (2016).

126. Campbell, S., Maitland, D. & Hoare, T. Enhanced Pulsatile Drug Release from Injectable Magnetic Hydrogels with Embedded Thermosensitive Microgels. *ACS Macro Lett.* **4**, 312–316 (2015).

127. Ashley, G. W., Henise, J., Reid, R. & Santi, D. V. Hydrogel drug delivery system with predictable and tunable drug release and degradation rates. *Proc. Natl. Acad. Sci.* **110**, 2318–2323 (2013).

128. Garripelli, V. K. *et al.* Matrix metalloproteinase-sensitive thermogelling polymer for bioresponsive local drug delivery. *Acta Biomater.* **7**, 1984–1992 (2011).

129. Emens, L. A. & Middleton, G. The interplay of immunotherapy and chemotherapy: Harnessing potential synergies. *Cancer Immunol. Res.* **3**, 436–443 (2015).

130. Weichselbaum, R. R., Liang, H., Deng, L. & Fu, Y. X. Radiotherapy and immunotherapy: A beneficial liaison? *Nat. Rev. Clin. Oncol.* **14**, 365–379 (2017).

131. Shurin, G. V., Tourkova, I. L., Kaneno, R. & Shurin, M. R. Chemotherapeutic Agents in Noncytotoxic Concentrations Increase Antigen Presentation by Dendritic Cells via an IL-12-Dependent Mechanism. *J. Immunol.* **183**, 137–144 (2009).

132. Francis, D. M. *et al.* Blockade of immune checkpoints in lymph nodes through locoregional delivery augments cancer immunotherapy. *Sci. Transl. Med.* **12**, 1–12 (2020).

133. Chow, M. T. *et al.* Intratumoral Activity of the CXCR3 Chemokine System Is Required for the Efficacy of Anti-PD-1 Therapy. *Immunity* **50**, 1498-1512.e5 (2019).

134. Postow, M. A., Sidlow, R. & Hellmann, M. D. Immune-Related Adverse Events Associated with Immune Checkpoint Blockade. *N. Engl. J. Med.* **378**, 158–168 (2018).

135. Xie, Y. Q., Wei, L. & Tang, L. Immunoengineering with biomaterials for enhanced cancer immunotherapy. *Wiley Interdiscip. Rev. Nanomedicine Nanobiotechnology* **10**, 1–23 (2018).

136. Wang, C. *et al.* In situ formed reactive oxygen species – responsive scaffold with gemcitabine and checkpoint inhibitor for combination therapy. *Sci. Transl. Med.* **10**, eaan3683 (2018).

137. Wang, C., Ye, Y., Hochu, G. M., Sadeghifar, H. & Gu, Z. Enhanced

Cancer Immunotherapy by Microneedle Patch-Assisted Delivery of Anti-PD1 Antibody. *Nano Lett.* **16**, 2334–2340 (2016).

138. Chuang, Y. C. *et al.* Adjuvant Effect of Toll-Like Receptor 9 Activation on Cancer Immunotherapy Using Checkpoint Blockade. *Front. Immunol.* **11**, 1–14 (2020).

139. Ma, G. & Wu, C. Microneedle, bio-microneedle and bio-inspired microneedle: A review. *J. Control. Release* **251**, 11–23 (2017).

140. Lee, A. L. Z., Ng, V. W. L., Gao, S., Hedrick, J. L. & Yang, Y. Y. Injectable hydrogels from triblock copolymers of vitamin E-functionalized polycarbonate and poly(ethylene glycol) for subcutaneous delivery of antibodies for cancer therapy. *Adv. Funct. Mater.* **24**, 1538–1550 (2014).

141. Yang, C. *et al.* Hydrogels with prolonged release of therapeutic antibody: Block junction chemistry modification of 'ABA' copolymers provides superior anticancer efficacy. *J. Control. Release* **293**, 193–200 (2019).

142. Chua, C. Y. X. *et al.* Nanofluidic drug-eluting seed for sustained intratumoral immunotherapy in triple negative breast cancer. *J. Control. Release* **285**, 23–34 (2018).

143. Chua, C. Y. X. *et al.* Intratumoral Nanofluidic System for Enhancing Tumor Biodistribution of Agonist CD40 Antibody. *Adv. Ther.* **3**, 2000055 (2020).

144. Leconet, W. *et al.* Anti-PSMA/CD3 bispecific antibody delivery and antitumor activity using a polymeric depot formulation. *Mol. Cancer Ther.* **17**, 1927–1940 (2018).

145. Aliperta, R. *et al.* Cryogel-supported stem cell factory for customized sustained release of bispecific antibodies for cancer immunotherapy. *Sci. Rep.* **7**, 42855 (2017).

146. Choi, B. D. *et al.* CAR-T cells secreting BiTEs circumvent antigen escape without detectable toxicity. *Nat. Biotechnol.* **37**, 1049–1058 (2019).

147. Delgado-López, P. D. & Corrales-García, E. M. Survival in glioblastoma: a review on the impact of treatment modalities. *Clin. Transl. Oncol.* **18**, 1062–1071 (2016).

148. Lim, M., Xia, Y., Bettegowda, C. & Weller, M. Current state of immunotherapy for glioblastoma. *Nat. Rev. Clin. Oncol.* **15**, 422–442 (2018).

149. Gedeon, P. C. *et al.* Checkpoint inhibitor immunotherapy for glioblastoma: current progress, challenges and future outlook. *Expert Rev. Clin. Pharmacol.* **13**, 1147–1158 (2020).

150. Keskin, D. B. *et al.* Neoantigen vaccine generates intratumoral T cell responses in phase Ib glioblastoma trial. *Nature* **565**, 234–239 (2019).

151. Schumacher, T. N. & Schreiber, R. D. Neoantigens in cancer

immunotherapy. *Science* **348**, 69–74 (2015).

152. Vora, P. *et al.* The Rational Development of CD133-Targeting Immunotherapies for Glioblastoma. *Cell Stem Cell* **26**, 832–844 (2020).

CHAPTER 2. COMPETITIVE AFFINITY RELEASE FOR LONG TERM DELIVERY OF ANTIBODIES FROM HYDROGELS

Author's Preface:

The following chapter was published in Angewandte Chemie International Ed. under the citation:

Huynh V, and Wylie RG. Competitive affinity release for long term delivery of antibodies from hydrogels.

I was responsible for all the experimental design and execution in this chapter. Dr. Wylie and I both contributed to the analysis of the results. I wrote the first draft of the manuscript and Dr. Wylie provided editorial input to generate the final draft of the paper.

2.1 Abstract

With increased clinical use of antibody, long term delivery strategies are needed to decrease injection frequency and improve health outcomes. A three-component drug delivery system was developed for competitive affinity release of a streptavidin-antibody conjugate from agarose-desthiobiotin hydrogels via controlled dissolution of sparingly soluble biotin derivatives. The antibody conjugate was localized in the hydrogel through streptavidin-desthiobiotin complexation. Dissolution of sparingly soluble biotin derivatives irreversibly disrupts streptavidin-desthiobiotin complexation for controlled release of the antibody conjugate. Release was tuned by altering the total biotin derivative concentration without further hydrogel or antibody modification. We demonstrated first order tunable release of bioactive Avastin®, a therapeutic anti-VEGF antibody, from a non-cytotoxic system for over 100 days.

2.2 Introduction

Clinical use of antibody therapeutics is growing due to high throughput discovery of treatment targets;[1,2] establishment of antibody humanization[2] has also lowered incidence of side effects.[3,4] Antibodies account for a quarter of all biopharmaceutical sales[5] with 30 FDA approved antibodies and many more in development.[6] Antibodies are administered by frequent injections[7] or infusions of large doses to achieve therapeutic benefit.[8] For example, the antibody Avastin® (bevacizumab)[9,10], and biosimilars are intravitreally injected every 4-6

weeks to treat wet age related macular degeneration.[11,12] Controlled release formulations for localized sustained antibody release are being investigated to maintain therapeutic concentrations with fewer injections and side effects while improving health outcomes and patient compliance.

Sustained antibody delivery strategies currently use nanoparticles,[13] chemically modified hydrogels,[12,14] or composite hydrogels[15–17] for controlled release at disease sites.[18] Water-swollen hydrogels are an attractive vehicle as they maintain protein bioactivity[19] and modulate release through protein-hydrogel interactions and porosity.[14,19,20] Hydrogel affinity release systems are being developed for increased control over release rates, where the protein has a specific affinity for the hydrogel.[21,22] Early iterations took advantage of the natural binding affinity of certain growth factors (e.g. fibroblast growth factor 2) for heparin or other glycosaminoglycans.[23–28] To expand affinity release to other proteins, non-intrinsic protein-hydrogel binding interactions are being developed using peptides, aptamers and proteins.[29–31]

Affinity release rates are controlled by tuning the strength of protein-hydrogel interactions. However, long term delivery is difficult to achieve because required affinities would lower protein release below therapeutic levels. The majority of affinity based release occurs over the first 1 to 3 weeks.[32] Furthermore, tailoring affinity may require the development of new interactions or complex protein and hydrogel modifications.[21]

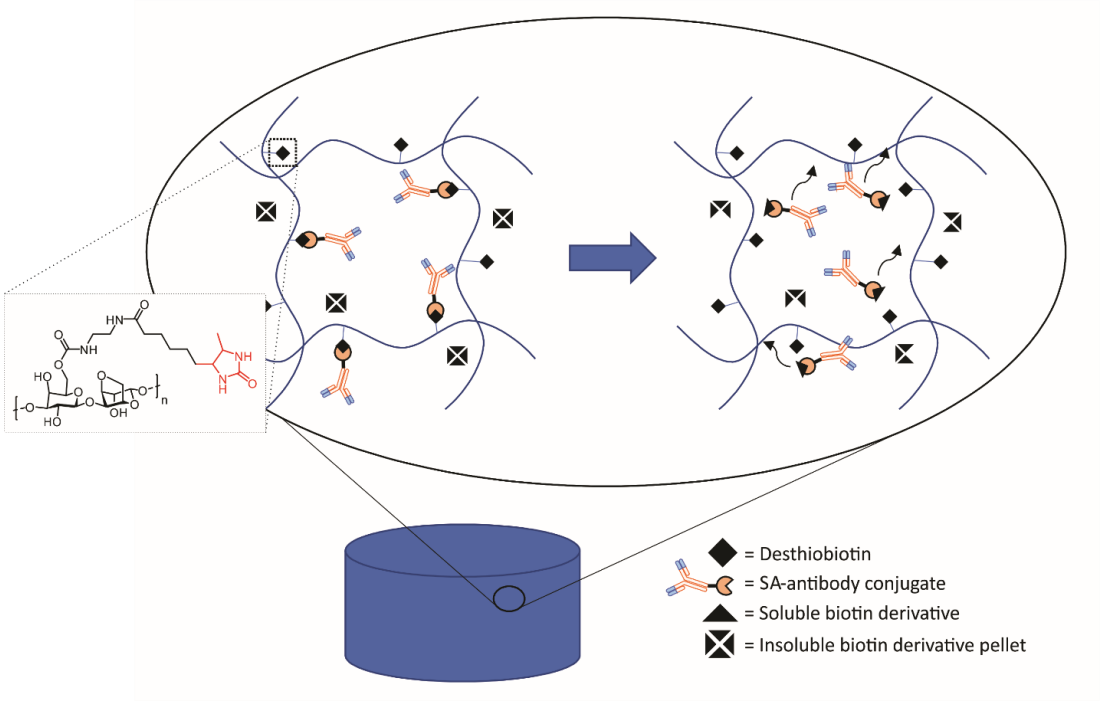

Figure 2.1 Schematic of SA-Antibody release from AgD hydrogels with sparingly soluble biotin derivatives. SA-antibody complexation with AgD is disrupted by the dissolution of solid biotin derivative pellets, releasing the antibody conjugate from the hydrogel.

2.3 Results and discussion

With the goal of keeping a constant hydrogel-antibody conjugate pair for long term antibody delivery, a three-component system was developed for tunable competitive affinity release. Unlike affinity systems, competitive affinity release results from the disruption of protein-hydrogel interactions by a competitive

binder, whose concentration and affinity influence release. The streptavidin (SA)-antibody conjugate is captured in an agarose-desthiobiotin (AgD) hydrogel through desthiobiotin-SA complexation, which is then disrupted by dissolution of sparingly soluble biotin derivative pellets to competitively bind SA (**Figure 2.1**). Incorporation of biotin derivatives above their solubility limit continually replenishes the soluble fraction. Immobilized desthiobiotin has a reported K_D of 10^{-12} M for avidin[33] and SA[34], and biotin derivatives have reported K_Ds for SA in the nM to pM range[35]. Direct measurement of biotin derivative affinities was hindered by low solubilities, however biotins with greater aqueous solubilities could be analyzed by ITC.

An AgD polymer and 3 biotin derivatives were synthesized; boc-biotin was commercially sourced (**Figure 2.2A, Figure S 2.1**). A non-degrading matrix, agarose, was chosen to isolate the drug delivery system from hydrogel dynamics. AgD (6.2 mmol desthiobiotin per mol of agarose repeat units) was synthesized by coupling NHS-desthiobiotin to aminated agarose (**Figure S 2.1A**). Biotin derivatives were synthesized by reacting long chain amines to biotin (**Figure S 2.1B**); activity of saturated biotin derivative solutions, a combination of concentration and affinity, was characterized by HABA displacement from Avidin.[36] Values were expressed as the equivalent biotin concentration required for the same activity. Generally, greater carbon content decreased activity, where saturated solutions of boc-biotin, octyl-biotin, and oleyl-biotin had equivalent

biotin concentrations of 146±1, 23±1 and 1.8±0.2 µM, respectively (**Figure 2.2B**); hexadecyl-biotin was below the detection limit.

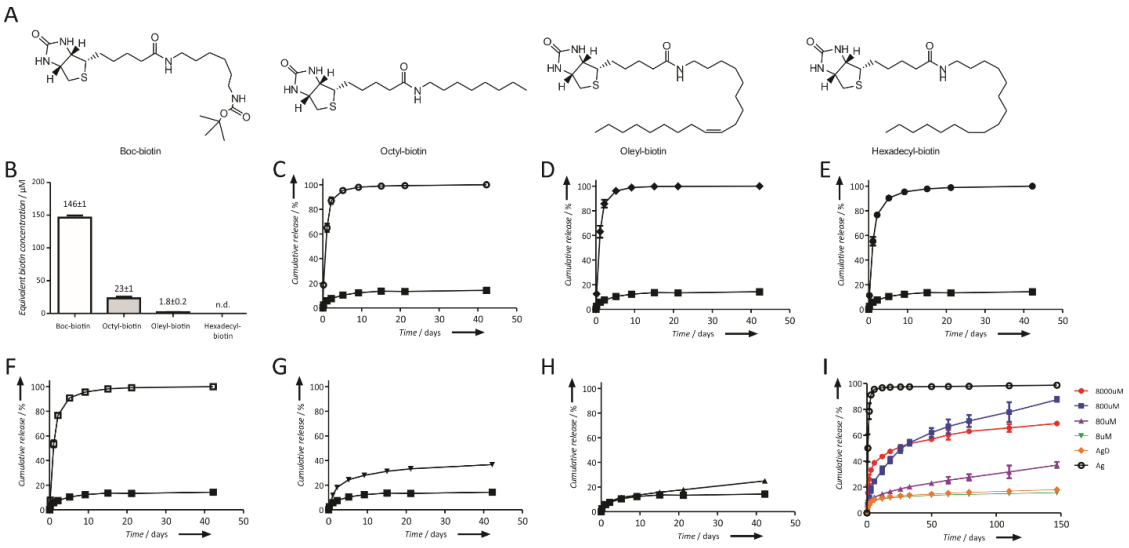

Figure 2.2 Structures and activity of biotin derivatives and corresponding release of SA. (A) Structures of biotin derivatives. (B) Activity of saturated biotin derivative solutions determined by HABA displacement from Avidin expressed as equivalent biotin concentrations required for the same activity (mean ± standard deviation, n=3); hexadecyl-biotin was below the detection limit. (C-H) Release of 1.9 µM fluorescent SA from hydrogels with different biotin derivatives at 8 mM; all graphs include SA release from AgD hydrogels without biotin derivatives (black squares): (C) without AgD (deshtiobiotin) or biotin derivatives; (D) biotin; (E) boc-biotin; (F) octyl-biotin; (G) oleyl-biotin; and (H) hexadecyl-biotin (mean ± standard deviation, n=4) over a period of 40 d. (I) Release of 1.9 µM fluorescent

SA from agarose and AgD hydrogels with different oleyl-biotin concentrations (mean ± standard deviation, n=4) over a period of 150 d.

To identify biotin derivatives for controlled release, we studied fluorescent SA release from AgD hydrogels as a function of biotin derivative activity. 1 wt% (w v^{-1}) AgD gels containing SA (1.9 μM) and sparingly soluble biotin derivatives (8 mM) were immersed in PBS, and fluorescence from released SA was tracked over time. Biotin, boc-biotin, and octyl-biotin disrupted SA-desthiobiotin complexation and produced SA release profiles similar to gels without desthiobiotin (**Figure 2.2C-F**). Oleyl-biotin and hexadecyl-biotin resulted in sustained SA release after an initial burst (24.50±0.89 % and 11.60±1.30 %, respectively (**Figure 2.2G-H**). AgD gels without biotin did not release SA after an initial burst due to complete SA complexation because the desthiobiotin concentration was much greater than the interaction's K_D. First-order effective release rate constants (k_{eff}) were calculated for gels without biotin, oleyl-biotin and hexadecyl-biotin as a function of SA concentration (**Figure S 2.7, Table S 2.1**). k_{eff} for oleyl-biotin and hexadecyl-biotin were statistically identical ($p=.949$) but both differed from gels without biotin ($p<0.0001$). Biotin derivatives with low activity (**Figure 2.2**) yield indistinguishable first-order release rates.

SA release was tuned by altering total oleyl-biotin concentration and quantified by k_{eff} values (**Figure 2.2I, Figure S 2.8**). 0 and 8 μM oleyl-biotin had

low k_{eff}, indicating little release and interference in SA-desthiobiotin complexation. 80 µM oleyl-biotin released SA linearly ($r^2 = 0.95$) from day 12 to 150 with a k_{eff} 4 times greater than gels without biotin. 800 and 8000 µM oleyl-biotin further increased k_{eff} by factors of 16.8 and 7 compared to gels without biotin (**Figure S 2.8, Table S 2.1**). The faster release rate of 800 µM oleyl-biotin indicates a higher soluble oleyl-biotin concentration, which may be due to dissolution differences between particles of different dimensions. As expected, 8 mM oleyl-biotin in figures 2G and 2I had similar k_{eff} ($p=0.25$); release curve differences were due to the initial burst. Therefore, long term delivery is achievable and SA release is dependent on oleyl-biotin concentration.

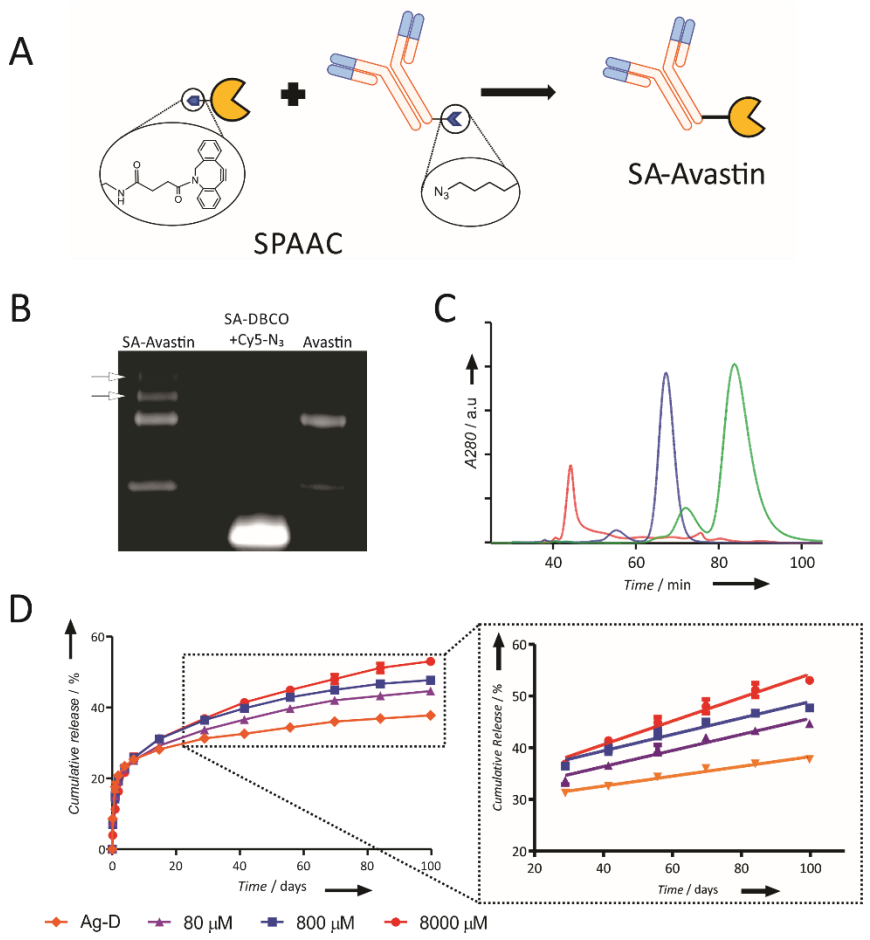

Figure 2.3 SA-Avastin® synthesis, characterization, and release from AgD with oleyl-biotin. (A) Synthesis of SA-Avastin® from Avastin®-azide and SA-DBCO. (B) Fluorescent SDS-PAGE image of SA-Avastin®-647, SA-DBCO reacted with azide-Cy5 fluorescent dye, and Avastin®-azide modified with Alexa-647. Arrows highlight SA-Avastin® fluorescent band shifts indicating successful conjugation. (C) UV absorption SEC trace (280 nm) of SA-Avastin® (red), Avastin®-azide (blue), and SA-DBCO (green). See figure S5 for Avastin® and SA traces. (D) Release of 2 µM fluorescent SA-Avastin® from AgD hydrogels

with different oleyl-biotin concentrations (mean ± standard deviation, n=3). Linear regression analysis of SA-Avastin® release from AgD gels between 29 and 100 days.

To quantify SA-antibody release, we synthesized a SA-Avastin® conjugate by Avastin®-azide and SA-DBCO cycloaddition (**Figure 2.3A, Figure S 2.2A**). Avastin®-azide was first modified with NHS-Alexa-647 to ensure release profiles directly track Avastin®. SA-Avastin® synthesis was confirmed by fluorescent SDS-PAGE (**Figure 2.3B**) and size exclusion chromatography (SEC, **Figure 2.3C, Figure S 2.5)**. SA-Avastin® biotin binding capacity was confirmed by SEC (**Figure S 2.6**) and the number of biotin binding sites was determined to be 5.91±0.20 by fluorescence after saturation with biotin-fluorescein (**Figure S 2.2**), suggesting ~1-2 SAs per Avastin®.

After an initial burst of ~25%, SA-Avastin® release rates from AgD hydrogels were dependent on oleyl-biotin concentration (**Figure 2.3D**). Between 29 to 100 days, gels with 80, 800 and 8000 µM oleyl-biotin released SA-Avastin® linearly ($r^2 > 0.92$) with k_{eff} 1.8, 2.1 and 3.1 times that of gels without oleyl-biotin, respectively (**Figure 2.3D, Figure S 2.9, Table S 2.1**). All k_{eff} were significantly different from each other ($p<0.0001$), except 80 and 800 µM oleyl-biotin ($p=0.055$). Therefore, long term release of SA-Avastin® can be tailored by oleyl-biotin concentration. After the initial burst, 0, 80, 800, and 8000 µM oleyl-

biotin gels released 12.8±0.3%, 19.6±0.6%, 22.7±0.6%, and 28.05±0.73% of loaded SA-Avastin® content, respectively, slow release will continue at longer time scale. Agarose gels without desthiobiotin released > 90% of SA-Avastin® within 10 days (**Figure S 2.3**). Without oleyl-biotin, SA-Avastin® had a larger k_{eff} than SA, which was mostly likely from SA-Avastin®'s decreased affinity for biotin analogues such as desthiobiotin and biotin derivatives. A dialysis equilibrium binding experiment between biotin-fluorescein and SA-Avastin® yielded a K_D of ~10 nM (**Table S 2.2**) compared to 0.14 nM for SA[37].

Other competitive systems may be developed for applications where desthiobiotin, biotin derivatives or SA are not suitable. Low immunogenic SA[38] may be used for *in vivo* applications where immunogenicity is of concern. New competitive binding systems with similar binding kinetics could also be developed. The system is amenable to applications requiring transparency such as ocular implantation,[39] as oleyl-biotin concentrations < 80 µM did not decrease gel transparency (**Figure S 2.4**) and sustained SA and SA-Avastin® release.

Previous affinity delivery systems utilized interactions to slow diffusional release of proteins from hydrogels for 7-40 days.[23 25,29,40] Competitive affinity extended protein release to 100-150 days. Competitive affinity release is governed by the apparent affinity between the protein and the hydrogel, which is a function of the protein's affinity for the hydrogel (K_D for SA-Avastin® and desthiobiotin), competing ligand (biotin derivative) concentration, and affinity of the competing

ligand for the protein (K_D for SA-Avastin® and biotin derivative). Therefore, competitive affinity has several opportunities to control protein release (**Table S 2.3**).

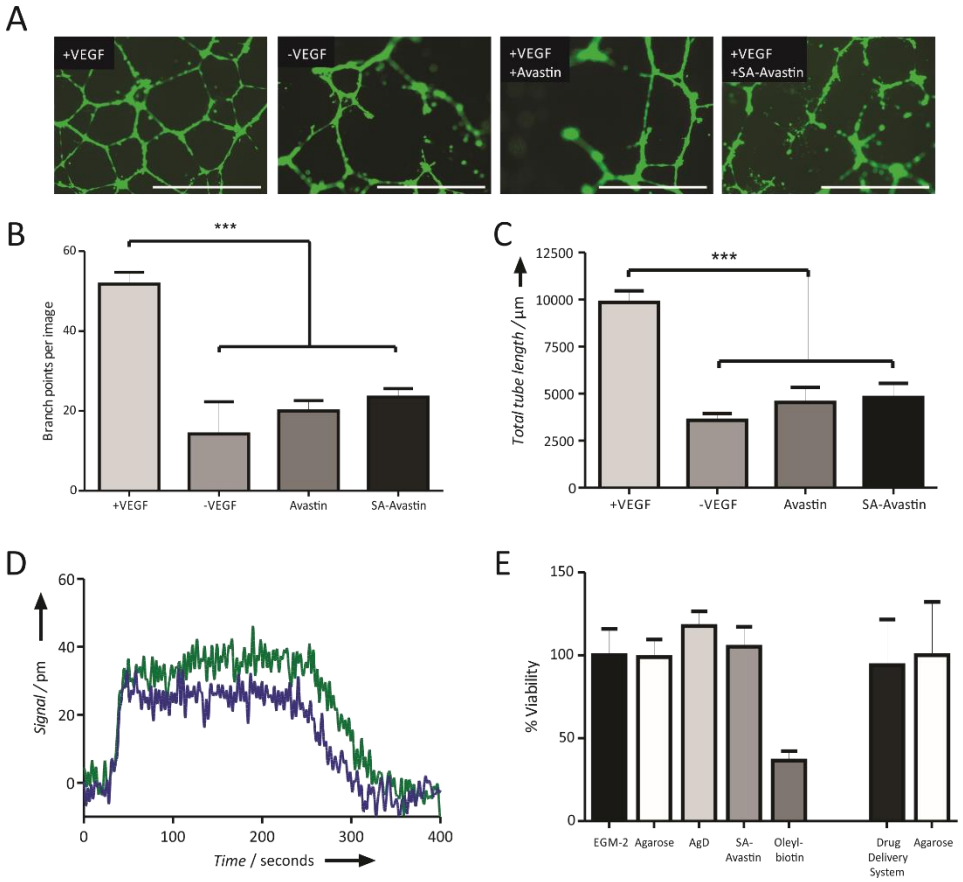

Figure 2.4 Activity of modified antibody and cytotoxicity of drug delivery components (A) Tube formation of HUVECs seeded on the surface of Geltrex® gels supplemented with 25 ng ml^{-1} VEGF, 0 ng mL^{-1} VEGF, 25 ng ml^{-1} VEGF + Avastin®, and 25 ng ml^{-1} VEGF + SA-Avastin® (scale bar = 1 mm, n=3). (B) Branch point analysis and (C) total tube length from HUVEC tube formation

assays. Condition with 25 ng ml^{-1} VEGF was significantly different from 0 ng ml^{-1} VEGF, 25 ng ml^{-1} VEGF + 1 µM Avastin®, and 25 ng ml^{-1} VEGF + 1 µM SA-Avastin® (mean ± standard deviation n=3; $p<0.001$). (D) LSPR traces of 7 µg mL^{-1} SA-Avastin® (green) released after 100 days and 50 µg mL^{-1} Avastin® on a VEGF modified chip. SA-Avastin® showed a greater signal because it was conjugated with Alexa 647.[42] (E) First 5 columns describe HUVEC viability in the presence of drug delivery components normalized to positive control in EGM-2, conditions were: 1 mg mL^{-1} agarose (solution), 1 mg mL^{-1} AgD (solution), 0.67 µM SA-Avastin®, and 2 mM oleyl-biotin (mean ± standard deviation n=3). Last 2 columns describe HUVEC viability when seeded in direct contact with non-cytotoxic agarose or the drug delivery system (AgD gels with 8 mM oleyl-biotin and 1.9 µM SA-DBCO, mean ± standard deviation n=3).

SA-Avastin® retained VEGF165 (VEGF) inhibitory activity, and the drug delivery system was non-cytotoxic. VEGF inhibition was confirmed by human umbilical vein endothelial cell (HUVEC) tube formation assays (**Figure 2.4A-C**). No VEGF, SA-Avastin® and Avastin® conditions had the same degree of tube formation, with no significant difference in branch points or tube length ($p > 0.05$, **Figure 2.4B-C**).[41] The VEGF containing control had approximately twice as many branch points and total tube length as all other conditions ($p < 0.001$). Therefore, SA-Avastin® and Avastin® inhibited VEGF to the same degree. SA-

Avastin® released at 100 days was confirmed to retain VEGF binding properties by localized surface plasmon resonance (LSPR) binding experiments (**Figure 2.4D**). The system was also determined to be non-cytotoxic towards HUVECs by comparing AgD gels containing SA-DBCO and oleyl-biotin with non-cytotoxic agarose gels ($p > 0.05$, **Figure 2.4E**). SA-Avastin® alone was also determined to be non-cytotoxic. When components were tested, only 2mM of oleyl-biotin pellets in direct contact with HUVECs demonstrated toxicity, which was not observed when cells were seeded on hydrogels containing 8 mM of oleyl-biotin pellets (**Figure 2.4E**). Therefore, the system is non-cytotoxic in non or slow degrading hydrogels.

This is the first demonstration of competitive affinity release controlled by ligand dissolution for bioactive therapeutic antibodies amenable to long term delivery. Antibody conjugate first-order release was tuned by varying biotin derivative concentration instead of protein-hydrogel affinity. Long term antibody delivery systems may prove clinically useful by decreasing injection frequency while improving health outcomes and patient compliance.

Acknowledgements. This work was supported by the Natural Sciences and Engineering Research Council (NSERC), Canada Foundation for Innovation: John R. Evans Leaders Fund (CFI-JELF), Ontario Research Fund - Research Infrastructure (ORI-RI), and McMaster University.

2.4 References

(1) Elvin, J. G.; Couston, R. G.; Van Der Walle, C. F. *Int. J. Pharm.* **2013**, *440* (1), 83–98.

(2) Carter, P. J. *Nat. Rev. Immunol.* **2006**, *6* (5), 343–357.

(3) Liu, J. K. H. *Annals of Medicine and Surgery*. **2014**, *3* (4), 113–116.

(4) Marasco, W. A.; Sui, J. *Nat. Biotechnol.* **2007**, *25* (12), 1421–1434.

(5) Chung, J. *Exp. Mol. Med.* **2017**, *49* (3), e304.

(6) Ecker, D. M.; Jones, S. D.; Levine, H. L. *mAbs*. **2015**, *7* (1), 9–14.

(7) Wang, W.; Wang, E. Q.; Balthasar, J. P. *Clin. Pharmacol. Ther.* **2008**, *84* (5), 548–558.

(8) Booth, B. a; Vidal Denham, L.; Bouhanik, S.; Jacob, J. T.; Hill, J. M. *Drugs Aging* **2007**, *24* (7), 581–602.

(9) Meyer, C. H.; Holz, F. G. *Eye* **2011**, *25* (6), 661–672.

(10) Ba, J.; Peng, R. S.; Xu, D.; Li, Y. H.; Shi, H.; Wang, Q.; Yu, J. *Drug Design, Development and Therapy*. **2015**, *9*, 5397–5405.

(11) Park, D. H.; Sun, H. J.; Lee, S. J. *International Ophthalmology*. **2016**, *37* (5), 1–10.

(12) Schweizer, D.; Serno, T.; Goepferich, A. *European Journal of*

Pharmaceutics and Biopharmaceutics. **2014**, *88* (2), 291–309.

(13) Mekaru, H.; Lu, J.; Tamanoi, F. *Adv. Drug Deliv. Rev.* **2015**, *95*, 40–49.

(14) Simovic, S.; Diener, K. R.; Bachhuka, A.; Kant, K.; Losic, D.; Hayball, J. D.; Brownc, M. P.; Vasilev, K. *Mater. Lett.* **2014**, *130*, 210–214.

(15) Wang, Y.; Wei, Y. T.; Zu, Z. H.; Ju, R. K.; Guo, M. Y.; Wang, X. M.; Xu, Q. Y.; Cui, F. Z. *Pharm. Res.* **2011**, *28* (6), 1406–1414.

(16) Pakulska, M. M.; Elliott Donaghue, I.; Obermeyer, J. M.; Tuladhar, a.; McLaughlin, C. K.; Shendruk, T. N.; Shoichet, M. S. *Sci. Adv.* **2016**, *2* (5), e1600519–e1600519.

(17) Fletcher, N. A.; Babcock, L. R.; Murray, E. A.; Krebs, M. D. *Mater. Sci. Eng. C* **2016**, *59*, 801–806.

(18) Stanwick, J. C.; Baumann, M. D.; Shoichet, M. S. *Int. J. Pharm.* **2012**, *426* (1–2), 284–290.

(19) Guziewicz, N.; Best, A.; Perez-Ramirez, B.; Kaplan, D. L. *Biomaterials* **2011**, *32* (10), 2642–2650.

(20) Schweizer, D.; Schönhammer, K.; Jahn, M.; Göpferich, A. *Biomacromolecules* **2013**, *14* (1), 75–83.

(21) Pakulska, M. M.; Miersch, S.; Shoichet, M. S. *Science.* **2016**, *351* (6279), aac4750-aac4750.

(22) Fu, A. S.; von Recum, H. A. In *Engineering Polymer Systems for Improved Drug Delivery*; 2013; 429–452.

(23) Pike, D. B.; Cai, S.; Pomraning, K. R.; Firpo, M. A.; Fisher, R. J.; Shu, X. Z.; Prestwich, G. D.; Peattie, R. A. *Biomaterials* **2006**, *27* (30), 5242–5251.

(24) Chen, W. C. W.; Lee, B. G.; Park, D. W.; Kim, K.; Chu, H.; Kim, K.; Huard, J.; Wang, Y. *Biomaterials* **2015**, *72*, 138–151.

(25) Sakiyama-Elbert, S. E.; Hubbell, J. a. *J. Control. Release* **2000**, *65* (3), 389–402.

(26) Willerth, S. M.; Johnson, P. J.; Maxwell, D. J.; Parsons, S. R.; Doukas, M. E.; Sakiyama-Elbert, S. E. *J. Biomed. Mater. Res. Part A* **2007**, *80* (1), 13–23.

(27) Nie, T.; Baldwin, A.; Yamaguchi, N.; Kiick, K. L. *J. Control. Release* **2007**, *122* (3), 287–296.

(28) Liu, Y.; Cai, S.; Shu, X. Z.; Shelby, J.; Prestwich, G. D. *Wound Repair Regen.* **2007**, *15* (2), 245–251.

(29) Vulic, K.; Shoichet, M. S. *J. Am. Chem. Soc.* **2012**, *134* (2), 882–885.

(30) Lin, C. C.; Anseth, K. S. *Adv. Funct. Mater.* **2009**, *19* (14), 2325–2331.

(31) Battig, M. R.; Soontornworajit, B.; Wang, Y. *J. Am. Chem. Soc.* **2012**, *134* (30), 12410–12413.

(32) Bhakta, G.; Rai, B.; Lim, Z. X. H.; Hui, J. H.; Stein, G. S.; van Wijnen, A. J.; Nurcombe, V.; Prestwich, G. D.; Cool, S. M. *Biomaterials* **2012**, *33* (26), 6113–6122.

(33) Masson, M.; Yun, K.; Haruyama, T.; Kobatake, E.; Aizawa, M. *Anal. Chem.* **1995**, *67* (13), 2212–2215.

(34) Busse, S.; Scheumann, V.; Menges, B.; Mittler, S. *Biosens. Bioelectron.* **2002**, *17* (8), 704–710.

(35) Germeroth, A. I.; Hanna, J. R.; Karim, R.; Kundel, F.; Lowther, J.; Neate, P. G. N.; Blackburn, E. A.; Wear, M. A.; Campopiano, D. J.; Hulme, A. N. *Org. Biomol. Chem.* **2013**, *11* (44), 7700.

(36) Chignell, C. F.; Starkweather, D. K.; Sinha, B. K. *J. Biol. Chem.* **1975**, *250* (14), 5622–5630.

(37) Aslan, F. M.; Yu, Y.; Mohr, S. C.; Cantor, C. R. *Proc. Natl. Acad. Sci. U. S. A.* **2005**, *102* (24), 8507–8512.

(38) Yumura, K.; Ui, M.; Doi, H.; Hamakubo, T.; Kodama, T.; Tsumoto, K.; Sugiyama, A. *Protein Sci.* **2013**, *22* (2), 213–221.

(39) Colthurst, M. J.; Williams, R. L.; Hiscott, P. S.; Grierson, I. *Biomaterials*. 2000, pp 649–665.

(40) Peattie, R. A.; Pike, D. B.; Yu, B.; Cai, S.; Shu, X. Z.; Prestwich, G. D.;

Firpo, M. A.; Fisher, R. J. *Drug Deliv.* **2008**, *15* (6), 389–397.

(41) Hasan, J.; Shnyder, S. D.; Bibby, M.; Double, J. A.; Bicknel, R.; Jayson, G. C. *Angiogenesis*. **2004**, *7* (1), 1–16.

(42) Anker, J. N.; Hall, W. P.; Lyandres, O.; Shah, N. C.; Zhao, J.; Van Duyne, R. P. *Nature Materials*. **2008**, *7* (6) 442–453.

2.5 Supplementary Information

2.5.1 Materials and Methods

Materials. All materials were purchased from Sigma-Aldrich (Oakville, ON) unless otherwise specified. N'-biotinyl-N'-boc-1,6-hexanediamine (Boc-biotin) was obtained from Toronto Research Chemicals (Toronto, ON), and DBCO-PEG4 NHS from Click Chemistry Tools (Scottsdale, AZ). Alexa Fluor™ 488 Streptavidin conjugate, Alexa Fluor™ 647 NHS ester (succinimydyl ester) and Geltrex™ were purchased from Thermo Fisher Scientific (Burlington, ON). CellTiter 96® AQueous One Solution Cell Proliferation Assay, human umbilical vein endothelial cells (HUVECs), EBM-2, EGM™-2 Bulletkit™, Calcein AM, and fetal bovine serum (FBS) were purchased from Cedarlane (Burlington, ON) and used as per supplied protocols. Recombinant human VEGF 165 (VEGF) was obtained from Peprotech (Rocky hill, NJ), and Avastin® from the Boston Children's Hospital (BCH) pharmacy (Boston, MA). Dialysis membranes and solvents were obtained from Spectrum Labs (Rancho Dominguez, CA) and Caledon Labs (Georgetown, ON), respectively. Carboxyl sensor LSPR chips were acquired from Nicoya Lifesciences (Kitchener, ON).

Synthesis of agarose-desthiobiotin (AgD). Carbonyldiimidazole (CDI, 86 mg, 0.53 mmol) was added to a solution of agarose (500 mg) in dry DMSO (25 mL) and reacted under nitrogen. After 2h, ethylenediamine (106 µL, 1.59 mmol) and triethylamine (TEA, 296 µL, 2.12 mmol) were added and stirred overnight under

nitrogen. The solution was then diluted with 25 mL of warm water and dialyzed against 5 L of distilled water (12-14k MWCO) over 3 days with a minimum of 6 water exchanges. Agarose-amine was isolated by lyophilization. Desthiobiotin (120 mg, 0.56 mmol) was reacted with N-(3-dimethylaminopropyl)-N'-ethylcarbodiimide hydrochloride (EDC, 325 mg, 1.70 mmol) and N-hydroxysuccinimide (NHS, 200 mg, 1.74 mmol) in DMF (10 mL) overnight under nitrogen, which was then added to a solution of agarose-amine (400 mg) in dry DMSO (30 mL) and stirred overnight under nitrogen. The product was purified by dialysis against 5 L of distilled water over 3 days with 6 water exchanges (12-14k MWCO) and lyophilized to yield a white powder. Desthiobiotin content in AgD was quantified by detecting amine loss after desthiobiotin conjugation using fluorescamine. Agarose-amine and AgD were dissolved at 10 mg mL^{-1} in DMSO, 50 µL of the agarose samples were then mixed with 50 µL of 6 mM fluorescamine in DMSO with excess TEA. Fluorescence was read (Ex 390 nm, Em 475 nm) after 10 minutes, and a standard curve was constructed from N-(2-aminoethyl)acetamide.

Synthesis of biotin derivatives. EDC (117 mg, 0.61 mmol) and NHS (70 mg, 0.61 mmol) were added to a solution of biotin (100 mg, 0.41 mmol) in dry DMF (5 mL) and stirred overnight under nitrogen. The corresponding amine (1.83 mmol) and TEA (86 µL, 0.61 mmol) were added to the reaction, which was then left for an additional 24 h. Octyl-biotin and oleyl-biotin were precipitated with a

saturated sodium carbonate aqueous solution, collected and washed with water and diethyl ether (octyl-biotin: 118 mg, 81% yield; oleyl-biotin: 127 mg, 63% yield). The hexadecyl-biotin reaction was concentrated under vacuum, and the resulting solid was washed with distilled water followed by recrystallization in methanol (23 mg, 12% yield). Hexadecyl-biotin: ^{1}H NMR (600 MHz, DMSO-d_6): δ: 7.75 (t, J= 5.6, 1H), 4.37 (t, J=5.6, 1H), 4.16 (d, J=6.2, 1H), 3.13 (dd, J=12,6.1, 1H), 3.04 (q, J=6.7, 2H), 2.85 (dd, J= 12.4, 5, 1H), 2.07 (t, J= 7.4, 2H), 1.65 (m, 1H), 1.52 (m, 3H), 1.28 (m, 29H), 0.90 (t, J= 6.6, 3H). Oleyl-biotin: ^{1}H NMR (600 MHz, DMSO- d_6): δ: 7.71 (t, J=6, 1H), 5.39 (m, 2H), 4.30 (t, J= 6, 1H), 4.12 (t, J= 6, 1H), 3.09 (dd, J= 6, 1H), 3.00 (q, J= 6, 2H), 2.82 (dd, J= 12, 6, 1H), 2.23 (t, J= 9, 2H) 2.03 (t, J= 6, 2H), 1.6 (m, 1H), 1.49 (m, 3H), 1.31 (m, 28H), 0.85 (t, J= 12, 3H) Octyl-biotin: ^{1}H NMR (600 MHz, DMSO- d_6): δ: 7.71 (t, J= 6, 1H), 4.30 (t, J= 6, 1H), 4.12 (t, J= 6, 1H), 3.09 (dd, J= 6, 1H), 3.01 (q, J= 6, 2H), 2.82 (dd, J= 12,6, 1H), 2.17 (t, J= 6, 1H), 2.03 (t, J= 9, 2H), 1.60 (m, 1H), 1.49 (m, 3H), 1.30 (m, 13H), 0.86 (t, J= 9, 3H).

Biotin derivative activity. Biotin derivative activities, a combination of solubility and affinity, at physiological pH were determined by a HABA/Avidin displacement assay. Saturated biotin derivative solutions were prepared by sonicating biotin pellets in PBS for 30 minutes followed by filtering through a 0.2 μm syringe filter. Saturated biotin derivative solutions were then added to a HABA/Avidin solution as per product instructions, and absorbance was measured

at 500 nm. Loss of absorbance was correlated to biotin concentration, as calculated using the HABA/Avidin complex extinction coefficient (34500 M^{-1} cm^{-1}).[1]

6-azido hexyl succinimidyl carbonate (azide linker) synthesis. A bifunctional azide succinimidyl carbonate molecule was synthesized similar to a previously reported procedure.[2] Briefly, 6-chloro-1-hexanol (25 g, 183 mmol) was added to sodium azide (32.5 g, 500 mmol) in water and refluxed for 20 h. The mixture was subsequently cooled and extracted with ethyl acetate. The organic layer was dried over magnesium sulfate and concentrated under vacuum to yield 6-azido hexanol. 6-azido hexanol (143 mg, 1 mmol) and triphosgene (500 mg, 1.7 mmol) were dissolved in anhydrous THF under nitrogen. 160 µL of pyridine was then added dropwise and reacted for 10 min. The precipitate was removed by filtration and the solution concentrated under vacuum, yielding the chloroformate as an oil. The oil was dissolved in 15 mL of anhydrous THF with NHS (350 mg, 3 mmol). Pyridine (250 µL) was then added and reacted under nitrogen for an additional 10 min. The resulting solution was concentrated, dissolved in ethyl acetate and washed with 0.1 M HCl, water, sat. aq. $NaHCO_3$, water, and brine. The solution was dried over magnesium sulfate and concentrated to yield a yellow oil (157mg, 50.4% yield). ^{1}H NMR (600 MHz, $CDCl_3$): δ: 4.33 (t, J= 6, 2H), 3.28 (t, J= 6, 2H), 2.84 (s, 4H), 1.77 (m, 2H), 1.62 (m, 2H), 1.43 (m, 4H).

Avastin®-azide synthesis. 4.7µL of 10 mg mL^{-1} 6-azido hexyl succinimidyl carbonate solution in DMF was added to 500 µL of 5 mg mL^{-1} Avastin® in PBS pH 7.4 and reacted for 1.5 h at room temperature. Avastin®-azide was purified by size exclusion chromatography (SEC, Superdex S200 column), and azide content was determined by MALDI (8.6 azides per Avastin®). For release experiments, Avastin®-azide was fluorescently labelled prior to conjugation with SA. Avastin®-azide was reacted with 10 molar equivalents of NHS-Alexa Fluor™ 647 in PBS overnight at 4ºC and subsequently dialyzed against PBS at 4ºC (MWCO 13-16K). Fluorescent Avastin®-azide was determined to contain 2.12 molecules of Alexa 647 per Avastin® by UV-Vis absorption according to the manufacturer's procedure.

SA-DBCO synthesis. 45 µL of 10 mg mL^{-1} DBCO-PEG_4-NHS ester was added to 1 mL of 5 mg mL^{-1} streptavidin (SA), reacted overnight at 4ºC and purified by SEC (Superdex S200 column). SA-DBCO contained an average of 7.5 DBCOs per SA as determined by UV-VIS absorption (Fig. S2A). Degree of DBCO conjugation on SA was calculated by UV absorbance and using a formula previously reported with DBCO and SA extinction coefficients of 12000 $M^{-1}cm^{-1}$ (309 nm) and 41326 M^1cm^{-1} (280 nm), respectively.[3] Formula is as follows:

$$Number\ of\ DBCO\ per\ SA = \frac{A_{309}DBCO \times \varepsilon_{280}SA}{\epsilon_{309}DBCO \times A_{280C}SA}$$

Where the corrected A_{280C} absorbance is calculated by the following equation:

$$A_{280C}SA = A_{280}SA - (A_{309}DBCO - CF_{DBCO})$$

Where CF_{DBCO} is the correction factor for DBCO at 280nm with a value of 1.089.

SA-Avastin® synthesis. 50µL of 2.5mg mL^{-1} SA-DBCO in PBS was added to 500 µL of 0.7 mg mL^{-1} fluorescent Avastin®-azide in PBS at pH 7.4, reacted overnight and purified by SEC (Superdex S200 column). Fluorescent SA-Avastin® (SA-Avastin®-647) synthesis was confirmed via SDS-PAGE and SEC (Fig. 3B-C).

SA-Avastin® biotin binding capacity. Biotin binding capacity of SA-Avastin® was confirmed by adding excess biotin-fluorescein to SA-Avastin®-647. Briefly, 100 µL of 0.7 mg mL^{-1} SA-Avastin®-647 and 2 µL of 1 mg mL^{-1} biotin-fluorescein in PBS were incubated at room temperature for 1 h. SA-Avastin®-647 complexed with biotin-fluorescein was purified by automated SEC with a fraction collector. 200 µL of each fraction was added to an opaque 96 well plate and fluorescence was measured at wavelengths corresponding to Alexa Fluor™ 647 (Ex 651 Em 672) and biotin-fluorescein (Ex 490, Em 524) on a Biotek Cytation5™ plate reader. A chromatogram was constructed by plotting fluorescent intensities as a function of fraction number. Purified SA-Avastin®-647 saturated with biotin-fluorescein was excited at 495 nm and 651 nm to acquire emission spectrums, and calculate the number of biotin binding sites per Avastin® in SA-Avastin®-647.

Fluorescent SA and SA-Avastin® release studies. A 2 wt% (w v^{-1}) AgD solution in PBS was mixed with Alexa Fluor™ 488 labeled SA (SA-488) and

incubated at 37ºC for 2 h. A suspension of biotin derivative in PBS was prepared at the appropriate concentration and added to the AgD solution to yield 1.9 µM of SA-488, and 1 wt% (w v^{-1}) AgD. The solution was immediately dispensed into an opaque 96 well plate and 60 µL gels were formed after incubation at 4ºC for 1 h. 200 µl PBS was dispensed overtop the gels, and replaced at specific time intervals. Released SA-488 fluorescence from the supernatant was measured using a Biotek Cytation5™ plate reader (Ex 495 nm, Em 519 nm). SA-Avastin®-647 release was performed similar to SA-488 with a SA-Avastin®-647 concentration of 2 µM (determined from Alexa 647 fluorescence).

HUVEC cytotoxicity assay. Cytotoxicity of individual drug delivery components were screened by seeding 5,000 HUVECs per well in EGM-2™ media in a tissue culture treated 96 well plate. Samples were then supplemented with different drug delivery components: (1) PBS; (2) 1 mg mL^{-1} agarose; (3) 1 mg mL^{-1} AgD; (4) 0.1 mg mL^{-1} (0.67 µM) SA-Avastin®; and (5) 1 mg mL^{-1} (2 mM) oleyl-biotin. After overnight incubation (37ºC 5% CO_2), 20 µL of MTS reagent was added and incubated for an additional 4 h. Absorbance (490 nm) was read, and results were normalized to a positive control (HUVECs in EGM-2™). To screen the cytotoxicity of the full drug delivery system, a solution of 1 wt% (w v^{-1}) AgD, 8000 µM oleyl-biotin suspension, and 0.1 mg mL^{-1} (1.9 µM) SA-DBCO were incubated at 37ºC overnight. 60 µL gels were then formed in a 96 well tissue culture treated plate with 1% (w v^{-1}) agarose gels as a control. Gels were sterilized

by UV for 1h and 5,000 HUVECs in 200 µL of EGM-2 media were seeded on gel surfaces. After an overnight incubation (37ºC 5% CO_2), 20 µL of the MTS reagent was added to the media and incubated for another 4h (37ºC 5% CO_2). Absorbance (490 nm) was measured and normalized to agarose control gels.

SA-Avastin® bioactivity. 10,000 HUVECs were seeded on 60 µL Geltrex® gels in 4 different media conditions: (1) EBM-2 with 0.5% FBS; (2) EBM-2 with 0.5% FBS and VEGF; (3) EBM-2 with 0.5% FBS, VEGF, and Avastin®; and, (4) EBM-2 with 0.5% FBS, VEGF, and SA-Avastin®. Avastin® and SA-Avastin® were pre-incubated in EBM-2 with VEGF for 1 h at 37ºC. Cells were incubated (37ºC 5% CO_2) for 24 h, stained with Calcein AM and imaged on a Biotek Cytation5™ microscope. Number of branch points and total tube length were counted according to established protocols.[4,5]

SA-Avastin® LSPR Binding. SA-Avastin®'s binding to VEGF165 was confirmed by LSPR binding experiments (OpenSPR from Nicoya Lifesciences instrument). VEGF165 was immobilized onto a carboxyl sensor chip (Nicoya Lifesciences) via the immobilization kit provided. Briefly, the running buffer, PBS, was flowed at 20 µL min^{-1}, aliquots of EDC and NHS were mixed at a 1:1 ratio and 200 µL was injected for 5 min to activate the carboxyl groups of the chip. 250 µL of 8 µg mL^{-1} of VEGF165 in 10 mM sodium acetate buffer at pH 5.5 was injected for an additional 5 min. 200 µL of a blocking solution from the provided immobilization kit was then injected for 5 min. The chip was then

washed with running buffer until the signal stabilized. SA-Avastin® released from AgD gels after 100 days and fresh Avastin® were sequentially injected at a flow rate of 20 µL min^{-1}. The chip was regenerated with running buffer at 50 µL min^{-1} for 15 min. SA-Avastin® and Avastin® were injected on a control surface without VEGF165 to ensure non-specific binding was minimal, no signal was observed.

Equilibrium binding of SA-Avastin® with biotin-fluorescein. 250 µL of 0.7 mg/mL of SA-Avastin® labeled with Alexa 647 was incubated with 10 µL of 1 mg/mL biotin-fluorescein overnight at room temperature. The mixture was then purified by SEC. Fractions were collected (4 mL), transferred into a dialysis bag (MWCO 13-16k) and subsequently submerged in 6 mL of PBS. Fluorescence inside and outside the dialysis bag were taken to confirm equilibrium was reached. Once equilibrium was reached, fluorescence was measured to determine biotin-fluorescein concentration inside and outside of the dialysis bag, and SA-Avastin® concentration inside the dialysis bag by comparison to calibration curves. Samples were boiled to ensure biotin-fluorescein was unbound from SA-Avastin® to avoid fluorescence quenching. Fluorescence from Alexa 647 provided the SA-Avastin® concentration, fluorescence from fluorescein inside the dialysis bag provided the total (bound and unbound) biotin-fluorescein concentration, and fluorescein fluorescence outside the dialysis bag provided the

free (unbound) biotin-fluorescein concentration. The K_D was estimated using the factional saturation equation:

$$\frac{v}{n} = \frac{[\text{biotin fluorescein}]}{[\text{biotin fluorescein}] + K_D}$$

Where v = [bound biotin-fluorescein]/[total SA-Avastin], n = 5.91 (number of biotin binding sites per SA-Avastin), and [biotin-fluorescein] = the concentration of free (unbound) biotin-fluorescein.

2.5.2 Supplementary Figures and Tables

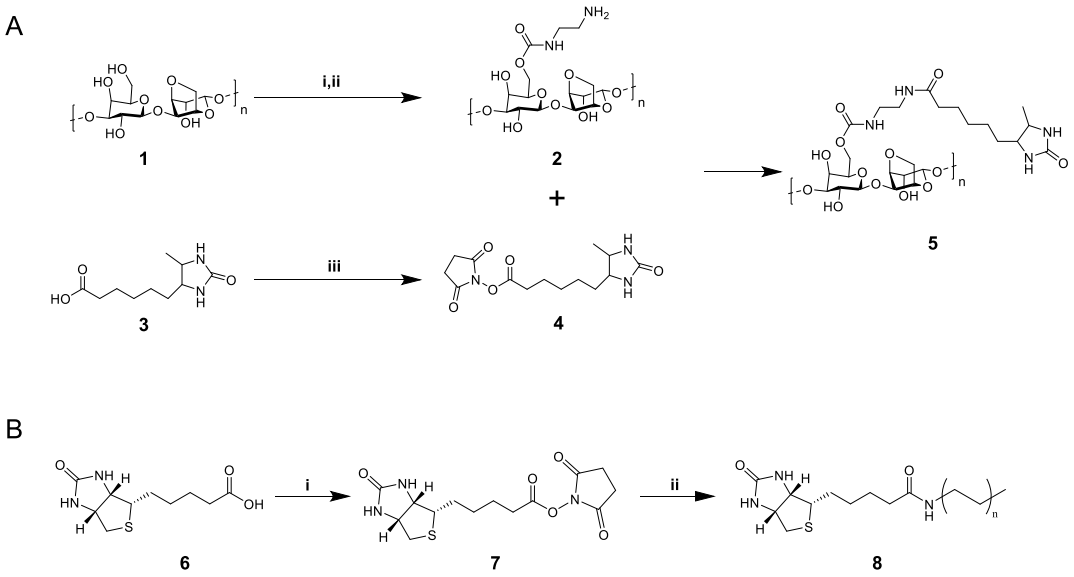

Figure S 2.1 Synthesis of AgD hydrogel and biotins. (A) Synthesis of AgD. Agarose (1) was aminated with carbonyl diimidazole (i) and ethylene diamine (ii),

then reacted with NHS-desthiobiotin (4) to yield AgD (5), where 6.2 mmol per mol of agarose repeat units contained desthiobiotin. NHS-desthiobiotin was synthesized by reacting desthiobiotin (3) with EDC and NHS (iii). (B) Synthesis of sparingly soluble biotin derivatives (8) by reacting biotin (6) with EDC and NHS (i) resulting in Biotin-NHS ester (7) followed by the corresponding amines (ii).

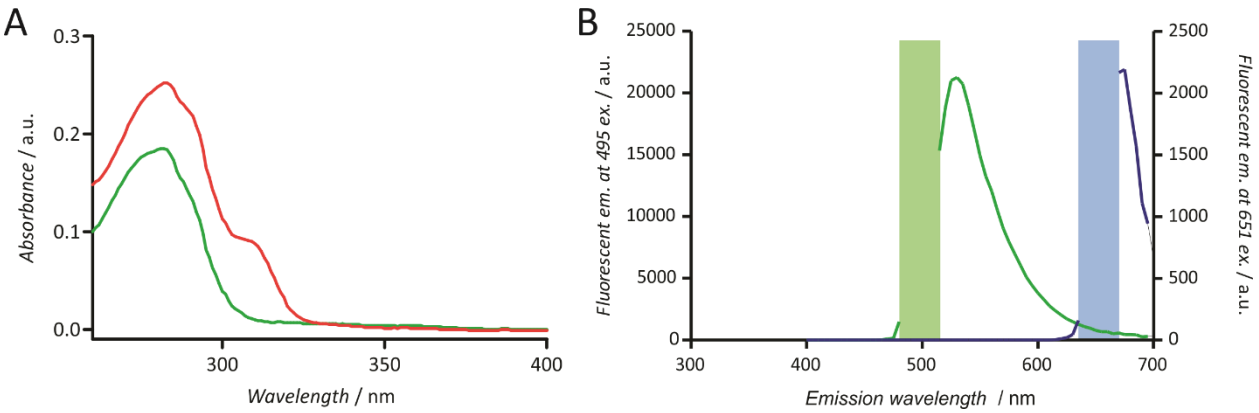

Figure S 2.2 Characterization of SA-DBCO and SA-Avastin (A) UV-Vis spectrum of SA-DBCO (red) and SA (green). (B) Fluorescent emission spectra of SA-Avastin®-647 saturated with biotin-fluorescein when excited at 495±9 nm (green) and 651±9 nm (blue). Boxes represent excitation wavelengths.

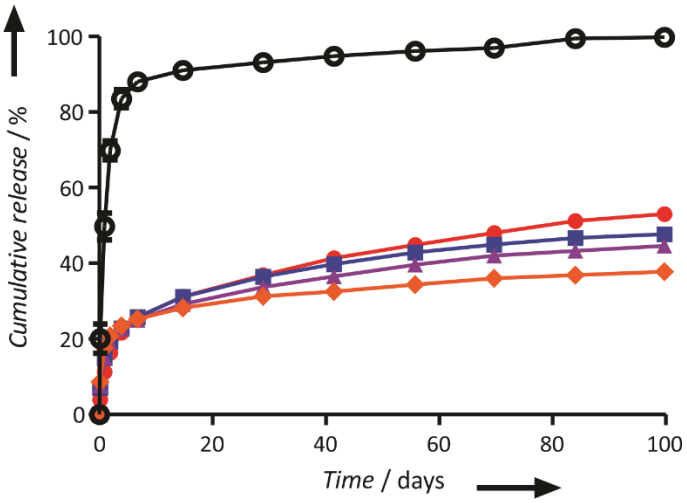

Figure S 2.3 Release of SA-Avastin® from agarose and AgD hydrogels with oleyl-biotin. Samples are AgD (orange diamond), 80 µM oleyl-biotin and AgD (purple triangle), 800 µM oelyl-biotin and AgD (blue square), 8000 µM oleyl-biotin and AgD (red circle), and agarose without biotin (white circle; mean ± standard deviation n=3).

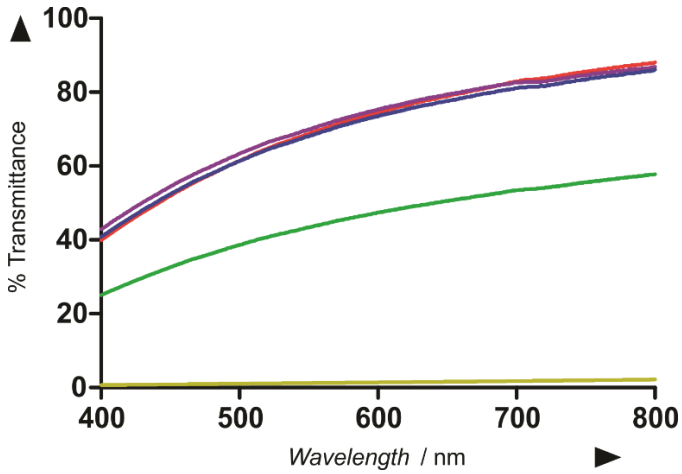

Figure S 2.4 Percent transmittance of 1 wt% (w v^{-1}) agarose hydrogels with different total concentrations (soluble and insoluble) of oleyl-biotin of 0 µM (red), 8 µM (purple), 80 µM (blue), 800 µM (green), 8000 µM (yellow).

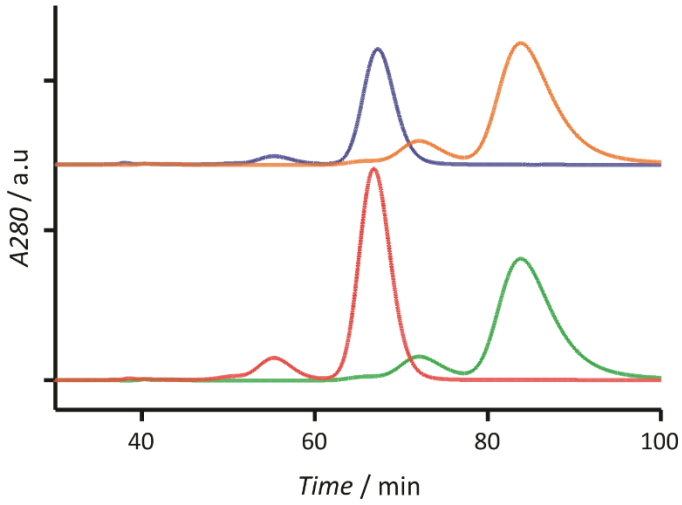

Figure S 2.5 SEC UV (280 nm) chromatograms of purified Avastin®-azide (blue) and SA-DBCO (orange) compared to Avastin® (red) and SA (green).

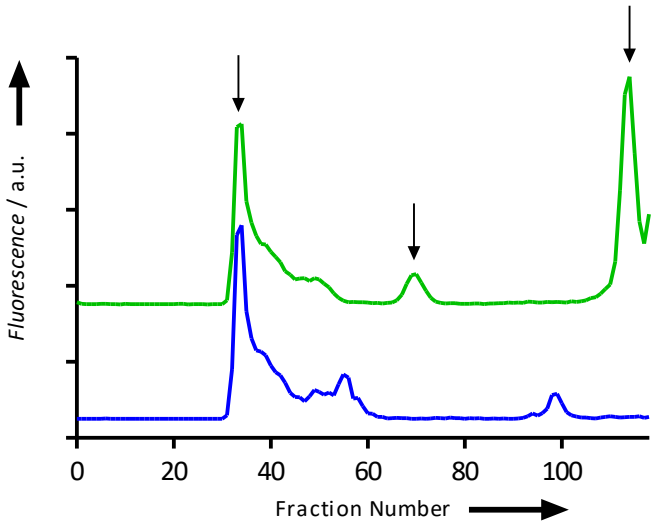

Figure S 2.6 SEC confirmation of SA-Avastin®'s ability to bind biotin by mixing fluorescent SA-Avastin® (modified with Alexa-647) with biotin-fluorescein. Fluorescence traces (Ex 490, Em 524 (green) and Ex 651, Em 672 (blue)) indicate the SA-Avastin® peak (fraction 35) contained fluorescein and Alexa-647, confirming SA-Avastin® complexation with biotin. Arrows indicate SA-Avastin®, unreacted SA-DBCO and unbound biotin-fluorescein.

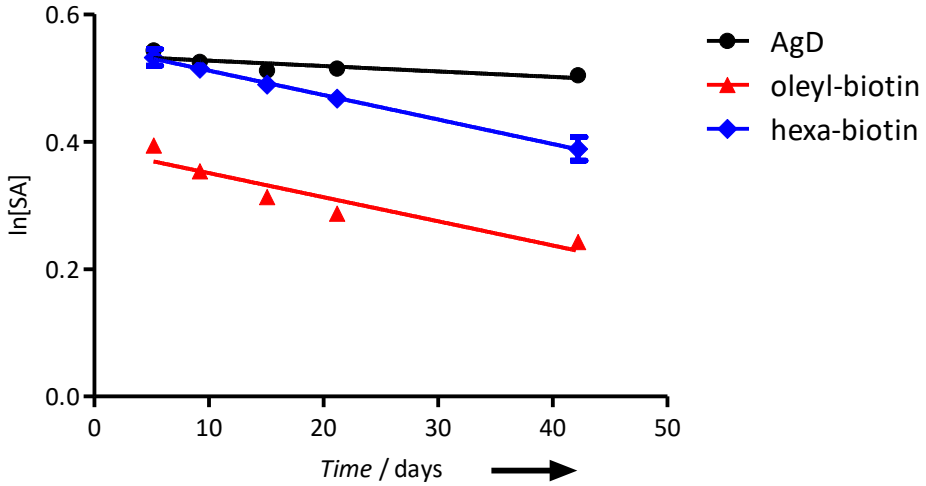

Figure S 2.7 First-order plots of SA release from AgD gels without biotin, 8mM oleyl-biotin and 8mM hexadecyl-biotin. Only release data after day 5 was included to analyze release without the initial burst. Effective release rates (k_{eff}) are equal to the magnitude of the slope.

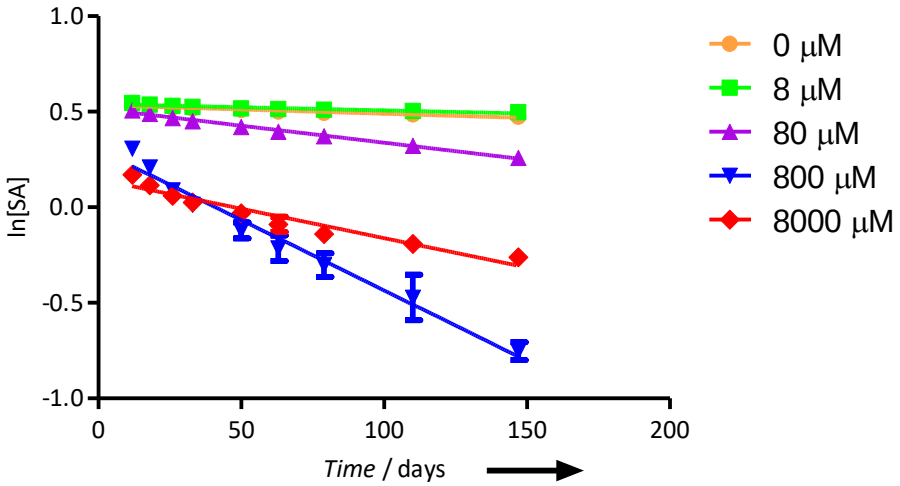

Figure S 2.8 First order plots of SA release from AgD gels with 0, 8, 80, 800, and 8000 oleyl-biotin. Only release data after day 12 was included to analyze release without the initial burst. Effective release rates (k_{eff}) are equal to the magnitude of the slope.

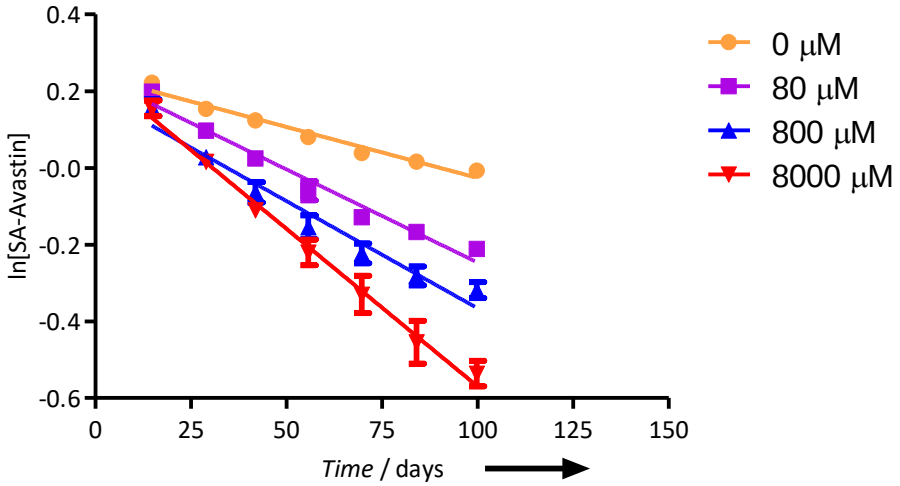

Figure S 2.9 First order plots of SA-Avastin® release from AgD gels with 0, 80, 800, and 8000 oleyl-biotin. Only release data after day 14 was included to analyze release without the initial burst. Effective release rates (k_{eff}) are equal to the magnitude of the slope.

Table S 2.1 Effective release rates (k_{eff}) assuming first order release with respect to SA or SA-Avastin® concentrations for all release profiles.

Corresponding figure	Protein	Biotin derivative	Concentration of biotin derivative / µM	k_{eff} / days^{-1}
2C, S7	SA	none	-	$8.5 \times 10^{-4} \pm 1.7 \times 10^{-4}$
2G, S7	SA	Oleyl-biotin	8000	$3.8 \times 10^{-3} \pm 3.4 \times 10^{-4}$
2H, S7	SA	Hexadecyl-biotin	8000	$3.8 \times 10^{-3} \pm 1.7 \times 10^{-4}$
2I, S8	SA	none	-	$4.4 \times 10^{-4} \pm 2.2 \times 10^{-5}$
2I, S8	SA	Oleyl-biotin	8	$3.3 \times 10^{-4} \pm 2.2 \times 10^{-5}$
2I, S8	SA	Oleyl-biotin	80	$1.8 \times 10^{-3} \pm 6.3 \times 10^{-5}$
2I, S8	SA	Oleyl-biotin	800	$7.4 \times 10^{-3} \pm 2.8 \times 10^{-4}$
2I, S8	SA	Oleyl-biotin	8000	$3.1 \times 10^{-3} \pm 1.6 \times 10^{-4}$
3D, S9	SA-Avastin®	none	-	$2.7 \times 10^{-3} \pm 1.3 \times 10^{-4}$
3D, S9	SA-Avastin®	Oleyl-biotin	80	$4.9 \times 10^{-3} \pm 2.2 \times 10^{-4}$
3D, S9	SA-Avastin®	Oleyl-biotin	800	$5.6 \times 10^{-3} \pm 3.0 \times 10^{-4}$
3D, S9	SA-Avastin®	Oleyl-biotin	8000	$8.2 \times 10^{-3} \pm 2.8 \times 10^{-4}$

Table S 2.2 Quantification of total and free biotin-fluorescein, and SA-Avastin® from dialysis equilibrium binding experiment to calculate K_D.

[biotin-fluorescein] (bound + free)	[biotin-fluorescein] (free)	[SA-Avastin®]	[biotin-fluorescein] (bound)	K_D
120 nM	6.3 nM	48 nM	113.7 nM	9.4 nM

Table S 2.3 A comparison of traditional affinity and competitive affinity release systems in hydrogels.

	Traditional affinity	Competitive affinity
Release mechanism	Decreased rate of protein diffusion in hydrogels through protein-hydrogel interactions.	Disruption of the protein-hydrogel interaction by dissolution of the biotin derivative.
Release rate	Determined by the K_D between the hydrogel and protein.	Determined by the total biotin derivative concentration.

Length of release limitations	Determined by the K_D between the hydrogel and protein.	Determined by the lifetime of insoluble biotin derivative pellets.
Tuning of release	Tuned by changing the K_D between the hydrogel and protein.	Tuned by controlling the soluble biotin's activity (concentration and affinity).

2.5.3 Supplementary References

(1) Chignell, C. F.; Starkweather, D. K.; Sinha, B. K. *J. Biol. Chem.* **1975**, *250* (14), 5622–5630.

(2) Santi, D. V.; Schneider, E. L.; Reid, R.; Robinson, L.; Ashley, G. W. *Proc. Natl. Acad. Sci.* **2012**, *109* (16), 6211–6216.

(3) Liu, D.; Yang, J.; Wang, H. F.; Wang, Z.; Huang, X.; Wang, Z.; Niu, G.; Hight Walker, A. R.; Chen, X. *Anal. Chem.* **2014**, *86* (12), 5800–5806.

(4) Hasan, J.; Shnyder, S. D.; Bibby, M.; Double, J. A.; Bicknel, R.; Jayson, G. C. *Angiogenesis*. **2004**, *7*(1), 1–16.

(5) Brown, K. J.; Maynes, S. F.; Bezos, a; Maguire, D. J.; Ford, M. D.; Parish, C. R. *Lab. Invest.* **1996**, *75* (4), 539–555.

CHAPTER 3. INFLUENCE OF HYDROPHOBIC CROSSLINKERS ON CARBOXYBETAINE COPOLYMER STIMULI RESPONSE AND HYDROGEL BIOLOGICAL PROPERTIES

Author's Preface:

The following chapter was published in *Langmuir* under the citation:

Huynh V, Jesmer AH, Shoiab, MM and Wylie RG. Influence of hydrophobic crosslinkers on carboxybetaine copolymer stimuli response and hydrogel biological properties.

I was responsible for all the experimental design and execution in this chapter. Dr. Wylie, Alex Jesmer, M. Muneeb Shoiab and I contributed to the analysis of the results. I wrote the first draft of the manuscript and Dr. Wylie provided editorial input to generate the final draft of the paper.

3.1 Abstract

Poly(carboxybetaine) (pCB) hydrogels do not elicit a foreign body response due to their low-fouling properties, making them ideal implantable materials for in vivo drug and cell delivery. Current reported pCB hydrogels are crosslinked using cytotoxic UV-initiated radical polymerization limiting clinical and in vivo translation. For clinical translation, we require in situ and biorthogonal crosslinking of pCB hydrogels that are both low-fouling and low-swelling to limit non-specific interactions and minimize tissue damage, respectively. To this end, we synthesized carboxybetaine (CB) random copolymers (molecular weight (MW): ~7-33 kDa; Đ: 1.1-1.36) containing azide (pCB-azide) or strained alkyne (Dibenzocyclooctyne (DBCO); pCB-DBCO) that rapidly crosslink upon mixing. Unlike CB homopolymers and other CB copolymers studied, high DBCO content pCB-$DBCO_{30}$ (30% DBCO mole fraction) is thermoresponsive with an upper critical solution temperature (UCST; cloud point of ~20°C at 50 g/L) in water due to electrostatic associations. Due to the anti-polyelectrolyte effect, pCB-$DBCO_{30}$ is salt responsive and is soluble even at low temperatures in 5 M NaCl, which prevents zwitterion electrostatic associations. pCB-azide and pCB-DBCO with 0.05 to 0.16 crosslinker mole fractions rapidly formed 10 wt % hydrogels upon mixing that were low-swelling (increase of ~10% in wet weight) while remaining low-fouling to proteins (~10-20 μg cm^{-2}) and cells, making them suitable for in vivo applications. pCB-X_{31} hydrogels composed of pCB-$azide_{32}$ and pCB-$DBCO_{30}$ formed opaque gels in water and physiological conditions that shrunk to

~70% of their original wet weight due to pCB-$DBCO_{30}$'s greater hydrophobicity and interchain electrostatic interactions, which promotes non-specific protein adsorption (~35 μg cm^{-2}) and cell binding. Once formed, the electrostatic interactions in pCB-X_{31} hydrogels are not fully reversible with heat or salt. Although, pCB-X_{31} hydrogels are transparent when initially prepared in 5 M NaCl. This is the first demonstration of a thermo and salt responsive CB copolymer that can tune hydrogel protein and cell fouling properties.

Keywords: upper critical solution temperature, anti-polyelectrolyte effect, zwitterionic hydrogels, in situ gelation, low-fouling, low-swelling, biorthogonal click crosslinking

3.2 Introduction

Hydrogels are versatile biomaterials for localized drug and cell delivery with numerous biomedical applications, including cancer therapies and regenerative medicine.[1–3] To mimic the natural extracellular environment, hydrogels are also being used for 3D cell culture and bioprinting to increase drug screening efficiency and better understand complex disease mechanisms.[4–10] Hydrogels are prepared by crosslinking natural or synthetic polymers, such as alginate and polyethylene glycol (PEG), into water swollen networks. Their tunable chemical and mechanical properties make them highly versatile biomaterials to provide specific environments for in vitro cell studies and tissue engineering applications. For in vivo applications, hydrogels may be directly

implanted as pre-formed gels or administered as solutions for in situ gelation upon injection.[11,12] In situ gelation requires covalent or physical crosslinks that form upon mixing two or more components, or through a phase transition triggered by an environmental change, such as temperature driven hydrophobic interaction assembly.[13–16]

To minimize the risk of the foreign body response (FBR), hydrogels should be low-fouling to minimize the non-specific binding of proteins and cells.[17] Excessive protein binding alters the hydrogel's biochemical environment leading to unwanted cell-hydrogel interactions and may elicit an immune response known as the FBR.[18] The FBR leads to the formation of a collagenous fibrous capsule that impedes drug and cell release from the implant.[18,19] Hydrogel size, shape, roughness, porosity and chemical composition influence the FBR intensity.[17,20–23] Because the FBR is commonly initiated by protein binding, hydrogels that prevent protein adsorption onto their surface can mitigate or reduce the FBR.[17,24,25] To this end, current research is investigating low-fouling polymers for hydrogel formation.[26]

Zwitterionic polymers are low-fouling materials increasingly used for hydrogels and surface coatings for biomedical devices.[17,25,27,28] Due to electrostatic interactions with water molecules, zwitterionic polymers form a strong water shell to prevent protein adsorption, which provides its low-fouling properties. For example, surfaces grafted with zwitterionic polymers adsorb less

protein than surfaces modified with polyethylene glycol, a common polymer used for biomaterial development.[29] Poly(carboxybetaine) (pCB) has been shown to adsorb less protein (two times less than poly(sulfobetaine)(pSB)), mitigate the FBR, and decrease the immune response towards polymer conjugates to a greater extent than other zwitterionic polymers such as pSB.[17,30,31] pCB hydrogels do not induce collagen capsule formation or an FBR three months post-implantation in immunocompetent mice.[17]

For clinical applications, injectable hydrogels should be low-swelling to prevent nerve compression, tissue damage and hydrogel displacement from the desired site of installation.[32,33] Current pCB hydrogels may be limited by their high swelling degree, which results in an increase in wet weight of 150 to 325%.[29,34] To decrease hydrogel swelling ratios, the concentration of hydrophobic groups or crosslinks in the hydrogel can be increased.[32,35]

pCB hydrogels have previously been formed via radical polymerization using a UV activated photoiniator, dimethacrylate crosslinker and methacrylate CB monomer.[29,34] Due to the poor tissue penetration UV light, pCB hydrogels are usually formed prior to implantation.[17] Ideally, pCB gels would be administered through minimally invasive injections and crosslinked using bio orthogonal chemistries. Several crosslinking chemistries have been developed for injectable in situ gelling hydrogels[11] including: (1) aldehyde-hydrazide;[36] (2) furan – maleimide cycloaddition;[37] (3) thiol-ene reaction;[38] and, (4) strain promoted

azide-alkyne cycloaddition (SPAAC).[39] Azide and strained alkyne functionalities for SPAAC crosslinking are unreactive towards biomolecules and therefore do not promote covalent protein immobilization.[11,39,40] Biorthogonal SPAAC crosslinking is also suitable for cell encapsulation or injectable drug and cell delivery systems.[39–42]

Here, we report the synthesis and characterization of low-fouling and low-swelling SPAAC crosslinked hydrogels formed by mixing poly(carboxybetaine-azide) (pCB-azide$_\chi$, where χ represents the mole fraction percent) and poly(carboxybetaine-dibenzocyclooctyne) (pCB-DBCO$_\chi$) random copolymers for in situ gelation (**Figure 3.1**). The mole fraction of azide and DBCO content was varied to study their influence on polymer and hydrogel properties. Unlike CB homopolymers, pCB-DBCO$_{30}$ is a thermoresponsive polymer with an upper critical solution temperature (UCST) of ~20°C in pure water due to the promotion of electrostatic interactions by pendant DBCO groups; to the best of our knowledge, this is the first report of a CB copolymer with an observable UCST. Hydrogels with azide and DBCO mole fractions of 0.16 or lower produced low-fouling (low non-specific protein and cell binding) and low-swelling (~10% increase in wet weight) transparent hydrogels. Hydrogels with azide and DBCO mole fractions of ~0.3 formed zwitterion electrostatic interactions that resulted in gel shrinking (~30% decrease in wet weight) and promoted non-specific protein binding and cell adhesion.

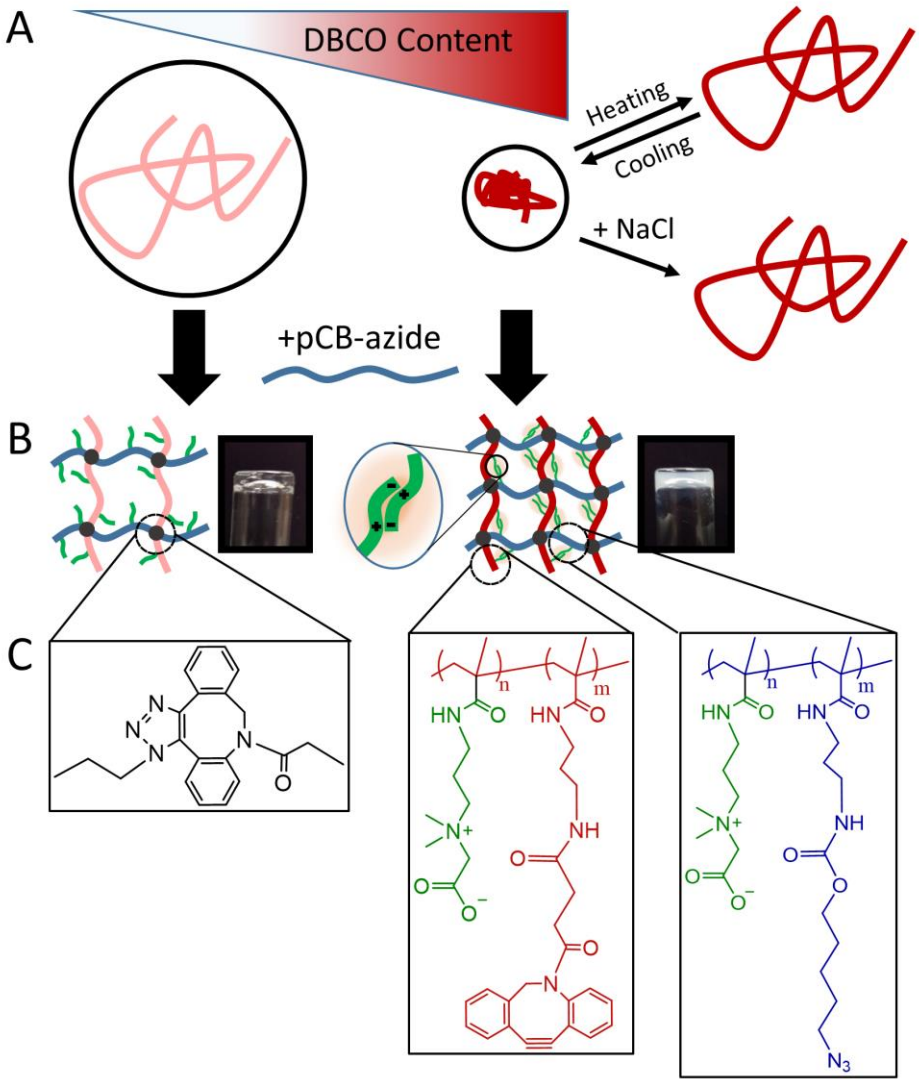

Figure 3.1 Stimuli responsive pCB-DBCO$_{30}$ and its influence on hydrogel properties. (A) Increasing DBCO content within CB copolymers results in a temperature and salt responsive copolymer with an aqueous UCST and anti-polyelectrolyte properties, whereas low DBCO content copolymers do not exhibit

a UCST. (B) In situ crosslinking of low DBCO content polymers with pCB-azide yields transparent, low-fouling and low-swelling hydrogels. High DBCO content pCB-$DBCO_{30}$ crosslinked with pCB-$azide_{32}$ yields opaque, fouling and de-swelling gels due to zwitterion electrostatic associations. (C) Chemical structures of the triazole ring (formed after SPAAC), pCB-DBCO and pCB-azide.

3.3 Materials and methods

3.3.1 Materials N-[3-(dimethylamino)propyl]methacrylamide, poly(ethylene glycol) methyl ether methacrylate (M_n 500), tert-butyl bromoacetate, 2,4,6 trinitrobenzene sulfonic acid, trifluoroacetic acid (TFA), 4-Cyano-4-(phenylcarbonothioylthio)pentanoic acid, 4,4'-azobis(4-cyanovaleric acid), triethylamine, sodium dodecyl sulfate (SDS) and bovine serum albumin (BSA) were purchased from Sigma Aldrich (Oakville, ON, Canada). N-(3-aminopropyl)methacrylamide hydrochloride (APMA) was purchased from Polysciences, Inc. (Warrington, PA). VA-044 was purchased from Toronto Research Chemicals (North York, ON, Canada). Alexa Fluor 647 NHS ester, Hyclone DMEM-F12, Presto Blue reagent, calf bovine serum (CBS), Calcein AM and Hoechst stain were obtained from Thermo Fisher Scientific (Burlington, ON, Canada). 6-azidohexyl-succinimidyl carbonate (NHS-azide) was synthesized according previously published procedures.[43] PBS at pH 7.4 contained 10 mM sodium phosphate and 137 mM NaCl.

3.3.2 Carboxybetaine monomer synthesis Carboxybetaine (CB) was synthesized according to previously established procedures.[44] Briefly, 7.75 g of N-[3-(dimethylamino)propyl]methacrylamide was dissolved in 100 mL of dry acetonitrile under N_2. Tert-butyl bromoacetate (10 g) was added, and reaction was kept at 50°C overnight. The reaction was cooled to room temperature and the product was precipitated with 250 mL of ether. The white precipitate was collected by vacuum filtration, washed with ~100 mL of ether, and dried overnight in a vacuum oven at 60°C. The tert-butyl group was removed by reacting 12 g of the white solid with 10 mL of TFA for 2 h at room temperature, followed by precipitation with 100 mL of ether. The precipitate was collected, washed with an additional 100 mL of ether and dried overnight in a vacuum oven at 60°C. The product was then dissolved in water and lyophilized to yield 8 g (83% yield). ^{1}H NMR (D_2O, 600 MHz) δ: 5.63 (s, 1H), 5.34 (s, 1H), 4.10 (s, 2H), 3.53 (m, 2H), 3.28 (t, J = 6.42, 2H), 3.18 (s, 6H), 1.96 (m, 2H), 1.85 (s, 3H).

3.3.3 Nomenclature for copolymers. Poly(carboxybetaine-co-(aminopropyl)methacrylamide) (pCB-APMA) were referenced as pCB-APMA$_{\#}$, where # represents the APMA mole fraction. Therefore, pCB-APMA$_5$'s APMA mole fraction is 5% and CB 95%. pCB-azide$_{\#}$ and pCB-DBCO$_{\#}$ are referenced in the same manner as pCB-APMA$_{\#}$. pCB-X hydrogels formed by mixing pCB-azide and pCB-DBCO copolymers of similar azide or DBCO fraction are referred to as pCB-X$_{\#}$, where # represents the averaged azide and DBCO mole fraction of

the copolymers prior to gelation. For example, pCB-X_5 hydrogels are formed by mixing pCB-azide$_5$ and pCB-DBCO$_5$.

3.3.4 pCB-APMA$_x$ copolymer synthesis. pCB-APMA$_5$, pCB-APMA$_{11}$, pCB-APMA$_{16}$, and pCB-APMA$_{31}$ were synthesized as follows: CB monomer (1 g) and APMA-HCl (20 mg for pCB-APMA$_5$, 41 mg for pCB-APMA$_{11}$, 87 mg for pCB-APMA$_{16}$, and 260 mg for pCB-APMA$_{31}$) were dissolved in 1 M acetate buffer pH 5.2. Separately, 4-Cyano-4-(phenylcarbonothioylthio)pentanoic acid (2.6 mg for pCB-APMA$_5$, 7.3 mg for pCB-APMA$_{11}$, 7.6 mg for pCB-APMA$_{16}$, and 8.8 mg for pCB-APMA$_{31}$) was dissolved in dioxane and added to the monomer solutions resulting in a 1 M monomer (CB + APMA) solution of 5:1 acetate buffer to dioxane. pH was adjusted between 3 to 4 and VA-044 was added at a 1:5 molar equivalents compared to 4-Cyano-4-(phenylcarbonothioylthio)pentanoic acid. The solution was transferred to a Schlenk flask and degassed with three freeze-pump-thaw cycles under nitrogen. The reaction vessel was then immersed in a 40°C oil bath and reacted for 3 d under constant stirring. The solution was then dialyzed against water and lyophilized, yielding a pink powder (700-760 g).

3.3.5 pCB-DBCO synthesis. DBCO precursors were synthesized as follows: 300 mg of each polymer (pCB-APMA$_4$, pCB-APMA$_{11}$, pCB-APMA$_{16}$, and pCB-APMA$_{30}$) was dissolved in dry methanol and reacted overnight at room temperature with NHS-DBCO ester (19.6 mg for pCB-X_5, 30.2 mg for pCB-X_{11}, 105.5 mg for pCB-X_{16}, 280.9 mg for pCB-X_{31}) and triethylamine (13.6 μL for

pCB-X_5, 17.4 μL for pCB-X_{11}, 30.5 μL for pCB-X_{16}, 400 μL for pCB-X_{31}) under N_2. An amine detection assay (TNBS) as outlined below, confirmed complete amine consumption. The polymer was then precipitated by adding 40 mL ether and dried overnight under vacuum. The polymer was dissolved in 5-7 mL of water and washed with 3 x 10 mL of DCM. The water layer was collected and lyophilized to yield ~270 mg of pCB-DBCO.

3.3.6 pCB-azide synthesis. pCB-azide was synthesized in a similar manner to pCB-DBCO. Each polymer (300 mg) was dissolved in 10 mL of dry methanol and reacted overnight with 6-azidohexyl-succinimidyl carbonate (NHS-azide; 13.8 mg for pCB-X_5, 21.3 mg for pCB-X_{11}, 74.6 mg for pCB-X_{16}, 227.8 mg for pCB-X_{31}) and triethylamine (13.6 μL for pCB-X_5, 17.4 μL for pCB-X_{11}, 30.5 μL for pCB-X_{16}, 400 μL for pCB-X_{31}). The polymer was precipitated with 40 mL of ether and dried overnight under vacuum. The polymer was then dissolved in 5-7 mL of water and washed with 3 x 10 mL of DCM. The water fraction was collected and lyophilized, yielding ~290 mg pCB-azide.

3.3.7 TNBS assay. Complete amine consumption of pCB-APMA after DBCO and azide derivatization was confirmed using a 2,4,6 trinitrobenzensulfonic acid (TNBS) assay. Briefly, 65 μL of 0.2 mg mL^{-1} pCB-APMA samples in 0.1 M pH 9.2 Borax buffer were mixed with 65 μL of a 4.2 mM TNBS aqueous solution in a 96 well plate. Samples were then incubated in the dark at room temperature for 45

minutes and absorbance at 420 nm was measured on a Biotek Cytation 5 plate reader. All samples were performed in triplicate.

3.3.8 Gel permeation chromatography (GPC) analysis. Polymer molecular weights (M_w, M_n) were determined by GPC analysis using an Agilent 1260 infinity II GPC system equipped with an Agilent 1260 infinity RI detector, and a GE Healthcare Superose 6 Increase 10/300 GL with 10 mM PBS running buffer. The column was calibrated using polyethylene glycol (PEG) standards (M_n of 3,000 to 60,000).

3.3.9 Quantifying gelation time. Gelation times were determined by the vial inversion test. Briefly, 100 μL gels in a 1.8 mL vial were formed by mixing equal volumes of 100 mg mL^{-1} of pCB-azide and pCB-DBCO solutions. Vials were inverted every 15 s until flow was no longer observed.

3.3.10 Hydrogel swelling studies. Gels (100 μL) were formed in pre-weighed 2 mL microcentrifuge tubes, incubated for 3 h at room temperature and weighed to determine initial wet weight (W_o). The gels were centrifuged at 16,000 g for 5 minutes. After gels were formed, 1 mL of 10 mM PBS was pipetted over the gels and incubated at 37°C. At specific time intervals, PBS was removed (a Kimwipe™ was used to gently blot the gel surface) and the tubes were weighed (W_t). 1 mL of PBS was replenished over the gels. Gel weight at each time interval was determined by subtracting the weight of the tube, weight was normalized to initial weight prior to swelling.

3.3.11 Mechanical testing. The Young's modulus of the hydrogels was determined using a parallel plate compression method on a Cellscale Microsquisher®. Pre-swollen cylindrical hydrogels 3 mm in diameter and 1 mm in height were loaded onto the stage. Hydrogels underwent compressive strains from 0 to 10% at a rate of 0 – 5 μm s^{-1}. The resulting force – displacement data was converted to stress-strain curves. Young's moduli were estimated from the slope of the linear regression model of the stress-strain curves at a strain of 0 – 10%.

3.3.12 Influence of temperature on phase separation temperature of pCB-DBCO$_{30}$. pCB-DBCO$_{30}$ was dissolved at 50 mg mL^{-1} in either ultrapure water or 5 M NaCl; pCB-azide was dissolved at 50 mg mL^{-1} in ultrapure water. Turbidity measurements were performed in a quartz cuvette at a wavelength of 550 nm with heating or cooling at a rate of 0.2°C per minute on an Agilent Cary 5000 UV Vis NIR equipped with an Agilent Peltier heating element.

3.3.13 pCB-X turbidity as a function of gelation medium. To determine the influence of ionic strength on electrostatic interactions within pCB-X hydrogels, gels (60 μL) were prepared in ultrapure water, 5 M NaCl, PBS and media (DMEM-F12 with 10% CBS) in a clear 96 well plate and incubated at 37°C. After 12 h, absorbance was read at 550 nm. All samples were performed in triplicate.

3.3.14 Influence of salt on PEGMA-X$_{27}$ and pCB-X$_{31}$ hydrogels. PEGMA-X$_{27}$ or pCB-X$_{31}$ hydrogels (60 μL) were formed in either water or 5 M NaCl and

allowed to gel for 2 h at room temperature in a 96 well plate. The OD550 of the gels were then measured on a Biotek Cytation 5 plate reader.

3.3.15 Swelling of pCB-X_{31} gels prepared in water. pCB-X_{31} gels (60 μL) were formed in ultrapure water in pre-weighed 2 mL microcentrifuge tubes and incubated for 2 h at room temperature. 1 mL of ultra-pure water or 5 M NaCl was pipetted over the gels and incubated at room temperature for 48 h. The solutions were then removed from the gels and tubes were weighed. Gel weight was determined by subtracting the weight of the tube, weight was normalized to initial weight prior to swelling.

3.3.16 pCB-X_{31} turbidity upon changes in salt concentration. 60 μL pCB-X_{31} gels were formed in ultrapure water or 5 M NaCl in a clear bottom 96 well plate and incubated for 2 h at room temperature. Initial OD550 readings were taken using a Biotek Cytation 5 plate reader. 200 μL of ultrapure water was pipetted over pCB-X_{31} gels formed in 5 M NaCl and 200 μL 5 M NaCl was pipetted over pCB-X_{31} gels formed in water. Gels were incubated over 7 days, and supernatant solutions were exchanged daily to ensure complete solution exchange. OD550 measurements were then taken.

3.3.17 Fluorescent BSA (BSA-647) synthesis. AlexaFluor 647 NHS ester (15 μL at 10 mg mL^{-1}) in DMF was added to a BSA solution (2.5 mg in 500 μL of PBS) and reacted for 3 h at room temperature. The reaction mixture was then dialyzed

against PBS (MWCO 12-14k) for 3 d at 4°C. The fluorescent protein was stored at -20°C in the dark**.**

3.3.18 Non-specific binding of BSA-647. pCB-X gels (60 µL at 100 mg mL^{-1}) in 10 mM PBS were formed in a 96 well plate and incubated for 3 h at room temperature. A 60 µL 0.5 mg mL^{-1} BSA-647 solution was pipetted onto the gels and incubated at 37°C for 3 h. The supernatant was removed, and the gels were washed twice with 10 mM PBS. Gels were immersed into a 240 µL solution of 10 mM PBS and 8% SDS and incubated overnight at room temperature. The mixture was then boiled for 20 min to extract residual BSA-647 from the gels. 100 µL of the solution was added to a black 96 well plate and fluorescence was measured using a Biotek Cytation 5 plate reader (651 nm excitation, 672 nm emission). Each condition was performed in triplicate. The concentration of BSA-647 in solution was calculated using a calibration curve composed of BSA-647 solutions of known concentration.

3.3.19 Presto Blue assay. Polymer precursors were dissolved in 10 mM PBS at 100 mg mL^{-1} and sterilized using a 0.2 µm filter. 60 µL gels were prepared in a clear 96 well plate. Subsequently, 200 µL of DMEM-F12 supplemented with 10 % CBS was pipetted over the gels and incubated at 37°C for 3 d. The media was removed and 3,000 NIH 3T3 cells in 100 µL of media per well were seeded on the surface of the gels. The gels were then incubated at 37°C and 5% CO_2. After 24h, 12 µL of presto blue reagent was pipetted into the wells and incubated at 37°C

and 5% CO_2 for 18 h to assess metabolic activity. Fluorescence was measured using a Biotek Cytation 5 plate reader (560 nm excitation and 590 nm emission) and normalized to a tissue culture plate control.

3.3.20 Cell adhesion assay. Gels were prepared as outlined in the Presto Blue assay. DMEM-F12 supplemented with 10% CBS (200 μL) was pipetted over the gels and incubated overnight at 37°C and 5% CO_2. Media was then removed and 3,000 cells in 100 μL of media per well were seeded on the gel surfaces. Gels were then incubated at 37°C and 5% CO_2. After 16 h, Calcein AM and Hoechst stains were added to the wells and incubated for 10 min at 37°C. Gels were then imaged using a Biotek Cytation 5 imager. Opaque pCB-X_{31} gels were inverted for imaging.

3.3.21 Statistical analysis. All samples were conducted in triplicate and expressed as mean ± standard deviation. All statistical analysis was performed using GraphPad Prism 5. $P < 0.05$ is indicated by *, $P < 0.01$ by **, and $P < 0.001$ by ***.

3.4 Results and discussion

3.4.1 Synthesis and characterization of pCB-azide and pCB-DBCO. To determine the influence of azide and DBCO content on CB copolymer and pCB-X hydrogel physical and biological properties, we synthesized pCB-APMA copolymers with 4 different CB:APMA ratios for modification with NHS-azide or

NHS-DBCO (**Figure 3.1C**). In situ gelling hydrogels were formed by mixing pCB-azide and pCB-DBCO with similar substitution rates.

To achieve reproducible polymer MW and dispersity (Đ < 1.4, **Figure 3.2**), copolymers were synthesized using reversible addition-fragmentation chain-transfer (RAFT) polymerization at pH 3-4 to minimize hydrolysis or aminolysis of the chain transfer agent (CTA). CB:APMA ratios were controlled by varying feed ratios during polymerization. The number average MW (M_n) was kept constant for three pCB-APMA copolymers (~7 to 10 kDa); a larger M_n (~25 kDa) was required for pCB-$APMA_5$ to form hydrogels to achieve a minimum number of crosslinks for gelation after azide and DBCO modification.

Primary amines of all pCB-APMA polymers were completely reacted with either NHS-azide or NHS-DBCO to yield pCB-azide and pCB-DBCO; amine consumption was monitored by the TNBS assay. Relative azide or DBCO to CB (X: CB) content was determined by ^{1}H NMR, azide or DBCO peak intensities were compared to the methyl group of the polymer backbone (**Figure S 3.1**). The azide mole fraction for the four different pCB-azide copolymers were calculated to be 0.05, 0.11, 0.16 and 0.32; the DBCO mole fraction for the four different pCB-DBCO copolymers were 0.04, 0.11, 0.17 and 0.30 (**Table S 3.1**). The azide and DBCO mole fractions for the four pCB-APMA copolymers were in good agreement, supporting the accuracy of the NMR quantification method. NMR's were conducted at low concentrations to ensure polymers were solubilized.

A

Polymer	M_w	M_n	Đ
pCB-APMA$_5$	33 380	24 516	1.36
pCB-APMA$_{11}$	7 828	7 104	1.10
pCB-APMA$_{16}$	10 658	9 061	1.18
pCB-APMA$_{31}$	12 795	10 575	1.21

B

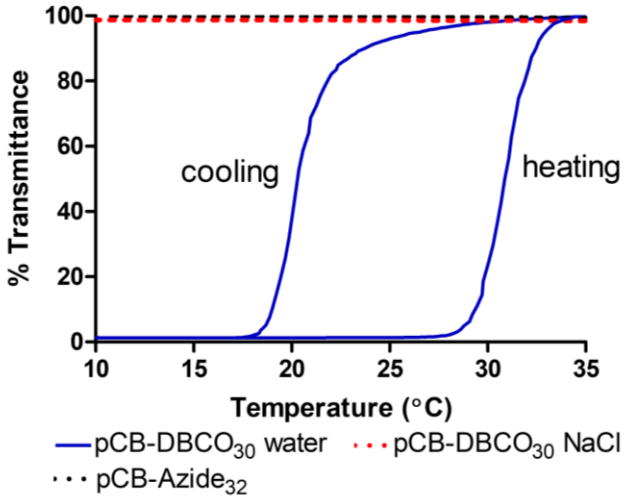

Figure 3.2 Characterization of CB copolymers and phase separation response of pCB-DBCO$_{30}$ to temperature and salt. (A) GPC characterization of pCB-APMA$_X$. (B) Turbidity curves for 5 wt % solutions of pCB-DBCO$_{30}$ in water, pCB-azide$_{32}$ in water and pCB-DBCO$_{30}$ in 5 M NaCl. 5 wt % solutions represent the same pCB-DBCO concentration in 10 wt % pCB-X hydrogels. The UCST of pCB-DBCO$_{30}$ is ~20°C.

3.4.2 Stimuli responsive CB copolymer. Although CB homopolymers do not exhibit a UCST, zwitterionic polymers such as pSB experience a UCST due to intra- and interchain electrostatic association of zwitterionic groups, which can be interrupted by the addition of counter ions.[45] It has been suggested that the charge density between the cationic and anionic groups in a pSB (3.0 e nm^{-3} and -4.5 e nm^{-3}) are better matched for zwitterionic associations than those found in pCB (3.0 e nm^{-3} and -5.3 e nm^{-3}; numbers for CB with a 2 CS between charges).[46] CB homopolymers do not have sufficient zwitterionic associations to exhibit a UCST or anti-polyelectrolyte properties. Furthermore, significant zwitterionic associations for CB homopolymers with a 1 CS between the charges, as explored here, have never been reported.

The addition of rigid hydrophobic groups to SB copolymers increases their aqueous UCST while maintaining anti-polyelectrolyte properties; hydrophobic groups promote electrostatic interactions of zwitterionic groups by decreasing polymer hydration.[47] In this study, we observed an aqueous UCST for pCB-$DBCO_{30}$, the copolymer with the greatest amount of the hydrophobic and rigid DBCO moiety (**Figure 3.2B**). In the presence of 5 M NaCl, no UCST was observed for pCB-$DBCO_{30}$, indicating anti-polyelectrolyte properties. The electrostatic interactions are also reversible upon the addition of salt; an insoluble 5 wt % pCB-$DBCO_{30}$ sample at 4°C dissolved upon the addition of salt (data not

shown). Therefore, pCB-$DBCO_{30}$ in water forms salt responsive electrostatic interactions upon cooling.

To investigate if DBCO-DBCO hydrophobic interactions also contribute to phase separation, solutions of 5 wt % pCB-$DBCO_{30}$ in water and 5 M NaCl were heated to 90°C; phase separation due to hydrophobic DBCO interactions would produce a lower critical solution temperature (LCST) and phase separate at higher temperatures. No LCST was observed when samples were heated to 90°C even in 5M NaCl, which promotes hydrophobic interactions. Therefore, hydrophobic interactions within pCB-$DBCO_{30}$ are not responsible for polymer phase separation.

As expected, pCB-$azide_{32}$ in water did not display a UCST (**Figure 3.2B**) because the pendant azide moiety is a less rigid and hydrophobic than DBCO, consistent with previously reported aliphatic modifications of zwitterionic polymers.[55] A minimum threshold of hydrophobicity is required for CB copolymers to exhibit a UCST, which was only observed with pCB-$DBCO_{30}$.

A

Hydrogel	Gelation Time	X: CB Units	Modification %
pCB-X_5	75 s	1: 20.7	4.6
pCB-X_{11}	135 s	1: 8.3	10.8
pCB-X_{16}	15 s	1: 5.2	16.2
pCB-X_{31}	<5 s	1: 2.3	30.7

B

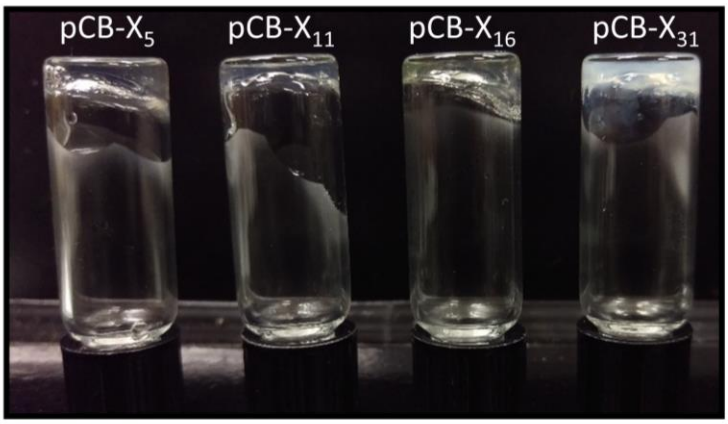

Figure 3.3 Gelation of pCB-X hydrogels. (A) 10 wt % pCB-X hydrogel gelation times in PBS, and crosslinker (DBCO or azide) mole fractions for pCB-X hydrogels as calculated by ^{1}H NMR. (B) Photograph of inverted pCB-X hydrogels in vials.

3.4.3 Gelation of pCB-X hydrogels. Previously reported pCB hydrogels were formed by radical polymerization of methacrylated monomers and bifunctional crosslinkers, which results in inconsistent crosslink densities and polymer lengths.[17,48] The use of copolymers with well defined crosslinker mole fractions

enables the study of azide and DBCO content on chemical, mechanical and biological properties of copolymers and hydrogels. The crosslinking moieties should be well distributed along the polymer chain as both monomers are methacrylamides with similar reactivities in RAFT polymerization. However, studies can be performed to determine the optimal rate of addition of each monomeric subunit to achieve equal distribution of monomers through the polymer.

Gelation was dependent on copolymer concentration, azide/DBCO content, and polymer MW. All 10 wt % pCB-X hydrogels formed between <5 s and 135 s (**Figure 3.3A)**; 5 wt % hydrogels formed between 3 and 6 min except pCB-X_{11}, which failed to gel within 30 min (**Figure S 3.2)** due pCB-X_{11}'s lower MW than pCB-X_5 and lower azide/DBCO content than pCB-X_{16} and pCB-X_{31}. Greater azide/DBCO content decreased gelation times for hydrogels composed of polymers with similar MW (pCB-X_{11}, pCB-X_{16} and pCB-X_{31}, **Figure 3.3A**). pCB-X_{31} gelled instantaneously (< 5 s) due to the high azide/DBCO content when compared to the other hydrogels. 10 wt % hydrogels were studied further because their gelation times (compared to 5 wt % gels) are more suitable for biological in situ gelling applications.[49] In this study, the pCB-X hydrogels are non-degradable to determine their properties independent of degradation, which is important for long term implants. Previously, the degradation rate of azide-DBCO crosslinked hydrogels has been tuned by introducing hydrolytic bonds adjacent to the azide

moiety.[50] Therefore, pCB-X hydrogels with different degradation rates can be developed, if required.

3.4.4 Swelling and mechanical properties of pCB-X hydrogels. pCB-X gels swelled less than previously reported pCB hydrogels crosslinked through radical mechanisms*;* low swelling gels are required for implantation to minimize tissue damage and compression.[32] pCB-X_5 to pCB-X_{16} gels were made in PBS and their initial wet weight (W_o) was recorded; after immersion in PBS at 37°C their equilibrium wet weight (W_t) was only ~10% greater than W_o (**Figure 3.4A**) compared to 150 to 325% for pCB hydrogels crosslinked through radical chemistry.[48,51] The lower swelling degree of pCB-X_5 to pCB-X_{16} gels may be attributed to increased hydrophobic content (e.g. DBCO) and greater control over crosslink density, which may result in less chain reorientation after gelation.[34] pCB-X_{31} decreased to ~70% of its initial wet weight due to increased hydrophobicity from higher DBCO content and CB electrostatic interactions, as discussed in section 3.2 and 3.5.

Compression tests on pCB-X hydrogels determined that the Young's modulus increased with the number of crosslinkers per polymer chain (**Figure 3.4B**). Using NMR and GPC data, the number of crosslinkers per chain was calculated to be 5, 3, 7 and 15 for pCB-X_5, pCB-X_{11}, pCB-X_{16} and pCB-X_{31} hydrogels, respectively. pCB-X_{11} had the smallest Young's modulus because it had the least crosslinker units per polymer chain. It should be noted that polymer

MW was determined by GPC data calibrated to PEG standards; therefore, the number of crosslinks should only be viewed as a trend and not absolute values.

Although pCB-X_{16} and pCB-X_{31} hydrogels had different swelling ratios (**Figure 3.4A**), their similar stiffness (**Figure 3.4B**) implies that increasing hydrophobic content and electrostatic interactions has minimal impact on mechanical properties. pCB-$DBCO_{30}$ in pCB-X_{31} hydrogels can form interchain electrostatic interactions, contributing to pCB-X_{31}'s unique deswelling and turbidity properties. The CB unit within pCB-$DBCO_{30}$ has 1 carbon spacer (CS) between charges, whose electrostatic interactions have been shown to minimally increase the mechanical strength of hydrogels.[52] A CS of 2 between CB charges increases the strength of the electrostatic interactions, which may have a greater influence on hydrogel mechanical properties.[52] Therefore, electrostatic interactions in pCB-X_{31} hydrogels have a significant impact on hydrogel hydration and hydrophobicity but not mechanical properties, which may be due to the presence of salts that reduced number of electrostatic interactions.

The low pCB-X stiffness (<10 kPa) mimics the mechanical properties of soft neural tissue.[53] For cell delivery applications, mechanical stiffness must be controlled to favor therapeutically advantageous cellular activities. For example, pCB-X hydrogels have the appropriate stiffness to deliver neural stem cells for the regeneration of neurons.[54]

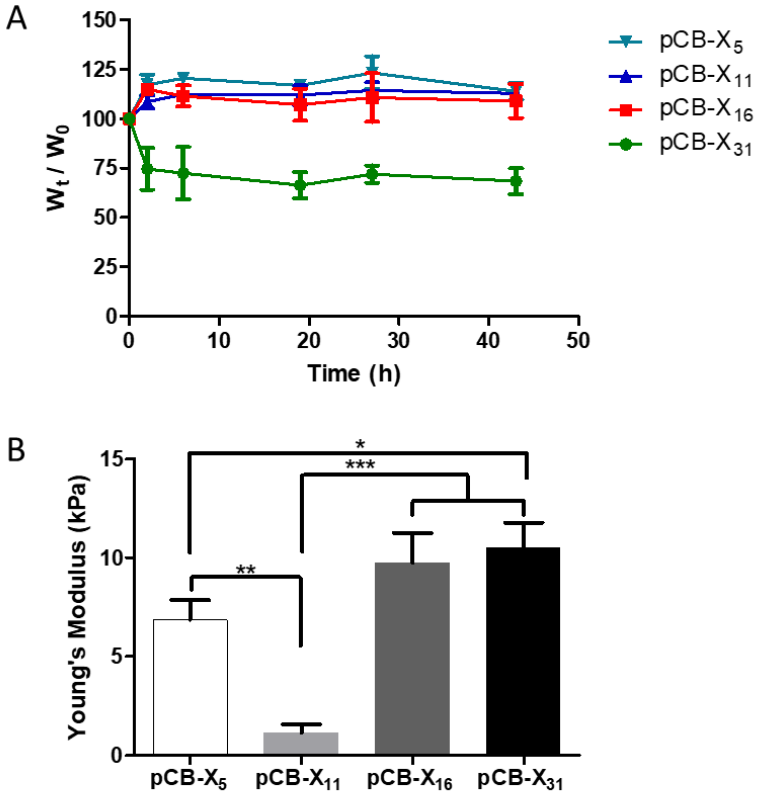

Figure 3.4 pCB-X hydrogel swelling and mechanical properties. (A) pCB-X_5, PCB-X_{11} and pCB-X_{16} hydrogels were low-swelling, and pCB-X_{31} hydrogels shrunk when exposed to PBS. All hydrogels were first prepared in PBS, and then immersed in PBS. W_o refers to hydrogel wet weight prior to immersion in PBS. Swelling ratios of pCB-X hydrogels with different crosslinker densities are reported (mean ± standard deviation, n = 3). (B) Young's modulus of the 10 wt %

pCB-X hydrogels formed in PBS with different crosslinker densities (mean ± standard deviation, n = 3, one-way ANOVA with Bonferroni's post hoc test).

3.4.5 Electrostatic interactions within pCB-X hydrogels. The turbidity and hydration of pCB-X_{31} hydrogels can be attributed to the unique properties of pCB-$DBCO_{30}$, a temperature and salt responsive copolymer that exhibits a UCST (~20°C) in pure water (**Figure 3.2B**). 10 wt % pCB-X_{31} hydrogels made from pCB-$azide_{32}$ and pCB-$DBCO_{30}$ produced opaque gels when prepared in pure water, PBS and cell culture media (DMEM:F12 with 10% CBS), and transparent gels in 5 M NaCl (**Figure 3.5A-B**), indicating the presence of anti-polyelectrolyte properties and electrostatic associations similar to pCB-$DBCO_{30}$. pCB-X_{16} gels were slightly turbid in water due to decreased solubility from electrostatic associations (**Figure 3.5A**), but to a much lower extent than pCB-X_{31}.

To help elucidate the influence of DBCO on hydrophobicity and CB electrostatic interactions within hydrogels, we compared the transparency of pCB-X_{31} to poly(oligo(ethylene glycol) methyl ether methacrylate (PEGMA) hydrogels with azide/DBCO crosslinkers (PEGMA-X; similar crosslinker mole fraction as pCB-X_{31} gels; **Figure 3.5C**). Similar to pCB, PEGMA polymers contain a polypropylene backbone with pendant hydrophilic side chains; PEGMA contains non-ionic poly(ethylene glycol) methyl ether side chains (MW 396 g mol^{-1}) and pCB contains CB. PEGMA polymers have a LCST due to hydrophobic

association of the polymer backbone and PEG groups,[55] which are promoted by the addition of salt.[56] When prepared in 5M NaCl, PEGMA gels decreased in transparency, whereas pCB-X_{31} gels increased in transparency. Therefore, the addition of salt has an opposite effect on azide/DBCO crosslinked pCB-X_{31} and PEGMA-X hydrogels; pCB-X_{31}'s response to salt is not the result of hydrophobic DBCO interactions but the anti-polyelectrolyte effect, due to DBCO's promotion of CB electrostatic interactions.

To further elucidate the importance of electrostatic interactions on hydrogel shrinking, pCB-X_{31} gels were prepared in water and then soaked in water or 5 M NaCl (**Figure 3.5D**). Immediately after preparation, the opaque gels were weighed to determine W_o and then soaked in either water or 5 M NaCl for 2 days. Gels soaked in water shrunk due to the continued formation of electrostatic interactions that increase hydrophobicity; whereas gels soaked in 5 M NaCl did not significantly shrink or swell because the salt prevented further electrostatic associations within the gel. Interestingly, the gels (that were prepared in pure water) remained opaque after immersion in 5 M NaCl, indicating the pre-formed electrostatic associations are not reversible in pCB-X_{31} hydrogels, unlike uncrosslinked pCB-$DBCO_{30}$. pCB-X_{31} hydrogels were immersed in 5 M NaCl for 3 days and no effect was seen. Therefore, the formation of electrostatic interactions increases hydrophobicity and encourages the expulsion of water, which results in pCB-X_{31} hydrogel shrinking.

To further probe the response of pCB-X_{31} gels to changing salt concentrations and the dynamics of electrostatic associations, we followed the turbidity of gels made in water and 5 M NaCl that were subsequently immersed in 5 M NaCl and water, respectively (**Figure 3.5E**). Similar to the gel swelling study, gels made in water and immersed in 5 M NaCl remained opaque with no change in transparency, further indicating that pre-formed electrostatic associations are stable within the hydrogel. Transparent gels prepared in 5 M NaCl and immersed in water increased in turbidity but remained less opaque than pCB-X_{31} gels initially made in water. Therefore, interchain polymer electrostatic associations can form after gelation but to a lower extent than pCB-X_{31} gels initially prepared in water, likely due to limited polymer rearrangement after the formation of covalent crosslinks in 5 M NaCl.

Unlike pCB- $DBCO_{30}$, pCB-X_{31} hydrogels are not thermoresponsive. No increase in transparency was observed when opaque pCB-X_{31} hydrogels were heated to 60°C (**Figure S 3.4**). The lack of responsiveness of opaque pCB-X_{31} hydrogels may be due to the covalent azide/DBCO crosslinks that the limit polymer rearrangement and swelling required to increase hydrogel hydration and disrupt electrostatic associations. Crosslinking also increases the hydrophobicity of pCB-$azide_{32}$ after reaction with pCB-$DBCO_{30}$, increasing hydrogel hydrophobic content and potential for electrostatic associations. Increasing hydrophobic content alone should shift pCB-X_{31}'s UCST relative to pCB-

$DBCO_{31,}$ but pCB-X_{31} gels appeared to remain opaque even upon heating to ~90°C in the presence of 5 M NaCl (data not shown). When prepared in water, pCB-X_{31} gels most likely form a stable collapsed network comprised of covalent azide/DBCO crosslinks and interchain electrostatic associations promoted by hydrophobic DBCO content.

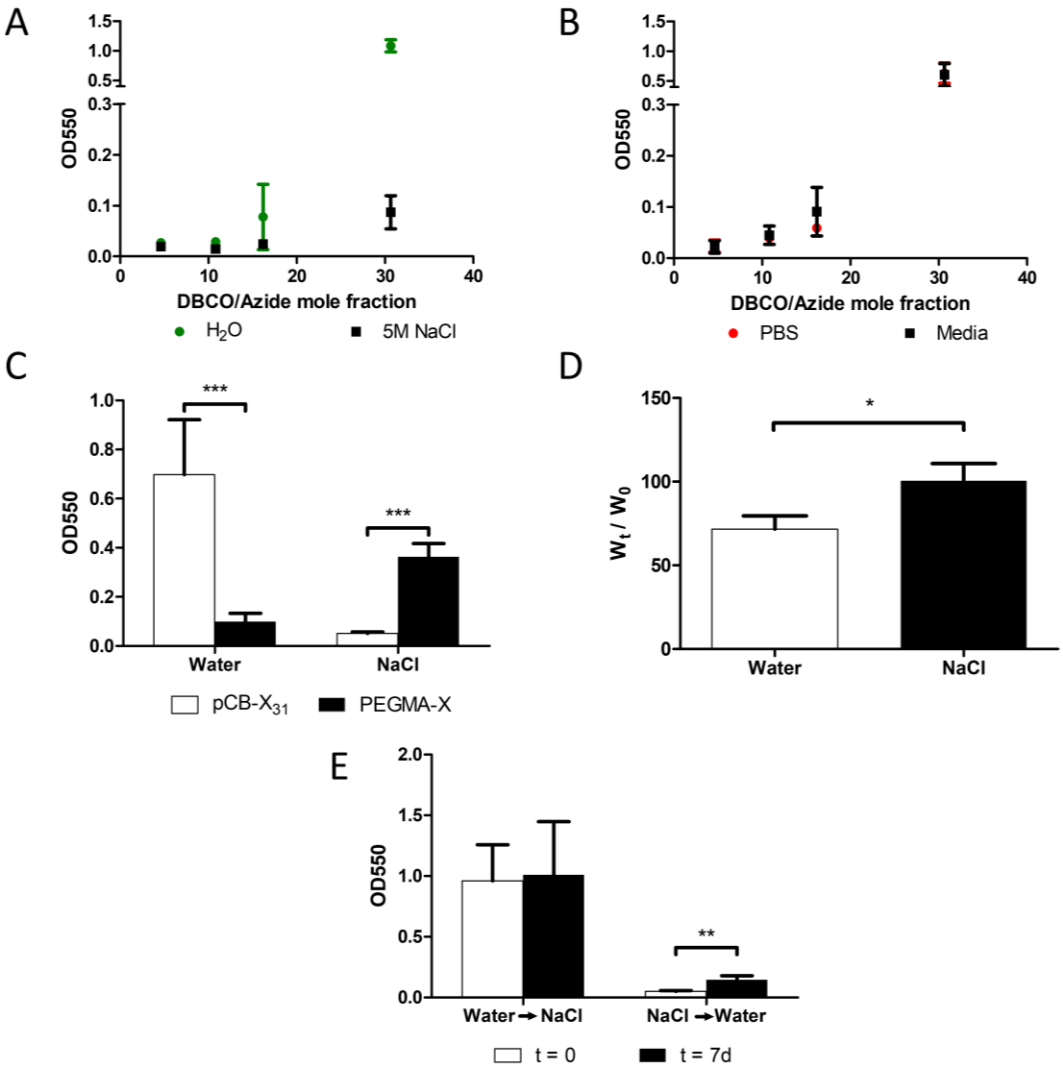

Figure 3.5 Influence of salt on pCB-X hydrogel electrostatic interactions, turbidity and swelling. Optical density at 550 nm (OD550) was used to follow changes in hydrogel turbidity due to phase separation. (A) OD550 of pCB-X gels when prepared in water or 5 M NaCl. pCB-X_{31} hydrogels increased in transparency at high ionic strength. (B) Comparison of pCB-X gel OD550 when prepared in PBS or media (10% CBS in DMEM-F12). (C) Comparison of pCB-

X_{31} and PEGMA-X gels response to gelation in water and 5 M NaCl. (D) Swelling of pCB-X_{31} gels prepared in water followed by immersion in water or 5 M NaCl, where initial weight (W_o) was measured immediately after gelation and swollen weight (W_t) was measured 2 days after immersion. (E) Change in the OD550 of pCB-X_{31} gels with increasing or decreasing salt concentrations. pCB-X_{31} prepared in water (t = 0) were immersed in 5 M NaCl (t = 7 d) and pCB-X_{31} prepared in 5 M NaCl (t = 0) were immersed in water (t = 7 d).

3.4.6 Non-specific binding of BSA to pCB-X gels. Hydrogels that non-specifically bind proteins may elicit a foreign body response, reducing hydrogel effectiveness for in vivo applications. Under physiological conditions, hydrogels must be well hydrated and not contain hydrophobic bonding pockets for protein fouling. To characterize protein fouling to pCB-X hydrogels, the non-specific binding of fluorescent BSA-647 on hydrogel surfaces was assessed. Hydrogels were soaked in a solution of BSA-647 for 2 h, rinsed to remove unbound protein and exposed to an SDS solution to extract bound protein for quantification by fluorescence using a BSA-647 calibration curve.

Because pCB's low-fouling properties are attributed to a strong hydration shell,[17,31] pCB-X_{31}'s higher degree of hydrophobicity under cell culture media conditions will decrease hydration and increase non-specific protein binding.[58] In PBS, pCB-X_{31} hydrogel surfaces bound the most BSA at 33.8 μg cm^{-2}, the

remaining three pCB-X gel surfaces bound 10 to 20 μg cm^{-2} (**Figure 3.6**), which is comparable to other reported low-fouling zwitterionic hydrogels with BSA adsorption of ~ 10 to 25 μg cm^{-2}.[59] No significant difference was observed between pCB-X_5, pCB-X_{11}, and pCB-X_{16} (one-way ANOVA, $p > 0.05$). pCB-X_{31} had the greatest DBCO content and degree of electrostatic associations that both decrease hydrogel hydration and increase hydrophobicity, which was evident from swelling experiments where pCB-X_{31} shrunk in PBS or water.

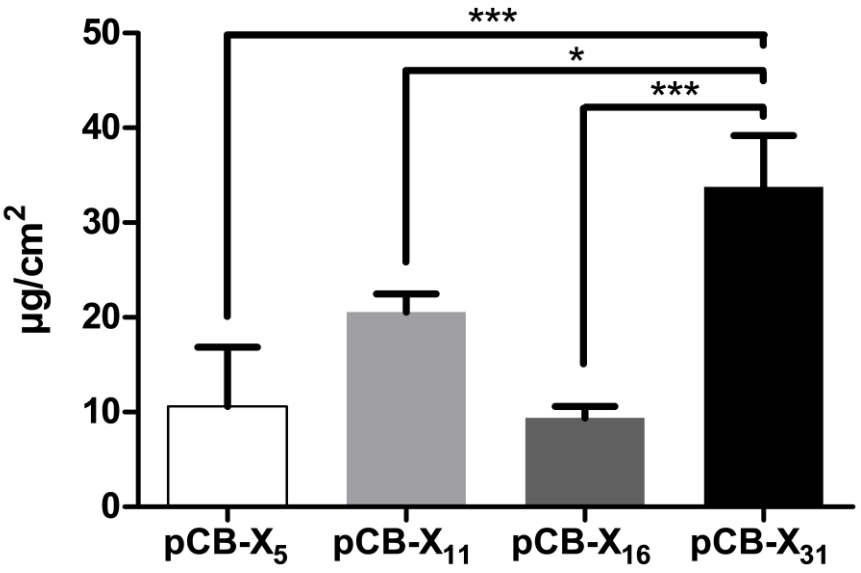

Figure 3.6 Non-specific binding of BSA-647 on pCB-X hydrogel surfaces.

Non-specific BSA binding to pCB-X_5, pCB-X_{11} and pCB-X_{16} is similar to other reported zwitterionic hydrogels.[59] The transparent, less hydrophobic pCB-X_5, pCB-X_{11} and pCB-X_{16} gels bound statistically the same amount of BSA-647. The opaque pCB-X_{31} hydrogel bound the most protein, likely due to hydrophobic interactions. Data was expressed as μg cm^{-2} by estimating the surface area of the

gel in a 96 well plate (mean ± standard deviation, n = 3, one-way ANOVA with Bonferroni's post hoc test).

3.4.7 Cell adhesion and metabolic activity on pCB-X hydrogel surfaces. To relate cell fouling properties to the hydrophobicity pCB-X gels, the adhesion and metabolic activity of NIH 3T3 fibroblasts on the gel surfaces were assessed. After incubating pCB-X gels in 10% CBS in DMEM-F12 for 3 days to saturate non-specific protein binding sites, 3,000 cells were seeded on the hydrogel surfaces. After a 24 h incubation, the cells were stained with Hoechst and Calcein AM for fluorescent imaging. Cells were also cultured on tissue culture plastic (TCP) as a positive cell adhesion control (**Figure 3.7A-C**).

Cell adhesion increased on pCB-X hydrogels with increasing DBCO content due to increased hydrophobicity, which promotes in protein fouling. pCB-X_5 hydrogels had the lowest DBCO content and prevented the adhesion of cells, which formed large non-adhered clusters on the gel surface (**Figure 3.7D-F**). Cell spreading and single cell adhesion were not observed on pCB-X_5 gels, which have minimal hydrophobic interactions and electrostatic associations to promote protein binding and cell adhesion. Cells cultured on gels with intermediate DBCO content, pCB-X_{11} and pCB-X_{16}, formed smaller clusters compared to pCB-X_5 gels (**Figure 3.7G-L**). Cell spreading and single cells were also observed on pCBX_{11} and pCB-X_{16} gels, indicating higher fouling surfaces than pCB-X_5. Therefore,

pCB-X_{11} and pCB-X_{16} gels have slightly greater hydrophobicity than pCB-X_5 gels that results in a small increase in cell adhesion.

pCB-X_{31} gels formed significant electrostatic associations and shrunk under physiological conditions, indicating the greater hydrophobic content promoted protein binding and cell adhesion. Due to the high opacity and background fluorescence, brightfield and Calcein AM images could not be obtained for pCB-X_{31} gels. DNA Hoechst staining revealed a large amount of cell spreading and single cells across the surface of the pCB-X_{31} hydrogels (**Figure 3.7M**). Cell adhesion results are in good agreement with non-specific BSA binding and swelling data, where the higher protein adsorption and lower hydration of pCB-X_{31} hydrogels encouraged cell adhesion.

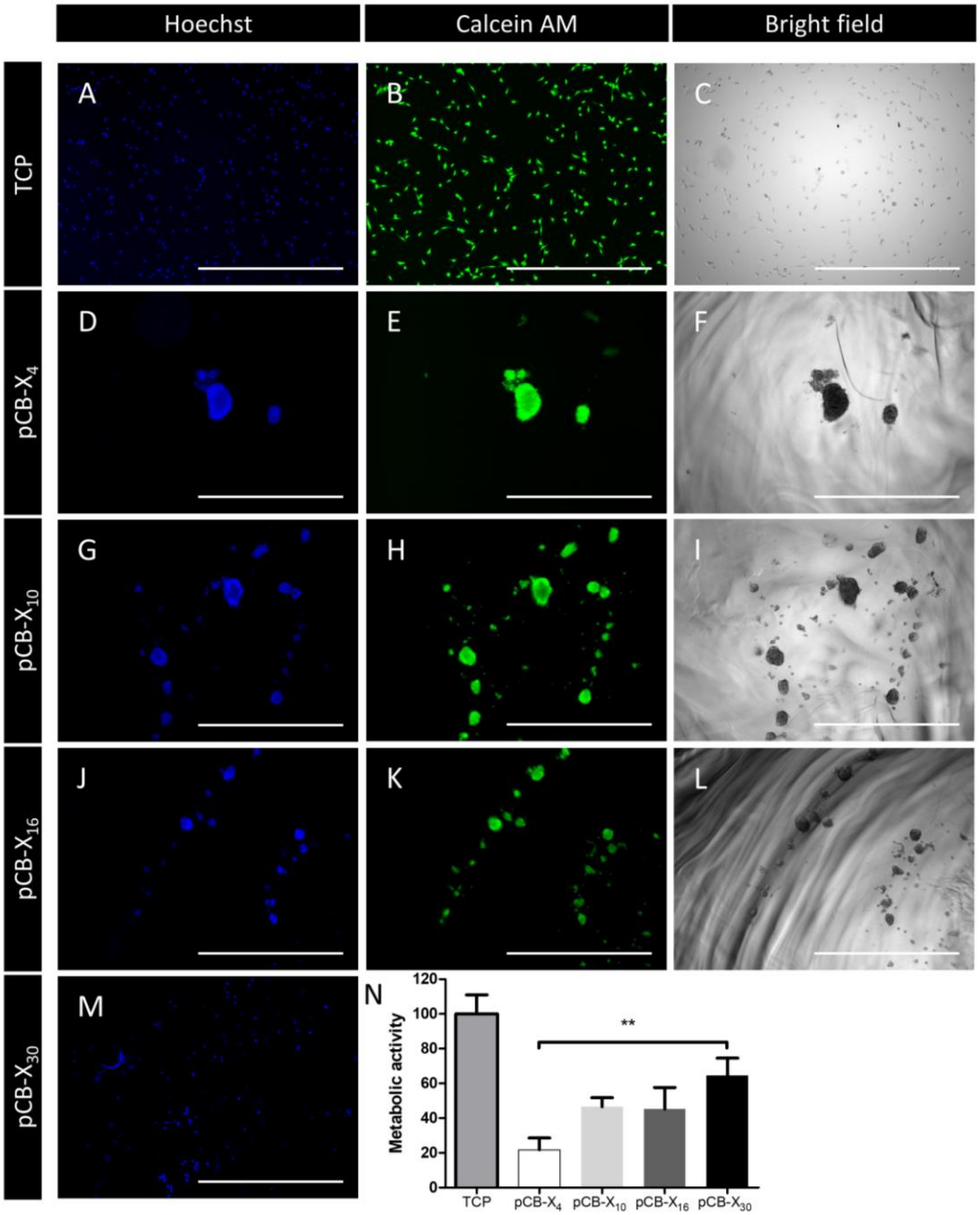

Figure 3.7 Non-specific NIH 3T3 fibroblast adhesion on pCB-X hydrogels.

Cell adhesion was greater on pCB-X hydrogels with higher DBCO content due to increased non-specific protein binding. Cells were seeded on the surface of gels

pre-soaked in 10% CBS in DMEM-F12 and incubated for 24 h. Cells were then stained with Hoescht and Calcein AM. Fluorescent and brightfield images were acquired. The opacity and high background of pCB-X_{31} gels prevented the acquisition of brightfield and Calcein AM images. (A-C) Cells cultured on TCP were included as a positive control for adhesion. (D-F) Cells formed large non-adhered clusters on pCB-X_5 gels. (G-M) Higher crosslinker densities resulted in increasing levels of cell adhesion, with the greatest cell adhesion on pCB-X_{31} gels. All scale bars represent 1000 μm. Higher magnification images are provided in Fig. S3. (N) Relative metabolic activity of fibroblasts cultured on the surface of pCB-X hydrogels as determined by the Presto blue assay normalized against a TCP control (mean ± standard deviation, n = 3, one-way ANOVA with Bonferroni's post hoc test). TCP was significantly different from all pCB-X conditions ($p < 0.05$). Metabolic activity increased with crosslinker density due to increased degrees of cellular adhesion.

The metabolic activity of fibroblasts on pCB-X hydrogel surfaces was quantified to confirm cell adhesion data as adhesion increases metabolic activity.[56] Following the same trend as cell adhesion, pCB-X_5 had the lowest level of metabolic activity, according to the Presto Blue assay. pCB-X_{11} and pCB-X_{16} hydrogels had similar intermediate levels of metabolic activity. pCB-X_{31} produced the greatest amount of metabolic activity (**Figure 3.7N**) but remained lower than cells cultured on tissue culture plastic (TCP).

3.4.8 Further discussion

Although many polymers exhibit a USCT, there are not many examples of polymers that transition under mild or physiological conditions. For example, poly(ethylene oxide) (PEO),[60] poly(vinyl methyl ether) (PVME)[61] and poly(hydroxyethyl methacrylate (PHEMA)[62] have UCSTs above 100°C.[63] Some examples of polymers with UCSTs suitable for biological applications have been developed. pSB copolymers with benzyl comonomers is both salt and temperature responsive with a tunable UCST between 5 and 80°C.[47] Ureido-derivatized polymers (e.g. poly(allylurea), PU) also exhibit a UCST and have been shown to selectively capture and separate proteins by chilling protein-polymer solutions below the polymer's UCST.[64] This work demonstrates that pCB-DBCO$_{30}$ also has a UCST under mild conditions, which may result in bioseparation applications by capturing and releasing biomolecules or cells. pCB-DBCO30's UCST of ~20°C is ideal for biomolecule applications; solutions can be chilled to 4°C for polymer-polymer association and heated to 37°C to reverse polymer-polymer associations.

The development of low-fouling, low-swelling and in situ gelling hydrogels, such as pCB-X$_5$, is critical for local drug and cell delivery in the fields of tissue engineering and cancer immunotherapy. The regeneration of tissue after significant trauma (e.g. stroke, heart attack, spinal cord injury) may require the local delivery of specific biological factors, drugs and stem/progenitor cells. In cancer immunotherapy, the local delivery of checkpoint inhibitors and immune

cells from hydrogels has been shown to improve tumor killing and survival in animal models.[12,65] For long term delivery, low-fouling gels can reduce the FBR and prevent the formation of a fibrous collagen capsule around the hydrogel, which would impede drug or cell release. As explained previously, low-swelling in situ gelling hydrogels are required to prevent hydrogel displacement from the injection site and minimize tissue compression and damage. Therefore, pCB-X_5 hydrogels have the required properties for cell and drug delivery and may prove useful in the fields of tissue engineering and cancer immunotherapy.

3.5 Conclusions

Increasing hydrophobic DBCO content in CB copolymers promotes intra/interchain electrostatic associations to yield temperature and salt responsive polymers, the first such demonstration for a CB copolymer. pCB-$DBCO_{30}$ exhibits an aqueous UCST upon cooling and heating from the association and dissociation of electrostatic zwitterion interactions. Due to the anti-polyelectrolyte effect, pCB-$DBCO_{30}$ does not form electrostatic associations in 5 M NaCl, preventing phase separation at low temperature. pCB-X hydrogel swelling and fouling properties can be tuned by controlling DBCO content and gelation medium to promote or hinder electrostatic interactions that increase hydrogel hydrophobicity and turbidity. When pCB-$DBCO_{30}$ is crosslinked with pCB-$azide_{32}$ to yield pCB-X_{31}, hydrogel transparency is dependent on the gelation medium; pCB-X_{31} is transparent when prepared in 5 M NaCl but opaque in water,

PBS or media. Once formed, the electrostatic associations are stabilized by the hydrogel structure and do not easily dissociate when exposed to high salt concentrations or temperature. Minimizing DBCO content in pCB-DBCO results in hydrated low-fouling and low-swelling pCB-X hydrogels after in situ gelation, which may prove useful as injectable hydrogels for applications in drug and cell delivery.

Acknowledgements. This work was supported by the Natural Sciences and Engineering Research Council (NSERC), Canada Foundation for Innovation: John R. Evans Leaders Fund (CFI-JELF), Ontario Research Fund - Research Infrastructure (ORI-RI), and McMaster University. We would also like to thank Dr. Alex Adronov and Stuart McNelles for donation of NHS-DBCO and access to the Agilent Cary 5000 UV Vis NIR, and Dr. Todd Hoare for access to the CellScale MicroSquisher.

3.6 References

(1) Ta, H. T.; Dass, C. R.; Dunstan, D. E. Injectable Chitosan Hydrogels for Localised Cancer Therapy. *J. Control. Release*. **2008**, *126* (3), 205–216.

(2) Yu, L.; Chang, G. T.; Zhang, H.; Ding, J. D. Injectable Block Copolymer Hydrogels for Sustained Release of a PEGylated Drug. *Int. J. Pharm.* **2008**, *348* (1–2), 95–106.

(3) Hoare, T. R.; Kohane, D. S. Hydrogels in Drug Delivery: Progress and

Challenges. *Polymer*. **2008**, *49* (8), 1993–2007.

(4) Drury, J. L.; Mooney, D. J. Hydrogels for Tissue Engineering: Scaffold Design Variables and Applications. *Biomaterials*. **2003**, *24* (24), 4337–4351.

(5) Rosales, A. M.; Vega, S. L.; DelRio, F. W.; Burdick, J. A.; Anseth, K. S. Hydrogels with Reversible Mechanics to Probe Dynamic Cell Microenvironments. *Angew. Chemie - Int. Ed.* **2017**, *56* (40), 12132–12136.

(6) Lambert, C. R.; Nijsure, D.; Huynh, V.; Wylie, R. G. Hydrogels with Reversible Chemical Environments for in Vitro Cell Culture. *Biomed. Mater.* **2018**, *13* (4), 045002.

(7) Wylie, R. G.; Ahsan, S.; Aizawa, Y.; Maxwell, K. L.; Morshead, C. M.; Shoichet, M. S. Spatially Controlled Simultaneous Patterning of Multiple Growth Factors in Three-Dimensional Hydrogels. *Nat. Mater.* **2011**, *10* (10), 799–806.

(8) Choi, S. H.; Kim, Y. H.; Hebisch, M.; Sliwinski, C.; Lee, S.; D'Avanzo, C.; Chen, H.; Hooli, B.; Asselin, C.; Muffat, J.; et al. A Three-Dimensional Human Neural Cell Culture Model of Alzheimer's Disease. *Nature* **2014**, *515* (7526), 274–278.

(9) Bertassoni, L. E.; Cardoso, J. C.; Manoharan, V.; Cristino, A. L.; Bhise, N.

S.; Araujo, W. A.; Zorlutuna, P.; Vrana, N. E.; Ghaemmaghami, A. M.; Dokmeci, M. R.; et al. Direct-Write Bioprinting of Cell-Laden Methacrylated Gelatin Hydrogels. *Biofabrication* **2014**, *6* (2), 024105.

(10) Murphy, S. V.; Atala, A. 3D Bioprinting of Tissues and Organs. *Nat. Biotechnol*. **2014**, *32* 773–785.

(11) Jiang, Y.; Chen, J.; Deng, C.; Suuronen, E. J.; Zhong, Z. Click Hydrogels, Microgels and Nanogels: Emerging Platforms for Drug Delivery and Tissue Engineering. *Biomaterials*. **2014**, *35* (18), 4969–4985.

(12) Stephan, S. B.; Taber, A. M.; Jileaeva, I.; Pegues, E. P.; Sentman, C. L.; Stephan, M. T. Biopolymer Implants Enhance the Efficacy of Adoptive T-Cell Therapy. *Nat. Biotechnol.* **2015**, *33* (1), 97–101.

(13) Rodell, C. B.; Kaminski, A. L.; Burdick, J. A. Rational Design of Network Properties in Guest-Host Assembled and Shear-Thinning Hyaluronic Acid Hydrogels. *Biomacromolecules* **2013**, *14* (11), 4125–4134.

(14) Gupta, D.; Tator, C. H.; Shoichet, M. S. Fast-Gelling Injectable Blend of Hyaluronan and Methylcellulose for Intrathecal, Localized Delivery to the Injured Spinal Cord. *Biomaterials* **2006**, *27* (11), 2370–2379.

(15) Ruel-Gariépy, E.; Leroux, J.C. In Situ-Forming Hydrogels - review of Temperature-Sensitive Systems. *Eur. J. Pharm. Biopharm.* **2004**, *58* (2), 409–426.

(16) Zou, H.; Guo, W.; Yuan, W. Supramolecular Hydrogels from Inclusion Complexation of α-Cyclodextrin with Densely Grafted Chains in Micelles for Controlled Drug and Protein Release. *J. Mater. Chem. B* **2013**, *1* (45), 6235.

(17) Zhang, L.; Cao, Z.; Bai, T.; Carr, L.; Ella-Menye, J.-R.; Irvin, C.; Ratner, B. D.; Jiang, S. Zwitterionic Hydrogels Implanted in Mice Resist the Foreign-Body Reaction. *Nat. Biotechnol.* **2013**, *31* (6), 553–556.

(18) Chung, L.; Maestas, D. R.; Housseau, F.; Elisseeff, J. H. Key Players in the Immune Response to Biomaterial Scaffolds for Regenerative Medicine. *Adv. Drug Deliv. Rev.* **2017**, *114*, 184–192.

(19) Ratner, B. D. A Pore Way to Heal and Regenerate: 21st Century Thinking on Biocompatibility. *Regen. Biomater.* **2016**, *3* (2), rbw006.

(20) Vegas, A. J.; Veiseh, O.; Doloff, J. C.; Ma, M.; Tam, H. H.; Bratlie, K. M.; Li, J.; Bader, A. R.; Langan, E.; Olejnik, K.; et al. Combinatorial Hydrogel Library Enables Identification of Materials That Mitigate the Foreign Body Response in Primates. *Nat. Biotechnol.* **2016**, *34* (3), 345–352.

(21) Madden, L. R.; Mortisen, D. J.; Sussman, E. M.; Dupras, S. K.; Fugate, J. A.; Cuy, J. L.; Hauch, K. D.; Laflamme, M. A.; Murry, C. E.; Ratner, B. D. Proangiogenic Scaffolds as Functional Templates for Cardiac Tissue Engineering. *Proc. Natl. Acad. Sci. U. S. A.* **2010**, *107* (34), 15211–15216.

(22) Veiseh, O.; Doloff, J. C.; Ma, M.; Vegas, A. J.; Tam, H. H.; Bader, A. R.; Li, J.; Langan, E.; Wyckoff, J.; Loo, W. S.; et al. Size- and Shape-Dependent Foreign Body Immune Response to Materials Implanted in Rodents and Non-Human Primates. *Nat. Mater.* **2015**, *14* (6), 643–651.

(23) Rodriguez, P. L.; Harada, T.; Christian, D. a; Pantano, D. a; Tsai, R. K.; Discher, D. E. Minimal "Self" Peptides That Inhibit Phagocytic Clearance and Enhance Delivery of Nanoparticles. *Science* **2013**, *339* (6122), 971–975.

(24) Swartzlander, M. D.; Barnes, C. A.; Blakney, A. K.; Kaar, J. L.; Kyriakides, T. R.; Bryant, S. J. Linking the Foreign Body Response and Protein Adsorption to PEG-Based Hydrogels Using Proteomics. *Biomaterials* **2015**, *41*, 26–36.

(25) Jain, P.; Hung, H. C.; Lin, X.; Ma, J.; Zhang, P.; Sun, F.; Wu, K.; Jiang, S. Poly(Ectoine) Hydrogels Resist Nonspecific Protein Adsorption. *Langmuir* **2017**, *33* (42), 11264–11269.

(26) Chandorkar, Y.; Krishnamurthy, R.; Basu, B. The Foreign Body Response Demystified. *ACS Biomater. Sci. Eng.* **2018**, in press. DOI: 10.1021/acsbiomaterials.8b00252

(27) Wang, W.; Lu, Y.; Xie, J.; Zhu, H.; Cao, Z. A Zwitterionic Macro-Crosslinker for Durable Non-Fouling Coatings. *Chem. Commun.* **2016**, *52*

(25), 4671-4674.

(28) Cao, B.; Tang, Q.; Li, L.; Humble, J.; Wu, H.; Liu, L.; Cheng, G. Switchable Antimicrobial and Antifouling Hydrogels with Enhanced Mechanical Properties. *Adv. Healthc. Mater.* **2013**, *2* (8), 1096-1102.

(29) Ladd, J.; Zhang, Z.; Chen, S.; Hower, J. C.; Jiang, S. Zwitterionic Polymers Exhibiting High Resistance to Nonspecific Protein Adsorption from Human Serum and Plasma. *Biomacromolecules* **2008**, *9* (5), 1357-1361.

(30) Liu, S.; Jiang, S. Zwitterionic Polymer-Protein Conjugates Reduce Polymer-Specific Antibody Response. *Nano Today* **2016**, *11* (3), 285–291.

(31) Zhang, P.; Sun, F.; Tsao, C.; Liu, S.; Jain, P.; Sinclair, A.; Hung, H.-C.; Bai, T.; Wu, K.; Jiang, S. Zwitterionic Gel Encapsulation Promotes Protein Stability, Enhances Pharmacokinetics, and Reduces Immunogenicity. *Proc. Natl. Acad. Sci. U. S. A.* **2015**, *112* (39), 12046–12051.

(32) Kamata, H.; Kushiro, K.; Takai, M.; Chung, U. Il; Sakai, T. Non-Osmotic Hydrogels: A Rational Strategy for Safely Degradable Hydrogels. *Angew. Chemie - Int. Ed.* **2016**, *55* (32), 9282–9286.

(33) Kamata, H.; Akagi, Y.; Kayasuga-Kariya, Y.; Chung, U.; Sakai, T. "Nonswellable" Hydrogel Without Mechanical Hysteresis. *Science* **2014**, *343* (6173), 873–875.

(34) Carr, L. R.; Xue, H.; Jiang, S. Functionalizable and Nonfouling

Zwitterionic Carboxybetaine Hydrogels with a Carboxybetaine Dimethacrylate Crosslinker. *Biomaterials* **2011**, *32* (4), 961-968.

(35) Hoffman, A. S. Hydrogels for Biomedical Applications. *Adv. Drug Deliv. Rev.* **2012**, *64*, 18–23.

(36) Smeets, N. M. B.; Bakaic, E.; Patenaude, M.; Hoare, T. Injectable and Tunable Poly(Ethylene Glycol) Analogue Hydrogels Based on Poly(Oligoethylene Glycol Methacrylate). *Chem. Commun.* **2014**, *50*, 3306–3309.

(37) Nimmo, C. M.; Owen, S. C.; Shoichet, M. S. Diels-Alder Click Cross-Linked Hyaluronic Acid Hydrogels for Tissue Engineering. *Biomacromolecules* **2011**, *12* (3), 824-830.

(38) Nair, D. P.; Podgórski, M.; Chatani, S.; Gong, T.; Xi, W.; Fenoli, C. R.; Bowman, C. N. The Thiol-Michael Addition Click Reaction: A Powerful and Widely Used Tool in Materials Chemistry. *Chem. Mater.* **2014**, *26* (1), 724–744.

(39) Hodgson, S. M.; Bakaic, E.; Stewart, S. A.; Hoare, T.; Adronov, A. Properties of Poly(Ethylene Glycol) Hydrogels Cross-Linked via Strain-Promoted Alkyne-Azide Cycloaddition (SPAAC). *Biomacromolecules* **2016**, *17* (3), 1093–1100.

(40) DeForest, C. A.; Anseth, K. S. Cytocompatible Click-Based Hydrogels

with Dynamically Tunable Properties through Orthogonal Photoconjugation and Photocleavage Reactions. *Nat. Chem.* **2011**, *3*, 925-931.

(41) Brudno, Y.; Pezone, M. J.; Snyder, T. K.; Uzun, O.; Moody, C. T.; Aizenberg, M.; Mooney, D. J. Replenishable Drug Depot to Combat Post-Resection Cancer Recurrence. *Biomaterials* **2018**, *178*, 373-382.

(42) Madl, C. M.; Katz, L. M.; Heilshorn, S. C. Bio-Orthogonally Crosslinked, Engineered Protein Hydrogels with Tunable Mechanics and Biochemistry for Cell Encapsulation. *Adv. Funct. Mater.* **2016**, *26* (21), 3612–3620.

(43) Huynh, V.; Wylie, R. G. Competitive Affinity Release for Long-Term Delivery of Antibodies from Hydrogels. *Angew. Chemie - Int. Ed.* **2018**, *57* (13), 3406–3410.

(44) Cao, Z.; Yu, Q.; Xue, H.; Cheng, G.; Jiang, S. Nanoparticles for Drug Delivery Prepared from Amphiphilic PLGA Zwitterionic Block Copolymers with Sharp Contrast in Polarity between Two Blocks. *Angew. Chemie - Int. Ed.* **2010**, *49* (22), 3771–3776.

(45) Bai, T.; Liu, S.; Sun, F.; Sinclair, A.; Zhang, L.; Shao, Q.; Jiang, S. Zwitterionic Fusion in Hydrogels and Spontaneous and Time-Independent Self-Healing under Physiological Conditions. *Biomaterials* **2014**, *35* (13), 3926-3933.

(46) Ashley, G. W.; Henise, J.; Reid, R.; Santi, D. V. Hydrogel Drug Delivery System with Predictable and Tunable Drug Release and Degradation Rates. *Proc. Natl. Acad. Sci. U. S. A.* **2013**, *110* (6), 2318–2323.

(47) Xiao, S.; Ren, B.; Huang, L.; Shen, M.; Zhang, Y.; Zhong, M.; Yang, J.; Zheng, J. Salt-Responsive Zwitterionic Polymer Brushes with Anti-Polyelectrolyte Property. *Curr. Opin. Chem. Eng.* **2018**, *19*, 86–93.

(48) Shao, Q.; Mi, L.; Han, X.; Bai, T.; Liu, S.; Li, Y.; Jiang, S. Differences in Cationic and Anionic Charge Densities Dictate Zwitterionic Associations and Stimuli Responses. *J. Phys. Chem. B* **2014**, *118* (24), 6956–6962.

(49) Woodfield, P. A.; Zhu, Y.; Pei, Y.; Roth, P. J. Hydrophobically Modified Sulfobetaine Copolymers with Tunable Aqueous UCST through Postpolymerization Modification of Poly(Pentafluorophenyl Acrylate). *Macromolecules* **2014**, *47* (2), 750–762.

(50) Patenaude, M.; Smeets, N. M. B.; Hoare, T. Designing Injectable, Covalently Cross-Linked Hydrogels for Biomedical Applications. *Macromol. Rapid Commun*. **2014**, *35* (6), 598-617.

(51) Zhao, W.; Zhu, Y.; Zhang, J.; Xu, T.; Li, Q.; Guo, H.; Zhang, J.; Lin, C.; Zhang, L. A Comprehensive Study and Comparison of Four Types of Zwitterionic Hydrogels. *J. Mater. Sci.* **2018**, *53 (19), 13813-13825.*

(52) Sinclair, A.; O'Kelly, M. B.; Bai, T.; Hung, H. C.; Jain, P.; Jiang, S. Self-

Healing Zwitterionic Microgels as a Versatile Platform for Malleable Cell Constructs and Injectable Therapies. *Adv. Mater.* **2018**, *30* (39), 1803087.

(53) Saha, K.; Keung, A. J.; Irwin, E. F.; Li, Y.; Little, L.; Schaffer, D. V.; Healy, K. E. Substrate Modulus Directs Neural Stem Cell Behavior. *Biophys. J.* **2008**, *95* (9), 4426-4438.

(54) Leipzig, N. D.; Shoichet, M. S. The Effect of Substrate Stiffness on Adult Neural Stem Cell Behavior. *Biomaterials* **2009**, *30* (36), 6867–6878.

(55) Sun, S.; Wu, P. On the Thermally Reversible Dynamic Hydration Behavior of Oligo(Ethylene Glycol) Methacrylate-Based Polymers in Water. *Macromolecules* **2013**, *46* (1), 236–246.

(56) Magnusson, J. P.; Khan, A.; Pasparakis, G.; Saeed, A. O.; Wang, W.; Alexander, C. Ion-Sensitive "Isothermal" Responsive Polymers Prepared in Water. *J. Am. Chem. Soc.* **2008**, *130* (33), 10852–10853.

(57) He, Y.; Shao, Q.; Tsao, H. K.; Chen, S.; Goddard, W. A.; Jiang, S. Understanding Three Hydration-Dependent Transitions of Zwitterionic Carboxybetaine Hydrogel by Molecular Dynamics Simulations. *J. Phys. Chem. B* **2011**, *115* (40), 11575-11580.

(58) Shao, Q.; Jiang, S. Molecular Understanding and Design of Zwitterionic Materials. *Adv. Mater.* **2015**, *27* (1), 15–26.

(59) Dong, D.; Li, J.; Cui, M.; Wang, J.; Zhou, Y.; Luo, L.; Wei, Y.; Ye, L.;

Sun, H.; Yao, F. In Situ “Clickable” Zwitterionic Starch-Based Hydrogel for 3D Cell Encapsulation. *ACS Appl. Mater. Interfaces* **2016**, *8* (7), 4442–4455.

(60) Dormidontova, E. E. Role of Competitive PEO-Water and Water-Water Hydrogen Bonding in Aqueous Solution PEO Behavior. *Macromolecules* **2002**, *35* (3), 987–1001.

(61) Van Durme, K.; Van Assche, G.; Nies, E.; Van Mele, B. Phase Transformations in Aqueous Low Molar Mass Poly(Vinyl Methyl Ether) Solutions: Theoretical Prediction and Experimental Validation of the Peculiar Solvent Melting Line, Bimodal LCST, and (Adjacent) UCST Miscibility Gaps. *J. Phys. Chem. B* **2007**, *111* (6), 1288–1295.

(62) Longenecker, R.; Mu, T.; Hanna, M.; Burke, N. A. D.; Stöver, H. D. H. Thermally Responsive 2-Hydroxyethyl Methacrylate Polymers: Soluble-Insoluble and Soluble-Insoluble-Soluble Transitions. *Macromolecules* **2011**, *44* (22), 8962–8971.

(63) Seuring, J.; Agarwal, S. Polymers with Upper Critical Solution Temperature in Aqueous Solution: Unexpected Properties from Known Building Blocks. *ACS Macro Lett.* **2013**, *2* (7), 597–600.

(64) Shimada, N.; Nakayama, M.; Kano, A.; Maruyama, A. Design of UCST Polymers for Chilling Capture of Proteins. *Biomacromolecules* **2013**, *14*

(5), 1452–1457.

(65) Huynh, V.; Jesmer, A. H.; Shoaib, M. M.; D'Angelo, A.; Rullo, A. F.; Wylie, R. Improved Efficacy of Antibody Cancer Immunotherapeutics through Local and Sustained Delivery. *ChemBioChem* **2018**, in press. DOI: 10.1002/cbic.201800579.

3.7 Supplementary Information

3.7.1 Supplementary figures

Table S 3.1 Table summarizing the pCB-azide$_x$ and pCB-DBCO$_x$ polymers. Azide and DBCO mole fractions calculated from from ^{1}H NMR integrations.

Polymer	Azide mole fraction	Az: CB Units	DBCO mole fraction	DBCO: CB Units
pCB-Azide$_5$	5.0	1: 19	-	-
pCB-DBCO$_4$	-	-	4.3	1: 22.3
pCB-Azide$_{10}$	10.8	1: 8.3	-	-
pCB-DBCO$_{11}$	-	-	10.9	1: 8.2
pCB-Azide$_{16}$	15.9	1: 5.1	-	-
pCB-DBCO$_{17}$	-	-	16.5	1: 5.1
pCB-Azide$_{32}$	31.8	1: 2.1	-	-
pCB-DBCO$_{30}$	-	-	29.6	1: 2.4

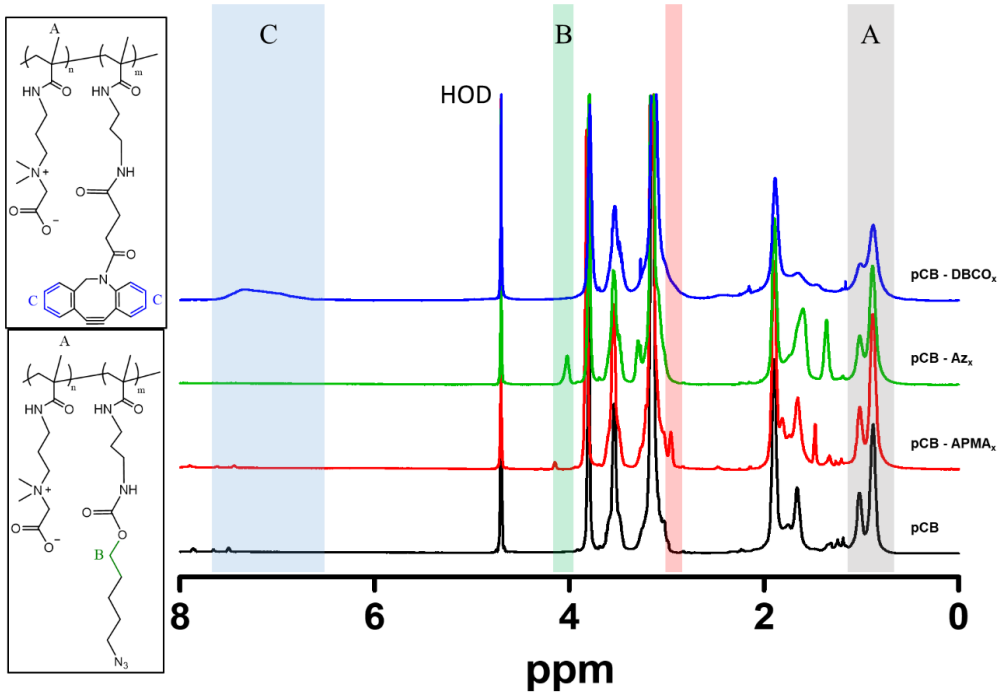

Figure S 3.1 ^{1}H NMR spectra of pCB copolymers compared against a reference pCB homopolymer. Shaded regions indicate unique resonances used for quantification of APMA (red), azide (green) and DBCO (blue). Black shaded region (A) highlights the methyl on the polymeric backbone integrating for 3 H. Integrations of APMA, azide or DBCO were compared to the methyl signal to determine mole fractions.

A

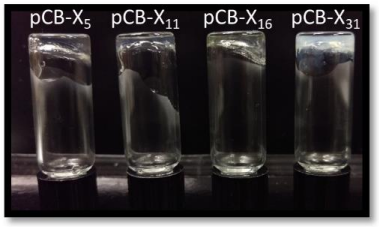

B

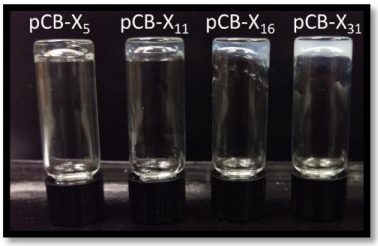

C

Gel	Weight %	Gelation time
pCB-X_5	10	1m 15s
pCB-X_{11}	10	2m 15s
pCB-X_{16}	10	15s
pCB-X_{31}	10	<5s
pCB-X_5	5	6m
pCB-X_{11}	5	>30m
pCB-X_{16}	5	3m
pCB-X_{31}	5	4m 15s

Figure S 3.2 (A) pCB-X gels at 10 wt % (B) pCB-X gels at 5 wt % (C) pCB-X gels and their corresponding gelation times.

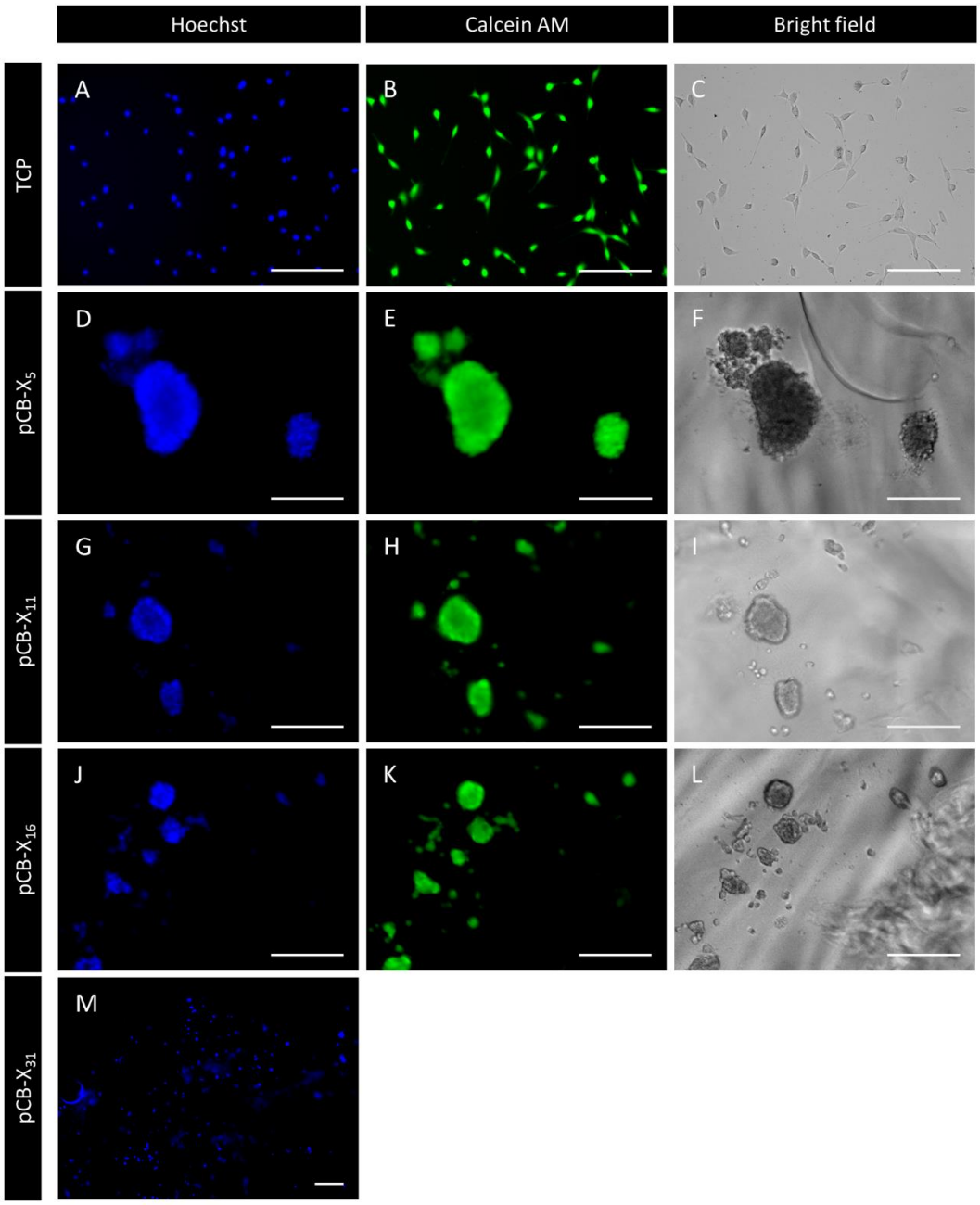

Figure S 3.3 Higher magnification images demonstrating non-specific NIH 3T3 fibroblast adhesion increased on pCB-X hydrogels with greater DBCO

content. Lower magnification images are presented in **Figure 3.7**. All scale bars represent 200 μm.

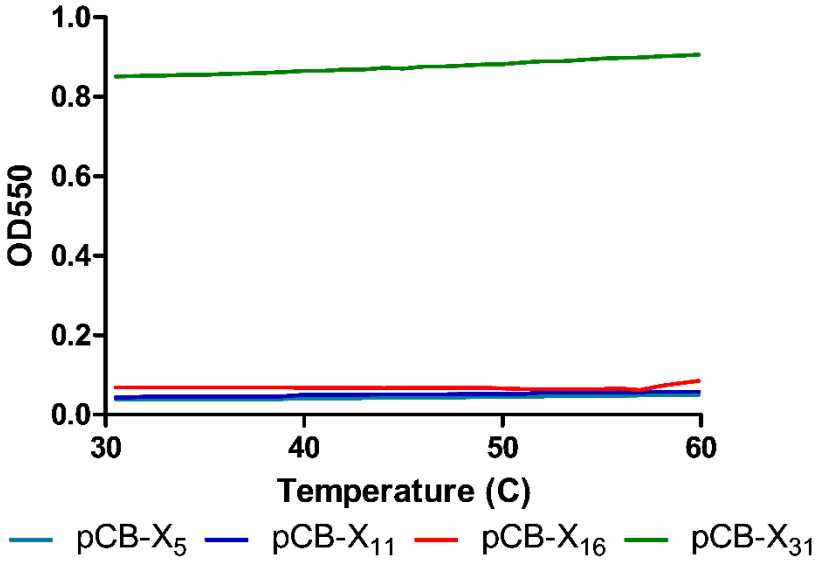

Figure S 3.4 Turbidity curves for pCB-X gels in PBS with increasing temperature. No significant change in turbidity was observed.

3.7.2 Supplementary Methods

PEGMA-X_{27} hydrogel synthesis. PEGMA-X_{27} was synthesized and characterized in a similar manner to pCB-X gels. Briefly, poly(ethylene glycol) methyl ether methacrylate (M_n 500, 1 g) and APMA-HCl (119 mg) was dissolved in 433 μL of water. Separately, 4-cyano-4-(phenylcarbonothioylthio)pentanoic acid (7.9 mg) and 4,4'-azobis(4-cyanovaleric acid) (1.6 mg) was dissolved in 217 μL of dioxane and added to the monomer solution. The pH of the solution was adjusted to 3 to 4. The solution was transferred to a Schlenk flask and degassed with three freeze-pump-thaw cycles under nitrogen. The reaction was then immersed in a 70°C oil bath and reacted overnight under constant stirring. The solution was then dialyzed against water (MWCO 12-14k) and lyophilized yielding PEGMA-$APMA_{27}$ as a pink oil (~900 mg). The APMA mole fraction was determine by proton NMR.

PEGMA-$APMA_{27}$ (300 mg) was dissolved in 5 mL of dry DMSO. Triethylamine (400 μL) and NHS-DBCO (280 mg) was added and reacted overnight under nitrogen at room temperature. The reaction was then dialyzed against methanol followed by water and lyophilized to yield a white solid (~300 mg yield).

Separately, PEGMA-$APMA_{27}$ (300 mg) was dissolved in 5 mL of dry DMSO. Triethylamine (400 μL) and NHS-azide (227.8 mg) was added and

reacted overnight under nitrogen at room temperature. Similarly, the reaction was dialyzed against methanol and then water and lyophilized (~310 mg).

CHAPTER 4. DISPLACEMENT AFFINITY RELEASE OF ANTIBODIES FROM INJECTABLE HYDROGELS

Author's Preface:

The following chapter was published in *ACS Applied Materials and Interfaces* under the citation:

Huynh V, and Wylie RG. Displacement affinity release of antibodies from injectable hydrogels.

I was responsible for all the experimental design and execution in this chapter. Dr. Wylie, and I both contributed to the analysis of the results. I wrote the first draft of the manuscript and Dr. Wylie provided editorial input to generate the final draft of the paper.

4.1 Abstract

Current methods to tune release rates of therapeutic antibodies (Abs) for local delivery are complex and routinely require bioconjugations that may reduce Ab bioactivity. To rapidly tune release profiles of bioactive Abs, we developed a biophysical interaction system within a neutravidin modified poly(carboxybetaine) hydrogel (pCB-NT) that tunes release rates of desthiobiotinylated Abs (D-Abs) using a constant hydrogel and D-Ab combination. Herein, we delivered desthiobiotinylated bevacizumab (D-Bv), a recombinant humanized monoclonal IgG1 Ab for anti-angiogenic cancer therapies. D-Bv's high affinity for pCB-NT (K_D $7.8x10^{-10}$ M; $t_{1/2}$ ~ 2 h) produces a slow D-Bv release rate (~ 5 ng d^{-1}) that is increased by the dissolution of hydrogel encapsulated biotin derivative pellets, which displaces D-Bv from pCB-NT binding sites. In contrast to traditional affinity systems, displacement affinity release of Abs (DARA) does not require Ab or hydrogel modifications for each unique release rate. D-Bv release rates were tuned by simply altering the total biotin derivative concentration; the effective first order (k_{eff}) and mass per day release rates were tuned 25 and 8-fold, respectively. Local surface plasmon resonance (LSPR) and bio-layer interferometry (BLI) confirmed D-Bv binding affinity for the corresponding ligand and Fc receptor, demonstrating the biophysical interaction system is amenable to anti-cancer Abs for receptor or cytokine blockade and immune cell recruitment to cancer cells.

Keywords: Biophysical interaction, displacement affinity release, tunable release, therapeutic antibodies, zwitterionic hydrogels.

4.2 Introduction

New cancer therapies selectively target antigens for cytokine/receptor blockade or immune cell recruitment, which can be achieved using antibodies (Abs) that act as inhibitors[1,2] or bivalent molecules for immune cell localization[3] and activation on cancer cells.[4,5] Although Abs demonstrate high in vitro potency, clinical trials indicate low efficacy against solid tumors due to poor tumor uptake, which necessitates frequent high-dose (> 1 g) intravenous (IV) infusions[6,7] that lead to fatal systemic side effects (e.g. cytokine release syndrome). To maintain effective tumor Ab concentrations without systemic toxicity, we require vehicles that sustain intra- or peritumoral Ab release after local injection.[8–10] Because different disease states will require unique therapeutic concentrations, release rates must be tuned to achieve maximum Ab efficacy for each tumor.[11] Therefore, we require injectable vehicles that tune Ab release without hindering anti-cancer activities.[12,13]

In situ gelling hydrogels localize Ab therapeutics at disease sites to bypass transport barriers and improve tumor uptake.[12,14] For example, when an Ab for checkpoint inhibition (anti-PD1) was intratumorally injected within a poly(vinyl alcohol) hydrogel, the survival rate in a melanoma mouse model improved by 50% over IV injections at 40 d.[15] Hydrogels should be composed of low-fouling polymers with limited tissue interactions to minimize adverse events (e.g. inflammation, tissue damage) and maintain Ab bioactivity.[16] Poly(carboxybetaine) (pCB) hydrogels are ideal for local Ab release due to its strong hydration shell that limits nonspecific interactions[17]; pCB gels have also been shown to improve the stability of encapsulated enzymes (e.g. uricase, organophosphorous hydrolase and chymotrypsin) while reducing their immunogenicity.[18–20] Furthermore, pCB hydrogels did not elicit a foreign body response (FBR) in a 3-month in vivo study.[21] We previously developed a hydrogel composed of CB copolymers that is injectable, and low-fouling; the hydrogel in situ crosslinks via strain-promoted alkyne-azide cycloaddition (SPAAC).[22] Although useful for initial Ab localization, hydrogels without a control delivery mechanism rapidly release Abs in a few days,[23] which may not be sufficient for complete tumor eradication.

To rapidly achieve different Ab release profiles, we require a system with: 1) different release rates using the same Ab and hydrogel combination; 2) limited Ab modification to retain inhibitor or bivalent activity; and, 3) an in situ gelling,

low-fouling hydrogel that maintains Ab activity. To this end, we developed **d**isplacement **a**ffinity **r**elease for **a**ntibodies (DARA), a 3-component biophysical release mechanism for desthiobiotinylated Abs (D-Abs) from neutravidin (NT) modified pCB hydrogels (pCB-NT) where release rates are controlled by the dissolution of encapsulated solid biotin derivative pellets (**Figure 4.1**). The sparingly soluble biotin derivative pellets dissolve over time and displace D-Ab from NT, release rates are controlled by varying pellet concentration in the hydrogel; higher biotin derivative pellet concentrations result in greater total surface area for dissolution, which increases the rate of biotin derivative dissolution and D-Ab release rates from the hydrogel. We have previously determined that the dissolution of oleylbiotin and hexadecylbiotin pellets provide appropriate soluble concentrations for the competitive displacement of streptavidin from agarose gels modified with desthiobiotin;[23] less hydrophobic biotin derivatives, such as octylbiotin, resulted in complete streptavidin displacement,[23] which leads to uncontrolled burst release profiles. NT was selected for its neutral charge that minimizes non-specific interactions compared to charged avidin and streptavidin. Moreover, NT is less immunogenic than avidin and streptavidin according to cytokine release assays (CRAs) in whole rat blood.[24] Upon exposure to whole blood of Sprague-Dawley rats, NT delivery complexes stimulated less cytokine production than avidin and streptavidin complexes. The pCB hydrogel forms through biorthogonal SPAAC crosslinking for in situ gelation (**Figure 4.2**), making it injectable for local delivery applications.[22]

In this study, we released desthiobiotinylated bevacizumab (D-Bv), an anti-angiogenic Ab that binds and inhibits vascular endothelial growth factor 165 (VEGF) for cancer treatments.[25] Bv is a recombinant humanized IgG1 Ab, and therefore acts as a model for other IgG1 antibody therapeutics; humanized Abs only differ in the complementarity determining region (CDR). As of 2018, 18 IgG1 antibodies have been approved by the Food and Drug Administration (FDA) for the treatment of cancer.[26]

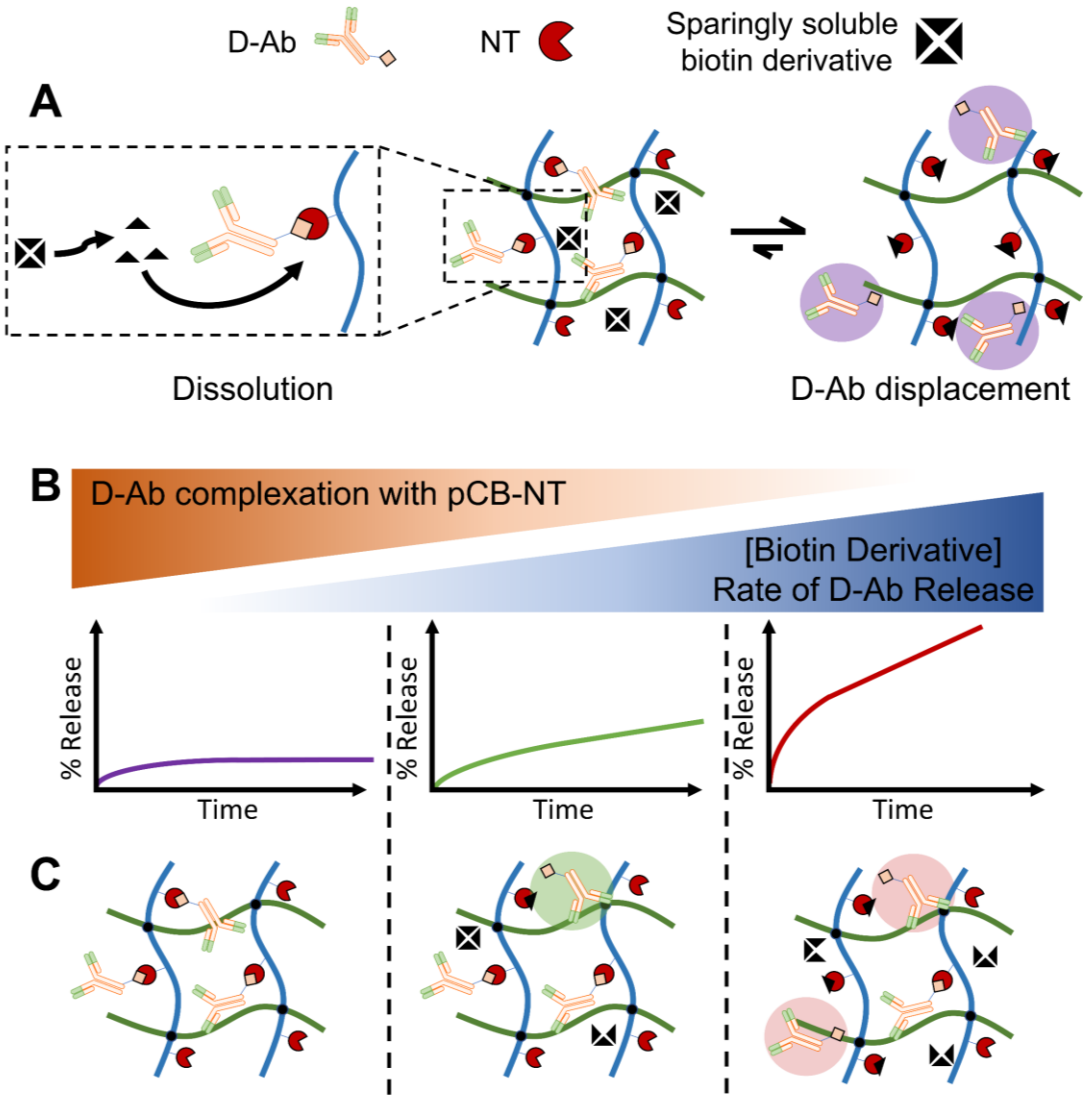

Figure 4.1 DARA mechanism: controlled D-Ab release from pCB-NT hydrogels tuned by dissolution of biotin derivative pellets. (A) Dissolution of hydrogel encapsulated solid biotin derivative pellets displaces D-Ab from pCB-NT binding sites, which increases the rate of D-Ab release from pCB-NT hydrogels. (B) D-Ab release rates are tuned by increasing the concentration of

sparingly soluble biotin derivative pellets encapsulated in the hydrogel. Higher concentrations of biotin derivative pellets decrease D-Ab complexation with pCB-NT and increase D-Ab release rates. (C) Schematic showing the displacement and release of D-Abs with increasing concentrations of encapsulated biotin derivative pellets.

4.3 Materials and methods

4.3.1 Materials. 4-Cyano-4-(phenylcarbonothioylthio)pentanoic acid, 4,4'-azobis(4-cyanovaleric acid), triethylamine, desthiobiotin, biotin, N-hydroxysuccinimide (NHS), 4-hydroxyazobenzne-2-carboxylic acid (HABA), HABA/Avidin solution (0.3 mM HABA, 0.45 mg mL^{-1} avidin, 0.3 M NaCl, 0.01 M HEPES, 0.01 M $MgCl_2$, 0.02 wt% NaN_3), agarose (Ag) and bovine serum albumin (BSA), lipopolysaccharide (LPS) were purchased from Sigma Aldrich (Oakville, ON, Canada). N-(3-aminopropyl)methacrylamide hydrochloride (APMA) was purchased from Polysciences, Inc. (Warrington, PA, USA). 3-(3-dimethylaminopropyl)-1-ethyl-carbodiimide hydrochloride (EDC-HCl) was obtained from Chem-Impex International Inc. (Wood Dale, IL, USA) Alexa Fluor 647 NHS ester, Alexa Fluor 488 NHS Ester, Hyclone DMEM-F12, Presto Blue reagent, calf bovine serum (CBS), fetal bovine serum (FBS), Neutravidin, $VEGF_{165}$, EZ-Link™ NHS-PEG4-biotin, ebioscience ELISA kits (IL-6, TNF-α,

IFNγ) were obtained from Thermo Fisher Scientific (Burlington, ON, Canada). EndoMax media was obtained from Wisent Bioproducts (St-Bruno, QC, Canada). Bevacizumab was obtained from the Boston Children's Hospital (BCH) pharmacy (Boston, MA, USA). LSPR chips and reagents were obtained from Nicoya Lifesciences (Kitchener, ON, Canada). Dialysis membranes were purchased from Spectrum Labs (Rancho Dominguez, CA, USA). 6-azidohexyl-succinimidyl carbonate (NHS-azide), carboxybetaine, oleylbiotin pellets, and hexadecylbiotin pellets were synthesized according previously published procedures.[22,23]

4.3.2 pCB hydrogel synthesis. pCB hydrogel precursors were synthesized according to previously established procedures.[22] Briefly, poly(carboxybetaine-co-aminopropyl methacrylamide) (pCB-APMA) was first synthesized using RAFT polymerization. To a Schlenk flask, CB monomer (1.5 g, 6.6 mmol) and APMA-HCl (11.8 mg, 6.6 μmol) were dissolved in 1 M acetate buffer pH 5.2. Separately, 4-Cyano-4-(phenylcarbonothioylthio)pentanoic acid (4.2 mg, 1.5 μmol) and 4,4'-azobis(4-cyanovaleric acid) (1.4 mg, 3 μmol) was dissolved in dioxane and added to the monomer solutions resulting in a 1 M monomer (CB + APMA) solution of 5:1 acetate buffer to dioxane. pH was then adjusted between 3 to 4. The solution was transferred to a Schlenk flask and degassed with three freeze-pump-thaw cycles under nitrogen. The reaction vessel was then immersed in a 75 °C oil bath and reacted for 1 d under constant stirring. The solution was then dialyzed against water and lyophilized, yielding a pink powder (1.2 g).

pCB-APMA polymers were further functionalized with azide or DBCO moieties. 500 mg of pCB-APMA was dissolved in 5 mL of dry MeOH with 50 μL (0.50 mmol) of triethylamine. Subsequently, NHS-azide (14 mg, 0.05 mmol) or NHS-DBCO (20 mg, 0.05 mmol) was added and reacted overnight under N_2 at room temperature. Polymers were then precipitated with 45 mL diethyl ether, dried and dissolved in 10-15 mL of deionized water. The aqueous solution was then extracted twice with ~ 20 mL dichloromethane (DCM) and the aqueous layer was then dialyzed against water for 1 d with 3 exchanges (MWCO 12-14k). The polymer was then lyophilized yielding a white powder (~ 473 mg). Polymer composition (% mol fraction; **Table S1**) were determined by ^{1}H NMR upon integrating the methylene peak in the backbone with unique resonances for pCB-Az (hydrogen adjacent to the carbamate bond) and pCB-DBCO (aromatic DBCO moieties) as identified in Figure S2.

4.3.3 NT-Az synthesis. 250 μL of 10 mg mL^{-1} NT dissolved in PBS was reacted overnight at room temperature with 8 μL of 10 mg mL^{-1} NHS-azide dissolved in DMF. NT-Az was then purified by automated size exclusion chromatography (SEC) on a GE Healthcare Superdex 200. The number of azide groups per NT was determined by MALDI mass spectrometry (Bruker UltrafleXtreme MALDI TOF/TOF in positive ion mode).

NT-Az was further modified with an Alexa Fluor 647 NHS ester dye. Briefly, 2 μL of 10 mg mL^{-1} Alexa-fluor 647 NHS ester dissolved in DMF was added to NT-Az (5 mg mL^{-1}) and incubated for 2 h at room temperature in the dark. The reaction mixture was dialyzed against PBS (MWCO 12k-14k) in the dark at 4 °C over 2 d with two exchanges.

4.3.4 D-Bv and B-Bv synthesis. Desthiobiotin (5 mg, 23 μmol), EDC-HCl (6.7 mg, 35 μmol) and NHS (3.2 mg, 28 μmol) was dissolved in 500 μL of N,N-dimethylformamide (DMF) and reacted overnight at room temperature under nitrogen. 11 μL of the reaction mixture (15 molar equivalents, 0.5 μmol) was added to 200 μL of 10 mg mL^{-1} bevacizumab (33 nmol) in borax buffer (0.1 M borax, 0.15 M NaCl, pH 8.5) and allowed to react overnight at room temperature. B-Bv was synthesized similarly. Briefly, biotin (5 mg, 20 μmol), EDC-HCl (5.9 mg, 31 μmol) and NHS (2.8 mg, 25 μmol) was dissolved in 500 μL DMF overnight and room temperature under nitrogen. 11 μL of the reaction mixture (15 molar equivalents, 0.5 μmol) was added to 200 μL of 10 mg mL^{-1} bevacizumab in borax buffer (0.1 M borax, 0.15 M NaCl, pH 8.5) and allowed to react overnight at room temperature.

D-Bv and B-Bv was then purified by automated SEC on a GE Healthcare Superdex 200. The number of desthiobiotin groups per Bv was determined using the HABA/Avidin reagent and calculated as per the provided protocol.

D-Bv was then further modified with Alexa Fluor 488 (AF-488) NHS ester. 2 μL of AF-488 NHS ester (10 mg mL^{-1}) in DMF was added to 100 μL D-Bv (5 mg mL^{-1}) in PBS and reacted for 3 h at room temperature in the dark. The reaction was then dialyzed against PBS (MWCO 12-14k) at 4 °C in the dark for 2 d with two exchanges yielding D-Bv-488. Fluorescently labelled B-Bv was synthesized in a similar manner.

4.3.5 SPR binding kinetic studies. Binding kinetics of D-Bv to VEGF and NT-Az was determined by localized surface plasmon resonance (LSPR) binding kinetics studies (Nicoya Lifesciences, Kitchener, ON, Canada). A carboxylated gold chip was modified with EDC and NHS, as per the manufacturers protocol. Using HBS-EP (Nicoya Lifesciences) running buffer, 100 μL of a 2 μg mL^{-1} VEGF solution was flowed (20 μL min^{-1}) across the chip. Remaining NHS-esters were reacted with ethanolamine. For D-Bv binding studies with VEGF, D-Bv was flowed across the VEGF modified chip at different concentrations (11, 33, 100, and 500 nM) and signal was recorded. The chip was regenerated using pH 1.5 glycine buffer (150 μL min^{-1}) between each D-Bv injection.

To determine the binding affinity of D-Bv to NT-Az, a 500 nM solution of D-Bv was flowed over a VEGF modified LSPR chip as previously described. After the chip was saturated with D-Bv, NT-Az was flowed across the same LSPR chip at different concentrations (10, 33, and 100 nM). After each run, pH 1.5 glycine buffer was used to disrupt D-Bv complexation with VEGF to

regenerate the VEGF modified chip. K_a and K_D constants were determined through the Tracedrawer software using a 1:1 binding model.

4.3.6 Bio-layer interferometry (BLI) binding kinetic studies. To demonstrate D-Bv's Fc domain bound CD16α receptors, a BLI (Octet Red 96) binding kinetics study was performed. Briefly, ThermoFischer EZ-Link NHS-PEG4-Biotin was dissolved in water (5 mg mL^{-1}) and 5 molar equivalents was added to an 8 mg mL^{-1} solution of CD16α dissolved in pH 6.5 PBS. Biotin modified CD16α was purified by buffer exchange with PBS using an Amicon Centrifugal filter (10 kDa MWCO).

Streptavidin modified BLI probes were wetted in kinetics buffer (PBS, 0.01% BSA, 0.01% Kathon, 0.002% Tween 20) for 15 min. Biotinylated CD16α was then immobilized onto the probe by incubating 200 nM of biotinylated CD16α with the probe in 1X kinetics buffer for 2 min. The probe was blocked with 5 wt % milk solution for 3 min. The probe was submerged in a 1 μM biotin solution to quench all remaining biotin binding sites. Probes were placed in a pH 2.2 10 mM glycine-HCl solution and subsequently immersed in kinetics buffer for 3 min to establish a baseline on the Octet Red 96 system. Probes were placed in solutions of D-Bv (0.63 μM - 5 μM) for 5 min to measure association and then kinetics buffer for 5 min to measure dissociation. K_D, k_{on} and k_{off} constants were estimated using Graphpad Prism 8 using a 1:1 binding model.

4.3.7 NT-Az immobilization and pCB-NT HABA displacement studies NT-Az-647 was incubated with pCB-DBCO (dissolved in PBS, 5 wt %) overnight at room temperature. 60 μL gels containing 5 wt % pCB and 0.1 mg mL^{-1} Neu-Az-647 were formed in a clear 96 well plate by adding 5 wt% pCB-Az to 5 wt % pCB-DBCO with conjugated NT-Az-647. After 30 min, gels were submerged in PBS and gel fluorescence (ex. 651 nm, em. 672 nm) and absorbance at 500 nm was tracked over time. Once fluorescence readings were stabilized, 60 μL of a 1 M HABA solution in PBS was then added over top the gels and incubated overnight. Fluorescence readings and A500 were read over time until A500 readings stabilized. Subsequently, 60 μL of 0.1 mg mL^{-1} desthiobiotin was then added over top the gels and fluorescence and A500 readings was tracked until equilibration.

4.3.8 D-Bv and B-Bv binding and displacement. pCB-DBCO (5 wt%) dissolved in PBS supplemented with 0.05 wt% BSA was incubated with NT-Az (0.1 mg mL^{-1}) overnight at room temperature. D-Bv (0.05 mg mL^{-1} or 0.025 mg mL^{-1}) or B-Bv (0.025 mg mL^{-1}) was then added and incubated overnight at room temperature in the dark.

60 μL 5 wt % pCB gels containing 0.1 mg mL^{-1} NT-Az and 50 μg mL^{-1} D-Bv or a combination of 25 μg mL^{-1} D-Bv and 25 μg mL^{-1} B-Bv were formed at the bottom of wells in a 96 well plate by adding pCB-Az (5 wt %) to the pCB-DBCO (5 wt %) protein solutions. Gels were formed for 30 min at room temperature in

the dark and initial fluorescent readings were taken (D-Bv: ex. 495 nm, em. 519 nm; B-Bv: ex. 651 nm, 672 nm). Gels were then immersed in PBS with 0.05 wt % BSA and fluorescence was tracked over time. Upon fluorescent reading stabilization, 200 μL of 0.1 mg mL^{-1} biotin dissolved in PBS with 0.05 wt % BSA was added over top the gels. Fluorescence readings were taken at specific time intervals and replenished with fresh 0.1 mg mL^{-1} biotin solutions after each reading.

4.3.9 D-Bv release assays. NT-Az and pCB-DBCO (5 wt %) in PBS with 0.05 wt % BSA was incubated overnight at room temperature. D-Bv-488 (50 μg mL^{-1}) was then added to the solution and incubated overnight at room temperature.

60 μL gels were then formed in the bottom of wells in a black 96 well plate by mixing the pCB-DBCO (5 wt %) protein solutions with pCB-Az (5 wt %) and a biotin derivative suspension in 0.05 wt % BSA in PBS. Gels were then incubated in the dark at room temperature for 1 h. Initial gel fluorescence readings were taken on a Biotek Cytation 5 plate reader (ex. 495 nm, em. 519 nm). 200 μL of 0.05 wt % BSA PBS solutions was then pipetted over top the gels. Supernatants (solutions on top of the gels) were taken at specific time intervals and replenished with 0.05 wt % BSA PBS. Supernatant fluorescence was read using a Biotek Cytation 5 plate reader (ex. 495 nm, em. 519 nm) and D-Bv amount was determined using a calibration curve.

4.3.10 Displacement potential of oleylbiotin and hexadecylbiotin. Oleylbiotin and hexadecylbiotin pellets were suspended in 5 wt % pCB, 0.05 wt % BSA solutions at 800 μM in microcentrifuge tubes and agitated at room temperature. At specific time intervals, the suspension was pelleted through centrifugation (16 000 g for 15 min) and 200 μL of the supernatant was collected. The pellet was then resuspended upon addition of 200 μL of fresh 5 wt % pCB, 0.05 wt % BSA solution. The supernatants were frozen at -20°C until further use.

The supernatants were then filtered through a 0.2 μm filter and 100 μL of the solution was added to 300 μL of the HABA/Avidin reagent (0.3 mM HABA, 0.45 mg mL^{-1} avidin) and incubated for 5 min. A500 was then read using an Agilent Cary 100 UV Vis. A HABA/Avidin solution exposed to an excess of biotin (1 mg mL^{-1}, 4 mM), for complete HABA displacement, was used as a positive control for maximum change in A500. Oleylbiotin and hexadecylbiotin potential displacement was calculated by change in A500 divided by maximum change in A500 (from biotin displacement).

4.3.11 Cytotoxicity. NIH 3T3 fibroblasts in DMEM-F12 10% CBS (5000 cells/well in 75 μL) or human umbilical vein endothelial cells (HUVECs) in EndoMax with 20% FBS (10,000 cells/well in 75 μL), were seeded in a 96 well plate and incubated overnight at 37 °C 5% CO_2. Subsequently, 25 μL of individual DARA delivery components were added to screen cytotoxicity of the following solutions in PBS with their corresponding final concentrations: pCB-

DBCO (5 mg mL^{-1}), pCB-Az (5 mg mL^{-1}), pCB-APMA (5 mg mL^{-1}), D-Bv (0.1 mg mL^{-1}), B-Bv (0.1 mg mL^{-1}), NT-Az (0.1 mg mL^{-1}), oleylbiotin (1 mg mL^{-1}), hexadecylbiotin (1 mg mL^{-1}) and pCB-NT (5 mg mL^{-1} pCB-DBCO reacted with and 0.1 mg mL^{-1} of NT-Az overnight in PBS). Cells were then incubated at 37 °C 5% CO_2 for 24 h. For NIH 3T3's, 11 µL of Presto blue reagent was then added to each well and incubated at 37 °C 5% CO_2 for 30 min. For HUVECs, 11 µL of alamar blue was added to each well and incubated at 37 °C 5% CO_2 for 1.5 h. Fluorescence was read on a Biotek Cytation 5 plate and normalized to control wells (25 µL of PBS in 75 µL DMEM-F12 with 10% CBS or EndoMax with 20% FBS).

Separately, 5 wt% pCB gels with and without the DARA system (800 µM oleylbiotin, 0.05 mg mL^{-1} D-Bv, 0.1 mg mL^{-1} NT-Az) were formed in a 96 well plate and incubated overnight at 37 °C 5% CO_2. NIH 3T3 fibroblasts in DMEM-F12 10% CBS media (5000 cells in 100 µL) or HUVECs in EndoMax with 20% FBS (10,000 cells in 100 µL), were then seeded on top of the gels and incubated at 37 °C 5% CO_2 for 24 h. 11 µL of Presto Blue reagent was added to each well and incubated at 37 °C 5% CO_2 for 30 min. Fluorescence was read on a Biotek Cytation 5 plate reader (ex. 560 nm, em. 590 nm). Fluorescence values were then normalized to cells plated on pCB gels without the DARA system.

4.3.12 Non-specific cell adhesion to pCB gels. pCB_{16} (10 wt%), $pCB_{2.5}$ (5 wt%) and Ag (1 wt%) gels (60 µL) were formed on the bottom of a clear 96 well plate

and allowed to gel for 30 min at 4°C. NIH 3T3 fibroblasts in DMEM-F12 10% CBS media (5000 cells in 100 μL) or HUVECs in EndoMax 20% FBS (10,000 cells in 100 μL) were seeded on top of the gels and incubated at 37 °C 5% CO_2 for 24 h. Brightfield micrographs were acquired on a Biotek Cytation 5 imager.

4.3.13 Immunogenicity. Fresh heparinized whole human blood (1 mL; approval acquired from the Hamilton Integrated Research Ethics Board, Project Number 5822-T) was incubated with either LPS (10 ng mL^{-1}), pCB-DBCO (5 nM, 1 mg mL^{-1}), NT-Az (100 nM, 6.7 μg mL^{-1}), pCB-NT polymer (5 mM pCB-DBCO with 100 nM NT-Az) or pCB gels (100 μL 5 wt %) containing 100 nM NT-Az and 1 mg mL^{-1} hexadecylbiotin. Solutions were incubated for 24 h at 37 °C. Plasma was then isolated from the whole blood by centrifugation at 2000 g for 10 min and frozen until further use. IFNγ, TNFα and IL-6 concentrations in the isolated plasma were then quantified using eBioscience ELISA kits, according to the provided protocols.

4.3.14 Statistical Analyses. All samples were performed in triplicate and expressed as mean ± standard deviation. All statistical analyses were performed using GraphPad Prism 8. $p < 0.05$ is indicated by *, $p < 0.01$ by **, $p < 0.001$ by ***.

4.4 Results and Discussion

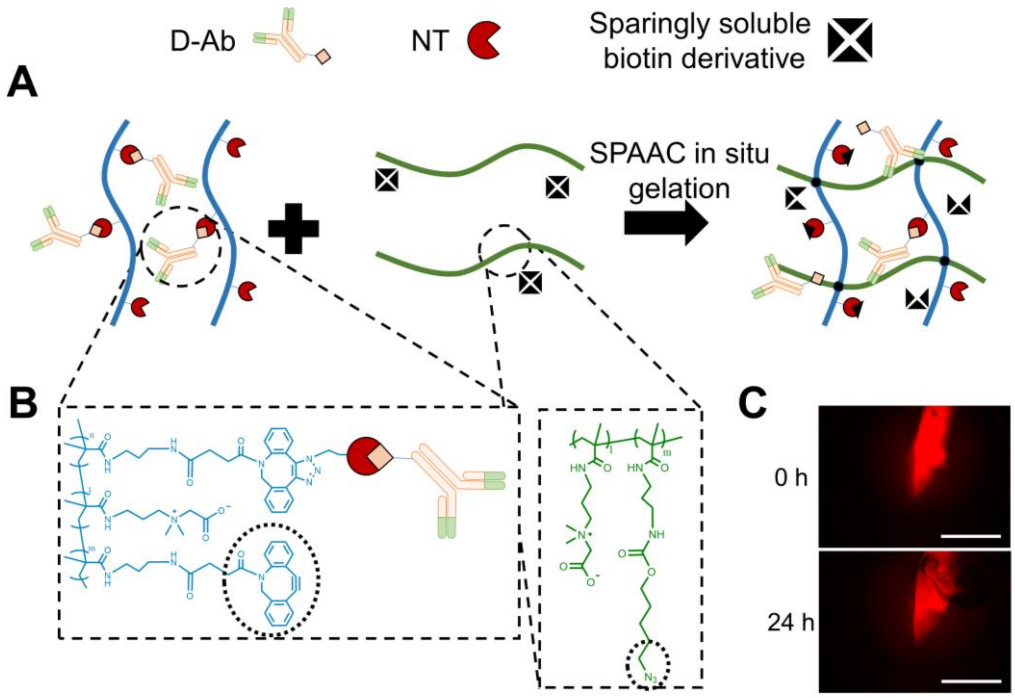

Figure 4.2 Preparation of pCB-NT hydrogels with encapsulated D-Bv and solid biotin derivative pellets. (A) pCB-DBCO (blue) modified with NT-Az was mixed with pCB-Az (green), D-Bv, and sparingly soluble biotin derivative pellets for in situ gelation. (B) Chemical structures of pCB-Az (green) and pCB-DBCO (blue) modified with NT-Az bound to D-Ab. Dashed circles highlight reactive strained alkyne and Az moieties for in situ crosslinking. (C) pCB-NT hydrogels with complete DARA systems are injectable. In situ gelling solutions of 10 µL 5 wt% pCB-NT (0.1 mg mL^{-1} fluorescent NT-Az) with the DARA system (800 µM hexadecylbiotin, 50 µg mL^{-1} D-Bv) were injected into 1 wt% agarose hydrogels using a syringe and 32 gauge needle. After 24 h, the localization of fluorescence

at the injection site and not throughout the agarose gels indicates the system is injectable. Non-gelling control injections without pCB-Az are presented in **Figure S 4.5**.

4.4.1 Synthesis of pCB-NT hydrogels for controlled release of D-Bv

We previously demonstrated that CB copolymers with < 5 mol% azide (Az) or dibenzocyclooctyne (DBCO) form in situ gelling, low-fouling pCB hydrogels.[22] Therefore, CB copolymers with 2.5 mol% Az (pCB-Az) and 2.3 mol% DBCO (pCB-DBCO) were synthesized for in situ gelation via strain promoted alkyne-azide cycloaddition (SPAAC); DBCOs were also used as immobilization sites for Az modified NT (NT-Az).

To prepare pCB-Az and pCB-DBCO, random copolymers of CB and N-(3-aminopropyl)methacrylamide (APMA) were first synthesized using reversible addition fragmentation transfer (RAFT) polymerization (**Figure S 4.1**), resulting in pCB-APMA (M_w 71 373 g mol^{-1}, M_n 65 404 g mol^{-1}, determined by gel permeation chromatography (GPC) calibrated with poly(ethylene glycol) (PEG) standards) with low dispersity (Đ = 1.09; **Table S 4.1A**). The M_W of pCB-APMA was selected to maximize CB content (~ 97.5 mol%) and retain low-fouling properties while maintaining sufficient amines for Az or DBCO derivatization for crosslinking and gelation. pCB-APMA amino groups were completely modified with N-hydroxysuccinimide ester (NHS) DBCO (NHS-DBCO) or Az (NHS-Az)

moieties to yield pCB-DBCO and pCB-Az copolymers, respectively (**Figure S 4.1**). ^{1}H NMR spectra of pCB-Az and pCB-DBCO (**Figure S 4.2**) determined Az and DBCO mole fractions of 2.5 mol% and 2.3 mol%, respectively (**Table S 4.1B**).

A single form of D-Bv was synthesized for all release experiments; the use of a D-Bv with a single functionalization degree avoids the re-modification of Bv for each unique release profile, which may decrease bioactivity. Bv was reacted with NHS-desthiobiotin to yield D-Bv with an average of 4.9 desthiobiotins per Bv, as determined by HABA/Avidin displacement assays (**Figure S 4.3**). For conjugation to pCB-DBCO prior to gelation with pCB-Az, NT was modified with NHS-Az to yield NT-Az with ~ 7.1 azides per NT, determined by MALDI MS (**Figure S 4.4**). Therefore, we synthesized single pCB-DBCO, pCB-Az, and D-Bv suitable for all release profiles in section 3.5.

To prepare in situ gelling hydrogels for controlled D-Bv release, pCB-DBCO was first modified with NT-Az and then D-Bv, which was subsequently mixed with a pCB-Az solution with biotin derivative pellets (**Figure 4.2**). Modification of pCB-DBCO with NT-Az at the studied concentrations did not influence hydrogel gelation time. A 200 µL mixture of 5 wt% pCB-Az with 800 µM hexadecylbiotin pellets and 50 µg mL^{-1} of D-Bv was mixed with 5 wt% pCB-DBCO modified with 0.1 mg mL^{-1} NT-Az (complete DARA system) for gelation in 9 min 45 sec according to gravitational flow analysis (**Figure S 4.5A**). To

demonstrate the delivery system is injectable, 10 µL of the same solution was injected into 1 wt% agarose gels after a 9 min pre-injection incubation in the syringe. To confirm gelation, NT-Az immobilized on pCB-DBCO was modified with Alexa Fluor 647 and fluorescent images were acquired at 0 and 24 h post-injection; fluorescence remained at the injection site, which indicates the system is in situ gelling and injectable (**Figure S 4.5B-C**). A control injection was performed without pCB-Az to prevent gelation (**Figure S 4.5D-E**). After 24 h, fluorescence was observed throughout the agarose hydrogel due to the diffusion of pCB-DBCO modified with fluorescent NT-Az.

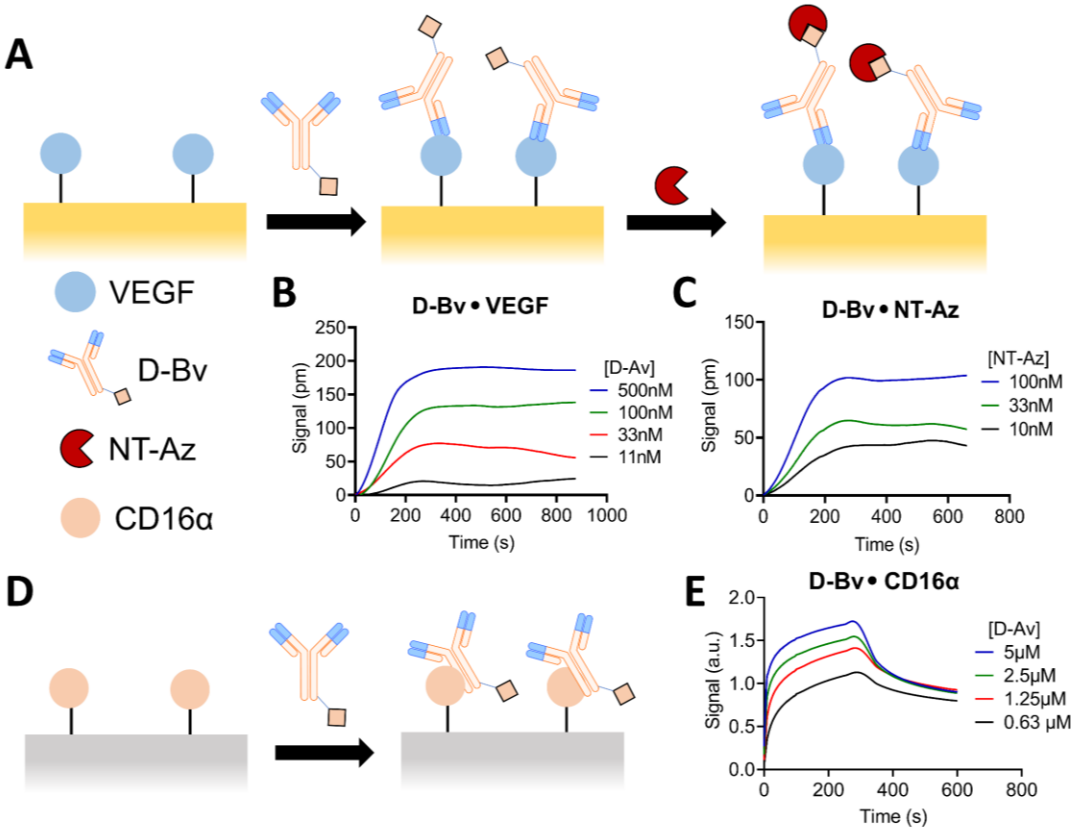

F

Interaction	k_{off} (s^{-1})	k_{on} ($M^{-1}s^{-1}$)	K_D (M)
D-Bv • VEGF	6.4×10^{-6}	2.9×10^{4}	2.2×10^{-10}
D-Bv • NT-Az	9.7×10^{-5}	1.2×10^{5}	7.8×10^{-10}
D-Bv • CD16α	7.1×10^{-3}	2.0×10^{4}	3.6×10^{-7}

Figure 4.3 D-Bv retains binding affinity for VEGF, NT-Az, and CD16α. (A) Schematic of D-Bv binding to VEGF immobilized on a gold LSPR sensor, followed by NT-Az binding to D-Bv. (B) LSPR sensorgram demonstrating concentration-dependent binding of D-Bv to VEGF modified gold sensors. (C) LSPR sensorgram demonstrating concentration-dependent binding of NT-Az to a VEGF gold sensor saturated with D-Bv. The long $t_{1/2}$ (~ 30 h) of the D-Bv/VEGF

complex allows for the characterization of the NT/D-Bv interaction. (D) Schematic of D-Bv binding to CD16α immobilized on a BLI sensor. (E) BLI sensorgram demonstrating concentration-dependent binding of D-Bv to CD16α modified surfaces, indicating the Fc portion of D-Bv is available for immune cell receptor binding. (F) k_{on}, k_{off} and K_D for D-Bv binding to VEGF, NT-Az and CD16α. Binding constants were calculated using a 1:1 binding model in Tracedrawer software (LSPR) and GraphPad Prism 8 (BLI).

4.4.2 LSPR and BLI determined binding kinetics of D-Bv for VEGF, NT-Az, and CD16α

To verify that desthiobiotinylation did not interfere with binding affinity for ligands and immune cell receptors, we studied the concentration-dependent binding of D-Bv to VEGF and CD16α, an FcγIII receptor for IgG1 Abs. The kinetics of D-Bv binding to NT-Az was also studied to characterize the Ab delivery system. Therefore, the association (k_{on}) and dissociation (k_{off}) rate constants for D-Bv binding to VEGF, NT-Az, and CD16α were determined. Limited steric inhibition should occur as desthiobiotinylation should be primarily on the Fc portion of the antibody.

Using a VEGF modified gold LSPR chip, D-Bv displayed concentration-dependent binding to VEGF (**Figure 4.3A-B**), with a calculated equilibrium dissociation constant (K_D) of 2.18 x 10^{-10} M (**Figure 4.3F**). Because of the slow dissociation of D-Bv from VEGF ($t_{1/2}$ ~ 30 h), NT-Az binding to D-Bv could be

followed on a VEGF LSPR chip pre-saturated with a 500 nM D-Bv solution (**Figure 4.3A**). Binding D-Bv to VEGF allowed for site-specific immobilization and sensor regeneration with pH 1.5 buffer, removing both D-Bv and NT-Az from the sensor. The required sequential injections (D-Bv and NT-Az) and continuous signal measurement was possible using the LSPR instrument but not readily achievable with BLI. NT-Az displayed concentration-dependent binding to desthiobiotin on D-Bv (**Figure 4.3C**), with a K_D of 7.8 x 10^{-10} M (**Figure 4.3F**). Due to proximity limitations, 1:1 binding was assumed for data processing because NT-Az is unlikely to bind multiple desthiobiotins on immobilized D-Bv. Furthermore, the use of excess NT-Az (~10 molar equivalents) minimized the probability for multivalent interactions. The binding affinity of D-Bv to VEGF and NT-Az was similar to previously published K_Ds (Bv – VEGF: 10^{-9} – 10^{-11} M; NT – desthiobiotin: 10^{-11}-10^{-13} M).[25,27,28]

Using CD16α modified surfaces for BLI detection, D-Bv showed concentration-dependent binding for CD16α (**Figure 4.3D-E**) with a calculated K_D of 3.6 x 10^{-7} M (**Figure 4.3F**) similar to previous reports for human IgG1s (7.2 x 10^{-7} M).[29] Therefore, the retained binding affinity for targeting ligands and immune cell Fc surface receptors indicates that desthiobiotin modification of Abs is tolerable for cytokine or receptor blockade (e.g. anti-angiogenesis, checkpoint inhibitors) and immune cell recruitment (e.g. antibody-dependent cellular toxicity (ADCC)). Desthiobiotin modification of IgG1 antibodies will not interfere with

bioactivity as demonstrated by the LSPR and BLI binding studies; the achieved degree of antibody functionalization with desthiobiotin is therefore suitable for delivery applications.

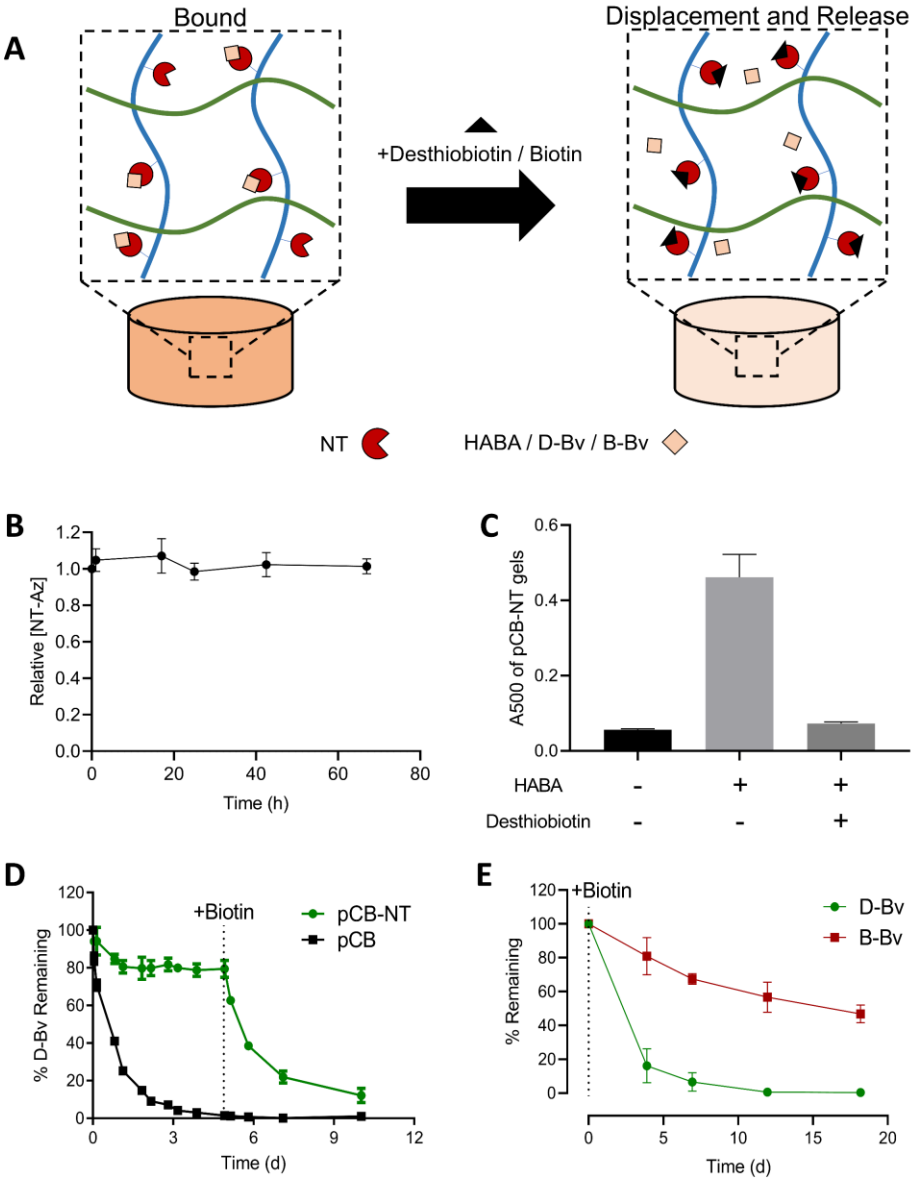

Figure 4.4 pCB-NT reversibly binds HABA and D-Bv for displacement by free desthiobiotin or biotin. (A) The addition of a competitive binder

(desthiobiotin or biotin) displaces and releases bound HABA, D-Bv or B-Bv from pCB-NT hydrogels. (B) After immobilization of fluorescent NT-Az (Alexa Fluor 647; 4 mg mL^{-1}), hydrogel fluorescence was tracked over 65 h. No significant change was observed indicating irreversible immobilization of NT-Az to pCB-DBCO in pCB-NT hydrogels (n = 3). (C) HABA binding to and displacement from pCB-NT was tracked A500; HABA increases in A500 upon NT binding. Without HABA, the gels showed minimal A500. After addition of HABA (0.5 M), an increase in A500 was observed due to NT binding. Addition of desthiobiotin (2.3×10^{-4} M) to HABA saturated pCB-NT gels, A500 decreased to background levels, indicating complete HABA displacement. (D) The fluorescence of pCB and pCB-NT gels with fluorescent D-Bv (333 nM) was followed over time after submersion in PBS. D-Bv was rapidly eliminated from pCB gels due to the lack of NT desthiobiotin binding sites. In contrast, ~ 80% of D-Bv remained in pCB-NT gels until submersion in a 410 μM biotin PBS solution, which rapidly displaced D-Bv from pCB-NT gels. (E) D-Bv released faster than B-Bv from pCB-NT gels submerged in PBS with 410 μM biotin, demonstrating B-Bv is less responsive to biotin mediated displacement due to its longer $t_{1/2}$.

4.4.3 Synthesis of pCB-NT gels and biotin mediated displacement of D-Bv

To achieve controlled release of D-Bv, the conjugation of NT-Az to pCB-DBCO should occur with 100% yield to avoid additional purification steps and

potential loss of NT-Az binding activity. To confirm complete NT-Az conjugation, fluorescent NT-Az (modified with Alexa Fluor 647) was first reacted with pCB-DBCO (5 wt%) before to the addition of pCB-Az to yield pCB-NT gels (5 wt%) with a final NT-Az concentration of 4 mg mL^{-1}. To ensure complete NT-Az conjugation, the fluorescence of pCB-NT gels submerged in PBS was temporally tracked; hydrogel fluorescence did not decrease over 65 h (**Figure 4.4B**), indicating complete conjugation of fluorescent NT-Az. We previously demonstrated that pCB gels with > 5 Az/DBCO mol% non-specifically bound cells,[22] which may hinder drug delivery applications. Because this study used pCB gels with ~2.5 Az/DBCO mol% with 4 mg mL^{-1} NT-Az, the immobilized NT-Az concentration can be increased to ~ 8 mg mL^{-1} by increasing Az/DBCO content to 5 mol%.

To demonstrate pCB-NT binds and releases biotin analogues, the reversible binding and competitive displacement of 4-Hydroxyazobenzene-2-carboxylic acid (HABA) was quantified (**Figure 4.4A, C**). HABA increases in absorbance at 500 nm (A500) upon binding NT (extinction coefficient of 35 500 M^{-1} cm^{-1}).[30] Addition of HABA (0.5 M; K_D ~ 10^{-6} M)[31] to pCB-NT gels resulted in an increase in A500 after equilibrium was reached. Subsequent addition of desthiobiotin ($2.3x10^{-4}$ M; K_D $7.8x10^{-10}$ M) returned A500 to background levels (**Figure 4.4C**), indicating complete displacement of HABA from pCB-NT. Therefore, conjugated NT in pCB-NT gels retained its ability to reversibly bind

and release biotin-like molecules. pCB-NT retains desthiobiotin binding and displacement capabilities.

To demonstrate biotin mediated displacement of D-Bv from pCB-NT gels, fluorescent D-Bv (modified with Alexa Fluor 647) was incorporated within pCB and pCB-NT gels, and gel fluorescence was tracked over time. The absence of NT for desthiobiotin complexation resulted in rapid D-Bv elimination from pCB gels when submerged in PBS (**Figure 4.4D**). In pCB-NT gels, ~80% of D-Bv (initial concentration of 3 mg ml^{-1}, **Figure S 4.6**) remained in the gel, indicating ~ 20% of D-Bv weakly bound pCB-NT (**Figure 4.4D, Figure S 4.6**). The remaining D-Bv did not release from pCB-NT until gels were submerged in PBS with 0.1 mg mL^{-1} biotin (**Figure 4.4D**), which displaced D-Bv from pCB-NT. The controlled displacement of D-Bv from pCB-NT gels demonstrates that the DARA method is suitable for biotin mediated displacement and release of D-Abs from hydrogels.

Because D-Bv release relies on biotin mediated displacement from pCB-NT gels, the $t_{1/2}$ of the D-Bv-NT interaction will contribute to displacement rates. To highlight the importance of the complex's $t_{1/2}$, we compared the displacement of fluorescent D-Bv and biotin modified Bv (B-Bv) from the same pCB-NT gels; D-Bv and biotin modified molecules have different $t_{1/2}$s of 2 h and ~ 1-4 d, respectively.[32] Immediately after gelation of pCB-NT with fluorescent D-Bv (Alexa Fluor 488; 0.025 mg mL^{-1}) and B-Bv (Alexa Fluor 647; 0.025 mg mL^{-1}), gels were submerged in PBS with 0.1 mg mL^{-1} of biotin. The release of D-Bv and

B-Bv was tracked by total gel fluorescence (**Figure 4.4E**). Due to its shorter $t_{1/2}$, D-Bv released faster than B-Bv from the hydrogel with effective first order release rates (k_{eff}s) of 4.3 x 10^{-1} d^{-1} and 4.1 x 10^{-2} d^{-1}, respectively (**Figure S 4.7**). The high concentration of free biotin (0.1 mg mL^{-1}) produces D-Bv and B-Bv release profiles that represent the maximum Ab release rate of each conjugate. Due to its long $t_{1/2}$, B-Ab release profiles cannot be tuned to occur in in less than multiple weeks. Therefore, D-Abs are more suitable for controlled release applications because its shorter $t_{1/2}$ allows for greater release rate tuning.

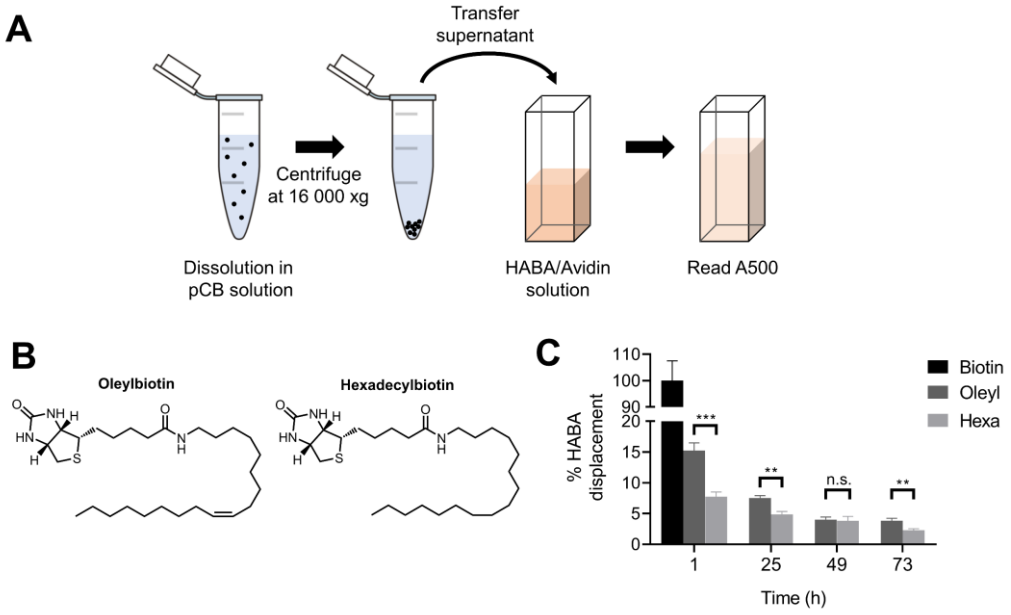

Figure 4.5 Displacement of HABA from avidin upon dissolution of biotin derivative pellets suspended in pCB solutions. (A) Oleylbiotin or hexadecylbiotin pellets were suspended and incubated in a 5 wt% pCB PBS solution. At different timepoints, suspensions were centrifuged to remove pellets,

supernatants were then transferred to HABA/Avidin solutions to measure HABA displacement from avidin by dissolved oleylbiotin or hexadecylbiotin. (B) Structures of oleylbiotin and hexadecylbiotin. (C) HABA displacement potential from oleylbiotin (Oleyl) and hexadecylbiotin (Hexa) pellet dissolution in 5 wt% pCB solutions over time. The percentage of displaced HABA was quantified by ΔA500 divided by maximum ΔA500 upon addition of excess free biotin, which represents 100% HABA displacement from avidin. Oleylbiotin pellets resulted in greater HABA displacement than hexadecylbiotin at 1, 25 and 73 h (mean + standard deviation, student's t-tests, n = 3).

4.4.4 Comparison of biotin derivative displacement potential

Two sparingly soluble biotin derivatives were studied to displace D-Bv from pCB-NT gels; oleylbiotin and hexadecylbiotin were synthesized by reacting the NHS ester of biotin with oleylamine and hexadecylamine, respectively, as previously described (**Figure 4.5B**).[23] Because the dissolution of biotin derivative pellets in pCB-NT hydrogels will determine D-Bv release rates and the presence of polymers influences dissolution,[33–35] we compared the displacement potential of solid oleylbiotin and hexadecylbiotin pellets (soluble + insoluble concentration was 800 μM) when suspended in a PBS solution of 5 wt% pCB (**Figure 4.5A**). Samples were centrifuged and supernatants were removed at 1, 25, 49 and 73 h for analysis with HABA/Avidin solutions to compare the relative HABA displacement potential from oleylbiotin and hexadecylbiotin pellet dissolution;

HABA displacement will result in a decrease in A500.[30] Results were standardized to HABA/Avidin solutions exposed to 1 mg mL^{-1} of unmodified biotin for complete HABA displacement, which quantifies the maximum change in A500 (**Figure 4.5C**). Oleylbiotin demonstrated greater HABA displacement at 1, 25 and 73 h (**Figure 4.5C**), indicating oleylbiotin will produce faster D-Bv release rates. Oleylbiotin and hexadecylbiotin both demonstrated greater HABA displacement at 1 h, explaining the influence of biotin derivative concentration on the initial burst release. Compared to Chapter 2, the switch from streptavidin to neutravidin altered the displacement of HABA. According to dynamic light scattering measurements, the supernatants of biotin derivatives in pCB solutions did not contain significant amounts of biotin derivative complexation (e.g. micelles; **Figure S 4.8**). Therefore, the dissolution of biotin derivative pellets in the presence of pCB can displace molecules from avidin binding sites.

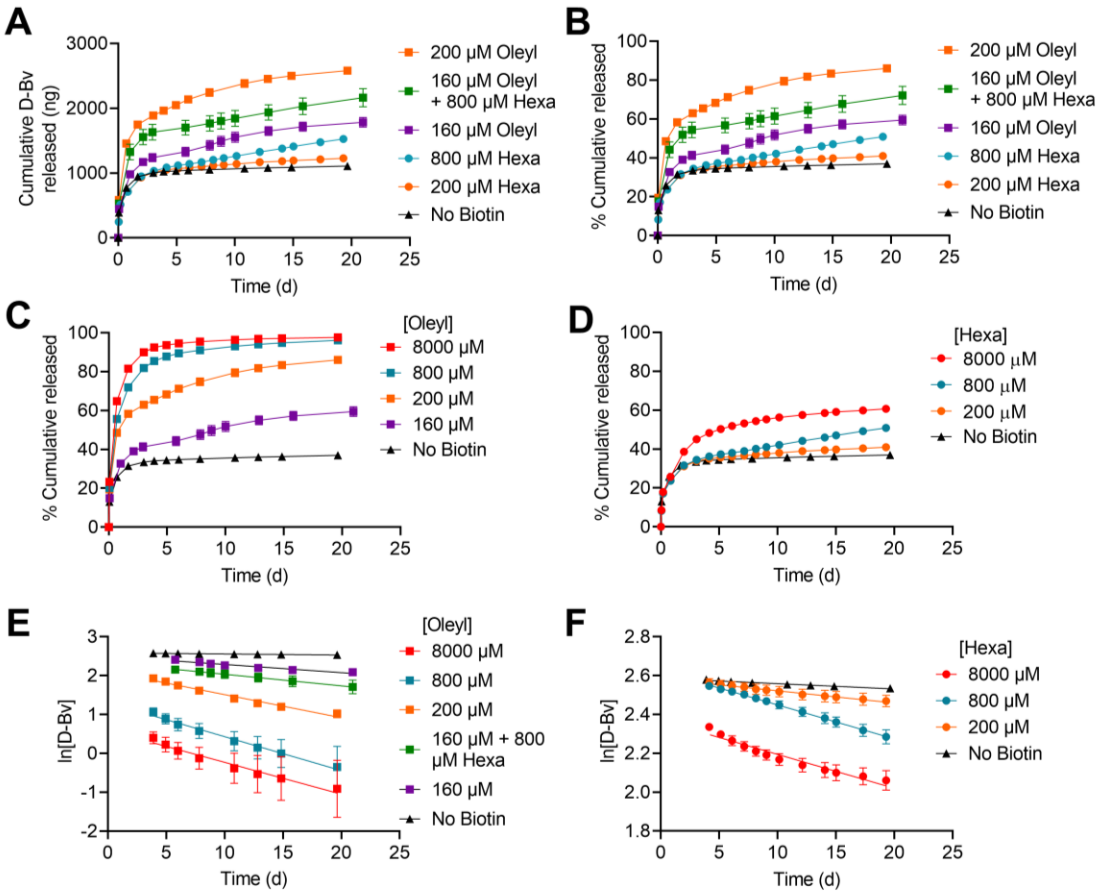

G

Biotin Derivative	Concentration of biotin derivative (µM)	k_{eff} (d^{-1})	R^2	Release rate after day 3 (ng d^{-1})	R^2
Oleyl	8000	$8.2 \times 10^{-2} \pm 1.5 \times 10^{-2}$	0.58	9.3 ± 1.5	0.64
Oleyl	800	$8.7 \times 10^{-2} \pm 9.9 \times 10^{-2}$	0.78	19.4 ± 2.1	0.79
Oleyl	200	$5.9 \times 10^{-2} \pm 3.4 \times 10^{-3}$	0.93	39.8 ± 2.9	0.90
Oleyl	160	$2.1 \times 10^{-2} \pm 2.3 \times 10^{-3}$	0.81	29.7 ± 3.5	0.80
Oleyl + Hexa	160 + 800	$3.0 \times 10^{-2} \pm 4.7 \times 10^{-3}$	0.68	30.8 ± 4.8	0.69
Hexa	8000	$1.7 \times 10^{-2} \pm 1.2 \times 10^{-3}$	0.86	17.0 ± 1.1	0.84
Hexa	800	$1.7 \times 10^{-2} \pm 6.9 \times 10^{-4}$	0.95	29.9 ± 1.0	0.96
Hexa	200	$6.3 \times 10^{-3} \pm 7.9 \times 10^{-4}$	0.65	12.4 ± 1.3	0.70
None	N/A	$2.8 \times 10^{-3} \pm 2.0 \times 10^{-4}$	0.89	5.3 ± 0.4	0.90

Figure 4.6 Controlled release of D-Bv (50 µg mL^{-1}) from pCB-NT hydrogels mediated by the dissolution of sparingly soluble biotin derivative pellets. (A-B) Conditions that achieved sustained release of D-Bv (initial concentration of 50

μg mL^{-1}) from pCB-NT gels with different concentrations of encapsulated oleylbiotin or hexadecylbiotin pellets expressed as (A) cumulative ng released or (B) % cumulative released. (C) All studied oleylbiotin release profiles of D-Bv from pCB-NT gels with different concentrations of oleylbiotin pellets, including 800 and 8000 μM oleylbiotin, which produced large burst releases that prevented sustained release. (D) All studied hexadecylbiotin release profiles of D-Bv from pCB-NT gels with different concentrations of hexadecylbiotin pellets, including 8000 μM hexadecylbiotin. (E-F) First order release plots of D-Bv from hydrogels using different total (E) oleylbiotin and (F) hexadecylbiotin concentrations after the initial burst release, day 3. Plots represent remaining D-Bv concentration in pCB-NT gels as a function of time. (G) Table summarizing calculated k_{eff}s, and ng d^{-1} D-Bv release rates after initial burst (after day 3), and corresponding R^2 values. All samples were performed in triplicate (mean ± standard deviation).

4.4.5 Biotin derivative mediated controlled release of D-Bv from pCB-NT gels

Controlled release of D-Bv was demonstrated by altering the total concentration of oleylbiotin or hexadecylbiotin pellets in pCB-NT gels with 50 μg mL^{-1} D-Bv. As higher local D-Ab concentrations are required, we must increase both the initial burst and sustained D-Ab release rate according to pharmacokinetic models.[36] Therefore, D-Bv release profiles where both the initial burst and post-burst (sustained) release rates increased with higher biotin

derivative concentrations are plotted as cumulative mass release (Figure 4.6**A**) and percent cumulative release (**Figure 4.6B**).

Due to its greater initial displacement potential (Figure 4.5**C**), oleylbiotin resulted in a larger D-Bv burst release from pCB-NT gels than hexadecylbiotin (**Figure 4.6C-D**), and higher biotin derivative concentrations produced larger bursts. After the initial burst (~ 3 d), D-Bv release followed first-order kinetics dependent on the remaining D-Bv concentration in the hydrogel (Figure 4.6**E, F**). The post-burst ng d^{-1} release rate of D-Bv was then proportional to the biotin derivative's concentration and remaining D-Bv in the gel. Without any biotin derivatives present, D-Bv slowly released at a rate of 5 ng d^{-1} with a k_{eff} of 2.8 x 10^{-3} d^{-1}, after an initial burst of ~ 35% (Figure 4.6**A, G**). Therefore, D-Bv's affinity and $t_{1/2}$ with pCB-NT (K_D ~ 7.8 x 10^{-10} M, $t_{1/2}$ ~ 2 h) determines the slowest achievable rate for D-Bv release.

To increase release rates beyond 5 ng d^{-1}, oleylbiotin pellets were incorporated within pCB-NT gels with 50 µg mL^{-1} D-Bv. Total concentrations of 160 and 200 µM oleylbiotin allowed for controlled D-Bv release, whereas 800 and 8000 µM oleylbiotin only produced rapid burst releases over ~ 3 d (Figure 4.6**C**) by preventing significant D-Bv complexation with pCB-NT. 160 and 200 µM oleylbiotin showed an initial D-Bv burst release of ~ 40% and ~ 60%, followed by controlled first-order D-Bv release over ~ 20 d with k_{eff}s of 2.1 x 10^{-2} and 5.9 x 10^{-2} d^{-1}, and release rates of 30 and 40 ng d^{-1}, respectively (Figure

4.6**C,G**). These results demonstrate D-Bv release from pCB-NT gels can be tuned by altering the total oleylbiotin concentration (~ 0-200 μM) to achieve release rates between 5 to 40 ng d^{-1} over ~ 20 d without modifying D-Bv or pCB-NT.

Due to its lower displacement potential, ≥ 200 μM hexadecylbiotin was required to increase D-Bv release rates from pCB-NT gels (**Figure 4.6D**). In agreement with the HABA displacement data (Figure 4.5**C**), hexadecylbiotin produced a smaller D-Bv burst release than oleylbiotin at all concentrations (**Figure 4.6C-D, G**). After the initial burst, 200 μM hexadecylbiotin produced D-Bv release rates slightly faster than the no biotin controls, with a k_{eff} of 6.3 x 10^{-3} d^{-1} and a release rate of 12 ng d^{-1} for over 20 d. 800 μM hexadecylbiotin further increased release rates to 30 ng d^{-1} with a k_{eff} of 1.7 x 10^{-2} d^{-1}. Interestingly, 8000 μM hexadecylbiotin increased D-Bv's initial burst but decreased D-Bv's sustained release to 17 ng d^{-1} while maintaining the same k_{eff} (1.7 x 10^{-2} d^{-1}) as 800 μM. Therefore, hexadecylbiotin pellets at 8000 μM have a lower D-Bv displacement potential compared to 800 μM hexadecylbiotin at longer timepoints, indicating the soluble concentration of hexadecylbiotin does not scale proportionately with increasing pellet concentrations. Furthermore, the release profile with 8000 μM hexadecylbiotin is biphasic upon first order analysis (**Figure 4.6F**), which is most likely due to higher soluble hexadecylbiotin concentrations at early timepoints from mixing during hydrogel preparation.

To determine if oleylbiotin and hexadecylbiotin pellet mixtures can be combined for further D-Bv release rate tuning, we combined 160 µM oleylbiotin with 800 µM hexadecylbiotin. The release profile was indistinguishable from 160 µM oleylbiotin promoted D-Bv release (31 vs 30 ng d^{-1}), indicating a of lack of synergism (Figure 4.6**A, G**).

If pellet dissolution maintains near constant soluble biotin derivative concentrations inside the hydrogel, we expect release to be first order with respect to hydrogel D-Bv concentration. To confirm that individual release rates are only dependent on D-Bv's concentration over time, first-order plots of post-burst release data as a function of remaining D-Bv concentration were constructed (Figure 4.6**E, F**). The linearity of the plots indicates that process is first-order with respect to D-Bv concentration.

Unlike traditional affinity systems where binding pairs are altered to tune release profiles,[37,38] the developed DARA system can tune D-Ab release rates by simply altering biotin derivative concentrations while maintaining a constant binding pair (D-Bv and pCB-NT). The rate of D-Ab release is proportional to the dissolution of the biotin derivative, which achieves near linear release between 3 and 20 d (**Figure S 4.9A-C**). D-Bv's k_{eff} and mass per day release rates were tuned 25 and 8-fold, respectively (**Figure 4.6G, Figure S 4.9D**), without modifying D-Bv or pCB-NT.

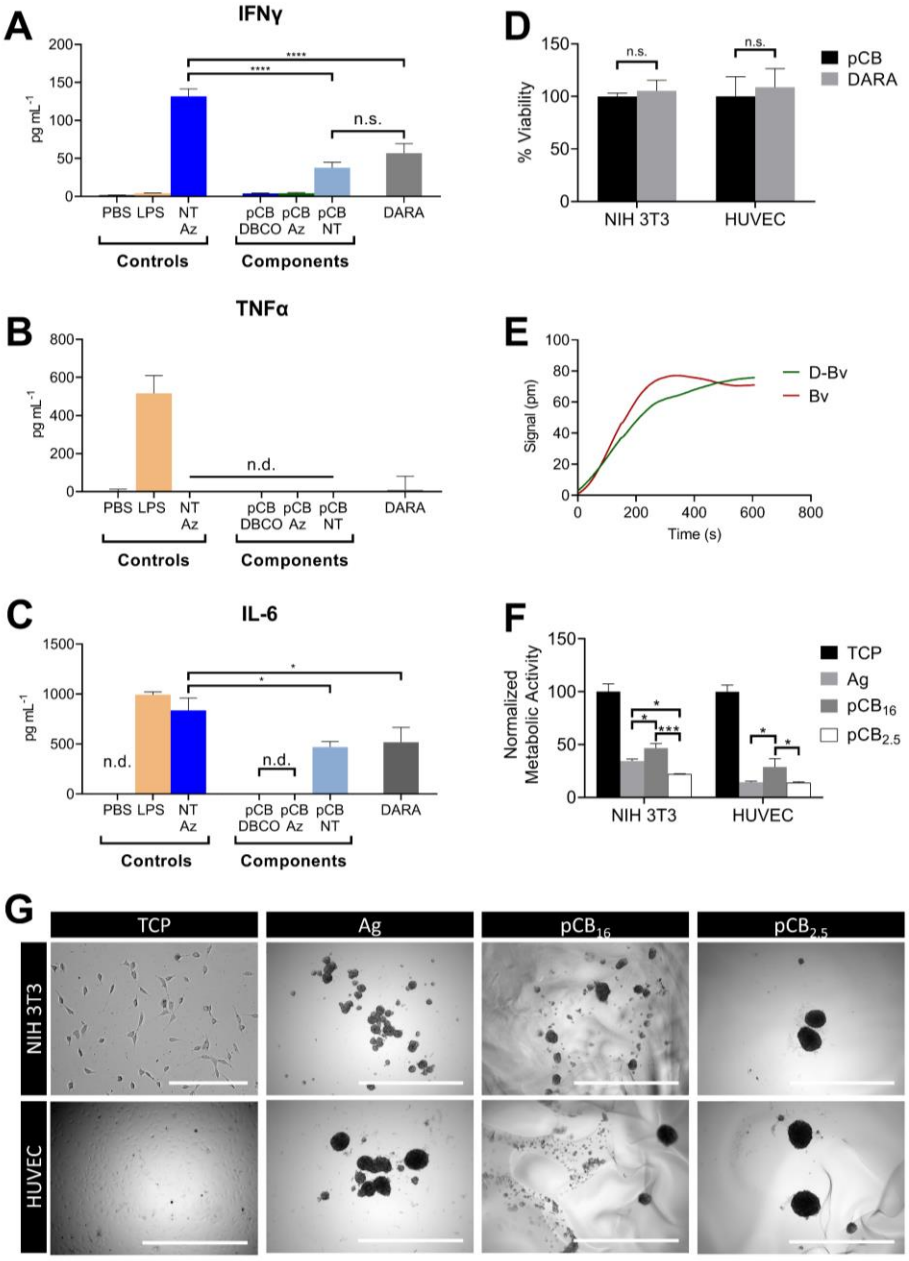

Figure 4.7 Biocompatibility of pCB-NT hydrogels and the DARA system. CRA for (A) IFNγ, (B) TNFα, and (C) IL-6 levels when pCB-DBCO, pCB-Az, pCB-NT, and the complete DARA system were exposed to whole human blood for 24 h. LPS and unconjugated NT-Az were included as positive controls

for cytokine production; PBS was included as a negative control. Samples containing pCB-NT increased cytokine production that remained lower than the unconjugated NT-Az control (n.d. = non-detectable; One-Way ANOVA Bonferroni post hoc test, $n = 3$, $p < 0.05$). (D) Cell viability of NIH 3T3 fibroblasts and HUVECs plated on pCB control gels and pCB-NT gels with the complete DARA system. No decrease in cell viability was observed upon exposure to the DARA system ($n = 3$, Student's t-test, $p > 0.05$). (E) LSPR sensorgram of released D-Bv, pooled from days 10 to 15, and unmodified Bv binding to a VEGF modified gold sensor; released D-Bv retained binding affinity for VEGF. (F-G) Fibroblasts and HUVECs did not adhere to pCB gels ($pCB_{2.5}$; ~ 2.4 mol% DBCO/Az) used in the DARA system as confirmed by (F) metabolic activity and (G) microscopy. In contrast, cells had greater metabolic activity and adhesion on pCB gels with greater DBCO/Az content (pCB_{16}; ~ 16 mol% DBCO/Az). Agarose gels and TCP were used as negative and positive controls, respectively (One Way ANOVA Tukey post hoc test, $n = 3$, $p < 0.05$). Scale bars are 1000 μm except for NIH 3T3 on TCP, which is 200 μm.

4.4.6 Biocompatibility of pCB-NT gels with the DARA system

Immunogenicity and cytotoxicity of the pCB-NT hydrogel and DARA system were assessed by CRAs[39] and cell viability assays, respectively. CRAs in whole human blood or with peripheral blood mononuclear cells are recommended

by the FDA to evaluate immunogenicity of antibody therapeutics.[40] In this case, CRAs were performed by incubating hydrogel components and the complete DARA system in fresh human whole blood for 24 h, plasma was then isolated for quantification of IFNγ, IL-6 and TNFα, known markers for inflammatory immune responses (**Figure 4.7A-C**).[24,39] LPS was included as a positive control for IL-6 and TNFα; LPS induced production of IFNγ is variable with a reported range of 9 to 193 pg mL^{-1} dependent on the blood source.[39] In our tests, LPS induced expression of IFNγ was 8.5 pg mL^{-1}, which is on the lower end of the reported range. Because NT has previously been reported to induce IFNγ in rat blood,[24] unconjugated NT-Az was included as a positive IFNγ control.

Only samples containing pCB-NT increased IFNγ and IL-6 levels, indicating an inflammatory response; no increase in TNFα was observed for any tested sample. Conjugation of NT-Az to pCB decreased the production of IFNγ and IL-6 when compared to unconjugated NT-Az. Therefore, pCB polymers and hydrogels can decrease NT immunogenicity, and improve the biocompatibility of drug delivery systems. The conjugation of pCB to proteins has previously been shown to reduce immunogenicity (e.g. organophosphorus hydrolase, uricase, asparaginase).[18,19,41,42]

To further decrease immunogenicity, previously reported low-immunogenic streptavidin mutants (e.g. LISA-314)[24,43–45] or biotin/desthiobiotin binding humanized FAB fragments developed by phage display technology can

be investigated. For cancer immunotherapy, the local production of IFNγ may be beneficial to enhance cytotoxic T cell (CTL) infiltration into tumors.[46–48] IL-6 has also been shown to increase CTL trafficking within the tumor environment.[49] Therefore, local production of cytokines by an implantable hydrogel may have advantages for specific applications.

Together with human blood cells tested above (CRAs), fibroblasts and endothelial cells represent the major classes of cells that many local delivery systems encounter upon implantation; most other cell types will be application specific. Therefore, we studied the viability of NIH 3T3 fibroblasts and HUVECs exposed to the drug delivery hydrogel. The viability of fibroblasts and HUVECs seeded on the surface of pCB gels was similar to cells on pCB-NT gels with the DARA system, indicating the DARA system does not negatively influence cell viability (**Figure 4.7D**); pCB gels have previously been shown not influence cell viability.[22] When components of the delivery system were screened individually, only high concentrations of oleylbiotin (2 μM) decreased cell viability (**Figure S 4.10**). When the same concentration of oleylbiotin was encapsulated in pCB-NT hydrogels, no decrease in cell viability was observed (Figure 4.7**D**). Therefore, the slow dissolution of oleylbiotin in gels does not influence cell viability and the hydrogel must be designed to avoid oleylbiotin pellet release to improve biocompatibility. High concentrations of hexadecylbiotin (2 μM) did not decrease cell viability, most likely due to its slower dissolution rate.

The pCB gels used in this study were confirmed to be non-adhesive towards fibroblasts and HUVECs. Non-specific cell adhesion can limit Ab transport from the hydrogel by creating a cellular barrier impeding drug elution. NIH 3T3 fibroblasts and HUVECs were seeded on tissue culture plastic (TCP; positive control), agarose gels (negative control), pCB gels used for the DARA system ($pCB_{2.5}$, ~ 2.4 mol% Az/DBCO) and pCB gels with greater hydrophobic Az and DBCO content (pCB_{16}, ~ 16 mol% Az/DBCO; Figure 4.7**F-G**). Cell adhesion was assessed by metabolic activity (Figure 4.7**F**), which increases with adhesion, and brightfield micrographs (**Figure 4.7G**). Cells seeded on $pCB_{2.5}$ had lower or similar metabolic activity to cells on non-adhesive agarose hydrogels, and much lower metabolic activity that cells on TCP and pCB_{16} (Figure 4.7**F**). No cell attachment was observed on $pCB_{2.5}$ gels; cells formed large clusters due to cell-cell binding (**Figure 4.7G**). As expected, cell adhesion was observed in the positive TCP control. Minor cell adhesion to pCB_{16} was observed by the formation of numerous smaller cell clusters. Consequently, pCB gels used for the DARA system with low Az/DBCO content (~ 2.4 mol%) prevents non-specific cell attachment and improves the biocompatibility of NT-Az and oleylbiotin.

To ensure D-Bv remained bioactive, the VEGF binding potential of released D-Bv was confirmed from pooled released fractions between days 10 and 15. D-Bv samples flowed over a VEGF modified gold LSPR sensor displayed a similar binding response as unmodified Bv from a stock solution, indicating

retention of bioactivity (**Figure 4.7E**). Released D-Bv was also injected over control gold LSPR surfaces without VEGF to ensure LSPR signal was not due to non-specific binding.

4.5 Conclusions

We developed a method to control D-Bv complexation rates within pCB-NT hydrogels (DARA) for local and sustained (first-order) release of bioactive Ab. The dissolution of encapsulated biotin derivative pellets controls the displacement of D-Bv from pCB-NT gels. By varying oleylbiotin or hexadecylbiotin pellet concentrations, k_{eff} and mass per day release rates were tuned 25- and 8-fold, respectively. Unlike most affinity systems, DARA tunes release rates with a constant Ab (D-Ab) and hydrogel (pCB-NT) pair. Importantly, D-Bv retained its binding affinity for both VEGF and CD16α, indicating the single chain variable fragments (scFv) and Fc domains remained bioactive. Therefore, the DARA method can be used to deliver IgG1 Abs for single agent targeting (e.g. anti-angiogenesis) or bispecific mechanisms for immune cell recruitment (e.g. ADCC).

Supporting Information

Methods for maximum D-Bv pCB-NT gel loading, gelation time determination, injection of pCB-NT gels, DLS; polymer characterization; polymer synthesis scheme; neutravidin characterization; D-Bv and B-Bv characterization; in situ gelation experiments; maximum D-Bv loading in pCB-NT hydrogels; first order

release plots of D-Bv and B-Bv from pCB-NT gels; DLS characterization of biotin derivatives; release rate graphs of D-Bv in ng d^{-1}; and cell viability data from DARA components.

Acknowledgements

This work was supported by the Natural Sciences and Engineering Research Council (NSERC; 2015-05429, 532019-18), New Frontiers Research Fund (NFRFE-2018-00943), Canada Foundation for Innovation: John R. Evans Leaders Fund (CFI-JELF; 34107), Ontario Research Fund - Research Infrastructure (ORI-RI; 34107), and McMaster University. V.H. would also like to acknowledge NSERC for scholarship funding. We would also like to thank Dr. Alex Adronov and Stuart McNelles for donation of NHS-DBCO. We thank Eden Kapcan and Anthony Rullo for D-Bv and CD16α BLI binding kinetic studies. We also thank Rashik Ahmed for help with DLS measurements.

4.6 References

(1) Parry, R. V.; Chemnitz, J. M.; Frauwirth, K. A.; Lanfranco, A. R.; Braunstein, I.; Kobayashi, S. V.; Linsley, P. S.; Thompson, C. B.; Riley, J. L. CTLA-4 and PD-1 Receptors Inhibit T-Cell Activation by Distinct Mechanisms. *Mol. Cell. Biol.* 2005, *25* (21), 9453–9553. DOI:

10.1128/MCB.25.21.9543.

(2) Kadioglu, E.; Wyser Rmili, C.; Laoui, D.; Cassará, A.; Kiialainen, A.; Schmittnaegel, M.; De Palma, M.; Mueller, H.-J.; Kienast, Y.; Rigamonti, N.; Ooi, C.-H. Dual Angiopoietin-2 and VEGFA Inhibition Elicits Antitumor Immunity That Is Enhanced by PD-1 Checkpoint Blockade. *Sci. Transl. Med.* 2017, *9* (385), eaak9670. DOI: 10.1126/scitranslmed.aak9670.

(3) Müller, D.; Kontermann, R. E. Bispecific Antibodies. *Handb. Ther. Antibodies Second Ed.* 2014, *1–4* (7), 265–310. DOI: 10.1002/9783527682423.ch11.

(4) Weiner, G. J. Building Better Monoclonal Antibody-Based Therapeutics. *Nat. Rev. Cancer* 2015, *15* (6), 361–370. DOI: 10.1038/nrc3930.

(5) Gotwals, P.; Cameron, S.; Cipolletta, D.; Cremasco, V.; Crystal, A.; Hewes, B.; Mueller, B.; Quaratino, S.; Sabatos-Peyton, C.; Petruzzelli, L.; Engelman, J. A.; Dranoff, G. Prospects for Combining Targeted and Conventional Cancer Therapy with Immunotherapy. *Nat. Rev. Cancer* 2017, *17* (5), 286–301. DOI: 10.1038/nrc.2017.17.

(6) Pardoll, D. M. The Blockade of Immune Checkpoints in Cancer Immunotherapy. *Nat. Rev. Cancer* 2012, *12* (4), 252–264. DOI: 10.1038/nrc3239.

(7) Topp, M. S.; Gökbuget, N.; Stein, A. S.; Zugmaier, G.; O'Brien, S.; Bargou, R. C.; Dombret, H.; Fielding, A. K.; Heffner, L.; Larson, R. A.; Neumann, S.; Foà, R.; Litzow, M.; Ribera, J. M.; Rambaldi, A.; Schiller, G.; Brüggemann, M.; Horst, H. A.; Holland, C.; Jia, C.; Maniar, T.; Huber, B.; Nagorsen, D.; Forman, S. J.; Kantarjian, H. M. Safety and Activity of Blinatumomab for Adult Patients with Relapsed or Refractory B-Precursor Acute Lymphoblastic Leukaemia: A Multicentre, Single-Arm, Phase 2 Study. *Lancet Oncol.* 2015, *16* (1), 57–66. DOI: 10.1016/S1470-2045(14)71170-2.

(8) Riley, R. S.; June, C. H.; Langer, R.; Mitchell, M. J. Delivery Technologies for Cancer Immunotherapy. *Nat. Rev. Drug Discov.* 2019, *18* (3), 175–196. DOI: 10.1038/s41573-018-0006-z.

(9) Huynh, V.; Jesmer, A. H.; Shoaib, M. M.; D'Angelo, A. D.; Rullo, A. F.; Wylie, R. G. Improved Efficacy of Antibody Cancer Immunotherapeutics through Local and Sustained Delivery. *ChemBioChem* 2019, *20* (6), 747–753. DOI: 10.1002/cbic.201800579.

(10) Norouzi, M.; Nazari, B.; Miller, D. W. Injectable Hydrogel-Based Drug Delivery Systems for Local Cancer Therapy. *Drug Discov. Today* 2016, *21* (11), 1835–1849. DOI: 10.1016/j.drudis.2016.07.006.

(11) Lee, A. L. Z.; Ng, V. W. L.; Gao, S.; Hedrick, J. L.; Yang, Y. Y. Injectable Hydrogels from Triblock Copolymers of Vitamin E-Functionalized

Polycarbonate and Poly(Ethylene Glycol) for Subcutaneous Delivery of Antibodies for Cancer Therapy. *Adv. Funct. Mater.* 2014, *24* (11), 1538–1550. DOI: 10.1002/adfm.201301307.

(12) Leach, D. G.; Young, S.; Hartgerink, J. D. Advances in Immunotherapy Delivery from Implantable and Injectable Biomaterials. *Acta Biomater.* 2019, *88*, 15–31. DOI: 10.1016/j.actbio.2019.02.016.

(13) Chen, Q.; Wang, C.; Chen, G.; Hu, Q.; Gu, Z. Delivery Strategies for Immune Checkpoint Blockade. *Adv. Healthc. Mater.* 2018, *7* (20), 1800424. DOI: 10.1002/adhm.201800424.

(14) Tibbitt, M. W.; Dahlman, J. E.; Langer, R. Emerging Frontiers in Drug Delivery. *J. Am. Chem. Soc.* 2016, *138* (3), 704–717. DOI: 10.1021/jacs.5b09974.

(15) Hu, X.; Zhang, X.; Gu, Z.; Ye, Y.; Dotti, G.; Wang, C.; Wen, D.; Liu, Z.; Yu, S.; Hu, Q.; Bomba, H.; Wang, J. In Situ Formed Reactive Oxygen Species–Responsive Scaffold with Gemcitabine and Checkpoint Inhibitor for Combination Therapy. *Sci. Transl. Med.* 2018, *10* (429), eaan3682. DOI: 10.1126/scitranslmed.aan3682.

(16) Zelikin, A. N.; Ehrhardt, C.; Healy, A. M. Materials and Methods for Delivery of Biological Drugs. *Nat. Chem.* 2016, *8* (11), 997–1007. DOI: 10.1038/nchem.2629.

(17) Chen, S.; Ladd, J.; Zhang, Z.; Jiang, S.; Hower, J. C. Zwitterionic Polymers Exhibiting High Resistance to Nonspecific Protein Adsorption from Human Serum and Plasma. *Biomacromolecules* 2008, *9* (5), 1357–1361. DOI: 10.1021/bm701301s.

(18) Zhang, P.; Sun, F.; Tsao, C.; Liu, S.; Jain, P.; Sinclair, A.; Hung, H.-C.; Bai, T.; Wu, K.; Jiang, S. Zwitterionic Gel Encapsulation Promotes Protein Stability, Enhances Pharmacokinetics, and Reduces Immunogenicity. *Proc. Natl. Acad. Sci. U. S. A.* 2015, *112* (39), 12046–12051. DOI: 10.1073/pnas.1512465112.

(19) Zhang, P.; Liu, E. J.; Tsao, C.; Kasten, S. A.; Boeri, M. V.; Dao, T. L.; DeBus, S. J.; Cadieux, C. L.; Baker, C. A.; Otto, T. C.; Cerasoli, D. M.; Chen, Y.; Jain, P.; Sun, F.; Li, W.; Hung, H.-C.; Yuan, Z.; Ma, J.; Bigley, A. N.; Raushel, F. M.; Jiang, S. Nanoscavenger Provides Long-Term Prophylactic Protection against Nerve Agents in Rodents. *Sci. Transl. Med.* 2019, *11* (473), eaau7091. DOI: 10.1126/scitranslmed.aau7091.

(20) Keefe, A. J.; Jiang, S. Poly(Zwitterionic)Protein Conjugates Offer Increased Stability without Sacrificing Binding Affinity or Bioactivity. *Nat. Chem.* 2012, *4* (1), 59–63. DOI: 10.1038/nchem.1213.

(21) Zhang, L.; Cao, Z.; Bai, T.; Carr, L.; Ella-Menye, J.-R.; Irvin, C.; Ratner, B. D.; Jiang, S. Zwitterionic Hydrogels Implanted in Mice Resist the Foreign-Body Reaction. *Nat. Biotechnol.* 2013, *31* (6), 553–556. DOI:

10.1038/nbt.2580.

(22) Huynh, V.; Jesmer, A. H.; Shoaib, M. M.; Wylie, R. G. Influence of Hydrophobic Cross-Linkers on Carboxybetaine Copolymer Stimuli Response and Hydrogel Biological Properties. *Langmuir* 2019, *35* (5), 1631–1641. DOI: 10.1021/acs.langmuir.8b03908.

(23) Huynh, V.; Wylie, R. G. Competitive Affinity Release for Long-Term Delivery of Antibodies from Hydrogels. *Angew. Chemie - Int. Ed.* 2018, *57* (13), 3406–3410. DOI: 10.1002/anie.201713428.

(24) Jain, A.; Barve, A.; Zhao, Z.; Jin, W.; Cheng, K. Comparison of Avidin, Neutravidin, and Streptavidin as Nanocarriers for Efficient SiRNA Delivery. *Mol. Pharm.* 2017, *14* (5), 1517–1527. DOI: 10.1021/acs.molpharmaceut.6b00933.

(25) Wang, Y.; Fei, D.; Vanderlaan, M.; Song, A. Biological Activity of Bevacizumab, a Humanized Anti-VEGF Antibody in Vitro. *Angiogenesis* 2004, *7* (4), 335–345. DOI: 10.1007/s10456-004-8272-2.

(26) Almagro, J. C.; Daniels-Wells, T. R.; Perez-Tapia, S. M.; Penichet, M. L. Progress and Challenges in the Design and Clinical Development of Antibodies for Cancer Therapy. *Front. Immunol.* 2018, *8*, 1751. DOI: 10.3389/fimmu.2017.01751.

(27) Masson, M.; Yun, K.; Haruyama, T.; Kobatake, E.; Aizawa, M. Quartz

Crystal Microbalance Bioaffinity Sensor for Biotin. *Anal. Chem.* 1995, *67* (13), 2212–2215. DOI: 10.1021/ac00109a047.

(28) Ngo, C.; Mehta, R.; Aggarwal, K.; Fikes, A. G.; Santos, I. C.; Greer, S. M.; Que, E. L. Pull-Down of Metalloproteins in Their Native States by Using Desthiobiotin-Based Probes. *ChemBioChem* 2019, *20*, 1003–1007. DOI: 10.1002/cbic.201800613.

(29) Li, P.; Jiang, N.; Nagarajan, S.; Wohlhueter, R.; Selvaraj, P.; Zhu, C. Affinity and Kinetic Analysis of Fcγ Receptor IIIa (CD16a) Binding to IgG Ligands. *J. Biol. Chem.* 2007, *282* (9), 6210–6221. DOI: 10.1074/jbc.M609064200.

(30) Green, N. M. Spectrophotometric Determination of Avidin and Biotin. *Methods Enzymol.* 1970, *18*, 418–424. DOI: 10.1016/0076-6879(71)18342-5.

(31) Repo, S.; Paldanius, T. A.; Hytönen, V. P. P.; Nyholm, T. K. M.; Halling, K. K. K.; Huuskonen, J.; Pentikäinen, O. T. T.; Rissanen, K.; Slotte, J. P.; Airenne, T. T.; Salminen, T. A.; Kulomaa, M. S. S.; Johnson, M. S. S. Binding Properties of HABA-Type Azo Derivatives to Avidin and Avidin-Related Protein 4. *Chem. Biol.* 2006, *13* (10), 1029–1039. DOI: 10.1016/j.chembiol.2006.08.006.

(32) Garlick, R. K.; Giese, R. W. Avidin Binding of Radiolabeled Biotin

Derivatives. *J. Biol. Chem.* 1988, *263* (1), 210–215.

(33) Wen, H.; Morris, K. R.; Park, K. Synergic Effects of Polymeric Additives on Dissolution and Crystallization of Acetaminophen. *Pharm. Res.* 2008, *25* (2), 349–358. DOI: 10.1007/s11095-007-9468-0.

(34) Raghavan, S. L.; Trividic, A.; Davis, A. F.; Hadgraft, J. Crystallization of Hydrocortisone Acetate: Influence of Polymers. *Int. J. Pharm.* 2001, *212* (2), 213–221. DOI: 10.1016/S0378-5173(00)00610-4.

(35) Wang, Y.; Lapitsky, Y.; Kang, C. E.; Shoichet, M. S. Accelerated Release of a Sparingly Soluble Drug from an Injectable Hyaluronan-Methylcellulose Hydrogel. *J. Control. Release* 2009, *140* (3), 218–223. DOI: 10.1016/j.jconrel.2009.05.025.

(36) Zheng, H. Intravenous Infusion. In *Applied biopharmaceutics and pharmacokinetics*; Shargel, L., Yu, A. B. C., Eds.; McGraw Hill Education, 2016; pp 131–148.

(37) Soontornworajit, B.; Zhou, J.; Shaw, M. T.; Fan, T. H.; Wang, Y. Hydrogel Functionalization with DNA Aptamers for Sustained PDGF-BB Release. *Chem. Commun.* 2010, *46* (11), 1857–1859. DOI: 10.1039/b924909e.

(38) Vulic, K.; Shoichet, M. S. Tunable Growth Factor Delivery from Injectable Hydrogels for Tissue Engineering. *J. Am. Chem. Soc.* 2012, *134* (2), 882–885. DOI: 10.1021/ja210638x.

(39) Finco, D.; Grimaldi, C.; Fort, M.; Walker, M.; Kiessling, A.; Wolf, B.; Salcedo, T.; Faggioni, R.; Schneider, A.; Ibraghimov, A.; Scesney, S.; Serna, D.; Prell, R.; Stebbings, R.; Narayanan, P. K. Cytokine Release Assays: Current Practices and Future Directions. *Cytokine* 2014, *66* (2), 143–155. DOI: 10.1016/j.cyto.2013.12.009.

(40) Grimaldi, C.; Finco, D.; Fort, M. M.; Gliddon, D.; Harper, K.; Helms, W. S.; Mitchell, J. A.; O'Lone, R.; Parish, S. T.; Piche, M. S.; Reed, D. M.; Reichmann, G.; Ryan, P. C.; Stebbings, R.; Walker, M. Cytokine Release: A Workshop Proceedings on the State-of-the-Science, Current Challenges and Future Directions. *Cytokine* 2016, *85*, 101–108. DOI: 10.1016/j.cyto.2016.06.006.

(41) Liu, M.; Johansen, P.; Zabel, F.; Leroux, J. C.; Gauthier, M. A. Semi-Permeable Coatings Fabricated from Comb-Polymers Efficiently Protect Proteins in Vivo. *Nat. Commun.* 2014, *19* (5), 5526. DOI: 10.1038/ncomms6526.

(42) Chinol, M.; Casalini, P.; Maggiolo, M.; Canevari, S.; Omodeo, E. S.; Caliceti, P.; Veronese, F. M.; Cremonesi, M.; Chiolerio, F.; Nardone, E.; Siccardi, A. G.; Paganelli, G. Biochemical Modifications of Avidin Improve Pharmacokinetics and Biodistribution, and Reduce Immunogenicity. *Br. J. Cancer* 1998, *78* (2), 189–197. DOI: 10.1038/bjc.1998.463.

(43) Yumura, K.; Ui, M.; Doi, H.; Hamakubo, T.; Kodama, T.; Tsumoto, K.; Sugiyama, A. Mutations for Decreasing the Immunogenicity and Maintaining the Function of Core Streptavidin. *Protein Sci.* 2013, *22* (2), 213–221. DOI: 10.1002/pro.2203.

(44) Kawato, T.; Mizohata, E.; Meshizuka, T.; Doi, H.; Kawamura, T.; Matsumura, H.; Yumura, K.; Tsumoto, K.; Kodama, T.; Inoue, T.; Sugiyama, A. Crystal Structure of Streptavidin Mutant with Low Immunogenicity. *J. Biosci. Bioeng.* 2015, *119* (6), 642–647. DOI: 10.1016/j.jbiosc.2014.10.025.

(45) Meyer, D. L.; Schultz, J.; Lin, Y.; Henry, A.; Sanderson, J.; Jackson, J. M.; Goshorn, S.; Rees, A. R.; Graves, S. S. Reduced Antibody Response to Streptavidin through Site-Directed Mutagenesis. *Protein Sci.* 2001, *10* (3), 491–503. DOI: 10.1110/ps.19901.

(46) Mandai, M.; Hamanishi, J.; Abiko, K.; Matsumura, N.; Baba, T.; Konishi, I. Dual Faces of IFNγ in Cancer Progression: A Role of PD-L1 Induction in the Determination of pro- and Antitumor Immunity. *Clin. Cancer Res.* 2016, *22* (10), 2329–2334. DOI: 10.1158/1078-0432.CCR-16-0224.

(47) Nakajima, C.; Uekusa, Y.; Iwasaki, M.; Yamaguchi, N.; Mukai, T.; Gao, P.; Tomura, M.; Ono, S.; Tsujimura, T.; Fujiwara, H.; Hamaoka, T. A Role of Interferon-γ (IFN-γ) in Tumor Immunity: T Cells with the Capacity to Reject Tumor Cells Are Generated but Fail to Migrate to Tumor Sites in

IFN-γ-Deficient Mice. *Cancer Res.* 2001, *61* (8), 3399–3405.

(48) Josephs, S. F.; Ichim, T. E.; Prince, S. M.; Kesari, S.; Marincola, F. M.; Escobedo, A. R.; Jafri, A. Unleashing Endogenous TNF-Alpha as a Cancer Immunotherapeutic. *J. Transl. Med.* 2018, *16* (1), 1–8. DOI: 10.1186/s12967-018-1611-7.

(49) Fisher, D. T.; Appenheimer, M. M.; Evans, S. S. The Two Faces of IL-6 in the Tumor Microenvironment. *Semin. Immunol.* 2014, *26* (1), 38–47. DOI: 10.1016/j.smim.2014.01.008.

4.7 Supplementary Information

4.7.1 Supplementary Methods

Maximum D-Bv loading in pCB-NT gels. NT-Az (4 mg mL^{-1}) was incubated with pCB-DBCO (dissolved in PBS, 0.05 wt% BSA, 5 wt%) overnight at room temperature. D-Bv-488 was then added to the solution and incubated in the dark at room temperature for 3 h. 60 μL gels containing 5 wt% pCB, 4 mg mL^{-1} NT-Az, 3 mg mL^{-1} D-Bv-488, were formed at the bottom of a black 96 well plate by adding 5 wt% pCB-Az to the 5 wt% pCB-DBCO solution and allowed to gel at room temperature for 30 min in the dark. Gels were then submerged in PBS, 0.05 wt% BSA and gel fluorescence (ex. 495 nm, em. 519 nm) was tracked over time.

Gelation time determination of pCB-NT with DARA system. pCB-DBCO (5 wt%) was incubated with NT-Az (0.2 mg mL^{-1}) for 3 h. D-Bv (0.1 mg mL^{-1}) was the added and the solution was incubated overnight. 100 μL of the solution was mixed with a 100 μL solution of pCB-Az (5 wt%) and hexadecylbiotin (800 μM) in a glass vial. Vials were tilted at 15 s intervals and gelation time was determined when no flow observed.

Injection of in situ gelling pCB-NT gels with DARA system into agarose hydrogels. A solution of pCB-DBCO (5 wt%) and 0.2 mg mL^{-1} NT-Az-647 in PBS was incubated overnight at room temperature in the dark. 10 μL of the solution was then mixed with 10 μL mixture of pCB-Az (5 wt%) with 800 μM

hexadecylbiotin. 10 μL of the mixture was immediately loaded in an air-tight Hamilton syringe with a 32 gauge needle. The mixture was incubated in syringe for 9 min prior to injection into a 200 μL 1 wt% agarose gel. Fluorescent micrographs were acquired using a Biotek Cytation 5 imager 0 and 24 h post-injection. A control injection was performed under the same conditions without pCB-Az to prevent in situ gelation.

Dynamic light scattering (DLS) measurements of biotin derivative solutions. Pellets (hexadecylbiotin and oleylbiotin) were suspended in 650 μL of a pCB solution (5 wt%, PBS) to a total concentration of 800 μM. After 1 h, samples were centrifuged at 16 000 g for 15 min and the supernatant was collected. DLS was performed on pCB solutions and supernatants using a Zetasizer Nano ZS Instrument (Malvern Instruments, Malvern UK). Autocorrelation functions were accumulated for two minutes at 37 °C with an angle θ of 173° and a 4 mW He-Ne laser operating at a wavelength of 633 nm. All measurements were performed using a 40 μL (ZEN0040) plastic cuvette. Each measurement consisted of ten runs, and the mean and standard deviation of five measurements are shown for each sample. The particle diameter detection limit was 0.6 – 6 μm. The viscosity value for water and a refractive index of 1.49 was used in the analysis of all measurements.

4.7.2 Supplementary table and figures

Table S 4.1 pCB-APMA, pCB-Az and pCB-DBCO characterization. (A) M_W and dispersity of pCB-APMA copolymer. (B) Composition results of pCB-Az and pCB-DBCO copolymers from ^{1}H NMR.

A

Polymer	M_w	M_n	Đ
pCB-APMA	71 373	65 404	1.09

B

Polymer	Mol % Azide	Az: CB Units	Mol % DBCO	DBCO: CB Units
pCB-Az	2.5	1: 39	-	-
pCB-DBCO	-	-	2.3	1: 43.4

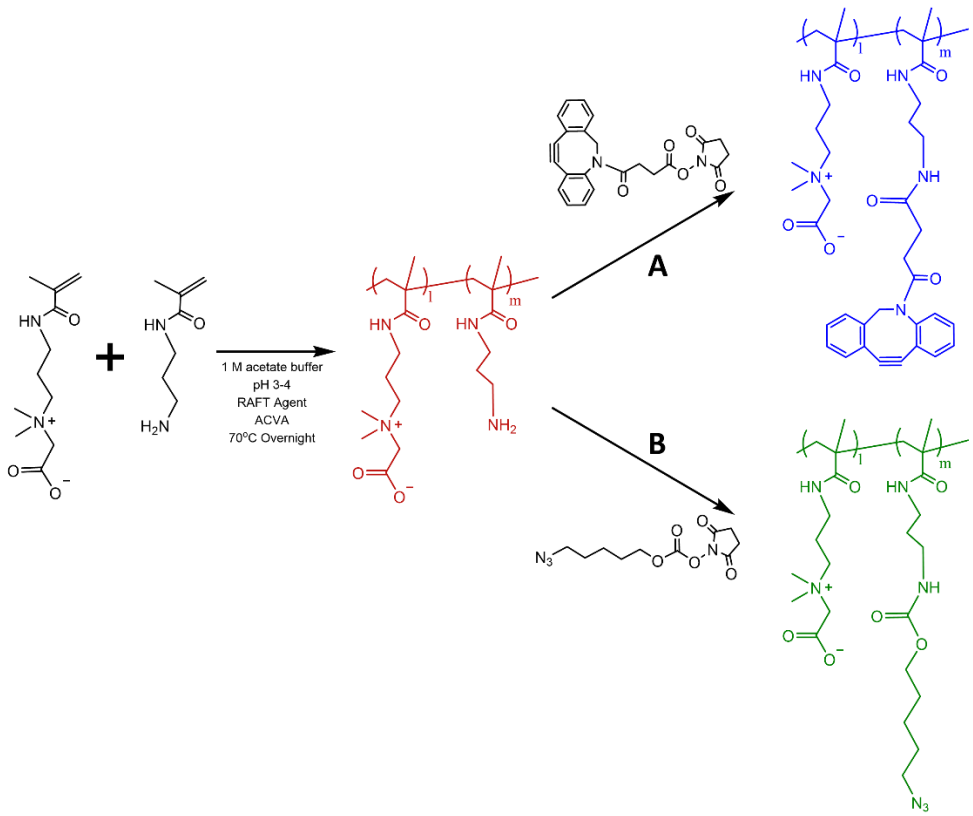

Figure S 4.1 Reaction scheme for pCB-Az and pCB-DBCO copolymers. CB monomer was polymerized with APMA-HCl. pCB-APMA was then reacted with either (A) NHS-DBCO or (B) NHS-azide yielding pCB-DBCO (blue) and pCB-Az (green), respectively.

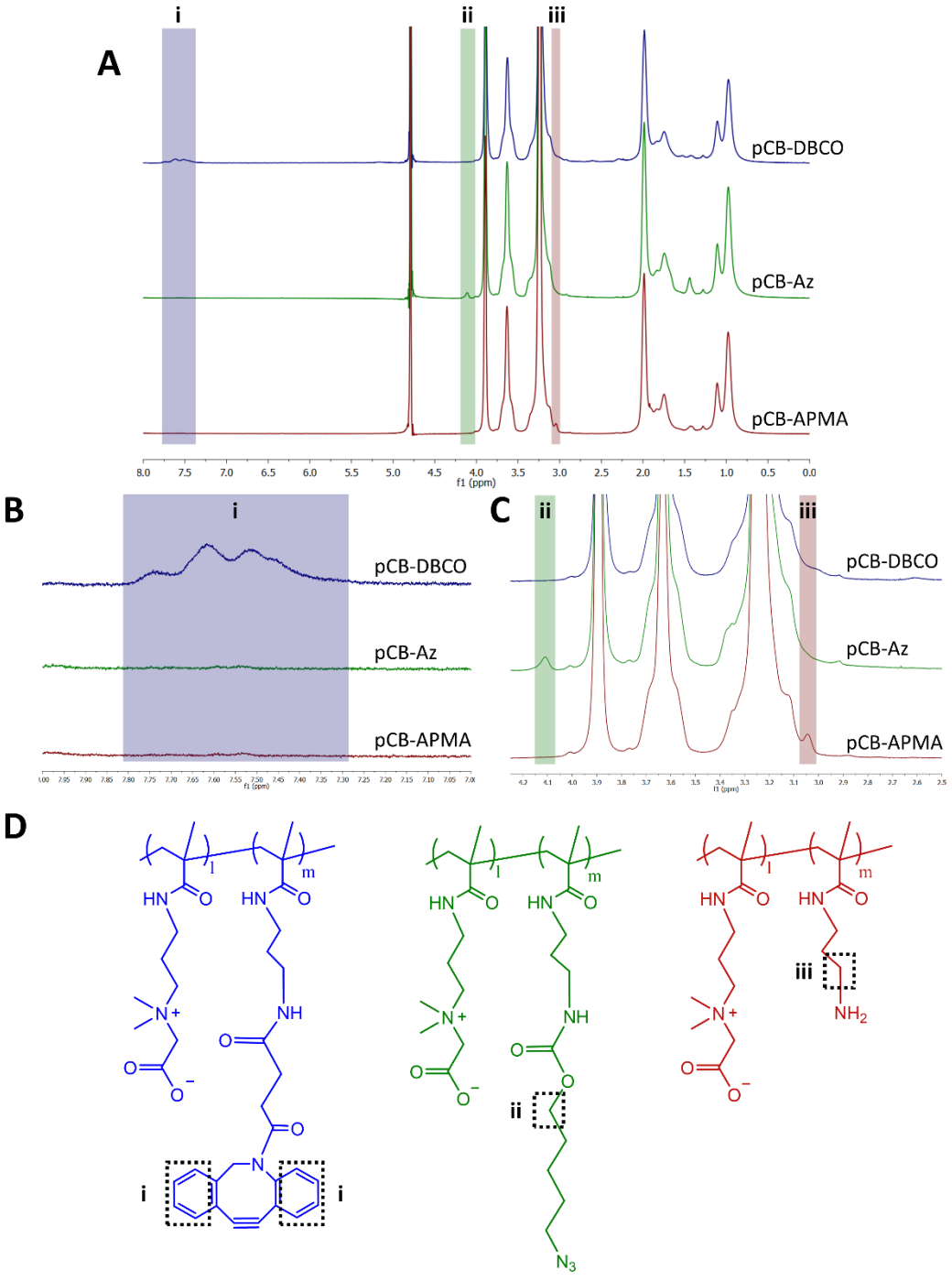

Figure S 4.2 ^{1}H NMR spectra of pCB-APMA, pCB-Az and pCB-DBCO. (A-C) ^{1}H NMR spectra of pCB-DBCO (blue), pCB-Az (green) and pCB-APMA

(red). Blue, red and green shaded area represent unique resonances to pCB-DBCO (i), pCB-Az (ii) and pCB-APMA (iii), respectively. These unique resonances were used to calculate mole fractions upon comparison to the backbone methylene peak (~ 1ppm). (D) Chemical structures of pCB-DBCO, pCB-Az and pCB-APMA. Assignments for the unique resonances are highlighted by dashed boxes labelled i, ii, and iii to determine mole fractions.

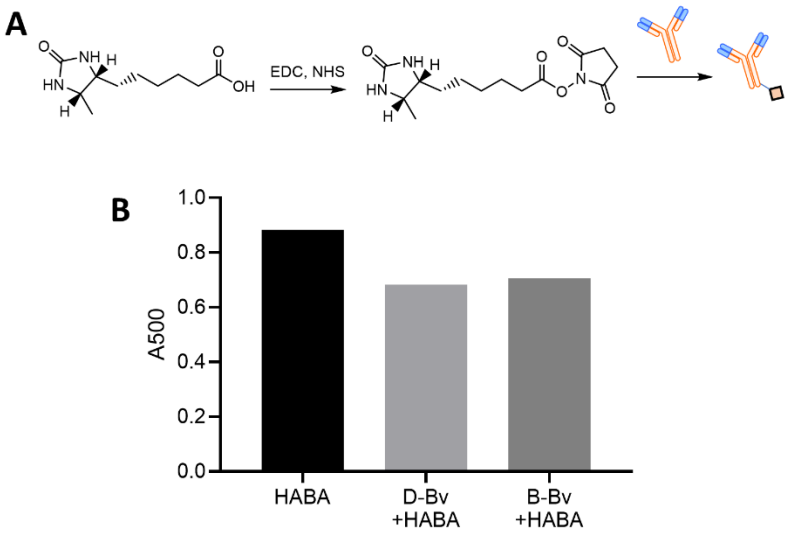

Figure S 4.3 Synthesis and characterization of D-Bv. (A) Synthesis of NHS-desthiobiotin, and conjugation to Bv's lysines. (B) A500 of a HABA-Avidin reagent without and with D-Bv or B-Bv. The decrease in A500 (due to HABA displacement from Avidin) was used to calculate number of desthiobiotins or biotins conjugated to D-Bv and B-Bv, respectively, yielding 4.9 desthiobiotins and 3.7 biotins per Bv.

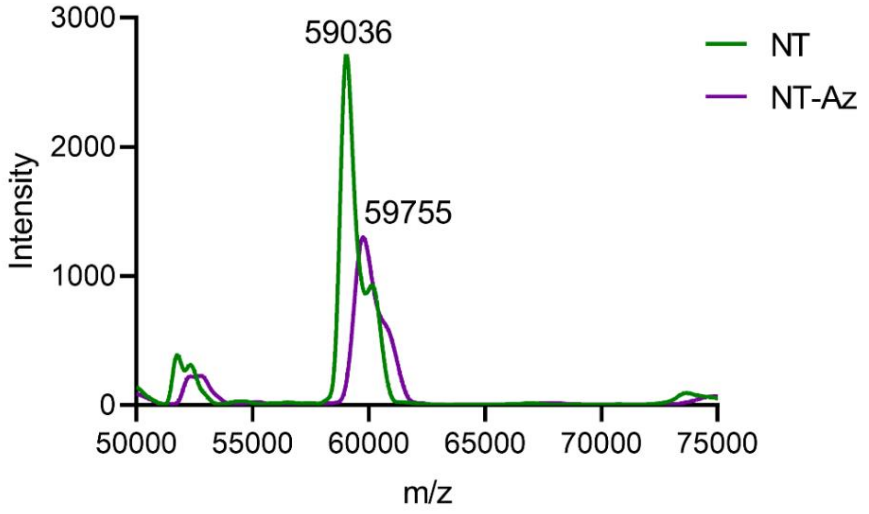

Figure S 4.4 MALDI spectra of NT and NT-Az. The greater M_W of NT-Az was due to azide conjugation, which indicated an average of 7.1 azides per NT.

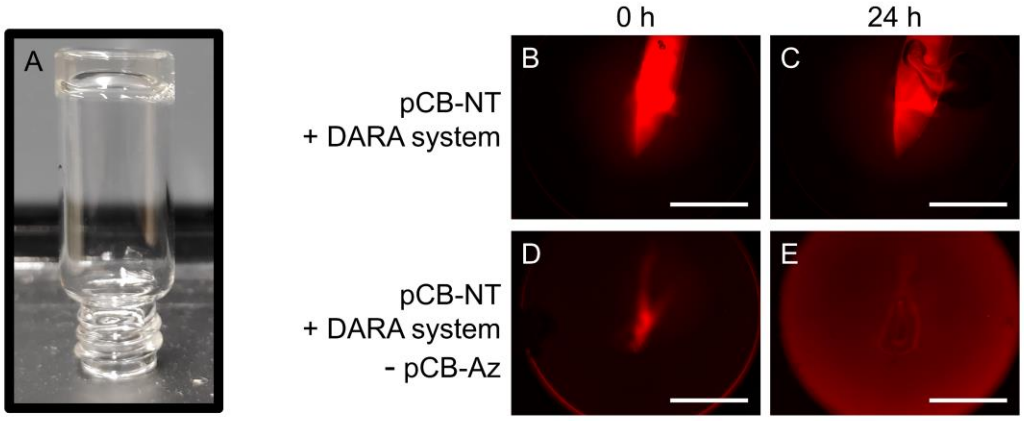

Figure S 4.5 In situ gelation of pCB-NT gels with DARA system. (A) Gravitational flow analysis confirmed a gelation time of 9 min 45 s for 5 wt% pCB-NT gels (0.1 mg mL^{-1} NT-Az) with the DARA system (800 µM hexadecylbiotin, 50 µg mL^{-1} D-Bv). (B-C) Injection of a 10 µL 5 wt% pCB-NT (0.1 mg mL^{-1} fluorescent NT-Az) in situ gelling solution with the DARA system

(800 µM hexadecylbiotin, 50 µg mL^{-1} D-Bv) using a syringe equipped with a 32 gauge needle into a 1 wt% agarose hydrogel. The mixture was incubated in the syringe for 9 min prior to injection. Fluorescent micrographs were taken 0 and 24 h post-injection. The lack of fluorescence in the agarose gel over 24 h indicates the hydrogel formed at the injection site. (D-E) A control injection of all components (5 wt % pCB-DBCO, 0.1 mg mL-^{1} NT-Az, 800 µM hexadecylbiotin, 50 µg mL^{-1} D-Bv) without pCB-Az to prevent in situ gelation. After a 9 min incubation in the syringe, the mixture was injected into 1 wt% agarose gels using the same procedure for B-C. Fluorescence throughout the agarose gel after 24 h indicates the hydrogel did not form.

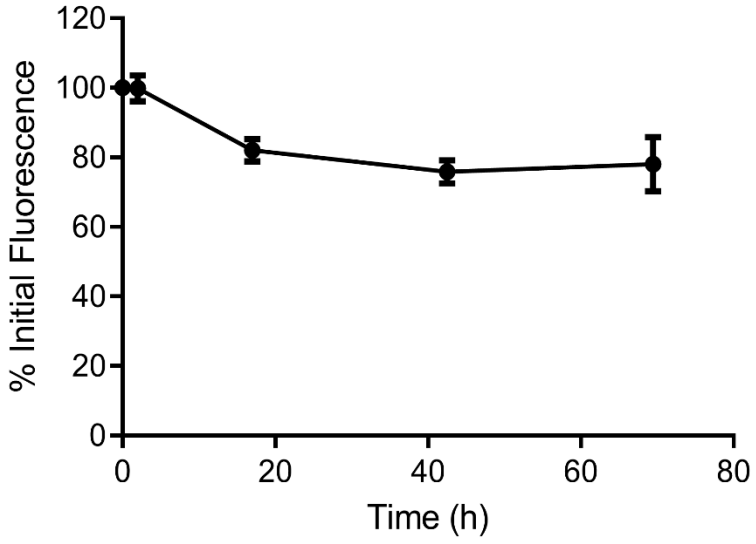

Figure S 4.6 D-Bv loading in pCB-NT gels. pCB-NT gels (4 mg mL^{-1} NT-Az) were formed in the presence of 3 mg mL^{-1} fluorescent D-Bv (Alexa Fluor 488) and submerged in PBS with 0.05 wt% BSA. Fluorescence was tracked over time. ~20% of D-Bv diffused from the gel, the remaining 80% remained in the gel.

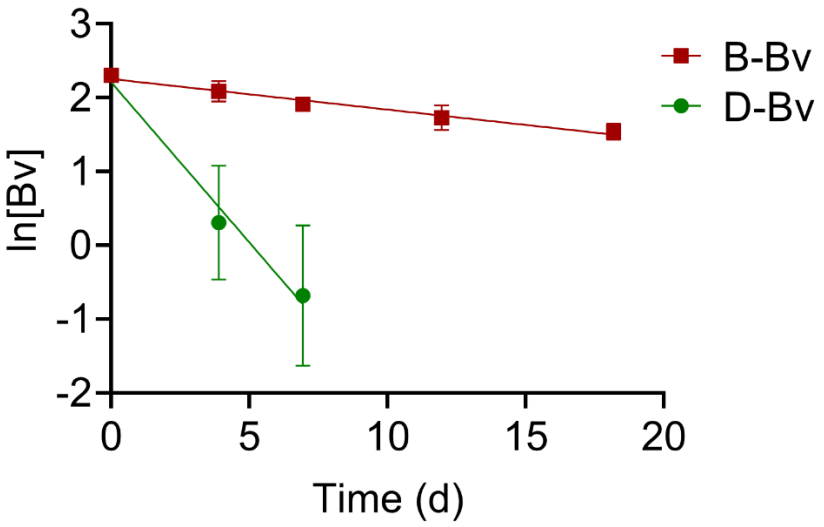

Figure S 4.7 First order release plots of D-Bv and B-Bv from pCB-NT gels.

First order release plots of D-Bv and B-Bv (25 μg mL^{-1}) from 5 wt % pCB-NT gels in the presence of 0.1 mg mL^{-1} biotin. Data corresponds to **Figure 4.4E**.

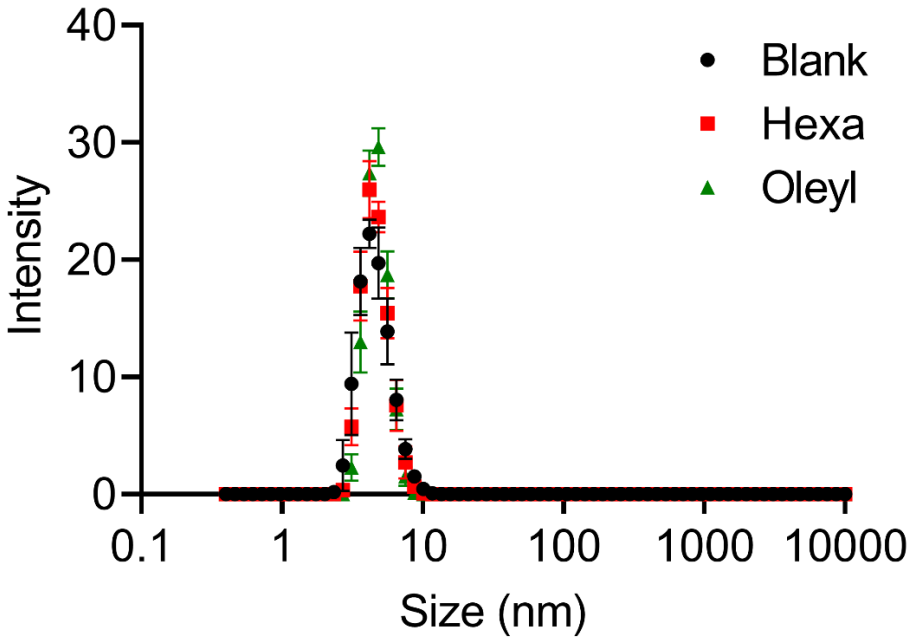

Figure S 4.8 Dynamic light scattering of supernatants from the dissolution of hexadecylbiotin (800 µM) and oleylbiotin (800 µM) pellets in pCB (5 wt%) PBS solutions. A control (Blank) of pCB (5 wt%) in a PBS solution was included. All samples were similar to the pCB control, indicating no significant biotin derivative complexes (e.g. micelles) were present in the supernatant.

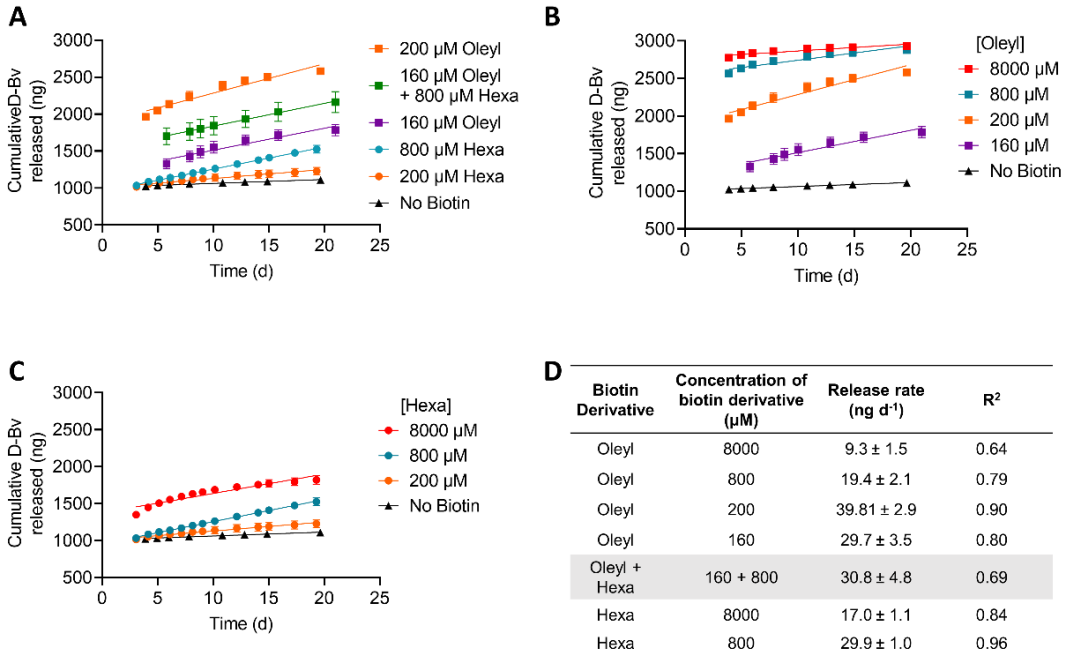

D

Biotin Derivative	Concentration of biotin derivative (µM)	Release rate (ng d^{-1})	R^2
Oleyl	8000	9.3 ± 1.5	0.64
Oleyl	800	19.4 ± 2.1	0.79
Oleyl	200	39.81 ± 2.9	0.90
Oleyl	160	29.7 ± 3.5	0.80
Oleyl + Hexa	160 + 800	30.8 ± 4.8	0.69
Hexa	8000	17.0 ± 1.1	0.84
Hexa	800	29.9 ± 1.0	0.96
Hexa	200	12.4 ± 1.3	0.70
None	N/A	5.3 ± 0.4	0.90

Figure S 4.9 Release rates of D-Bv (50 µg mL^{-1}) from pCB-NT gels with different biotin derivatives types and concentrations expressed as cumulative release in ng d^{-1}. Data only represents timepoints after the initial burst (after 3 d). (A) Release of D-Bv from pCB-NT gels with different oleylbiotin and hexadecylbiotin concentrations. (B) Release of D-Bv from pCB-NT gels with different oleylbiotin concentrations. (C) Release of D-Bv from pCB-NT gels with different hexadecylbiotin concentrations. (D) Table summarizing release rates in ng d^{-1} for each condition.

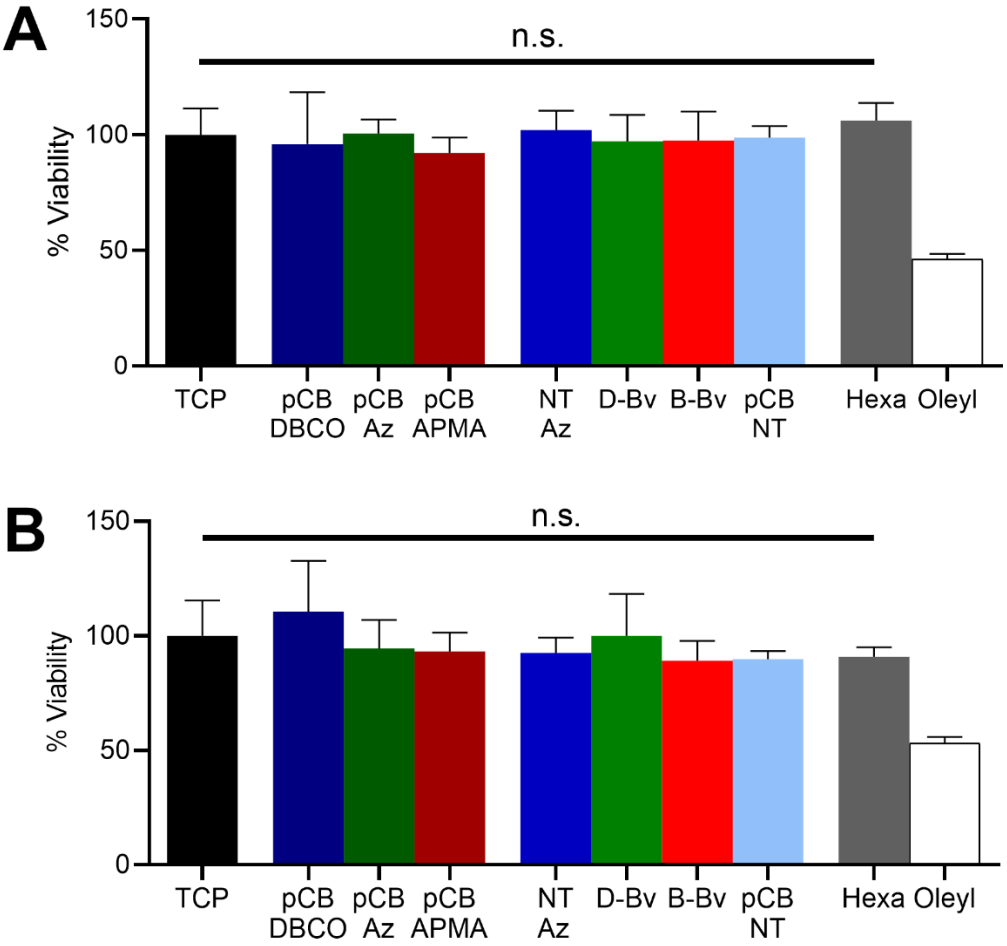

Figure S 4.10 Viability of (A) NIH 3T3 fibroblasts (5000 cells per well) and (B) HUVECs (10 000 cells per well) in the presence of DARA components normalized to TCP controls (n = 3). Concentrations were as follows: pCB-DBCO (5 mg mL^{-1}), pCB-Az (5 mg mL^{-1}), pCB-APMA (5 mg mL^{-1}), D-Av (0.1 mg mL^{-1}), B-Av (0.1 mg mL^{-1}), NT-Az (0.1 mg mL^{-1}), oleylbiotin (1 mg mL^{-1}), hexadecylbiotin (1 mg mL^{-1}) and pCB-NT (5 mg mL^{-1} pCB-DBCO reacted with 0.1 mg mL^{-1} of NT-Az overnight in PBS). Only oleylbiotin pellets demonstrated cytotoxicity when directly exposed to cells at high concentrations (1 mg mL^{-1}).

No cytotoxicity was observed when oleylbiotin pellets was encapsulated in the pCB-NT gels (**Figure 4.7D**).

CHAPTER 5. LOCAL INFUSION OF IMMUNOTHERAPEUTICS (LIIT) FROM AN INJECTABLE HYDROGEL FOR GLIOBLASTOMA TREATMENT

Author's Preface:

I performed all cellular assays, protein modifications, polymer synthesis and characterization. I also aided in the in vivo experiments. This work is being prepared for publication.

Acknowledgements:

I am grateful for the members of the Singh lab for their expertise and aid in performing the in vivo experiments as well as providing the DATE antibody and glioblastoma cells. In particular, Nazanin Tatari, Neil Savage and Dillon Mckenna for the help in designing and performing the in vivo experiments. Additionally, I thank Dr. Sheila Singh and Dr. Chitra Venugopal for their guidance in performing and designing these experiments.

5.1 Abstract

Antibody immunotherapeutics have poor efficacy against solid GBM tumors, when administered locoregionally or systemically due to systemic toxicity, physiological barriers that prevent tumor uptake, and short plasma and tissue half lives. Furthermore, the immunosuppressive environment within GBM tumors further decreases efficacy. Therefore, we propose to use an injectable poly(carboxybetaine) hydrogel incorporating a tunable drug delivery system (DAR) for the intratumoral local infusion of immunotherapeutics (LIIT), to bypasses the blood brain barrier (BBB) and maintain therapeutic concentrations of a dual antigen T cell engager (DATE) in tumor tissue. An in vitro 3D embedded spheroid glioblastoma model was developed and LIIT is being applied to identify combination therapies and an in vivo patient derived xenograft (PDX) mouse model.

5.2 Introduction

The success of immune checkpoint inhibitors, bispecific antibodies and chimeric antigen T cells (CAR T) have propelled immunotherapies to the forefront of cancer treatments.[1–3] Despite the remarkable success of immunotherapy, there has been little success with glioblastoma (GBM) and most other solid tumors because of poor drug localization to the tumor from physiological barriers (blood-brain barrier) and minimal adaptive immune response due to low tumor mutational burden,[4] a predictor for immune checkpoint

inhibitor efficacy.[5,6] Additionally, GBM has an immunosuppressive tumor immune microenvironment which further decreases the efficacy of immunotherapies.

Various treatment modalities are being explored for the treatment of GBM: (1) personalized neo-antigen vaccines that target tumor specific antigens (TSAs) identified through tumor biopsies;[7,8] (2) checkpoint inhibitors, which show limited efficacy due to the lack of an adaptive immune response;[6,9] and, (3) off the shelf IV bispecific therapies that show low efficacy due to transport barriers and rapid clearance, as well as systemic toxicity because the targeted tumor associated antigens (TAAs) have low specificity.[3,10] For example, CD19 targeting immunotherapies typically result in off target neurotoxicity from killing brain mural cells.[11]

To overcome physiological barriers and reduce off target effects, immunotherapeutics can be administered through local injections.[12] However, efficacy remains low as local therapeutic concentrations are not maintained with acceptable dosing frequencies.[13] Local sustained release of cancer immunotherapeutics near the site of the disease is therefore required.[14] Herein, we locally sustain the release of a DATE to target $CD133^+$ brain tumor initiating cells (BTICs). $CD133^+$ BTICs are associated with GBM tumor recurrence, as well as chemo- and radioresistant and are therefore a viable target.[15] Similar to BiTEs, the DATE is a bispecific antibody composed of a CD3-binding single chain

variable fragment (scFv) linked to a CD133-binding Fab through a flexible glycine linker. Simultaneous DATE binding to the CD3 and CD133 antigens on T cells and BTICs[16], respectively, results in major histocompatibility complex (MHC) independent activation of T cell cytolytic pathways.

Without sustained release, CD133 targeting DATEs did not hinder $CD133^+$ tumor growth in a PDX preclinical mouse model after intracranial injection because of their short intracranial half life of antibodies ($t_{1/2}$ ~15h).[16] To improve DATE efficacy, we intratumorally injected poly(carboxybetaine) hydrogels with DAR controlled release functionality, for the sustained release of the CD133 targeting DATE (**Figure 5.1**). We have also demonstrated that combination therapies of an αPD-1 antibody with DATE improves efficacy by enhancing T cell cytolytic activity.

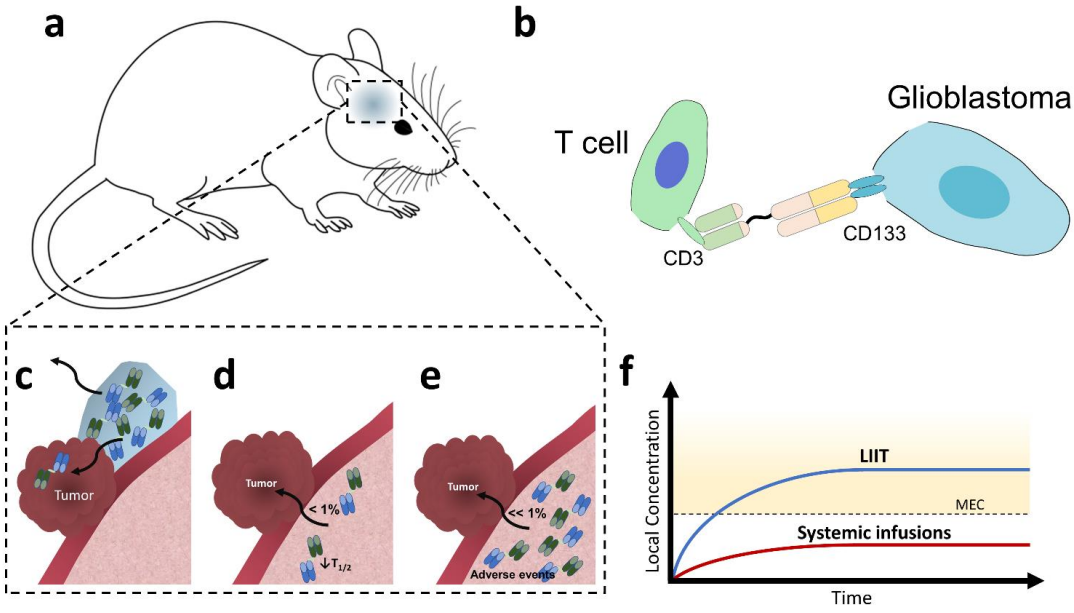

Figure 5.1 Local infusion of immunotherapeutic (DATE) from an injectable hydrogel sustains therapeutic DATE concentrations at the site of the tumor. (a) Intracranial injections of a DATE loaded hydrogel in a mouse PDX glioblastoma model (b) CD133 targeting DATE directs T cells to $CD133^{+}$ GBM cells for tumor killing. (c) Local infusions of DATE increase accumulation of DATE at the tumor. (d) IV injections result in poor accumulation at the site of the tumor. (e) High dose IV administrations result in adverse side effects without reaching therapeutic concentrations in solid tumors. (f) LIIT increases duration above the MEC at the disease site, whereas systemic infusions do not reach the MEC due to physiological barriers.

5.3 Materials and methods

Materials 4-cyano-4-(phenylcarbonothioylthio)pentanoic acid, 4,4'-azobis(4-cyanovaleric acid), TEA, desthiobiotin, N-hydroxysuccinimide (NHS) and bovine serum albumin (BSA) were purchased from Sigma-Aldrich (Oakville, ON, Canada). N-(3-aminopropyl)methacrylamide hydrochloride (APMA-HCl) was purchased from Polysciences Inc. (Warrington, PA). 3-(3-(dimethylamino)propyl)-1-ethyl-carbodiimide hydrochloride (EDC-HCl) was obtained form Chem-Impex International Inc. (Wood Dale, IL). Alexa Fluor 647 NHS ester, Alexa Fluor 488 NHS ester, neutravidin, IL-15 and all flow cytometry antibodies were obtained from Thermo Fisher Scientific (Burlington, ON, Canada). Cy7-Azide was obtained from Lumiprobe (Hunt Valley, Maryland). Dialysis membranes MWCO 12-14k were obtained from Spectrum Chemical Mfg. Crop. (New Brunswick, NJ). Immunocult™ XF-T media, IL-2, Heparin, rEGF, rhFGF, and Neurocult™ NS-A Proliferation Kit were obtained from Stemcell Technologies (Vancouver BC, Canada). XenoLight D-Luciferin was obtained from Perkin Elmer. InVivoMAb anti-PD-1 (αPD-1) antibody was obtained from Bio X Cell (Lebanon, NH). CD133 dual antigen T cell engager (DATE) was purchased from Centre for the Commercialization of Antibodies and Biologics. 6-azidohexyl-succinimidyl carbonate (NHS-azide), carboxybetaine, oleylbiotin pellets, hexadecylbiotin pellets, O-[1-(40methylphenylsulfonyl)-7-azido-2-heptyl]-O'-succinimidyl carbonate (DLAz-NHS) was synthesized according to previously published procedures.

Methods

pCB hydrogel synthesis pCB hydrogels were synthesized as previously described.

pCB-APMA Synthesis Carboxybetaine (CB) monomer was synthesized as previously described. CB monomer (1.5 g) and N-(3-aminopropyl)methacrylamide hydrochloride (APMA-HCl) were dissolved in 1M sodium acetate buffer (pH 5). Separately, 4-cyano-4-(phenylcarbonothioylthio)pentanoic acid (CTA) and 4,4'-azobis(4-cyanovaleric acid) was dissolved in dioxane first and then added to the monomer solution. The pH of the solution was adjusted to 3-4 and then transferred to a Schlenk flask and subject to 3 freeze-pump-thaw cycles, followed by a nitrogen backfill. The reaction was then initiated by immersing the reaction vessel in a 70°C oil bath. The reaction was held for 2d, then the solution was cooled and dialyzed against pH 3-4 water for 3d and lyophilized yielding a pink powder. ^{1}H NMR was performed determine molar % of APMA incorporation.

pCB-AzM Synthesis The degradable linker azide linker (DLAz-NHS) was synthesized as previously described. pCB-APMA was dissolved in dry methanol, subsequently 100 μL of TEA and 50 mg of the DLAz-NHS was added to the solution and reacted overnight at room temperature under N_2. The polymer was then precipitated in ether. The ether was then decanted and the product was then placed in a vacuum oven overnight (60°C) to remove residual ether. The product

was then dissolved in water, washed once with DCM and then dialyzed against water for 3h (MWCO 12-14k). The product was then lyophilized yielding a white powder. ^{1}H NMR was performed determine molar % of linker substitution.

pCB-DBCO Synthesis pCB-APMA was dissolved in dry methanol, subsequently 100 μL of TEA and 50 mg of the DBCO-NHS was added to the solution and reacted overnight at room temperature under N_2. The polymer was then precipitated in ether. The ether was then decanted and the product was then placed in a vacuum oven overnight (60°C) to remove residual ether. The product was then dissolved in water, washed once with DCM and then dialyzed against water for 3h (MWCO 12-14k). The product was then lyophilized yielding a white powder. ^{1}H NMR was performed determine molar % of DBCO substitution.

pCB hydrogel degradation studies (in vitro) 10 wt% gels (100 μL) were formed at the bottom of pre-weighed 2 mL microcentrifuge tubes and gelled at room temperature for 1 h. Subsequently, 1 mL PBS was pipetted over top the gels and incubated at 37°C. At specific time intervals, PBS was pipetted off the gels, a kimwipe was used to dab off residual PBS from the gels and gels were weighed.

pCB hydrogel degradation studies (in vivo) pCB-DBCO was dissolved in PBS (10 wt%) and reacted with 1 μL of Cy7-Azide (10 mg mL^{-1}) for 3 days at 4°C in the dark. This was then mixed with pCB-AzM dissolved in PBS (10 wt%), loaded onto a syringe equipped with a 32 gauge needle and reacted at room temperature for 3 minutes. Then 10 μL of the mixture was intracranially injected into NSG

mice. Fluorescent images were then taken of the mice using an IVIS at specific time points to determine the rate of degradation. Disappearance of the fluorescent signal signifies degradation of the gel and clearance of the degradation products.

Azide modification of Neutravidin Az-NHS dissolved in DMF (10 mg mL^{-1}) was added to Neutravidin (NT) dissolved in PBS (10 mg mL^{-1}) and reacted for 1 d at room temperature. NT-Az was then purified using size exclusion chromatography. Degree of modification was determined through MALDI.

Desthiobiotin modification of DATE Desthiobiotin (3 mg), EDC HCl (11 μg) and NHS (8 μg) were dissolved in 300 μL of dry DMF and reacted overnight at room temperature. 2.7 μL of the reaction mixture was then added to 200 μL DATE dissolved in 1X PBS (4.99 mg mL^{-1}) and reacted overnight at 4°C. The solution was then dialyzed against 1X PBS for 3 days at 4°C (MWCO 12-14k). Degree of desthiobiotinylation was determined through MALDI.

D-DATE was further modified with Alexa-Fluor 488. Briefly, 2 μL of Alexa-Fluor 488 NHS ester (10 mg mL^{-1}) in DMF was added to D-DATE (4.99 mg mL^{-1}) in PBS and reacted overnight in the dark. The fluorescent conjugate was then purified by dialyzing against PBS in the dark at 4°C for 2 days, yielding D-DATE-488.

In vitro release of D-DATE from hydrogel pCB-DBCO (100 mg mL^{-1} in PBS) was incubated with NT-Az overnight at room temperature. D-DATE-488 was then added to the solution and incubated overnight at room temperature in the

dark. pCB-AzM was then dissolved in PBS and mixed with a suspension biotin derivative in PBS. The two solutions were then mixed into a 96 well plate and gelled for 30 minutes at room temperature in the dark, yielding 60 μL 10 wt% pCB gels at the bottom of the 96 well plate which with 0.2 mg mL^{-1} NT-Az, 0.075 mg mL^{-1} D-DATE and different biotin concentrations (800 μM and 200 μM).

200 μL of PBS supplemented with 0.05% BSA was then pipetted over top the gels. The gels were then incubated at 37°C. At specific time intervals the PBS solution was carefully pipetted off and replenished with 200 μL of PBS (0.05% BSA) solution. The fluorescence of the supernatant solution was read using a Cytation 5 plate reader.

D-DATE binding and cytotoxicity Cytotoxicity assays were conducted to determine if modified D-DATE retained cytotoxic effects. 25 000 GBM FFLuc and BT935 FFLuc cells were seeded onto a 96 well plate. Different effector (T cell) concentrations and 50 nM (4 μg mL^{-1}) of DATE or D-DATE were then added. Co-culture was then incubated at 37°C, 5 % CO_2 for 24 h. Brightfield micrographs were then taken of each condition. Luciferin was then added, and luminescence was read using a Biotek Cytation 5 plate reader. Luminescence signals were then normalized to co-cultures with the same E:T ratio without the addition of DATE or D-DATE.

Similarly, a dose response curve was constructed assessing the cytotoxicity of DATE and D-DATE at different concentrations against GBM08 FFLuc and BT935 FFLuc cells. A 2:1 E:T ratio was used for this assay.

IL-15 and αPD-1 synergism cytotoxicity experiments IL-15 and PD-1 synergism with D-DATE was assessed through a similar cytotoxicity assay. 25 000 GBM8 FFLuc cells in XF-T were seeded onto a 96 well plate. 100 000 T cells (resulting in a 4:1 E:T ratio) in XF-T were then added. Solutions of αPD-1 (10 μg mL^{-1}), IL-15 (5 ng mL^{-1}) and/or D-DATE (50 nM 4 μg mL^{-1}) in PBS were then added to the wells. Cells were then incubated at 37°C 5% CO_2 for 1d, 3d and 5d. Luciferin was then added to each well and luminescence was read using a Biotek Cytation 5 plate reader. Luminescence signals were then normalized to co-cultures where no drug was added.

A similar experiment was performed using BT935 FFLuc cells.

Exhaustion Experiments T cells were expanded using established protocols. A co culture of GBM08 cells (600 000) were mixed with T cells (1 200 000 cells) resulting in a 2:1 E:T ratio. D-DATE (4 μg mL^{-1}, 50 nM) or αPD-1 (10 μg mL^{-1}) were then added to the cells and the cells were incubated for 4 days at 37°C 5% CO_2. Cells were then labelled with CD3, CD4, CD8a, LAG-3, TIM3 and PD-1 antibodies and flow cytometry analysis were performed. The exhaustion experiments were then repeated with a 2:1 E:T ratio.

Memory and Activation Experiments T cells were expanded using established protocols. A co-culture of GBM08 cells (600 000) were seeded with expanded T cells (1 200 000 cells) resulting in a 2:1 E:T ratio. D-DATE (4 ug mL^{-1}, 50 nM) or αPD-1 (10 ug mL^{-1}) was added and co-cultures were incubated for 10 days at 37 °C 5% CO_2. Cells were then labelled with CD4, CD45RO and CCR7 antibodies and flow cytometry analysis was performed. An experiment with similar conditions was performed to measure activation markers on T cells, CD25, CD69 and CD4.

D-DATE and αPD-1 release αPD-1 antibody was first modified with Alexa Fluor 647. Briefly, 1 µL of Alexa Fluor-647 (10 mg mL^{-1}) in DMF was added to 30 µL αPD-1 in PBS (9.67 mg mL^{-1}) and reacted for 3 h in the dark at room temperature. The solution was then dialyzed against PBS (MWCO 12-14k) for 2 days at 4°C in the dark.

pCB-DBCO (100 mg mL^{-1} in PBS) was incubated with NT-Az overnight at room temperature. D-DATE-488 was then added to the solution and incubated overnight at room temperature in the dark. pCB-AzM was then dissolved in PBS and mixed with a suspension biotin derivative in PBS. The two solutions were then mixed into a 96 well plate and gelled for 30 minutes at room temperature in the dark, yielding 60 µL 10 wt% pCB gels at the bottom of the 96 well plate which with 0.2 mg mL^{-1} NT-Az, 0.05 mg mL^{-1} D-DATE, 0.05 mg mL^{-1} αPD-1 and different 200 µM of hexadecylbiotin suspension.

200 μL of PBS supplemented with 0.05% BSA was then pipetted over top the gels. The gels were then incubated at 37°C. At specific time intervals the PBS solution was carefully pipetted off and replenished with 200 μL of PBS (0.05% BSA) solution. The fluorescence of the supernatant solution (ex: 495nm, em: 519nm for D-DATE; ex: 651nm, em: 672nm for PD-1) was read using a Cytation 5 plate reader.

in vivo efficacy GBM8 FFLuc (200 000 cells) were implanted into NSG mice and allowed to grow for 7 days until the presence of a tumor was seen through IVIS. Treatment initiates 7 days after initial implantation of the cells.

1 x 10^6 T cells expanded from established procedures were suspended in PBS (5 μL) and intracranially injected through a 32 gauge syringe. Subsequently, treatments were intracranially injected through a 32 gauge syringe as follows: 10 μL of PBS; 10 μL of 1.5 mg mL^{-1} DATE (15 μg); 10 μL of pCB hydrogel (10 wt%) mixed with 1.5 mg mL^{-1} DATE (15 μg); 10 μL of pCB hydrogel (10 wt%) with DARA (fast; 200 μM oleylbiotin pellets; 2 mg mL^{-1} NT) and 1.5 mg mL^{-1} D-DATE (15 μg); 10 μL of pCB hydrogel (10 wt%) with DARA (slow; 200 μM hexadecylbiotin pellets; 2 mg mL^{-1} NT) and 1.5 mg mL^{-1} D-DATE (15 μg).

Luciferin (100X) was injected intraperitoneally into mice at 10 μL per 1 g of bodyweight and allowed to circulate in the mouse for 10 minutes before imaging through the IVIS. Counts and total luminescence were used to measure tumor burden over time.

in vitro spheroid toxicity assay BT935 iRFP670 spheroids were produced using an Aggrewell 800 24 well plate according to supplied protocols (with 2000 cells per spheroid). The spheroids were grown in Neurocult complete medium (20 ng mL^{-1} EGF, 10 ng mL^{-1} bFGF, 2 μg mL^{-1} heparin) overnight and then harvested. Similarly, GBM08 eGFP spheroids were produced using an Aggrewell 800 24 well plate (500 cells/well) with the addition of 10% Matrigel to the Neurocult complete media. Spheroids were grown for 5 days to reach maturation. Separately, PBMC's were expanded via established protocols.

Hydrogels of different conditions were prepared. 5 μL of each condition was dispensed onto the bottom of a 384 well plate and incubated for 30 minutes at 37°C to ensure gelation. BT935 iRFP670 spheroids (average concentration 5 spheroids per 10 μL) were suspended in a 1 wt% HA/ 1 wt% collagen mixture to a concentration of 5 spheroids per 10 μL. 10 μL were then dispensed on top of the pCB gel. Separately, T cells were also suspended in the mixture (20 000 cells per 10 μL) and 10 μL dispensed on top of the spheroids. The ECM was cured at 37°C 5% CO_2 for 30 minutes. 75 μL of Fluorobrite media (10% FBS, 25mM HEPES, Glutamax supplemented), was then pipetted on top of the ECM mimic. Media was then frequently exchanged in order to mimic clearance. Fluorescence micrographs were taken using the Cytation 5 Imager at different time points.

Statistical Analyses All samples were performed in triplicate and expressed as mean ± standard deviation unless otherwise specified. All statistical analyses were performed using GraphPad Prism 8. $p < 0.05$ is indicated by *, $p < 0.01$ by ** and $p < 0.001$ ***.

5.4 Results and discussion

Injectable pCB hydrogels for sustained DATE release

pCB hydrogels were first synthesized, characterized and modified. The DAR system was then incorporated into the hydrogel. Tunable release of DATE was then demonstrated.

Injectable pCB hydrogels were fabricated as previously described (Chapter 3) with tunable DATE release rates (DAR; chapter 4). To degrade the hydrogel, a degradable bond (β eliminative carbamate bond) with a half-life ($t_{1/2}$) of 150 h was incorporated into the crosslinks.[17,18] Briefly, a pCB-APMA random copolymer was synthesized using RAFT polymerization (34 969 Da, 3.5 mol % amine, **Figure S 5.1**). The amines were then converted to either DBCO (pCB-DBCO) or a degradable azide linker (pCB-AzM) resulting in a ~4 mol% substitution according to ^{1}H NMR spectroscopy (**Figure S 5.2, Table S 5.1**). Gelation occurred in 3 minutes when the hydrogel precursors pCB-AzM and pCB-DBCO were mixed at 10 wt%. The hydrogel was confirmed to degrade over 40 days in PBS (**Figure S 5.3**). To assess safety and degradation of the hydrogels

in vivo, fluorescently (Cy7) labelled hydrogels were intracranially injected into mice (**Figure S 5.4**). The hydrogel or its degraded polymers were retained at the site of injection for up to 6 weeks. It is difficult to differentiate the fluorescence from the intact hydrogel or the degraded polymers, hence the difference between the degradation study in vitro vs degradation in vivo, as the clearance of free degraded polymers from the CNS is not immediate as it is in the simulated in vitro experiment. Clearance and degradation were evident from fluorescent signals in different parts of the body at the time points imaged (**Figure S 5.4**). Furthermore, the mice successfully survived all injections of the hydrogel signifying that the hydrogel can safely be injected with good tolerance. Therefore, it is a suitable drug delivery vehicle for sustained local delivery of DATE in the preclinical mouse model.

Sustained release of D-DATE

The DAR DDS was then incorporated into the pCB hydrogel for sustained D-DATE release. DATE and neutravidin (NT) were modified with desthiobiotin and NHS-azide respectively, resulting in shifts in MW (**Figure S 5.5**) corresponding to an average of 10 desthiobiotins per a DATE and 10 Az per a NT. DATE remained bioactive after desthiobiotin modification but the half maximal effective concentration (EC_{50}) against patient derived, high expressing $CD133^+$ glioblastoma cells GBM08 (Figure 5.2**a**) and BT935 (**Figure 5.2b**) increased after modification. The EC_{50} of the modified D-DATE was shifted from

17.5 pM and 126 pM to 106.9 pM and 1076.3 pM against GBM08 and BT935 respectively (**Table S 5.3**), a 5.33 fold and 7.43 fold change in EC_{50}. There was also no change in cytotoxicity when varying effector to target (E:T) ratios for GBM08 (**Figure 5.2c**) and BT935 (**Figure 5.2d**). Although EC_{50} is increased, local release can achieve intratumoral concentrations above the modified EC_{50}.

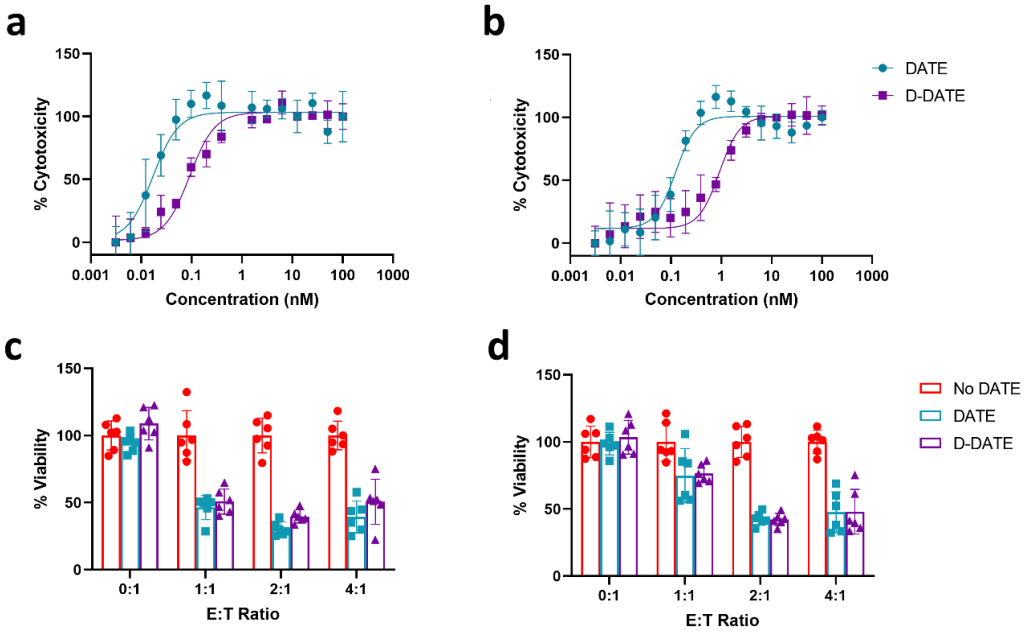

Figure 5.2 D-DATE is bioactive against CD133+ GBM cells. EC_{50} dose-response curves of D-DATE against GBM08 (a) or BT935 (b) cells at a 2:1 E:T ratio (n = 3, ± SD). Lines of best fit were plotted using Graphpad Prism 8 using

the dose response curve function. E:T ratio comparison of 50 nM DATE vs D-DATE against GBM08 (c) and BT935 (d). (n = 6, ± SD)

In vitro release of a desthiobiotinylated DATE (D-DATE) was performed, showing tunable DATE release rates for over 14 days (**Figure 5.3a, b, Table S 5.2**) upon varying the concentration and hydrophobicity of the competitive binder, biotin derivatives.

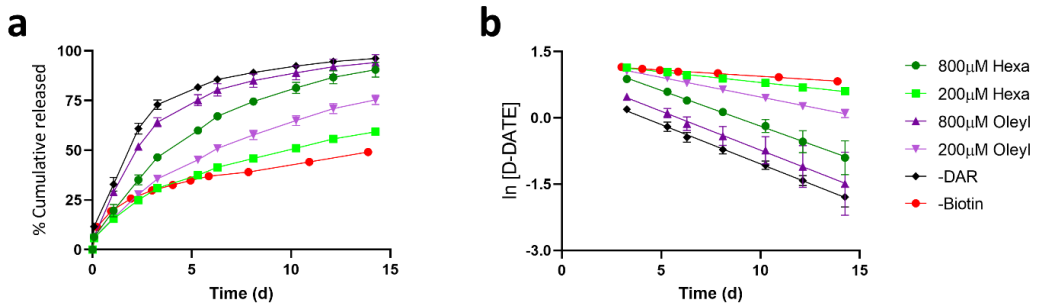

Figure 5.3 Release of bioactive D-DATE from pCB hydrogels (a) Cumulative release of D-DATE from a pCB hydrogel (10 wt%, n = 3, ± SD). (b) First order release graphs of cumulative release (n = 3, ± SD). -DAR refers to a hydrogel without NT or biotin derivatives. -Biotin refers to the DAR hydrogel systems without biotin derivatives.

To demonstrate that sustained release of DATE improves efficacy, an in vitro co-culture with two dosing timepoints at days 0 and 5 was conducted. While

keeping the total dose the same, dosing the DATE twice at day 0 and 5 retarded cell growth to a greater extent than one dose at day 0 (**Figure 5.4b, c**). A double dose of DATE reduced cancer cell growth to 48% and 8% of relative viability in GBM08 and BT935 cells respectively at day 12. Whereas a single dose of DATE resulted did not impede cell growth with cells showing 104% and 16% relative viability in GBM08 and BT935 cells respectively at day 12. Showing a ~50% reduction in viability for both cell types at day 12.

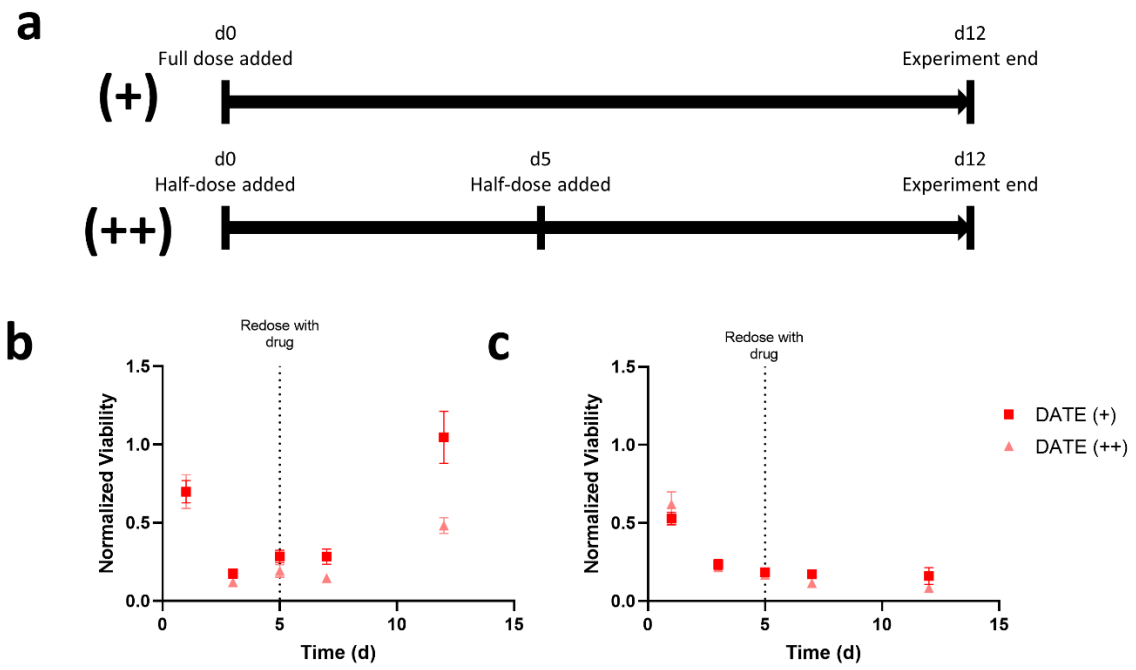

Figure 5.4 Multiple doses of DATE prolongs T cell mediated killing of GBM cells. Cell viability as measured through luminescence GBM cells in different conditions over time. (a) Legend and timeline of dose additions to cells. (+)

indicates one dose with the drug administered at day 0. (++) indicates two doses of the drug at day 0 and a second dose at day 5. Cell viability over time of GBM08 FFLuc (b) or BT935 FFLuc (c) cells co-cultured with T cells (2:1 E:T ratio) when exposed to DATE at different time points (n = 6, ± SD)

After tunable release of a bioactive D-DATE was confirmed, a preliminary in vivo experiment was performed. GBM08 firefly luciferase expressing (GBM08 FFLuc) cells were implanted into NOD-SCID-gamma (NSG) mice, treatments were administered after 7 days (**Figure 5.5a**). IVIS luminescent imaging was performed to track tumor size over time (**Figure 5.5b, c**). There is an increase in survival when the pCB hydrogel with DAR was implanted for sustained D-DATE release (**Figure 5.5d**). GBM08 PDX tumor models showing modest increase in survival is promising as this cell line is malignant and kills mice rapidly. For the slowest and longest D-DATE release profile (hexa), there is a prominent reduction in tumor size at Day 7 seen through IVIS images (**Figure 5.5b**) showing that longer D-DATE release profiles are efficacious.

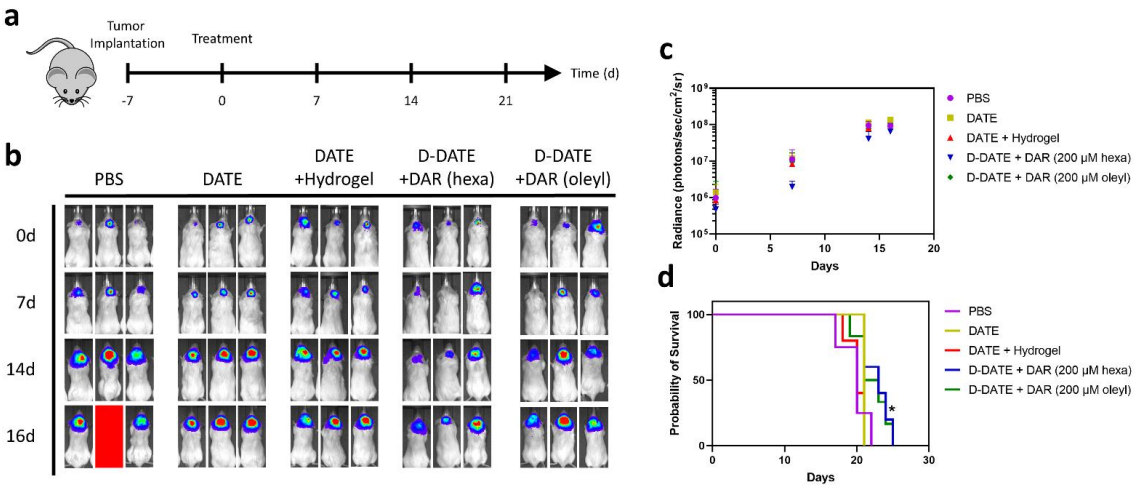

Figure 5.5 PDX glioblastoma mice with GBM08 FFLuc intracranial tumors treated with D-DATE sustained release hydrogels. (a) Timeline for tumor implantation and treatment initiation. (b) In vivo bioluminescence of GBM08 FFLuc tumors. (c) In vivo bioluminescent signals of GBM08 FFLuc tumors with different treatments. (d) Survival curves for different treatment groups (Kaplan Meier test).

Although the in vivo study showed promise, survival benefit remained minimal. To extend survival, we are exploring longer DATE release profiles and combination therapies with IL-15 and αPD-1 antibody (**Figure 5.6)**. Individually, IL-15 and αPD-1 improved DATE efficacy against both BT935 (**Figure 5.6a, c**) and GBM08 (**Figure 5.6b, d**). Interestingly, no improvement was observed when both IL-15 and αPD-1 were combined with or without DATE (**Figure 5.6c, d**). To assess if there were significant differences over time, the drug combination study was performed with multiple timepoints (1, 3, 5 days). All timepoints showed a

very similar trend, where the addition of IL-15 or αPD-1, but not both, improved DATE efficacy (**Figure S 5.6, Figure S 5.7**). As αPD-1 is a commonly used clinical therapy and checkpoint inhibitors in combination with a bispecific T cell engager (such as a DATE) have been shown to be synergistic,[19–22] αPD-1 was chosen for further study as a combination therapy with the CD133 DATE.

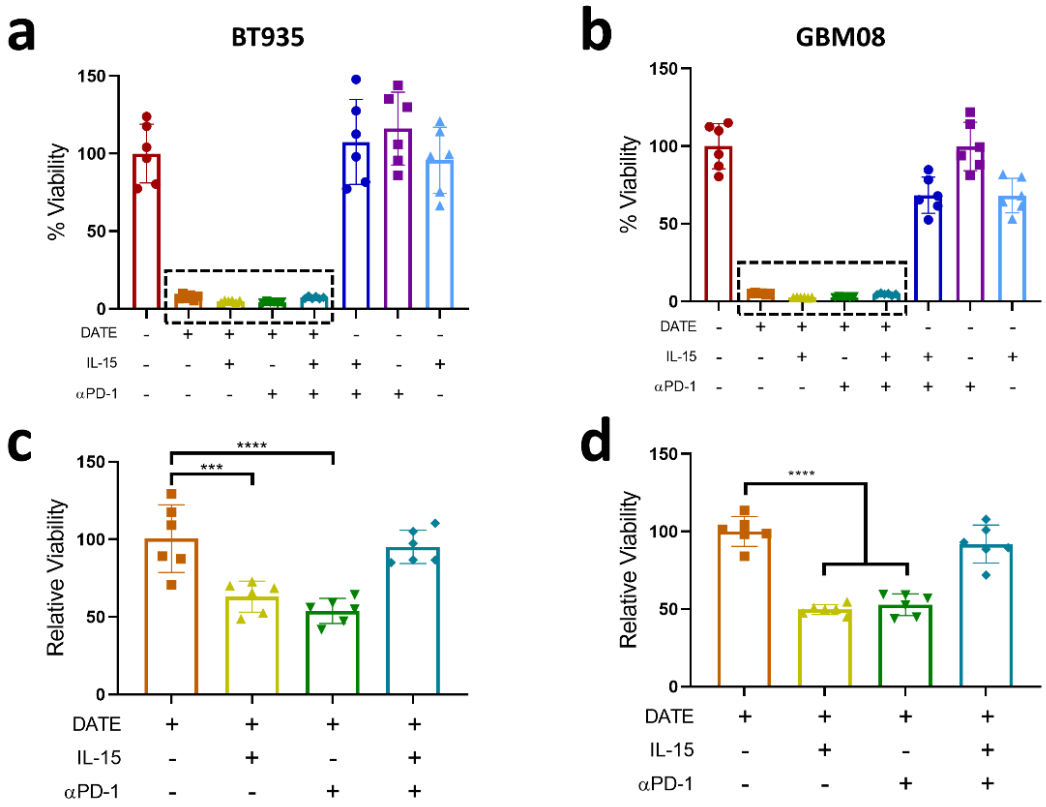

Figure 5.6 Combination therapy of αPD-1 or IL-15 enhance T cell mediated killing. Combination therapy efficacies against BT935 (a, c) or GBM08 (b, d) patient derived cell lines after 5 days of culture. Relative viability of BT935 (a) or GBM08 (b) with combination therapies normalized to no treatment. Relative

viability of BT935 (c) or GBM08 (d) with combination therapies normalized to DATE alone (n = 6, ± SD, one way ANOVA Tukey's post hoc test).

Sustained release of DATE but not αPD-1 is required to improve efficacy (**Figure 5.6**, **Figure S 5.8**); therefore, αPD-1 could be potentially introduced as a single injection without sustained release. The addition of αPD-1 significantly improved efficacy than either the single or double DATE conditions (**Figure 5.7a, b**). At day 12, the combination DATE + αPD-1 conditions had an ~80% and ~60% reduction in GBM08 and BT935 viability, respectively, compared with a single supplementation of DATE (**Figure 5.7c, d**). Without the addition of DATE, both cell lines proliferated and showed high levels of firefly luciferase expression and no cytotoxicity as expected (**Figure S 5.6, Figure S 5.7**). Interestingly, pre-exposing T cells to αPD-1 antibody shows a similar benefit as the simultaneous addition of DATE and αPD-1 (**Figure 5.7e**). This may be due to an increase in exhausted T cells (T_{ex}), as seen in an increase in LAG-3 expression on the T cell, indicative of a malfunctioning and overstimulated T cell.[19,23,24] Therefore, αPD-1 does not require sustained release to improve DATE efficacy.

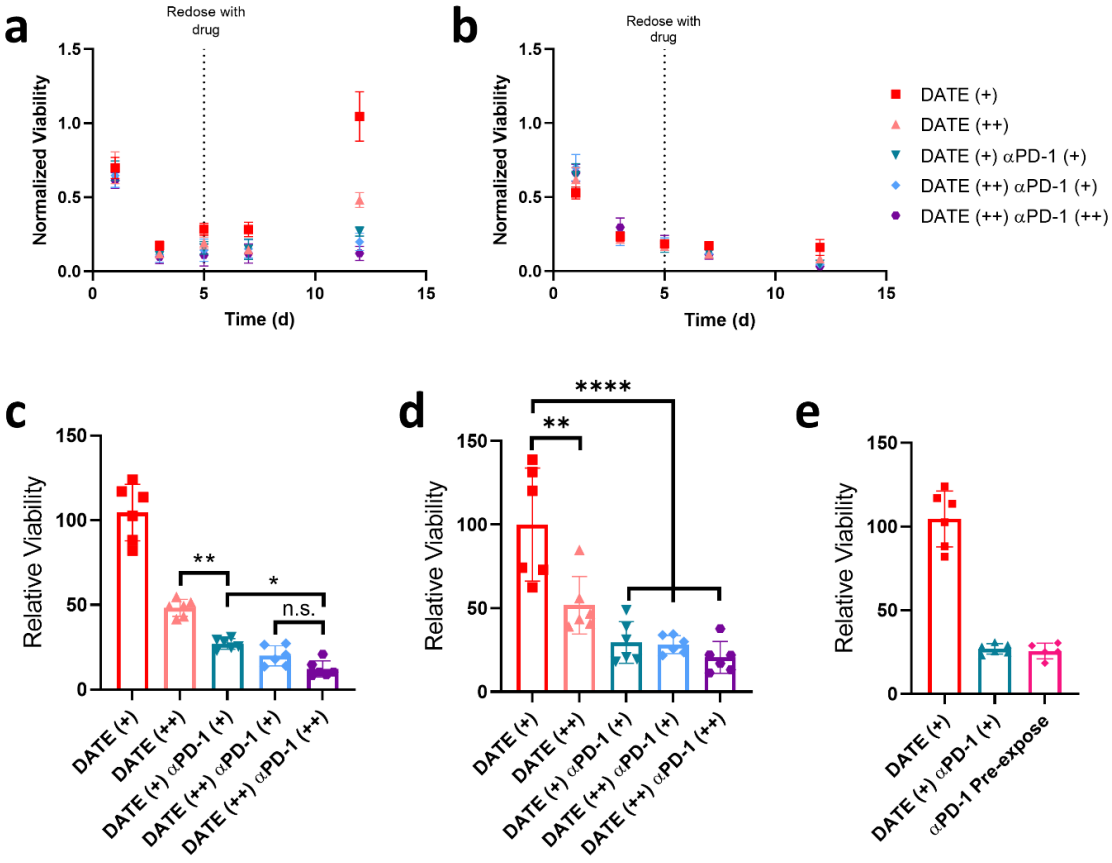

Figure 5.7 Multiple DATE doses as combination therapies for enhanced killing over time. Cell viability over time of GBM08 FFLuc (a) or BT935 FFLuc (b) cells co-cultured with T cells when exposed to DATE, αPD-1 antibody. (n = 6, ± SD) Percent viability of GBM08 FFLuc (c) or BT935 FFLuc (d) at day 12 when normalized to DATE (+) at day 0 (n = 6, one way ANOVA Tukey's post hoc test). e) Percent viability of cells at day 12 when normalized to DATE (+) with the

addition of a condition where T cells were pre-exposed αPD-1 condition and DATE was added at day 0. Normalized to DATE (+) at day 0.

Exhaustion markers on T cells resulting from chronic exposure of DATE and addition of αPD-1 were assessed using flow cytometry. The addition of αPD-1 reduced the expression of PD-1 and LAG-3 expression (**Figure 5.8a**), which are markers which indicate an overstimulated and exhausted T cell phenotype (T_{Ex}) resulting in a loss of cytotoxic activity. Furthermore, pre-exposure with αPD-1 resulted in a reduced population of T cells expressing PD-1 and LAG-3, signifying a smaller population of exhausted T cells (**Figure 5.8a**). There is no change in TIM3 expression levels in either condition (**Figure 5.8a**). Pre-exposure with αPD-1 showed a significant reduction in the number of cells which expressed high levels of both PD-1 and LAG-3 from 34.8% to <20% of cells with high expression levels of the two exhaustion markers (**Figure 5.8b**).

Activation and memory T cell markers were also assessed to ensure the DATE was stimulating T cells and to investigate the influence of αPD-1. CD69 and CD25 activation markers increased upon the addition of DATE but not αPD-1 as expected (**Figure S 5.9a, b**). These two markers signify the activation and T cell receptor (TCR) ligation by the DATE, which shows binding of the DATE to the T cell.[16,25,26] Changes in CCR7 and CD45RO (**Figure S 5.9c**) expression levels were also assessed for changes in T cell memory over time. There was a slight increase in the CD45RO expression levels, which is characteristic of T cell

activation by bispecific T cell engager modalities, which corresponds well with previous reported effect of bispecific T cell engagers which enrich T cell effector memory (T_{EM}).[26] Therefore, αPD-1 addition does not interfere or modulate the primary method of T cell activation through bispecific T cell engagers.

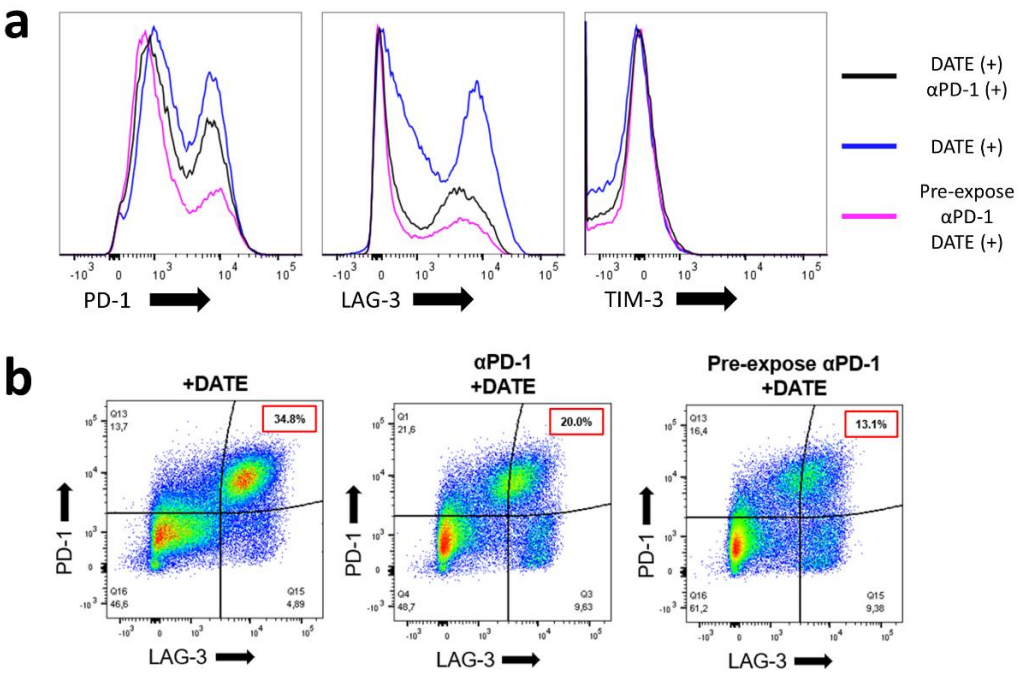

Figure 5.8 αPD-1 and DATE addition reduces expression of T cell exhaustion markers when co-cultured with GBM08. Flow cytometry data for T cells when co-cultured with GBM08 and exposed to 50 nM DATE and 10 μg mL^{-1} of αPD-1 after 14 days with a 2:1 E:T ratio. (a) Comparison of T cell expression of exhaustion markers PD-1, LAG-3, and TIM-3. Higher fluorescence intensity indicates higher expression levels of the corresponding marker. (b) 2D flow

cytometry charts of T cells expressing correlating individual cells and their respective levels of LAG-3 and PD-1 expression.

When exposed to αPD-1, T cells showed greater cytotoxicity and lower exhaustion marker expression. As previously hypothesized, this may be due to increasing the lifetime of cytotoxic T cell phenotypes, which results in greater cytotoxicity against cancer cells. Therefore, local administration of αPD-1 alongside DATE is beneficial in providing a stronger and sustained anti-cancer response, resulting in increased survival benefit. The release of a αPD-1 antibody does not interfere with tunable release of D-DATE (**Figure S 5.10**), therefore DAR-pCB is amenable to the simultaneous release of these two antibodies.

Determining the effect of DATE and αPD-1 combination therapies on both T cell and glioblastoma cell markers is of vital importance in optimizing bispecific immunotherapies. There is evidence that the use of BiTEs in an T cell exhaustion markers upregulation PD-1 and LAG-3 that corresponds to a malfunctioning and less cytotoxic T cell. The addition of αPD-1 has been shown to rescue T cells from this phenotype in chronic infections.[24] Furthermore, there is evidence that bispecific T cell engager therapy results in an upregulation of PDL-1 in the cancer cells, in conjunction with the upregulation of PD-1 on the T cells, resulting in the inhibition of cytotoxic pathways.[19,21,24]

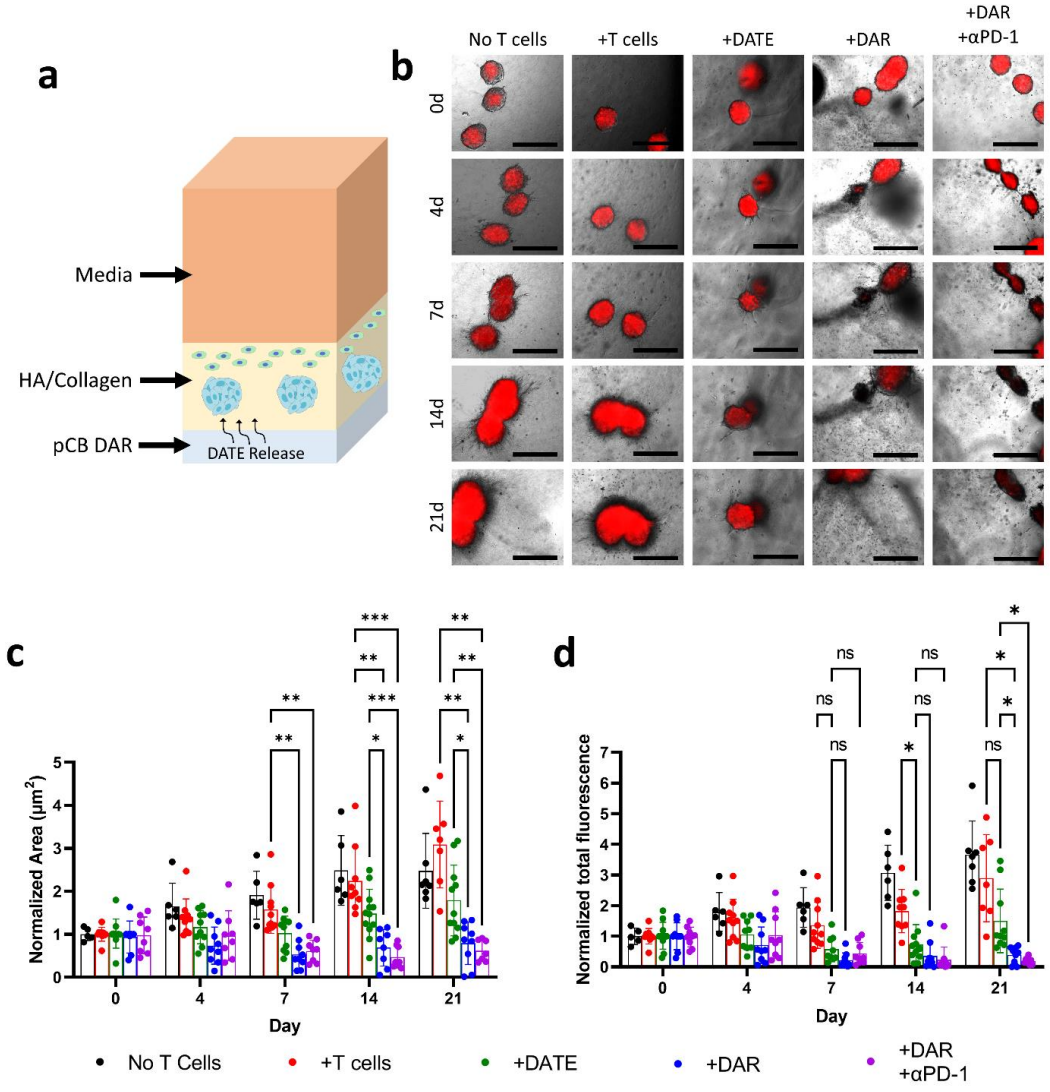

Figure 5.9 In vitro BT935 iRFP670 spheroid growth and killing as a function of DATE delivery method. (a) 3D embedded spheroid model. Spheroids and T cells imbedded within a 1% HA/collagen hydrogel. pCB-DAR loaded with DATE is placed at the bottom and slowly releases the DATE over time. (b) Fluorescence micrographs of embedded spheroids composed of BT935 iRFP670 cells (scale bar = 400 μm). (c) Fluorescence area normalized to day 0 of each condition. (d) Total

fluorescence signal of images taken normalized to day 0 of each condition (mean ± SD, 2-way ANOVA with Tukey's post-hoc test).

An in vitro spheroid assay was performed to simulate in vivo glioblastoma growth and the efficacy of DAR in vitro. BT935 expressing iRFP670 and T cells were embedded in a 1wt% HA 1wt% collagen matrix which mimics the components of the brain ECM (**Figure 5.9a**) and have been shown to promote cancer cell invasion and proliferation.[27,28] There is a decrease in spheroid fluorescence intensity in both fluorescent area (**Figure 5.9b, c, Figure S 5.11a**) and total fluorescence of the spheroids (**Figure 5.9d, Figure S 5.11b**) as time progresses with both the DAR and DAR +αPD-1 when compared to addition of DATE only at day 21. Indicating the effectiveness of the pCB-DAR system in continuously infusing the environment with DATE. However, there is no significant difference with the addition of αPD-1. Longer time periods may be necessary to illustrate the difference. In vitro spheroid efficacy demonstrates the effectiveness of the DAR system in sustaining therapeutic concentrations of DATE within the system, resulting in enhanced benefit and decrease growth over time (**Figure S 5.11**).

5.5 Conclusions

Here we first demonstrated that repeated dosing enhances the efficacy of a bispecific antibody. By maintaining therapeutic DATE concentrations through

repeated dosing of the DATE, cancer cell killing was enhanced in vitro for extended periods of time when compared to 1 dose. Therefore, the repeated dosing experiments demonstrated that continuous infusion of DATE in the tumor will promote DATE mediated tumor killing.

An initial in vivo experiment demonstrates DATE loaded pCB-DAR provides some benefit to overall survival in a GBM PDX mouse model, increasing median survival by 2 days. We also show through the incorporation of a tunable degradable bond, the hydrogel can be safely intracranially injected and degraded in a mouse. Therefore, the injectable DAR system for sustained release provides increased therapeutic benefit and enhances the therapeutic efficacy of the DATE.

To improve DATE efficacy even further, we combined DATE with an ICI (αPD-1) to enhance T cell mediated tumor killing; ICIs help prevent T cell exhaustion. Through the simple addition of the ICI, greater sustained cancer cell killing was observed when compared to repeated dosing of DATE alone. Therefore, the addition of an ICI with the DATE is an efficacious combination therapy.

We then developed an in vitro 3D spheroid tumor model to identify and determine the efficacy of different therapeutic release mechanisms and combination therapies. Treatment with pCB-DAR showed enhanced therapeutic benefit by decreasing GBM spheroid viability over time when compared to DATE

alone. Further providing evidence that sustained release of therapeutic DATE is necessary for inhibition of tumor growth, and continuous tumor killing by T cells.

Lastly, an additional final in vivo experiment will also be performed where we would increase drug loading as well as include αPD-1 as a combination therapy for improved efficacy. By increasing both the loading of the drug and including an αPD-1 inhibitor, we hypothesize that the in vivo experiment would result in a significant enhancement in tumor killing and increase survival.

5.6 References

1. Newick, K., O'Brien, S., Moon, E. & Albelda, S. M. CAR T Cell Therapy for Solid Tumors. *Annu. Rev. Med.* **68**, 139–152 (2017).

2. Weiner, G. J. Building better monoclonal antibody-based therapeutics. *Nature Reviews Cancer* vol. 15 361–370 (2015).

3. Huehls, A. M., Coupet, T. A. & Sentman, C. L. Bispecific T-cell engagers for cancer immunotherapy. *Immunol. Cell Biol.* **93**, 290–296 (2015).

4. Goodman, A. M. *et al.* Tumor mutational burden as an independent predictor of response to immunotherapy in diverse cancers. *Mol. Cancer Ther.* **16**, 2598–2608 (2017).

5. Lim, M., Xia, Y., Bettegowda, C. & Weller, M. Current state of

immunotherapy for glioblastoma. *Nat. Rev. Clin. Oncol.* **15**, 422–442 (2018).

6. Preusser, M., Lim, M., Hafler, D. A., Reardon, D. A. & Sampson, J. H. Prospects of immune checkpoint modulators in the treatment of glioblastoma. *Nat. Rev. Neurol.* **11**, 504–514 (2015).

7. Keskin, D. B. *et al.* Neoantigen vaccine generates intratumoral T cell responses in phase Ib glioblastoma trial. *Nature* **565**, 234–239 (2019).

8. Schumacher, T. N. & Schreiber, R. D. Neoantigens in cancer immunotherapy. *Science (80-.).* **348**, 69–74 (2015).

9. Khasraw, M., Reardon, D. A., Weller, M. & Sampson, J. H. PD-1 Inhibitors: Do they have a Future in the Treatment of Glioblastoma? *Clin. Cancer Res.* **26**, 5287–5296 (2020).

10. Goebeler, M. E. & Bargou, R. C. T cell-engaging therapies — BiTEs and beyond. *Nat. Rev. Clin. Oncol.* **17**, 418–434 (2020).

11. Parker, K. R. *et al.* Single-Cell Analyses Identify Brain Mural Cells Expressing CD19 as Potential Off-Tumor Targets for CAR-T Immunotherapies. *Cell* **183**, 126-142.e17 (2020).

12. Francis, D. M. *et al.* Blockade of immune checkpoints in lymph nodes through locoregional delivery augments cancer immunotherapy. *Sci. Transl. Med.* **12**, 1–12 (2020).

13. Ishihara, J. *et al.* Matrix-binding checkpoint immunotherapies enhance antitumor efficacy and reduce adverse events. *Sci. Transl. Med.* **9**, (2017).

14. Chen, Q. *et al.* In situ sprayed bioresponsive immunotherapeutic gel for post-surgical cancer treatment. *Nat. Nanotechnol.* **14**, 89–97 (2019).

15. Singh, S. K. *et al.* Identification of human brain tumour initiating cells. *Nature* **432**, 396–401 (2004).

16. Vora, P. *et al.* The Rational Development of CD133-Targeting Immunotherapies for Glioblastoma. *Cell Stem Cell* **26**, 832–844 (2020).

17. Santi, D. V., Schneider, E. L., Reid, R., Robinson, L. & Ashley, G. W. Predictable and tunable half-life extension of therapeutic agents by controlled chemical release from macromolecular conjugates. *Proc. Natl. Acad. Sci. U. S. A.* **109**, 6211–6216 (2012).

18. Shoaib, M. M. *et al.* Controlled degradation of low-fouling poly(oligo(ethylene glycol)methyl ether methacrylate) hydrogels. *RSC Adv.* **9**, 18978–18988 (2019).

19. Huang, A. C. *et al.* T-cell invigoration to tumour burden ratio associated with anti-PD-1 response. *Nature* **545**, 60–65 (2017).

20. Crawford, A. *et al.* A Mucin 16 bispecific T cell-engaging antibody for the treatment of ovarian cancer. *Sci. Transl. Med.* **11**, eaau7534 (2019).

21. Krupka, C. *et al.* Blockade of the PD-1/PD-L1 axis augments lysis of AML cells by the CD33/CD3 BiTE antibody construct AMG 330: Reversing a T-cell-induced immune escape mechanism. *Leukemia* **30**, 484–491 (2016).

22. Kamphorst, A. O. *et al.* Rescue of exhausted CD8 T cells by PD-1-targeted therapies is CD28-dependent. *Science (80-.).* **355**, 1423–1427 (2017).

23. Wherry, E. J. & Kurachi, M. Molecular and cellular insights into T cell exhaustion. *Nature Reviews Immunology* vol. 15 486–499 (2015).

24. Sakuishi, K. *et al.* Targeting Tim-3 and PD-1 pathways to reverse T cell exhaustion and restore anti-tumor immunity. *J. Exp. Med.* **207**, 2187–2194 (2010).

25. Herrmann, M. *et al.* Bifunctional PD-1 3 aCD3 3 aCD33 fusion protein reverses adaptive immune escape in acute myeloid leukemia. *Blood* **132**, 2484–2494 (2018).

26. Aigner, M. *et al.* T lymphocytes can be effectively recruited for ex vivo and in vivo lysis of AML blasts by a novel CD33/CD3-bispecific BiTE antibody construct. *Leukemia* **27**, 1107–1115 (2013).

27. Tevis, K. M., Colson, Y. L. & Grinstaff, M. W. Embedded Spheroids as Models of the Cancer Microenvironment. *Adv. Biosyst.* **1**, (2017).

28. Herrera-Perez, M., Voytik-Harbin, S. L. & Rickus, J. L. Extracellular matrix properties regulate the migratory response of glioblastoma stem

cells in three-dimensional culture. *Tissue Eng. - Part A* **21**, 2572–2582 (2015).

5.7 Supplementary information

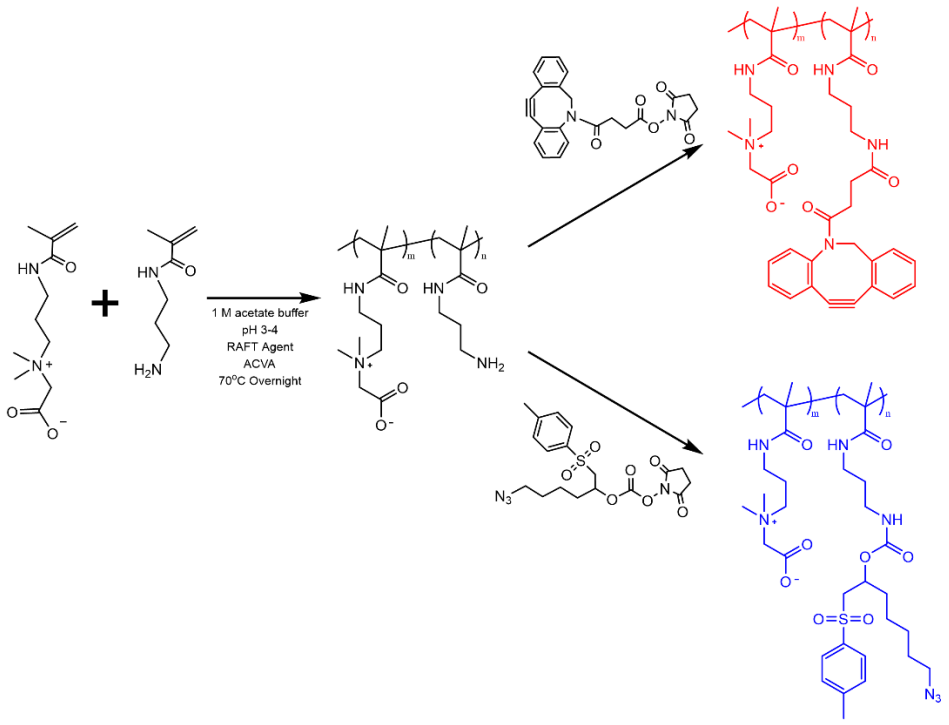

Figure S 5.1 pCB hydrogel synthesis. pCB-APMA copolymer was synthesized using RAFT. Amines were then modified to produce pCB-DBCO (red) and pCB-AzM (blue) precursors.

Table S 5.1 pCB polymer characterization. (a) pCB-APMA M_W characterization by GPC. APMA mol% determined through ^{1}H NMR. (b) pCB-DBCO and pCB-AzM substitution percentage as determined through ^{1}H NMR.

a

Polymer	M_W	M_n	Đ	APMA mol%
pCB-APMA	34 969	30 367	1.152	3.5

b

Polymer	% AzM	% DBCO
pCB-DBCO	-	3.8
pCB-AzM	4	-

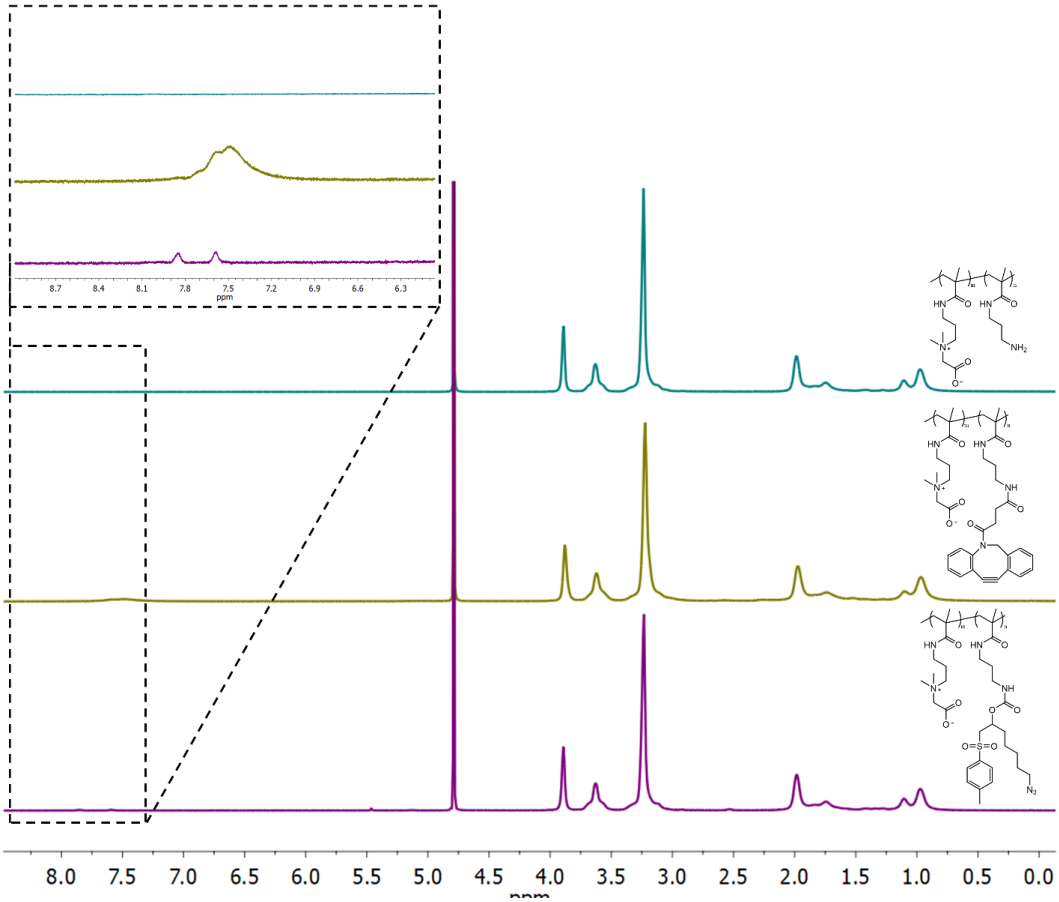

Figure S 5.2 ^{1}H NMR spectra of pCB-APMA (teal), pCB-DBCO (yellow) and pCB-AzM (purple). Highlighted portion indicates peaks used to determine substitution rate.

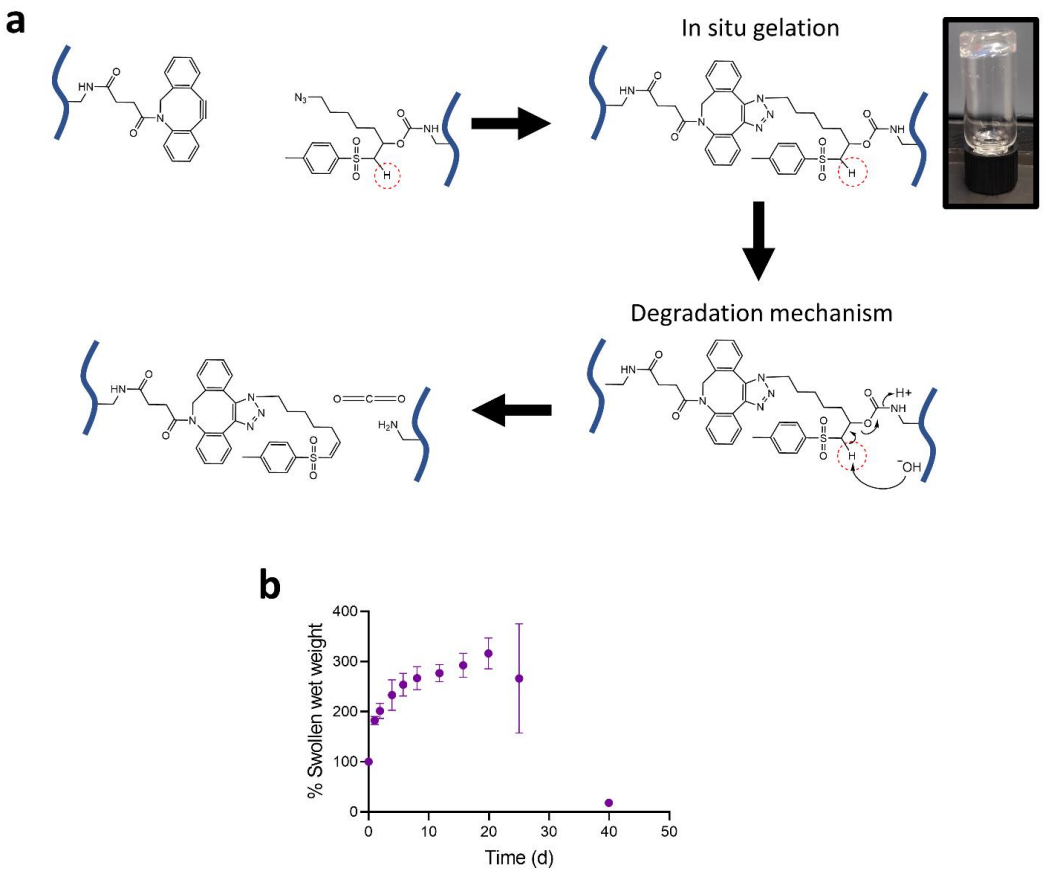

Figure S 5.3 pCB hydrogel in situ crosslinking mechanism and degradation.

(a) In situ crosslinking of hydrogel through SPAAC, followed by β elimination.

(b) In vitro hydrogel degradation in PBS pH 7.4 (n = 3, ± SD).

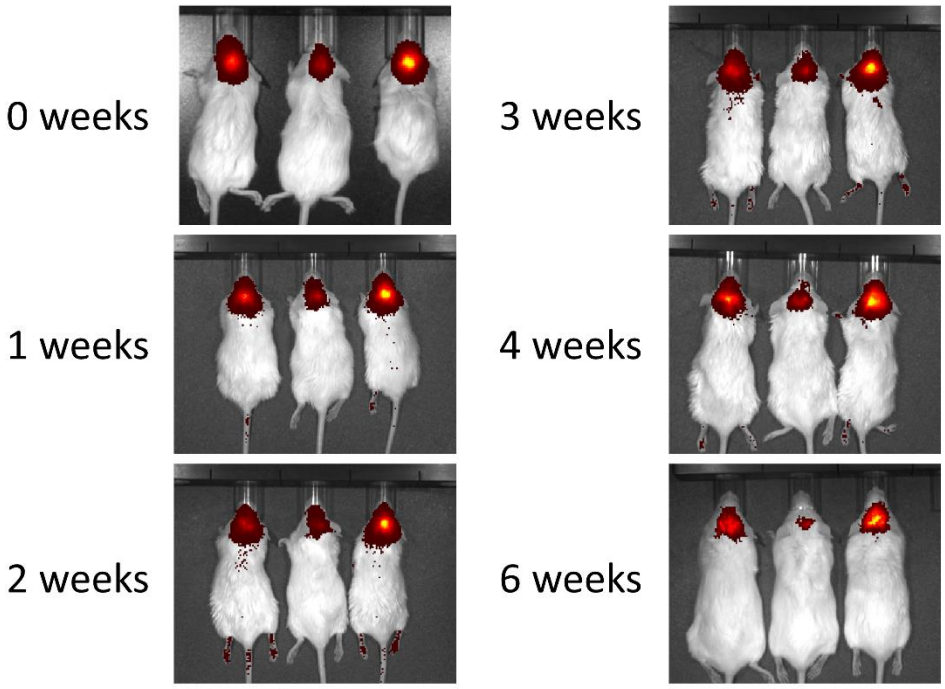

Figure S 5.4 In vivo degradation of a pCB hydrogel fluorescently tagged with Cy7 in NSG mice intracranially injected. Mice survived injection and fluorescence decreased over time indicating degradation and clearance of the degraded polymers.

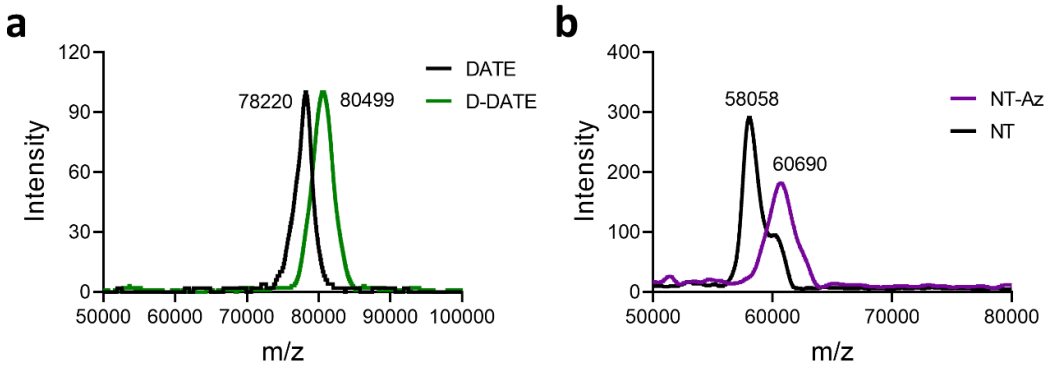

Figure S 5.5 MALDI-MS of modified proteins. (a) MALDI-MS of DATE and D-DATE showing ~10 desthiobiotins per DATE (b) MALDI-MS of NT and NT-Az showing ~9 Az moieties modified on a NT-Az.

Table S 5.2 Quantitative release values of D-DATE from a hydrogel. K_{eff} and rate of drug infusion obtained from linear regression model through GraphPad Prism 8.

Biotin	ng d^{-1} after 3d	R^2	K_{eff}	R^2
800 Hexa	152.2 ± 10.2	0.910	0.180 ± 0.014	0.876
200 Hexa	106.4 ± 3.7	0.975	0.047 ± 0.001	0.989
800 Oleyl	98.7 ± 9.8	0.823	0.167 ± 0.018	0.792
200 Oleyl	146.3 ± 6.8	0.955	0.088 ± 0.003	0.978
No Biotin	76.0 ± 3.6	0.958	0.028 ± 0.001	0.962
-DARA	76.1 ± 6.4	0.866	0.202 ± 0.015	0.887

Table S 5.3 EC_{50} values from dose-response curves of DATE and D-DATE. Factor indicates the magnitude in shift of EC_{50} of D-DATE to DATE from modification. EC_{50} values determined through GraphPad Prism 8, EC_{50} best fit function.

EC_{50}	GBM08	BT935
DATE	17.5 ± 4.3 pM	126.0 ± 30.1 pM
D-DATE	106.9 ± 56.9 pM	1076.3 ± 580.0 pM
Factor	5.326	7.43

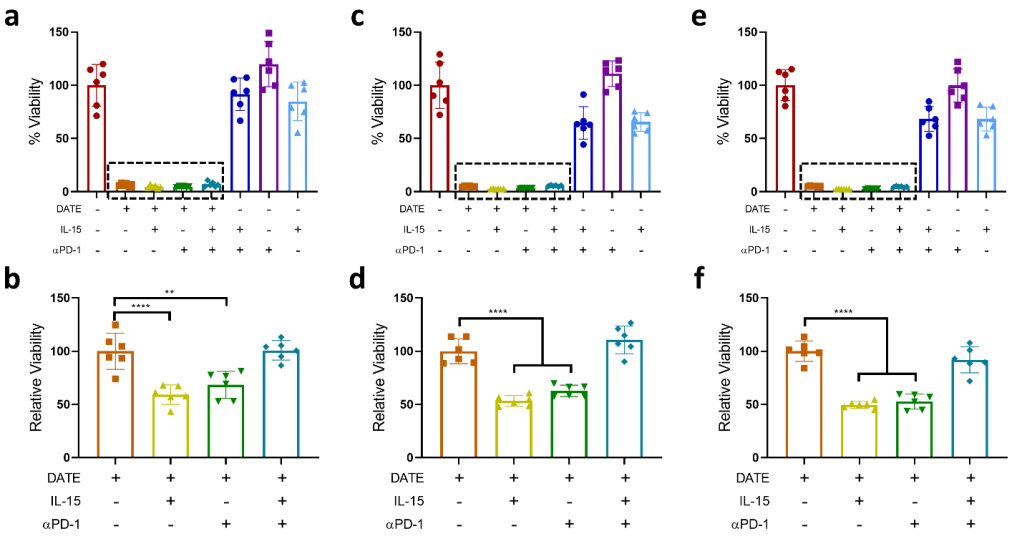

Figure S 5.6 In vitro screening of combination therapy combinations with DATE using GBM08 FFLuc cells. Cytotoxicity with a 4:1 E:T ratio after 1d (a, b), 3d (c, d) and 5d (e, f). Conditions normalized to no drug (a, c, e) and

normalized to addition of DATE only (b, d, f). Addition of 50 nM DATE and 10 µg mL^{-1} αPD-1 antibody. (n = 6, ± SD, one way ANOVA Tukey's post hoc test)).

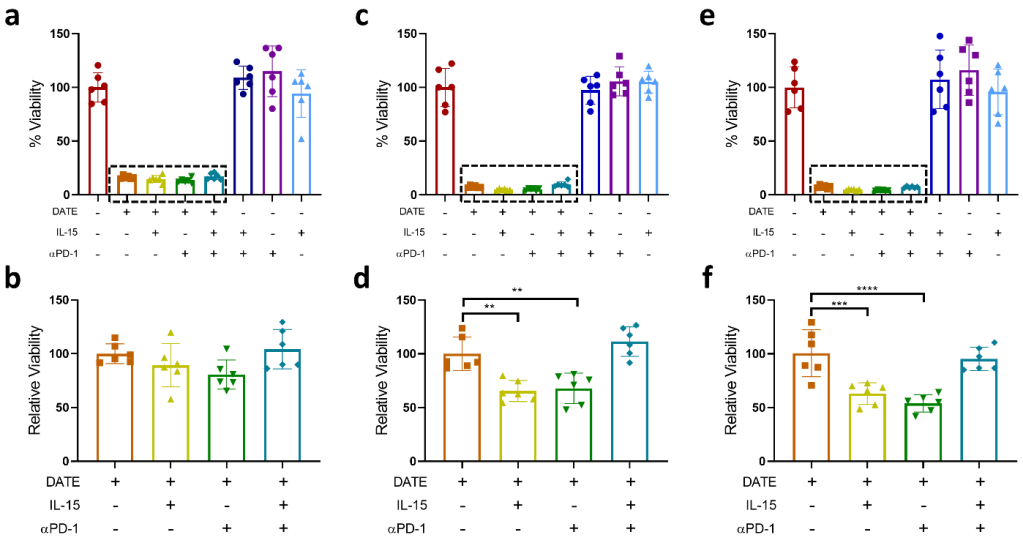

Figure S 5.7 In vitro screening of combination therapy combinations with DATE using BT935 FFLuc cells. Cytotoxicity with a 4:1 E:T ratio after 1d (a, b), 3d (c, d) and 5d (e, f). Conditions normalized to no drug (a, c, e) and normalized to addition of DATE only (b, d, f). Addition of 50 nM DATE and 10 µg mL^{-1} αPD-1 antibody. (n = 6, ±SD, one way ANOVA Tukey's post hoc test)).

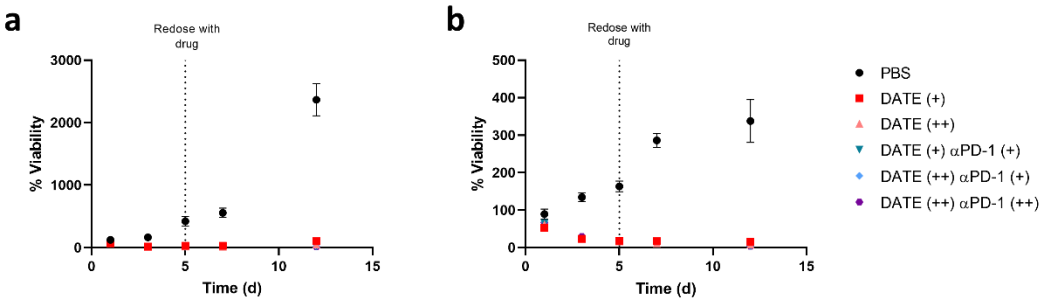

Figure S 5.8 Cell viability over time of glioblastoma cells normalized to no treatment (PBS). GBM08 FFLuc (a) or BT935 FFLuc (b) cells co-cultured with T cells (2:1 E:T) when exposed to DATE (50 nM), αPD-1 antibody (10 µg mL^{-1}). (+) signifies 1 dose with the drug administered at day 0. (++) signifying two doses of the drug with the first dose at day 0 and the second dose at day 5.

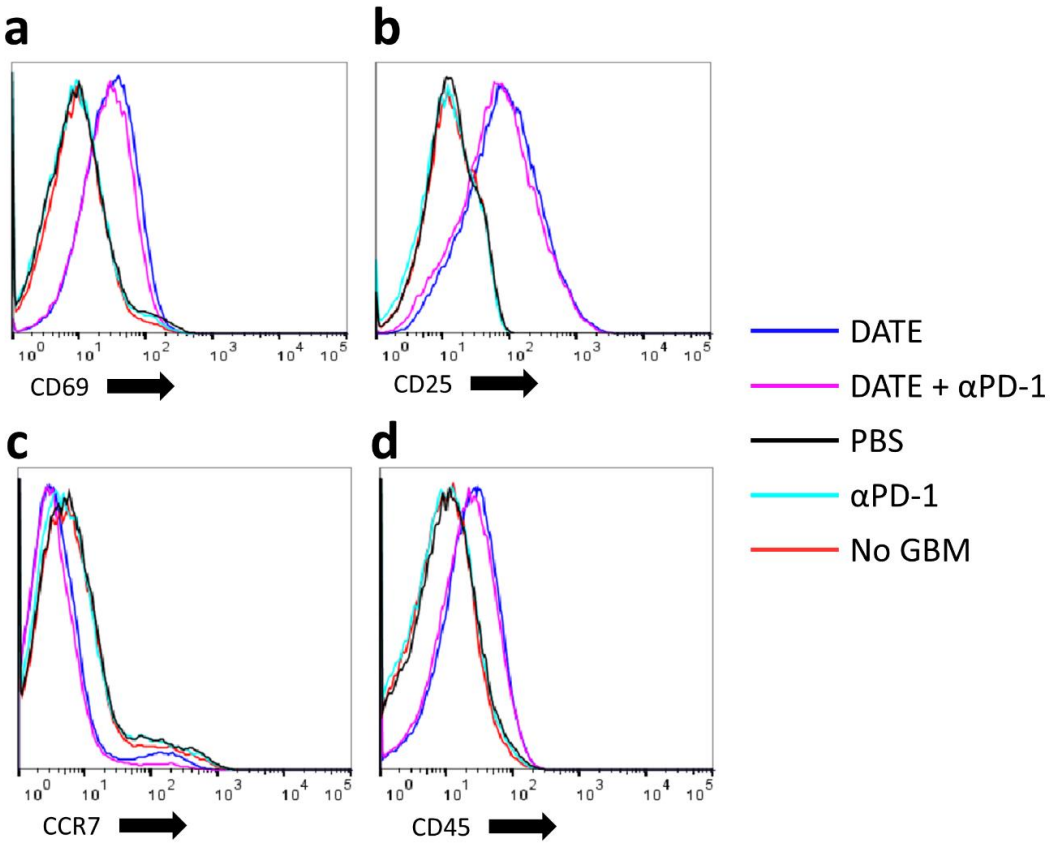

Figure S 5.9 Activation and memory markers on T cells when incubated with DATE (50 nM) and/or αPD-1 (10 µg mL^{-1}) after 5 days. CD69 (a) and CD25 (b) expression as T cell activation markers. CCR7 (c) and CD45RO (d) for T cell memory influence.

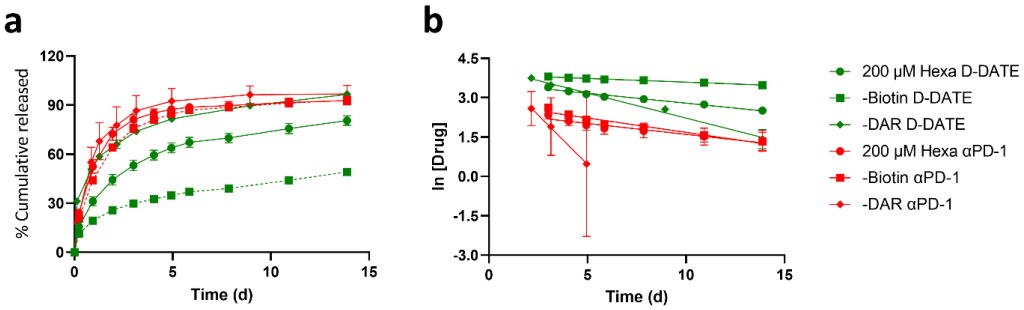

c

Biotin	ng d^{-1} after 3d	R^2	K_{eff}	R^2
200µM Hexa	102.6 ± 9.7	0.856	0.076 ± 0.005	0.900
No Biotin	76.0 ± 3.6	0.958	0.028 ± 0.001	0.962
-DARA	90.5 ± 7.6	0.934	0.189 ± 0.014	0.949

d

Biotin	ng d^{-1} after 3d	R^2	K_{eff}	R^2
200µM Hexa	40.9 ± 7.4	0.614	0.084 ± 0.015	0.633
No Biotin	62.2 ± 8.3	0.749	0.109 ± 0.012	0.820
-DARA	39.1 ± 21	0.251	0.088 ± 0.062	0.222

Figure S 5.10 Dual release of αPD-1 antibody (red) and D-DATE (green). (a) Cumulative release of the αPD-1 and D-DATE from a pCB hydrogel. (b) First order release plots of αPD-1 and D-DATE. K_{eff} and rate of infusion of dual release of D-DATE (c) and αPD-1 (d).

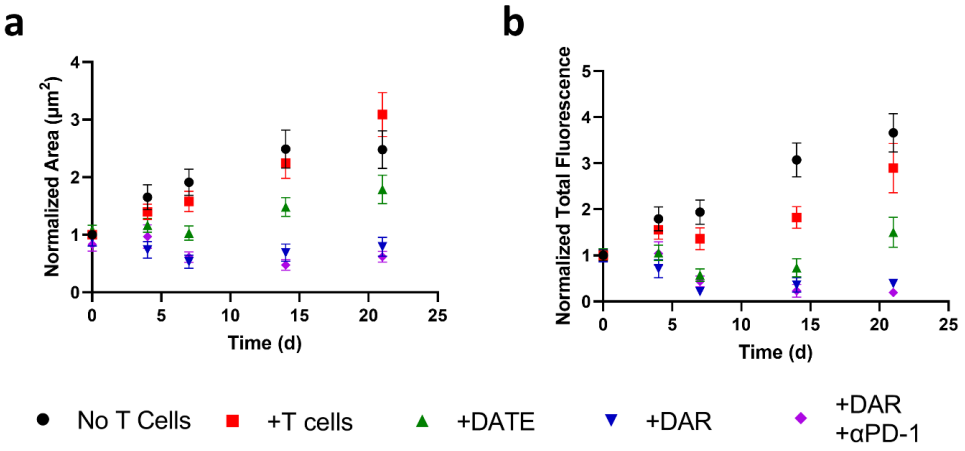

Figure S 5.11 Quantification of BT935 iRFP670 spheroid growth. (a) Fluorescent area of spheroid over time with respect to day 0. (b) Total fluorescence of spheroids over time with respect to day 0 (mean ± SEM).

CHAPTER 6. CONCLUSIONS

With a growing number of approved and in-development immunotherapeutics, biomaterials are needed to overcome transport barriers and immunosuppressive TIMEs to improve their safety and efficacy against solid tumors. Sustained and local immunotherapeutic delivery reduces systemic toxicity and maintains local therapeutic concentrations to maximize the duration and magnitude of the anti-cancer responses.[1–3]

6.1 Major Contributions

I developed an injectable poly(carboxybetaine) hydrogel with affinity controlled release with easily tunable release rates for the intratumoral delivery of immunotherapeutics for GBM. This thesis affirms the initial hypothesis demonstrating that sustained local release of a bispecific antibody improves efficacy in GBM treatments.

This thesis accomplishes the following major goals:

1. **Developed an easily tunable affinity based DDS for the delivery of a bioactive antibody**. Using a non-degradable agarose hydrogel as a model hydrogel, a competitive affinity release (CAR) mechanism composed of strong and reversible interactions of biotin and desthiobiotin to streptavidin was developed. The CAR DDS achieves

easily tunable release rates of a bioactive antibody amenable for long term applications.

2. **Developed an injectable and degradable in situ gelling poly(carboxybetaine) hydrogel using SPAAC chemistry suitable for local and sustained antibody delivery**. Using biorthogonal SPAAC chemistry, an in situ gelling, low-fouling, zwitterionic hydrogel was developed. Furthermore, I demonstrated the first pCB copolymer with a UCST due to ionic interactions.
3. **Introduced displacement affinity release (DAR) mechanism within in situ gelling pCB hydrogels for the local and sustained delivery of minimally modified antibodies and DATEs for GBM treatment.** With minimal modifications of the antibody, a displacement affinity release (DAR) system was developed that sustained and tuned the release of a bioactive antibody for >14 days from an injectable pCB hydrogel. The technology was also used to sustain and tune the release of a CD133 targeting DATE. The hydrogel with DAR remained low fouling and the hydrogel decreased the immunogenicity of the drug delivery components.
4. **Demonstrated how this delivery system can be efficacious against a PDX GBM mouse model**. Using DAR, I achieve local infusion of immunotherapeutics (LIIT), using a $CD133^+$ DATE in a PDX GBM mouse model as well as an in vitro spheroid model. I demonstrate

pCB-DAR can tune the release of the DATE. I further demonstrate that intracranial injections of the pCB-DAR DDS were well tolerated in vivo and can degrade and clear within a PDX mouse model. Furthermore, I demonstrate a survival benefit of LIIT in a GBM08 PDX mouse model. To increase efficacy and provide a more substantial survival benefit, I included αPD-1 antibody, thereby changing the T cell phenotype, and showed how this enhanced cancer killing in vitro. I the extend this and show the benefits of the DAR using a 3D embedded spheroid model of glioblastoma invasion. Demonstrating the efficacy of the release system in vitro, mimicking the in vivo conditions. Allowing for real time monitoring of efficacy.

In conclusion, the work described in this thesis demonstrated that low-fouling pCB hydrogels and displacement or competitive affinity release mechanisms can sustain and tune the release antibodies and immunotherapeutics for multiple weeks to maintain the MEC upon local injection into cancerous tissue. This technology and future renditions will aid in the treatment of solid tumors and other disease sites where antibody-based drugs encounter transport barriers and inhibitory immune environments.

6.2 Concluding Remarks

This thesis demonstrates the efficacy of LIIT in delivering a DATE in a GBM PDX mouse model, providing an example of using materials to enhance therapeutic efficacy. This thesis specifically shows development of a highly tunable affinity based drug delivery system and an amenable injectable, low-immunogenic hydrogel which can house said delivery system. This is the first reported use of a 3-component affinity based hydrogel release system where release rates were easily tuned through changing the concentration of a competitive binder and keeping the same affinity binding partners. We then utilize this system to locally deliver a bispecific antibody, extending the residence time of the antibody at the disease site, and showing a therapeutic benefit in a GBM PDX mouse model. Furthermore, we demonstrated the use of a 3D in vitro spheroid model can demonstrate the efficacy of the delivery system.

However, translation of this treatment modality requires the delivery of other therapies which correctly addresses the immunosuppressive GBM TIME and a corresponding animal which is a better representation of the human immune system. Furthermore, the current PDX mouse model requires exogenous delivery of T cells which is not a good representation of the T cell trafficking which occurs for effective immunotherapy. Syngeneic mouse models or humanized mice ($CD34^+$ hematopoietic stem cell transplanted NSG mice) can also provide insight into the immune cell recruitment without the need for exogenously implanted T

cells. Therefore, this thesis only demonstrated how pharmacokinetic parameters of the drug can be modulated to reach an efficacious treatment modality, translation of this treatment modality would require and understanding of T cell trafficking to the CNS. Additionally, the lack of a TSA or an efficacious TAA for GBM hinders the development of new drugs. A deeper biological understanding the immune-GBM interplay is necessary for future therapeutic modalities to be developed.

Future studies should aim towards using different affinity release interactions to achieve a broader range of release profiles and explore using immunomodulatory compounds that affect the TIME. Furthermore, in vivo studies testing the efficacy of releasing DATE with the addition of an αPD-1 ICI would be performed. The burgeoning field of immunoengineering has given rise to new innovative methods to enhance anti-cancer therapeutic efficacy. The field of materials science plays an important role in translating and dissecting cellular mechanisms which address the shortcomings of developed therapies such as enhancing the efficacy of vaccines and the effective delivery and activation of the immune system without incurring systemic toxicity. Current research efforts are focused on understanding the complex immune-cancer interplay and methods to modulate these interactions to create a translatable and robust anti-cancer response. By combining both engineering principles and a growing understanding of cancer mechanisms can we achieve translatable and effective therapies to treat a broad spectrum of cancers.

6.3 References

1. Han, X., Li, H., Zhou, D., Chen, Z. & Gu, Z. Local and Targeted Delivery of Immune Checkpoint Blockade Therapeutics. *Acc. Chem. Res.* **53**, 2521–2533 (2020).

2. Chen, Q., Wang, C., Chen, G., Hu, Q. & Gu, Z. Delivery Strategies for Immune Checkpoint Blockade. *Adv. Healthc. Mater.* **7**, 1800424 (2018).

3. Jin, Q., Liu, Z. & Chen, Q. Controlled release of immunotherapeutics for enhanced cancer immunotherapy after local delivery. *J. Control. Release* **329**, 882–893 (2020).